3. From the cosmic web to dark matter halos — theoretical

Outline

3.1 Overview

In this part, we present the effect of a large scale filamentary structure on the assembly of dark halos from a theoretical perspective.

3.2 "How does the cosmic web impact assembly bias?" (article)

The results presented here were published in Musso, Cadiou et al., 2018.

events.

Monthly Notices of the ROYAL ASTRONOMICAL SOCIETY

MNRAS **476,** 4877–4906 (2018) doi:10.1093/mnras/sty191

Advance Access publication 2018 January 26

How does the cosmic web impact assembly bias?

M. Musso,[1,2,3★] C. Cadiou,[1★] C. Pichon,[1,4] S. Codis,[5] K. Kraljic[6] and Y. Dubois[1]

[1] *Institut d'Astrophysique de Paris, CNRS and UPMC, UMR 7095, 98 bis Boulevard Arago, F-75014 Paris, France*
[2] *Institut de Physique Théorique, Université Paris Saclay and CEA, CNRS, F-91191 Gif-sur-Yvette, France*
[3] *East African Institute for Fundamental Research (ICTP-EAIFR), KIST2 Building, Nyarugenge Campus, University of Rwanda, Kigali, Rwanda*
[4] *Korea Institute of Advanced Studies (KIAS), 85 Hoegiro, Dongdaemun-gu, Seoul, 02455, Republic of Korea*
[5] *Canadian Institute for Theoretical Astrophysics, University of Toronto, 60 St. George Street, Toronto, ON M5S 3H8, Canada*
[6] *Aix Marseille Université, CNRS, LAM, Laboratoire d'Astrophysique de Marseille, Marseille, France*

Accepted 2018 January 17. Received 2018 January 17; in original form 2017 August 9

ABSTRACT

The mass, accretion rate, and formation time of dark matter haloes near protofilaments (identified as saddle points of the potential) are analytically predicted using a conditional version of the excursion set approach in its so-called upcrossing approximation. The model predicts that at fixed mass, mass accretion rate and formation time vary with orientation and distance from the saddle, demonstrating that assembly bias is indeed influenced by the tides imposed by the cosmic web. Starved, early-forming haloes of smaller mass lie preferentially along the main axis of filaments, while more massive and younger haloes are found closer to the nodes. Distinct gradients for distinct tracers such as typical mass and accretion rate occur because the saddle condition is anisotropic, and because the statistics of these observables depend on both the conditional means and their covariances. The theory is extended to other critical points of the potential field. The response of the mass function to variations of the matter density field (the so-called large-scale bias) is computed, and its trend with accretion rate is shown to invert along the filament. The signature of this model should correspond at low redshift to an excess of reddened galactic hosts at fixed mass along preferred directions, as recently reported in spectroscopic and photometric surveys and in hydrodynamical simulations. The anisotropy of the cosmic web emerges therefore as a significant ingredient to describe jointly the dynamics and physics of galaxies, e.g. in the context of intrinsic alignments or morphological diversity.

Key words: galaxies: evolution – galaxies: formation – galaxies: kinematics and dynamics – large-scale structure of Universe – cosmology: theory.

1 INTRODUCTION

The standard paradigm of galaxy formation primarily assigns galactic properties to their host halo mass. While this assumption has proven to be very successful, more precise theoretical and observational considerations suggest other hidden variables must be taken into account.

The mass–density relation (Oemler 1974), established observationally 40 yr ago, was explained (Kaiser 1984; Efstathiou et al. 1988) via the impact of the long-wavelength density modes of the dark matter (DM) field, allowing the proto-halo to pass earlier the critical threshold of collapse (Bond et al. 1991). This biases the mass function in the vicinity of the large-scale structure: the abundance of massive haloes is enhanced in overdense regions.

Numerical simulations have shown that denser environments display a population of smaller, older, highly concentrated 'stalled' haloes, which have stopped accreting and whose relationship with the environment is in many ways the opposite of that of large-mass actively accreting haloes that dominate their surroundings. This is the so-called assembly bias (e.g. Sheth & Tormen 2004; Gao, Springel & White 2005; Wechsler et al. 2006; Dalal et al. 2008; Paranjape & Padmanabhan 2017; Lazeyras, Musso & Schmidt 2017). More recently, Alonso, Eardley & Peacock (2015), Tramonte et al. (2017) and von Braun-Bates et al. (2017) have investigated the differential properties of haloes with respect to loci in the cosmic web. As they focused their attention to variations of the mass function, they also found them to vary mostly with the underlying density. Paranjape, Hahn & Sheth (2017) have shown that haloes in nodes and filaments behave as two distinct populations when a suitable variable based on the shear strength on a scale of the order of the halo's turnaround radius is considered.

In observations, galactic conformity (Weinmann et al. 2006) relates quenching of centrals to the quenching of their satellite galaxies. It has been detected for low- and high-mass satellite galaxies up to high redshift ($z \sim 2.5$, Kawinwanichakij et al. 2016) and

★ E-mail: mmusso@sas.upenn.edu (MM); cadiou@iap.fr. (CC)

fairly large separation (4 Mpc, Kauffmann et al. 2013). Recently, colour and type gradients driven specifically by the anisotropic geometry of the filamentary network have also been found in simulations (Laigle et al. 2017; Kraljic et al. 2018) using the Horizon-AGN simulation (Dubois et al. 2014), and observations using SDSS (Yan, Fan & White 2013; Martínez, Muriel & Coenda 2016; Poudel et al. 2017; Chen et al. 2017), GAMA (Alpaslan et al. 2016; Kraljic et al. 2018) and, at higher redshift, VIPERS (Malavasi et al. 2017) and COSMOS (Laigle et al. 2017). This suggests that some galactic properties do not only depend on halo mass and density alone: the co-evolution of conformal galaxies is likely to be connected to their evolution within the same large-scale anisotropic tidal field.

An improved model for galaxy evolution should explicitly integrate the diversity of the geometry of the environment on multiple scales and the position of galaxies within this landscape to quantify the impact of its anisotropy on galactic mass assembly history. From a theoretical perspective, at a given mass, if the halo is sufficiently far from competing potential wells, it can grow by accretion from its neighbourhood. It is therefore natural to expect, at fixed mass, a strong correlation between the accretion rate of haloes and the density of their environment (Zentner 2007; Musso & Sheth 2014b). Conversely, if this halo lies in the vicinity of a more massive structure, it may stop growing earlier and stall because its expected feeding will in fact recede towards the source of anisotropic tide (e.g. Dalal et al. 2008; Hahn et al. 2009; Ludlow, Borzyszkowski & Porciani 2014; Wang et al. 2011).

Most of the work carried out so far has focused on the role of the shear strength (a scalar quantity constructed out of the traceless shear tensor which does not correlate with the local density) measured on the same scale of the halo: as tidal forces act against collapse, the strength of the tide will modify the relationship of the halo with its large-scale density environments, and induce distinct mass assembly histories by dynamically quenching mass inflow (Hahn et al. 2009; Castorina et al. 2016; Borzyszkowski et al. 2016). Such local shear strength should be added, possibly in the form of a modified collapse model that accounts for tidal deformations, so as to capture e.g. the effect of a central on its satellites' accretion rate. This modified collapse model has been motivated in the literature on various grounds, e.g. as a phenomenological explanation of the scale-dependent scatter in the initial overdensity of proto-haloes measured in simulations (Ludlow et al. 2014; Sheth, Chan & Scoccimarro 2013) or as a theoretical consequence of the coupling between the shear and the inertia tensor which tends to slow down collapse (Bond & Myers 1996; Sheth, Mo & Tormen 2001; Del Popolo, Ercan & Gambera 2001). Notwithstanding, the position within the large-scale anisotropic cosmic web also directly conditions the local statistics, even without a modification of the collapse model, and affects different observables (mass, accretion rate, etc.) differently.

The purpose of this paper is to provide a mathematical understanding of how assembly bias is indeed partially *driven* by the anisotropy of large-scale tides imprinted in the so-called cosmic web. To do so, the formalism of excursion sets will be adapted to study the formation of structures in the vicinity of saddle points as a proxy for filaments of the cosmic web. Specifically, various tracers of galactic assembly will be computed conditional to the presence of such anisotropic large-scale structure. This will allow us to understand why haloes of a given mass and local density stall near saddles or nodes, an effect which is not captured by the density–mass relation, as it is driven solely from the traceless part of the tide tensor. This should have a clear signature in terms of the distinctions between contours of constant typical halo mass versus those of constant accretion rate, which may in turn explain the distinct mass and colour gradients recently detected in the above-mentioned surveys.

The structure of this paper is the following. Section 2 presents a motivation for extended excursion set theory as a mean to compute tracers of assembly bias. Section 3 presents the unconstrained expectations for the mass accretion rate and half-mass. Section 4 investigates the same statistics subject to a saddle point of the potential and computes the induced map of shifted mass, accretion rate, and half-mass time. It relies on the strong symmetry between the unconditional and conditional statistics. Section 5 provides a compact alternative to the previous two sections for the less theoretically inclined reader and presents directly the joint conditional and marginal probabilities of upcrossings explicitly as a function of mass and accretion rate. Section 6 reframes our results in the context of the theory of bias as the response of the mass function to variations of the matter density field. Section 7 wraps up and discusses perspectives. Appendix A sums up the definitions and conventions used in the text. Appendix B tests these predictions on realizations of Gaussian random fields (GRFs). Appendix C investigates the conditional statistics subject to the other critical points of the field. Appendix D presents the probability distribution function (PDF) of the eigenvalues at the saddle. Appendix E presents the covariance matrix of the relevant variables to the PDFs. Appendix F presents the relevant joint statistics of the field and its derivatives (spatial and with respect to filtering) and the corresponding conditional statistics of interest. Appendix G presents the generalization of the results for a generic barrier. Appendix H speculates about galactic colours.

2 BASICS OF THE EXCURSION SET APPROACH

The excursion set approach, originally formulated by Press & Schechter (1974), assumes that virialized haloes form from spherical regions whose initial mean density equals some critical value. The distribution of late-time haloes can thus be inferred from the simpler Gaussian statistics of their Lagrangian progenitors. The approach implicitly assumes approximate spherical symmetry (but not homogeneity), and uses spherical collapse to establish a mapping between the initial mean density of a patch and the time at which it recollapses under its own gravity.

According to this model, a sphere of initial radius R shrinks to zero volume at redshift z if its initial mean overdensity δ equals $\delta_c D(z_{\rm in})/D(z)$, where $D(z)$ is the growth rate of linear matter perturbations, $z_{\rm in}$ the initial redshift, and $\delta_c = 1.686$ for an Einstein–de Sitter universe, or equivalently, if its mean overdensity linearly evolved to $z = 0$ equals $\delta_c/D(z)$, regardless of the initial size. If so, thanks to mass conservation, this spherical patch will form a halo of mass $M = (4\pi/3)R^3\bar{\rho}$ (where $\bar{\rho}$ is the comoving background density) . The redshift z is assumed to be a proxy for its virialization time.

Bond et al. (1991) added to this framework the requirement that the mean overdensity in all larger spheres must be lower than δ_c, for outer shells to collapse at a later time. This condition ensures that the infall of shells is hierarchical, and the selected patch is not crushed in a bigger volume that collapses faster (the so-called *cloud-in-cloud* problem). The number density of haloes of a given mass at a given redshift is thus related to the volume contained in the largest spheres whose mean overdensity $\delta \equiv \delta(R)$ crosses δ_c. The dependence of the critical value δ_c on departures from spherical collapse induced by initial tides was studied by Bond & Myers (1996), and later

named "critical events" may be relevant parameters entering galaxy models, in particular to understand the evolution of galaxy properties that depend on the geometry of the accretion, such as their spin or their velocity-to-velocity-dispersion. This could readily be used to constrain further the assembly of dark matter halo by providing variables describing the evolution of the environnement.

In the current understanding of galaxy formation, the evolution of the baryons is driven by the cosmic web on large scales, while at small scales complex interactions between the gas, stars and AGNs and the dark matter halo drive most of the physics. While the impact of the cosmic web on halo formation can be studied to some extent from first principles, the complex physics at play in galaxy formation make the task much more tedious, if not impossible. This problem is usually tackled using cosmological simulations that reproduce as accurately as possible galaxy formation in a credible cosmological context. In this approach, a single testbed can be used to probe at the same time halo formation and galaxy formation. One of the questions these simulations can answer is the question of the link between dark matter halos and their galaxies. Indeed, some galaxy properties have been shown to be only weakly correlated to their halos'. One particular example, relevant to the formation of disks, is the spin of galaxy, which is found to be only weakly correlated to the halo disk (Hahn et al., 2010; Jiang et al., 2018) while the inner halo spin is well correlated with the galactic spin, which, at large redshifts is also well correlated to the principal axis of the large-scale tidal field. It has been suggested that one way for galaxies to grow a disk independently from their host halo's spin is through cold flows, which are the main driveway to funnel angular-momentum rich material from the cosmic web down to the innermost regions of the galaxies (Danovich et al., 2015; Nelson et al., 2015; Tillson et al., 2015), effectively connecting the large-scale environnement the spin of galaxies. Indeed, if the accretion history of the cold gas differ from that of the hot gas and DM, it can be expected that the response of the galaxy to the large scale perturbations will also be different, resulting in a differential evolution of the halo and its galaxy. Using a suite of numerical simulations and novel numerical methods, I have studied the formation of disk galaxies at large redshift and showed that the information acquired by the gas at large scale is transported to the inner regions of the halo and in the galaxy. In particular, cold flows are able to retain most of their angular momentum down to the inner halo. In the inner halo and around the disk, complex gravitational torques redistribute the angular momentum to the inner halo and the stellar component. I argue that this may lead to a good alignment of the inner halo and the galaxy, since their angular momentum is partially driven by their interaction with cold flows. This internal alignment is also expected to reflect the large-scale tidal field set by the cosmic web, as most of the anisotropic information is transported to the internal regions.

As a final conclusion, I have shown that the cosmic web is able to influence the assembly of dark matter halos. I have shown that one can build theoretical models in which part of the assembly bias can simply be interpreted as a large-scale environnement modulation, which cannot be parametrize easily in terms of the local properties of the field, both for dark matter halos and galaxies. I propose a set of parameters that are suited to the compact description of the evolution of the cosmic web and I argue that the geometry of the accretion onto galaxies via cold flows, and its evolution, can have a significant impact on the properties of galaxies, in particular against the ones sensible to the anisotropy of the flows, including notably the spin and the v/σ parameter. This is in particularly highlighted by a numerical study that showed that the angular momentum of the gas, set by the cosmic web, is effectively transported down to the galaxy where complex interactions redistribute it. I suggest that in order to capture effects beyond mass and density relations, new models of galaxy and halo formation should be augmented by parameters describing the non-local structure of the cosmic web at large-scales in terms of its critical points (nodes, filament and wall centers) but also in terms of their evolution, as described by critical that small halos growing in dense environnement are not able to accrete mass. As a consequence, these halos appear older resulting in an differential biasing as a function of formation time. In a similar way, Paranjape et al., 2018 suggested that the effect of halo concentration on the bias is well explained by a local quantification of the local tidal anisotropy. All these models are typically extensions of the halo model with new halo-centred probes of the larger-scale environnement.

Another possible approach followed in this dissertation is to relax the halo-centric assumption and work in the frame that sets the large scale environnement: the cosmic web. Indeed, due to the statistical properties of the initial conditions of the Universe, the different scales involved in galaxy formation and the formation of the cosmic web are coupled statistically. In particular, large-scale structures such as large filaments have an impact on the statistical properties of the field out of which halos grow, which has the effect of biasing halo assembly. One can argue that the assembly signal can explained simply in this biasing effect of the cosmic web: the cosmic web is responsible for driving the typical assembly history at fixed halo mass and local density.

This approach has already proven successful at providing a theoretical explanation to the spin-alignment problem (Codis et al., 2012). In this dissertation, I argue that the problem stated in these terms can also provide a valuable understanding of how halos grow, but also how their galaxy forms. Using an extension of the excursion set theory (Bond et al., 1991; Lacey and Cole, 1993; Mo and S. D. M. White, 1996), I showed in chapter 3 that the cosmic web, and in particular large scale filaments, biases the formation of dark matter halos. The formalism predicts that the variables entering the assembly history of the halo, namely the halo formation time and the accretion rate, are modulated by the cosmic web. As a result, at fixed final mass, halos forming close to nodes of the cosmic web are found to accrete more and have formed at later times, in agreement with n-body simulations for large-mass halos (Dalal et al., 2008; Gao et al., 2005; R. K. Sheth and Tormen, 2004; Wechsler et al., 2006). This effect complements other suggestions that the tide may be responsible for the assembly bias signal as it is purely geometric: as halos grow by accreting material, they also probe larger scales whose statistical structure is set by the cosmic web. I also argue that this provides a natural frame in which the assembly signal is simply a spatial modulation, or stated differently, different assembly histories are to be expected at different locations. This frame has since been used to show that, in hydrodynamical simulations, the cosmic web has also an effect on the assembly of galaxies. Kraljic et al., 2019 reported that the specific star formation rate and the velocity-to-velocity-dispersion ratio both present significant modulations in the direction of the filaments, highlighting that, indeed, filamentary structures can be used as a metric to parametrize the assembly of dark matter halos and galaxies therein.

Although a number of evidences are pointing towards an effect of the cosmic web on galaxy formation, the detailed physics that couples the former to the latter is still poorly understood. One of the issue lays in the description of the cosmic web itself, so that different methods may lead to different effects on galaxy formation. One key parameter to further study the effect of the cosmic web is then the question of its description, the challenge residing in its continuous and multi-scale nature. A large number of methods have been developed to tackle this issue and provide a clear frame in which galaxy properties can be studied (Bond et al., 1996; Sousbie et al., 2008 and Libeskind et al., 2018 for a review). In my dissertation, I suggest a new relevant parameter entering the formation of galaxies and dark halos, namely the evolution of the cosmic web. I present theoretical tool to account for it in a compact way and provide theoretical predictions of the evolution of the cosmic web in the Lagrangian space of the initial conditions and link them to the connectivity of the cosmic web Codis et al., 2018. Using an extension of the theory to the mildly non-linear regime, we show that one can connect our predictions to results obtained from n-body simulations. In particular, the formalism is able to detect halo merger events, but also filament- and wall-mergers in the Lagrangian initial conditions. I argue that these events,

by Sheth et al. (2001), who approximated it as a scale-dependent barrier. This will be further discussed in Section 7.2.

As the variation of $\delta(R)$ with scale resembles random diffusion, it is convenient to parametrize it with the variance

$$\sigma^2(R) \equiv \mathrm{Var}(\delta(R)) = \int \mathrm{d}k \frac{k^2 P(k)}{2\pi^2} W^2(kR) \tag{1}$$

of the stochastic process, smoothed with a real-space Top-Hat filter W,[1] rather than with R or M. In equation (1), $P(k)$ is the underlying power spectrum. The three quantities σ, R, and M are in practice interchangeable. The mass fraction in haloes of mass M at z is

$$\frac{M}{\bar\rho}\frac{\mathrm{d}n}{\mathrm{d}M} = \left|\frac{\mathrm{d}\sigma}{\mathrm{d}M}\right| f(\sigma), \tag{2}$$

where $\mathrm{d}n/\mathrm{d}M$ is the number density of haloes per unit mass (i.e. the mass function) and $f(\sigma)$ – often called the halo multiplicity – is the probability distribution of the first-crossing scale of the random walks, that is of the smallest σ (largest R) for which

$$\delta(R, \boldsymbol{r}) \equiv \int \frac{\mathrm{d}^3 k}{(2\pi)^3} \delta_{\mathrm{m}}(\boldsymbol{k}) W(kR) \mathrm{e}^{i\boldsymbol{k}\cdot\boldsymbol{r}} = \frac{\delta_{\mathrm{c}}}{D(z)}, \tag{3}$$

where δ_{m} is the (unsmoothed) matter density. The first-crossing requirement avoids double counting and guarantees that $f(\sigma)$ is a well-behaved probability distribution, and the resulting mass fraction is correctly normalized. In equation (3), the linear growth factor, $D(z)$, is defined as a function of redshift via

$$D(z) = \frac{H(a)}{H_0} \int_0^a \frac{\mathrm{d}a}{\sqrt{\Omega_{\mathrm{m}}/a + \Omega_\Lambda a^2}}, \text{ with } a = \frac{1}{1+z}. \tag{4}$$

At early time, $D(z)$ scales like $1/(1+z)$. Here, $H(a) = H_0\sqrt{\Omega_{\mathrm{m}}/a + \Omega_\Lambda a^2}$ is the Hubble constant.

The first-crossing probability, $f(\sigma)\Delta\sigma$, is the fraction of walks that cross the threshold between $\sigma - \Delta\sigma$ and σ for the first time. Considering discretized trajectories with a large number of steps $\sigma_1, \ldots, \sigma_N$ of width $\Delta\sigma \equiv \sigma_i - \sigma_{i-1}$ (corresponding to concentric spheres of radii $R_1, \ldots, R_N$), the first-crossing probability is the joint probability that $\delta_N > \delta_{\mathrm{c}}$ and $\delta_i < \delta_{\mathrm{c}}$ for $i < N$, with $\delta_i \equiv \delta(\sigma_i)$ and $\sigma_N = \sigma = N\Delta\sigma$. Hence, the distribution $f(\sigma)$ is formally defined as the limit

$$f(\sigma) \equiv \lim_{\Delta\sigma\to 0} \frac{1}{\Delta\sigma} \langle \vartheta(\delta_N - \delta_{\mathrm{c}}) \prod_i^{N-1} \vartheta(\delta_{\mathrm{c}} - \delta_i) \rangle, \tag{5}$$

where $\vartheta(x)$ is Heaviside's step function, and the expectation value is evaluated with the multivariate distribution $p(\delta_1, \ldots, \delta_N)$. This definition discards crossings for which $\delta_i > \delta_{\mathrm{c}}$ for any $i < N$, since $\vartheta(\delta_{\mathrm{c}} - \delta_i) = 0$, assigning at most one crossing (the first) to each trajectory. For instance, in Fig. 1, trajectory B would not be assigned the crossing marked with (3), since the trajectory lies above threshold between (1) and (2). Since taking the mean implies integrating over all trajectories weighed by their probability, $f(\sigma)$ can be interpreted as a path integral over all allowed trajectories with fixed boundary conditions $\delta(0) = 0$ and $\delta(\sigma) = \delta_{\mathrm{c}}$ (Maggiore & Riotto 2010).

In practice, computing $f(\sigma)$ becomes difficult if the steps of the random walks are correlated, as is the case for real-space Top-Hat filtering with a Λ cold dark matter (ΛCDM) power spectrum, and for most realistic filters and cosmologies. For this reason, more easily tractable but less physically motivated sharp cut-offs in Fourier

[1] The window function in Fourier space is $W(x) = 3j_1(x)/x$, j_1 being the spherical Bessel function of order 1.

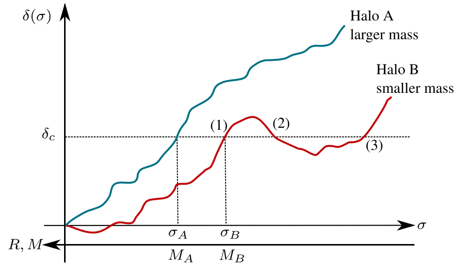

Figure 1. Pictorial description of the first-crossing and upcrossing conditions to infer the halo mass from the excursion set trajectory. The first-crossing condition on σ assigns at most one halo to each trajectory, with mass $M(\sigma)$. Upcrossing may instead assign several masses to the same trajectory (that is, to the same spatial location), thus overcounting haloes. Trajectory B in the figure has a first crossing (upwards) at scale σ_{B} (1), a downcrossing (2), and second upcrossing (3), but the correct mass is only given by σ_{B}. However, the correlation of each step with the previous ones makes turns in small intervals of σ exponentially unlikely: at small σ most trajectories will thus look like trajectory A. Thanks to the correlation between steps at different scales, for small σ (large M) simply discarding downcrossings is a very good approximation.

space have been often preferred, for which the correlation matrix of the steps becomes diagonal, treating the correlations as perturbations (Maggiore & Riotto 2010; Corasaniti & Achitouv 2011). The upcrossing approximation described below can instead be considered as the opposite limit, in which the steps are assumed to be strongly correlated (as is the case for a realistic power spectrum and filter). This approximation is equivalent to constraining only the last two steps of equation (5), marginalizing over the first $N-2$.

2.1 The upcrossing approximation to $f(\sigma)$.

Indeed, Musso & Sheth (2012) noticed that for small enough σ (i.e. for large enough masses), the first-crossing constraint may be relaxed into the milder condition

$$\delta' \equiv \frac{\mathrm{d}\delta}{\mathrm{d}\sigma} > 0; \tag{6}$$

that is, trajectories simply need to reach the threshold with positive slope (or with slope larger than the threshold's if δ_{c} depends on scale). This upcrossing condition may assign several haloes of different masses to the same spatial location. For this reason, while first crossing provides a well-defined probability distribution for σ (e.g. with unit normalization), upcrossing does not. However, since the first crossing is necessarily upwards, and downcrossings are discarded, the error introduced in $f(\sigma)$ by this approximation comes from trajectories with two or more turns. Musso & Sheth (2012) showed that these trajectories are exponentially unlikely if σ is small enough when the steps are correlated. The first-crossing and upcrossing conditions to infer the halo mass from excursion sets are sketched in Fig. 1: while the trajectory A would be (correctly) assigned to a single halo, the second upcrossing of trajectory B in the figure would be counted as a valid event by the approximation, and the trajectory would (wrongly) be assigned to two haloes. The probability of this event is non-negligible only if σ is large.

Returning to equation (5), expanding δ_{N-1} around δ_N gives

$$\vartheta(\delta_{\mathrm{c}} - \delta_{N-1}) \simeq \vartheta(\delta_{\mathrm{c}} - \delta_N) + \delta_{\mathrm{D}}(\delta_{\mathrm{c}} - \delta)\delta'\Delta\sigma, \tag{7}$$

where the crossing scale σ, giving the halo's final mass M, is defined implicitly in equation (3), as the solution of the equation $\delta(\sigma) = \delta_c/D$.[2] The assumption that this upcrossing is first crossing allows us to marginalize over the first $N-2$ variables in equation (5) without restrictions. The first term has no common integration support with $\vartheta(\delta_N - \delta_c)$, and only the second one – containing the Jacobian $(\delta' - \delta_c')$ – contributes to the expectation value (throughout the text, a prime will denote the derivative $\mathrm{d}/\mathrm{d}\sigma$). Adopting for convenience the normalized walk height $\nu \equiv \delta/\sigma$, for which $\langle \nu^2\rangle = 1$, the corresponding density of solutions in σ-space obeys

$$\left|\nu' - \nu_c'\right| \delta_D(\nu - \nu_c) = (|\delta'|/\sigma)\,\delta_D(\nu - \nu_c)\,, \tag{8}$$

where $\nu_c \equiv \delta_c/(\sigma D)$ is the rescaled threshold. The probability of upcrossing at σ in equation (5) is therefore simply the expectation value of this expression,

$$f_{\rm up}(\sigma) \equiv p_G(\nu = \nu_c)\int_0^\infty \mathrm{d}\delta' \delta' p_G(\delta'|\nu_c)\,, \tag{9}$$

where the integral runs over $\delta' > 0$ because of the upcrossing condition (6). Usually, one sets $D = 1$ at $z = 0$ for simplicity so that $\nu_c = \delta_c/\sigma$. For Gaussian initial conditions,[3] the conditional distribution $p_G(\delta'|\nu_c)$ is a Gaussian with mean ν_c and variance $1/\Gamma^2$, where

$$\Gamma^2 = \frac{1}{\langle\delta'^2\rangle - 1} = \frac{\gamma^2}{1-\gamma^2} = \frac{1}{\sigma^2\langle\nu'^2\rangle}\,, \tag{10}$$

and $\gamma^2 = \langle\delta'\delta\rangle^2/\langle\delta'^2\rangle\langle\delta^2\rangle$ is the cross-correlation coefficient between the density and its slope.[4] Thanks to this factorization, integrating equation (9) over δ' yields the fully analytical expression

$$f_{\rm up}(\sigma) = p_G(\nu_c)\frac{\mu}{\sigma}F(X)\,, \tag{11}$$

where p_G is a Gaussian with mean $\langle\nu\rangle = 0$ and variance $\mathrm{Var}(\nu) = 1$. For a constant barrier (see Appendix G for the generalization to a non-constant case), the parameters μ and X are defined as

$$\mu \equiv \langle\delta'|\nu_c\rangle = \nu_c\,, \quad \text{and} \quad X \equiv \frac{\mu}{\sqrt{\mathrm{Var}\,(\delta'|\nu_c)}} = \Gamma\nu_c\,, \tag{12}$$

with

$$F(x) \equiv \int_0^\infty \mathrm{d}y\,\frac{y}{x}\frac{\mathrm{e}^{-(y-x)^2/2}}{\sqrt{2\pi}} = \frac{1+\mathrm{erf}(x/\sqrt{2})}{2} + \frac{\mathrm{e}^{-x^2/2}}{x\sqrt{2\pi}}\,, \tag{13}$$

which is a function that tends to 1 very fast as $x \to \infty$, with correction decaying like $\exp(-x^2/2)/x^3$. It departs from one by $\sim$8 per cent for a typical $\Gamma\nu_c \sim 1$. Equation (11) can be written explicitly as

$$f_{\rm up}(\sigma) = \frac{\nu_c \mathrm{e}^{-\nu_c^2/2}}{\sigma\sqrt{2\pi}}F(\Gamma\nu_c)\,, \tag{14}$$

where the first factor in the right-hand side (RHS) of equation (14) is the result of Press & Schechter (1974), ignoring the factor of 2, they introduced by hand to fix the normalization. For correlated steps, their non-normalized result reproduces well the large-mass tail of $f(\sigma)$ (which is automatically normalized to unit and requires to correcting factor), but it is too low for intermediate and small masses. The upcrossing probability $f_{\rm up}(\sigma)$ also reduces to this result in the large-mass limit, when $\Gamma\nu_c \gg 1$ and $F(\Gamma\nu_c) \simeq 1$. However, for correlated steps $f_{\rm up}(\sigma)$ is a very good approximation of $f(\sigma)$ on a larger mass range. For a ΛCDM power spectrum, the agreement is good for halo masses as small as $10^{12}\,\mathrm{M}_\odot\,h^{-1}$, well below the peak of the distribution. The deviation from the strongly correlated regime is parametrized by $\Gamma\nu_c$, which involves a combination of mass and correlation strength: the approximation is accurate for large masses (small σ and large ν_c) or strong correlations (large Γ). Although Γ mildly depends on σ, fixing $\Gamma^2 \sim 1/3$ (or $\gamma \sim 1/2$) can be theoretically motivated (Musso & Sheth 2014c) and mimics well its actual value for real-space Top-Hat filtering in ΛCDM on galactic scales. The limit of uncorrelated steps ($\Gamma = 0$), whose exact solution is twice the result of Press & Schechter (1974), is pathological in this framework, with $f_{\rm up}$ becoming infinite. More refined approximation methods can be implemented in order to interpolate smoothly between the two regimes (Musso & Sheth 2014a).

From equation (11), a characteristic mass $M_\star$ can be defined by requesting that the argument of the Gaussian be equal to one, i.e. $\nu_c = 1$ or $\sigma(M_\star) = \delta_c/D$. This defines $M_\star$ implicitly via equation (1) for an arbitrary cosmology. This quantity is particularly useful because $f_{\rm up}(\sigma)$ does not have well-defined moments (in fact, even its integral over σ diverges). This is a common feature of first passage problems (Redner 2001), not a problem of the upcrossing approximation: even when the first-crossing condition can be treated exactly, and $f(\sigma)$ is normalized – it is a distribution function –, its moments still diverge. Therefore, given that the mean $\langle M\rangle$ of the resulting mass distribution cannot be computed, $M_\star$ provides a useful estimate of a characteristic halo mass.

2.2 Joint and conditional upcrossing probability

The purpose of this paper is to recompute excursion set predictions such as equation (11) in the presence of additional conditions imposed on the excursions. Adding conditions (like the presence of a saddle at some finite distance) will have an impact not only on the mass function of DM haloes, but also on other quantities such as their assembly time and accretion rate.

Let us present in full generality how the upcrossing probability is modified by such supplementary conditions. When, besides $\delta(\sigma) = \delta_c$ and the upcrossing condition, a set of N linear[5] functional constraints $\{\mathcal{F}_1[\delta], \ldots, \mathcal{F}_N[\delta]\} = \{v_1, \ldots, v_N\}$ on the density field is enforced, the additional constraints modify the joint distribution of ν and ν'. The conditional upcrossing probability may be obtained by replacing $p(\nu, \nu')$ with $p(\nu, \nu'|\{v\})$ in equation (9). For a Gaussian process, when the functional constraints do not involve δ', this replacement yields after integration over the slope

$$f_{\rm up}(\sigma, \{v\}) = p_G(\nu_c, \{v\})\frac{\mu_v}{\sigma}F(X_v)\,, \tag{15}$$

where $p_G(\nu_c|\{v\})$ is a Gaussian with mean $\langle\nu|\{v\}\rangle$ and variance $\mathrm{Var}\,(\nu|\{v\})$, while μv and Xv are defined as

$$\mu_v \equiv \langle\delta'|\nu_c, \{v\}\rangle\,, \quad X_v \equiv \frac{\mu_v}{\sqrt{\mathrm{Var}\,(\delta'|\nu_c, \{v\})}}\,, \tag{16}$$

and $\langle\delta'|\nu_c, \{v\}\rangle$ and $\mathrm{Var}\left(\delta'|\nu_c, \{v\}\right)$ are the mean and variance of the conditional distribution, $p_G(\delta'|\nu_c, \{v\})$ given by equations (F10) and (F11) and evaluated at $\delta = \delta_c$, while F is given by equation (13). Equation (15) is formally the conditional counterpart to equation

[2] A careful calculation shows that the step function should be asymmetric, so that $\vartheta(\delta - \delta_c) = 1$ when $\delta = \delta_c$ instead of 1/2.

[3] No conceptual complications arise in dealing with a non-Gaussian distribution, which is none the less beyond the scope of this paper.

[4] Recalling that $\langle\delta'\delta\rangle = \sigma$ so that $\gamma^2 = 1/\langle\delta'^2\rangle$.

[5] Indeed the saddle condition below imposes linear constraints on the contrast and the potential, since the saddle's height and curvature are fixed.

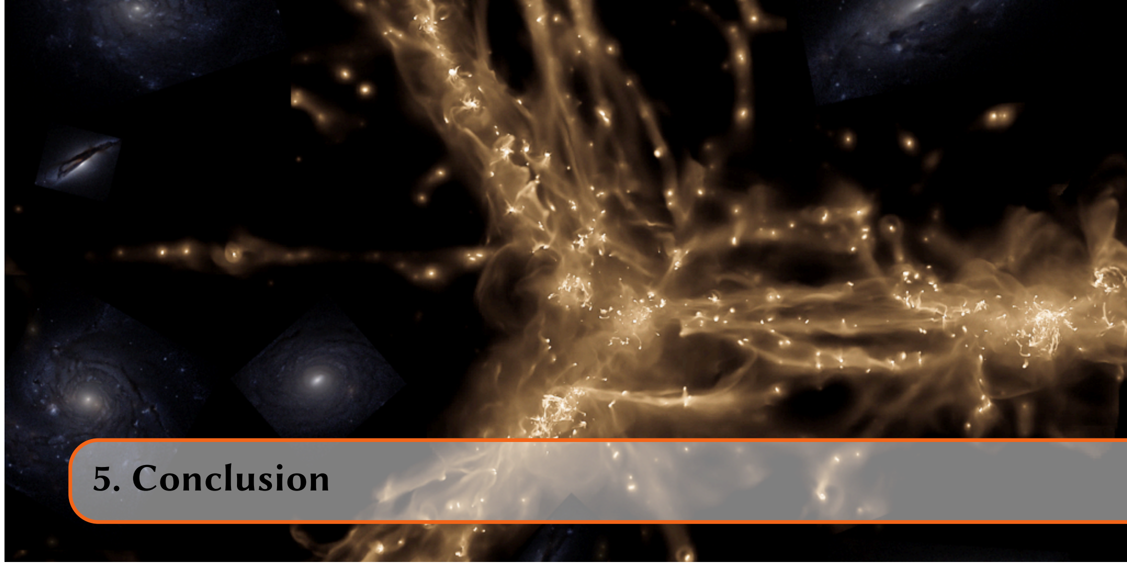

5. Conclusion

One of the success of the ΛCDM model is its ability to predict a significant number of properties of DM halos and their galaxies. In the classical model of galaxy formation, galaxy form out of the condensation of the gas in the potential well of their host halo. As such, this model is usually parametrized in terms of the mass of the halo — which sets the amount of gas available and the internal kinematics — and the local density — which regulates gas accretion and pair interactions. The classical model intrinsically supposes that halo properties, and as a consequence, galaxy properties are only influenced by their local environnement via the local density, with some extensions probing also the local tidal environnement (Alam et al., 2019) (TODO: citations). This model has proven successful at predicting a large number of galactic properties, such as their spatial clustering or their mass function.

However, it has been established that the clustering of dark matter halos, as measured by the halo bias, not only depends on halo mass but also on other halo properties such as formation time, concentration, spin and ellipticity (Gao et al., 2005; Gao and S. D. M. White, 2007; Hahn et al., 2007; Wechsler et al., 2006). This problem, commonly referred to as the "assembly-bias problem" can be rephrased as follow: the clustering of dark matter halos and their properties are correlated, beyond a mere mass and density relation. On large scales, surveys like the SDSS have revealed that the Universe is structured around voids, sheets, filaments and knots that form the cosmic web. Using a different approach, a growing number of evidence (Kraljic et al., 2018; Kraljic et al., 2019; Welker et al., 2014) have since showed that some halo and galaxy properties present distinct features at different locations in the cosmic web. One striking example is spin-alignments which have been measured for DM halos (e.g. Codis et al., 2012) and galaxies (e.g. Chisari et al., 2017), but also colour segregation (Kraljic et al., 2019; Laigle et al., 2018).

In the context of assembly bias, many extensions of the halo model have been suggested aimed to understand the modulation effects of the cosmic web in terms of local properties. In particular, it has suggested that the local tidal field may explain part of the assembly bias signal (e.g. Hahn et al., 2009; Ludlow et al., 2014) when formulated in terms of the formation time. Tidal forces induce a shear flow in the vicinity of small halos that flow along filaments on the cosmic web. One of the outcome is that the accretion rate of small halos is decreased by neighbouring structures, so

Table 1. List of variables for the three different probabilities studied in the text (upcrossing, accretion rate given upcrossing, and formation time given upcrossing), conditioned or not to the presence of the saddle point, split by whether they relate to the height of the excursion set trajectory or its slope. Variables like μ and X always appear as $\mu F(X)$ and describe the mean slope of the upcrossing trajectories given the different conditions (presence of the saddle and/or height $\nu_{\rm f}$ of the trajectory at formation). The unconditional case has $\mu = \nu_{\rm c}$ and $X = \Gamma\nu_{\rm c}$. The remaining variables appear as arguments of a Gaussian, and are used to define the typical values $\sigma_\star$, $\alpha_\star$, and $D_\star$ of the excursion set variables σ, α, and $D_{\rm f}$. The height-related variables describe the probability of reaching the collapse threshold $\nu_{\rm c}$ (unconditional or given the saddle), or the formation threshold $\nu_{\rm f}$ given $\nu_{\rm c}$ (with or without saddle). The slope-related ones describe the probability of having at upcrossing the slope corresponding to a given accretion rate. See also Table A1.

	Without saddle		With saddle	
	Height	Slope	Height	Slope
Upcrossing (σ)	$\nu_{\rm c}$	μ, X	$\nu_{{\rm c},\mathcal{S}}$	$\mu_{\mathcal{S}}, X_{\mathcal{S}}$
Accretion (α)		Y_α		$Y_{\alpha,\mathcal{S}}$
Formation ($D_{\rm f}$)	$\nu_{\rm f,\,c}$	$\mu_{\rm f}, X_{\rm f}$	$\nu_{{\rm f,c},\mathcal{S}}$	$\mu_{{\rm f},\mathcal{S}}, X_{{\rm f},\mathcal{S}}$

(11), while incorporating extra constraints corresponding to e.g. the large-scale Fourier modes of the cosmic web.

The brute force calculation of the conditional means and variances entering equation (15) can rapidly become tedious. To speed up the process, and gain further insight, one can write the conditional statistics of δ' in terms of those of δ and their derivatives. This is done explicitly in Appendix F1, which allows us to write explicitly the conditional probability of upcrossing at σ given $\{v\}$, obtained by dividing equation (15) by $p(\{v\})$, as

$$f_{\rm up}(\sigma|\{v\}) = -\nu'_{{\rm c},v}\,\frac{{\rm e}^{-\nu_{{\rm c},v}^2/2}}{\sqrt{2\pi}}\,F\left(-\frac{\nu'_{{\rm c},v}}{\sqrt{{\rm Var}\left(\nu'_v\right)}}\right), \tag{17}$$

given

$$\nu_{{\rm c},v} \equiv \frac{\delta_{\rm c} - \langle\delta|\{v\}\rangle}{\sqrt{{\rm Var}\,(\delta|\{v\})}}, \quad \text{and} \quad \nu'_{{\rm c},v} \equiv \frac{{\rm d}\nu_{{\rm c},v}}{{\rm d}\sigma}, \tag{18}$$

where these conditionals and variances can be expressed explicitly in terms of the constraint via equations (F8)–(F11). Equation (17) is therefore also formally equivalent to equation (14), upon replacing $\nu_{\rm c} \to \nu_{{\rm c},\,v}$ and $\langle \nu'^2\rangle \to \langle \nu_v'^2\rangle$ to account for the constraint. Remarkably, the conditional probability $f_{\rm up}(\sigma|\{v\})$ is thus simply expressed as an unconditional upcrossing probability for the effective unit variance process obtained from the conditional density.

The above-sketched formal procedure will be applied to practical constraints in the next section. For convenience and consistency, Table 1 lists all the variables that are introduced in the following sections, for the combinations of the various constraints (on the slope at crossing, on the height of the trajectory at $\sigma(M/2)$, and on the presence of a saddle) that will be imposed.

3 ACCRETION RATE AND FORMATION TIME

Let us first present the tracers of galactic assembly when there is no large-scale saddle. Specifically, this section will consider the DM mass accretion rate and formation redshift. It will compute the joint PDFs, the corresponding marginals, typical scales, and expectations. Its main results are the derivation of the conditional probability of the accretion rate – equation (25) – and formation time – equation (36) – for haloes of a given mass. The emphasis will be on derivation in the language of excursion set. The reader

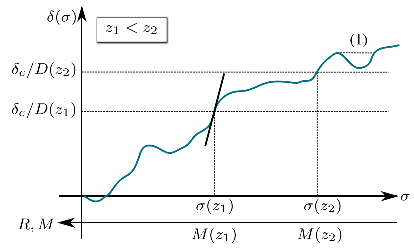

Figure 2. Pictorial representation of the procedure to infer accretion rates from excursion sets. As the redshift z grows, the barrier $\delta_{\rm c}/D(z)$ becomes higher and the first-crossing scale $\sigma(z)$ moves to the right, towards smaller masses. This procedure reconstructs the entire mass accretion history $M(z)$ from the first-crossing history $\sigma(D)$. As the two redshifts z_1 and z_2 in figure get close to each other, the difference between $\sigma(z_1)$ and $\sigma(z_2)$ is completely fixed by the slope of the trajectory. This deterministic relation connects the excursion set slope to the halo's instantaneous mass accretion rate. Finite jumps of the first-crossing σ after a downturn [where the inverse function $\sigma(\delta)$ becomes multivalued, as in (1)] cannot describe smooth accretion and are traditionally associated with large mergers.

only concerned with statistical predictions in terms of quantities of direct astrophysical interest may skip to Section 5.

Following Lacey & Cole (1993), the entire mass accretion history of the halo is encoded in the portion of the excursion set trajectory after the first crossing: solving the implicit equation (3) at all z enables to reconstruct $M(z)$. As the barrier $\delta_{\rm c}/D(z)$ decreases with time (since $D(z)$ grows as z decreases), the first-crossing scale moves towards smaller values (larger masses), thereby describing the accretion of mass on to the halo. Clearly, since $\delta(\sigma)$ is not monotonic, $M(z)$ is not a continuous function. Finite jumps of the first-crossing scale, corresponding to portions for which σ is not a global maximum of the interval [0, σ], can be interpreted as mergers (see trajectory B in Fig. 1, or the portion marked with (1) in Fig. 2). In the upcrossing approximation, the constraint $\delta'(\sigma) > 0$ discards the downward part of each jump.

3.1 Accretion rate

In the language of excursion sets, finding the mass accretion history is equivalent to reconstructing the function $\sigma(D)$ [where D was defined in equation (4)]: because the barrier grows as D decreases with z, the crossing scale σ moves towards larger values (smaller masses). Differentiating both sides of equation (3) with respect to z gives

$$\alpha \equiv -\frac{D}{\sigma}\frac{{\rm d}\sigma}{{\rm d}D} = \frac{\delta_{\rm c}}{\sigma\delta'} = \frac{\nu_{\rm c}}{\sigma(\nu' - \nu_{\rm c}')}, \tag{19}$$

where α measures the fractional change of the first-crossing scale $\sigma(M)$ with $D(z)$, and is related to the instantaneous relative mass accretion rate by

$$\frac{1}{M}\frac{{\rm d}M}{{\rm d}z} \equiv \frac{\dot M}{M} = \alpha\frac{{\rm d}\log D}{{\rm d}z}\left(-\frac{{\rm d}\log M}{{\rm d}\log\sigma}\right). \tag{20}$$

The upcrossing condition implies that $\alpha > 0$: excursion set haloes can only increase their mass, since ${\rm d}\log M/{\rm d}\log\sigma < 0$.

A pictorial representation of this procedure is given in Fig. 2. Equation (19) gives a relation between the accretion rate of the final haloes and the Lagrangian slope of the excursion set trajectories, which is statistically meaningful in the framework of excursion sets with correlated steps (because the slope then has finite variance). Note that α scales both like the inverse of the slope δ' and the logarithmic rate of change of σ with D. It also essentially scales like the relative accretion rate, $\dot{M}/M$ since in equation (20) $\mathrm{d}\log D/\mathrm{d}z$ is simply a time-dependent scaling, while on galactic scales, $(n \sim 2)$, $\mathrm{d}\log M/\mathrm{d}\log\sigma \sim -6$ (see also Section 5 and Appendix E for the generic formula).

Fixing the accretion rate establishes a local bidimensional mapping between $\{\nu, \nu'\}$, or $\{\delta, \delta'\}$, and $\{\sigma, \alpha\}$, defined as the solutions of the bidimensional constraint

$$\mathcal{C} \equiv \{\nu(\sigma) - \nu_c, \nu'(\sigma) - \nu_c' - \nu_c/\sigma\alpha\} = \mathbf{0}\,. \tag{21}$$

The density of points in the (σ, α) space satisfying the constraint is

$$|\det(\partial\mathcal{C}/\partial\{\sigma, \alpha\})|\,\delta_{\mathrm{D}}^{(2)}(\mathcal{C})\,. \tag{22}$$

Since $\partial(\nu - \nu_c)/\partial\alpha = 0$, the determinant in equation (22) is simply $|(\nu' - \nu_c')(\nu_c/\sigma\alpha^2)| = \nu_c^2/\sigma^2\alpha^3$, and is no longer a stochastic variable. Taking the expectation value of equation (22) gives

$$f_{\mathrm{up}}(\sigma, \alpha) = \frac{\nu_c^2}{\sigma^2\alpha^3}\,p_{\mathrm{G}}(\nu_c, \nu_c' + \nu_c/\sigma\alpha),$$
$$= \frac{\Gamma\nu_c^2}{\sigma\alpha^3}\frac{\mathrm{e}^{-\nu_c^2/2}}{\sqrt{2\pi}}\frac{\mathrm{e}^{-Y_\alpha^2/2}}{\sqrt{2\pi}}\,, \tag{23}$$

with [using the conditional mean $\mu = \nu_c$ from equation (12)]

$$Y_\alpha \equiv \frac{\nu_c/\alpha - \mu}{\sqrt{\mathrm{Var}\,(\delta'|\nu_c)}} = \Gamma(\sigma\nu_c' + \nu_c/\alpha)\,, \tag{24}$$

which is the joint probability of upcrossing at σ with accretion rate α.[6] This can be formally recovered setting $\langle\delta'|\nu_c, \alpha\rangle = \nu_c/\alpha$ and $\mathrm{Var}\left(\delta'|\nu_c, \alpha\right) \to 0$ in equation (16) (because the constraint fixes δ' completely), which gives $F(X_\alpha) = 1$ as needed.

The conditional probability of having accretion rate α given upcrossing at σ can be obtained taking the ratio of equations (23) and (14), which gives

$$f_{\mathrm{up}}(\alpha|\sigma) = \frac{\Gamma\nu_c}{\alpha^3}\frac{\mathrm{e}^{-Y_\alpha^2/2}}{\sqrt{2\pi}\,F(\Gamma\nu_c)}\,, \tag{25}$$

and represents the main result of this subsection. The exact form of $f_{\mathrm{up}}(\alpha|\sigma)$ from equation (25), as σ changes is shown in Fig. 3. This conditional probability has a well-defined mean value, which reads

$$\langle\alpha|\sigma\rangle = \int_0^\infty \mathrm{d}\alpha\,\alpha\,f_{\mathrm{up}}(\alpha|\sigma) = \frac{1 + \mathrm{erf}(\Gamma\nu_c/\sqrt{2})}{2F(\Gamma\nu_c)}\,; \tag{26}$$

however, the second moment $\langle\alpha^2|\sigma\rangle$ and all higher order statistics are ill defined. The nth moment is in fact proportional to the expectation value of $(1/\delta')^{n-1}$ (over positive slopes and given ν_c), which is divergent. Equation (25) shows that very small values of α (corresponding to very steep slopes) are exponentially unlikely, and very large ones (shallow slopes) are suppressed as a power law. Unlike $f_{\mathrm{up}}(\sigma)$, the conditional distribution $f_{\mathrm{up}}(\alpha|\sigma)$ is a well-defined normalized PDF. However, it is still an approximation to the exact PDF, as it assumes that the distribution of the slopes at first crossing is a (conditional) Gaussian. This assumption is accurate for steep slopes, but overestimates the shallow-slope tail, for which the exact first-crossing condition would impose a boundary condition $p_{\mathrm{G}}(\delta' = 0|\delta_c) = 0$. The higher moments of the exact conditional

[6] As expected, marginalizing equation (23) over $\alpha > 0$ gives back equation (11), upon setting $\Gamma\nu_c/\alpha = x$.

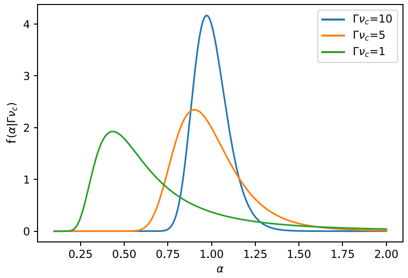

Figure 3. Plot of the conditional PDF $f_{\mathrm{up}}(\alpha|\sigma)$ of the accretion rate for values of σ corresponding to $\Gamma\nu_c = 10, 5$, and1. As the mass gets smaller, so does $\Gamma\nu_c$ and the conditional PDF moves towards smaller accretion rates α. Therefore, haloes of smaller mass tend to accrete less.

distribution of accretion rates should be convergent. However, even if this was not the case, let us stress that these divergences would not represent a pathology of excursion sets, but are instead a rather common feature of first-passage statistics in a cosmological context.

Regardless of convergence issues, it remains true that the estimate (26) of the mean $\langle\alpha|\sigma\rangle$ gets a significant contribution from the less accurate side of the distribution. One may therefore look for other more informative quantities. In analogy with $M_\star$, defined as the value of M for which $\nu_c = 1$, one can define the characteristic accretion rate $\alpha_\star$ as the value for which Y_α, the argument of the Gaussian in equation (25), equals one

$$\alpha_\star(\sigma) = \frac{\Gamma\nu_c}{1 + \Gamma\nu_c}\,. \tag{27}$$

For the above-mentioned typical value, it follows that $\alpha_\star(M_\star) = \left(\sqrt{3} - 1\right)/2 \approx 1/3$. Another useful quantity is the most likely value of the accretion rate, corresponding to the maximum $\alpha_{\max}$ of $f_{\mathrm{up}}(\alpha|\sigma)$. Requesting the derivative of the PDF to vanish, one gets

$$\alpha_{\max}(\sigma) = \frac{(\Gamma\nu_c)^2}{6}\left[\sqrt{1 + \frac{12}{(\Gamma\nu_c)^2}} - 1\right]. \tag{28}$$

All three quantities $\langle\alpha|\sigma\rangle$, $\alpha_\star$, and $\alpha_{\max}$ tend to 1 in the large-mass limit, and decrease for smaller masses. They thus contain some equivalent information on the position of the bulk of the conditional PDF of α at given mass. Hence, haloes of smaller mass accrete less on average.

3.2 Halo formation time

The formation time is conventionally defined as the redshift z_f at which a halo has assembled half of its mass. It is thus related to the height of the excursion set trajectory at the scale $\sigma_{1/2} \equiv \sigma(M/2)$ corresponding to the radius $R_{1/2} = R/2^{1/3}$. As the barrier $\delta_c/D(z)$ grows with z, and the first-crossing scale moves to the right towards higher values of σ, z_f is the redshift at which $\sigma_{1/2}$ becomes the first-crossing scale for that trajectory, if it exists. That is, neglecting for the time being the presence of finite jumps in the first-crossing scale (interpreted as mergers), one simply needs to solve for z_f the implicit relation $\delta(\sigma_{1/2}) = \delta_c/D(z_f)$, which makes z_f a stochastic variable. As described in Fig. 4, trajectories with the same upcrossing scale σ but different heights at $\sigma_{1/2}$ describe different formation times: a

Appendix A: Tracer particle algorithm

Let us describe here the pseudo-code underlying the tracer particle algorithm. The corresponding Fortran code is available upon request.

A.1. Gas to gas cells

The main function in charge of moving tracers between gas cells is called TreatCell. It takes as input the index of a cell and loops over all tracers in it. It requires all the (mass) fluxes to be stored. The pseudo code is the following.

```
function TreatCell(i_cell)
    m_cell ← MassOfCell(i_cell)
    F_net ← 0
    for i_dir ← 1, 2N_dim do                    ▷ Compute outgoing flux
        F ← GetFluxInDir(i_cell, i_dir)
        if F > 0 then
            F_net ← F_net + F
        end if
    end for
    tracers ← GetTracerParticlesInCell(i_cell)
    p_out ← F_net/m_cell     ▷ Probability to move part. out of cell
    for j_part in tracers do                    ▷ Loop on tracer particles
        r_1 ← DrawUniform(0, 1)
        if r_1 < p_out then
            r_2 ← DrawUniform(0, 1)
            for i_dir ← 1, 2N_dim do            ▷ Select a direction
                F ← GetFluxInDir(i_cell, i_dir)
                p = F/F_net
                if r_2 < p then                 ▷ Move in direction i_dir
                    MoveParticle(i_cell, j_part, i_dir)
                    break
                else
                    r_2 ← r_2 − p
                end if
            end for
        end if
    end for
end function
```

This function requires the MoveParticle function, which is defined as follow

```
function MoveParticle(i_cell, i_part, i_dir)
    F_tot ← GetFluxInDir(i_cell, i_dir)
    neighbors ← GetCellsOnFace(i_cell, i_dir)
    ī_dir ← GetOppositeDirection(i_dir)
    r ← DrawUniform(0, 1)
    for j_cell in neighbors do
        F ← − GetFluxInDir(j_cell, ī_dir)
        p ← F/F_tot
        if r < p then▷ Move particle to the centre of the cell
            SetParticleAtCenter(i_part, j_cell)
            break
        else                                    ▷ Proceed to next cell
            r ← r − p
        end if
    end for
end function
```

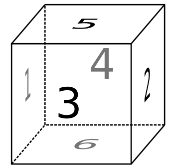

Fig. A.1. Cell faces numbering.

GetFluxInDir returns the mass that goes through the cell face in one timestep. Assuming that cell faces are numbered from 1 to 6 (left, right, top, bottom, front, rear, see Fig. A.1), GetOppositeDirection reads

```
function GetOppositeDirection(i_dir)
    mask ← [2, 1, 4, 3, 6, 5]
    return mask[i_dir]
end function
```

When looped over all cells, the algorithm treating all the tracers has complexity $O(N)$ where N is the total number of tracer particles and requires $O(N_{\mathrm{dim}}N_{\mathrm{cell}})$ memory to store the fluxes and $O(N)$ to store the tracer particles information.

A.2. AGN

Here we present how the volume of the jet is computed. We also present how the positions of the tracer particles in the jet are drawn. The function in charge of drawing position for the tracer particles in the jet is Tracer2Jet

```
function Tracer2Jet(j)
    loop
        c ← 2
        while c > 1 do
            a ← NormalDistribution(0, 1)
            b ← NormalDistribution(0, 1)
            c ← a^2 + b^2
        end while
        x ← r_AGN × a
        y ← r_AGN × b
        h ← Uniform(−2r_AGN, 2r_AGN)
        r^2 ← x^2 + y^2
        if |h| > r_AGN and (|h| − r_AGN)^2 + r^2 < r_AGN^2 then
            break
        else if |h| ≤ r_AGN then
            break
        end if
    end loop
                       ▷ We now have a position in the frame of the jet.
    u_z ← j/|j|
    u_x ← [j_y + j_z, −j_x + j_z, −j_x − j_y]
    u_x ← u_x/|u_x|
    u_y ← u_z ∧ u_x
    return x u_x + y u_y + h u_z
end function
```

Dubois, Y., Devriendt, J., Slyz, A., & Teyssier, R. 2012b, MNRAS, 420, 2662
Dubois, Y., Pichon, C., Devriendt, J., et al. 2013, MNRAS, 428, 2885
Dubois, Y., Volonteri, M., & Silk, J. 2014a, MNRAS, 440, 1590
Dubois, Y., Volonteri, M., Silk, J., Devriendt, J., & Slyz, A. 2014b, MNRAS, 440, 2333
Federrath, C., Glover, S. C. O., Klessen, R. S., & Schmidt, W. 2008, Phys. Scr. Vol. T, 132, 014025
Geen, S., Rosdahl, J., Blaizot, J., Devriendt, J., & Slyz, A. 2015, MNRAS, 448, 3248
Genel, S., Vogelsberger, M., Nelson, D., et al. 2013, MNRAS, 435, 1426
Haardt, F., & Madau, P. 1996, ApJ, 461, 20
Hennebelle, P., & Chabrier, G. 2011, ApJ, 743, L29
Iapichino, L., & Niemeyer, J. C. 2008, MNRAS, 388, 1089
Kereš, D., Katz, N., Weinberg, D. H., & Dave, R. 2005, MNRAS, 363, 2
Kimm, T., & Cen, R. 2014, ApJ, 788, 121
Kimm, T., Cen, R., Devriendt, J., Dubois, Y., & Slyz, A. 2015, MNRAS, 451, 2900
Kimm, T., Katz, H., Haehnelt, M., et al. 2017, MNRAS, 466, 4826
Kravtsov, A. V., Klypin, A. A., & Khokhlov, A. M. 1997, ApJS, 111, 73
Kroupa, P. 2001, MNRAS, 322, 231
Krumholz, M. R., & McKee, C. F. 2005, ApJ, 630, 250
McKinney, J. C., Tchekhovskoy, A., & Blandford, R. D. 2012, MNRAS, 423, 3083
Merloni, A., & Heinz, S. 2008, MNRAS, 388, 1011
Mitchell, N. L., McCarthy, I. G., Bower, R. G., Theuns, T., & Crain, R. A. 2009, MNRAS, 395, 180
Navarro, J. F., Frenk, C. S., & White, S. D. M. 1997, ApJ, 490, 493
Nelson, D., Vogelsberger, M., Genel, S., et al. 2013, MNRAS, 429, 3353
Nelson, D., Genel, S., Pillepich, A., et al. 2016, MNRAS, 460, 2881
Ocvirk, P., Pichon, C., & Teyssier, R. 2008, MNRAS, 390, 1326
Padoan, P., & Nordlund, Å. 2011, ApJ, 730, 40
Pichon, C., Pogosyan, D., Kimm, T., et al. 2011, MNRAS, 418, 2493
Planck Collaboration XIII. 2016, A&A, 594, A13
Power, C., Navarro, J. F., Jenkins, A., et al. 2003, MNRAS, 338, 14
Price, D. J., Wurster, J., Tricco, T. S., et al. 2018, PASA, 35, e031
Rasera, Y., & Teyssier, R. 2006, A&A, 445, 1
Rosdahl, J., & Blaizot, J. 2012, MNRAS, 423, 344
Rosdahl, J., Schaye, J., Dubois, Y., Kimm, T., & Teyssier, R. 2017, MNRAS, 466, 11
Silvia, D. W., Smith, B. D., & Shull, J. M. 2010, ApJ, 715, 1575
Springel, V. 2005, MNRAS, 364, 1105
Springel, V. 2010, MNRAS, 401, 791
Sutherland, R. S., & Dopita, M. A. 1993, ApJS, 88, 253
Teyssier, R. 2002, A&A, 385, 337
Teyssier, R., Pontzen, A., Dubois, Y., & Read, J. I. 2013, MNRAS, 429, 3068
Thornton, K., Gaudlitz, M., Janka, H.-T., & Steinmetz, M. 1998, ApJ, 500, 95
Tillson, H., Devriendt, J., Slyz, A., Miller, L., & Pichon, C. 2015, MNRAS, 449, 4363
Toro, E. F. 2009, Riemann Solvers and Numerical Methods for Fluid Dynamics: A Practical Introduction (Springer)
Trebitsch, M., Blaizot, J., Rosdahl, J., Devriendt, J., & Slyz, A. 2017, MNRAS, 470, 224
Tweed, D., Devriendt, J., Blaizot, J., Colombi, S., & Slyz, A. 2009, A&A, 506, 647
Vazza, F., Brunetti, G., Gheller, C., Brunino, R., & Brüggen, M. 2011, A&A, 529, A17
Vazza, F., Roediger, E., & Brüggen, M. 2012, A&A, 544, A103
Wadsley, J. W., Stadel, J., & Quinn, T. 2004, New Astron., 9, 137

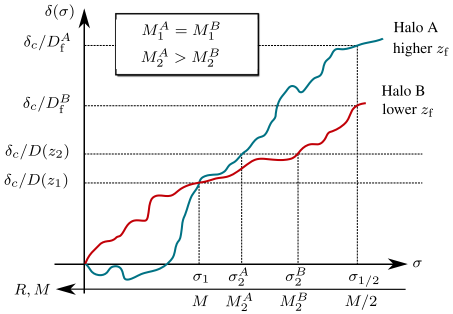

Figure 4. Pictorial representation of the interplay between accretion rate and formation time as inferred from excursion sets. Two haloes A and B upcross the threshold $\delta_c/D(z_1)$ at the same scale σ. At redshift z_1, they have therefore the same mass. Halo A has a steeper slope than halo B, and has thus a lower accretion rate. At a slightly larger redshift z_2, halo A crosses the higher threshold $\delta_c/D(z_2)$ at a lower σ, and its mass is thus larger than halo B's: halo A assembles its mass earlier, consistent with its lower accretion at z_1. At the half-mass scale $\sigma_{1/2} = \sigma(M/2)$, the trajectory of halo A is higher: its threshold δ_c/D_f has a value of D_f lower than halo B's at the same $\sigma_{1/2}$. Halo A has thus assembled half of its mass at a redshift z_f higher than halo B.

higher $\delta_{1/2}$ corresponds to a smaller $D(z_f)$ and thus to a halo with larger z_f, which assembled half of its mass earlier.

In the language of excursion sets, it is convenient to work with $D_f \equiv D(z_f)$ rather than with z_f. In terms of unit variance variables, haloes with formation time D_f correspond to trajectories satisfying

$$\nu_{1/2} \equiv \frac{\delta(\sigma_{1/2})}{\sigma_{1/2}} = \frac{\delta_c}{\sigma_{1/2} D_f} \equiv \nu_f \,, \tag{29}$$

where $\nu_{1/2}$ is the Gaussian variable at $\sigma_{1/2}$ and ν_f is the threshold at D_f. This constraint at $\sigma_{1/2}$ imposes a second condition on the trajectory after $\nu = \nu_c$, which selected the crossing scale σ. One then needs to transform the bidimensional constraint

$$\tilde{\mathcal{C}} \equiv \{\nu - \nu_c, \nu_{1/2} - \nu_f\} = \mathbf{0} \tag{30}$$

on $\{\nu, \nu_{1/2}\}$ into one for $\{\sigma, D_f\}$, which gives

$$\left|\det\left(\partial\tilde{\mathcal{C}}/\partial\{\sigma, D_f\}\right)\right| \delta_D^{(2)}(\tilde{\mathcal{C}}) = \left|\nu' - \nu_c'\right| \frac{\nu_f}{D_f} \delta_D^{(2)}(\tilde{\mathcal{C}}) \,, \tag{31}$$

thanks to the fact that $\partial(\nu_c - \nu)/\partial D_f = 0$.

The joint probability of upcrossing at σ having formation time D_f, denoted $f_{\rm up}(\sigma, D_f)$, is defined as the expectation value of equation (31) with the condition $\nu' > \nu_c'$. That is,

$$\begin{aligned} f_{\rm up}(\sigma, D_f) &\equiv \frac{\nu_f}{D_f} \int_{\nu_c'}^{\infty} d\nu' (\nu' - \nu_c')\, p_G(\nu_c, \nu', \nu_f) \,, \\ &= \frac{\nu_f}{D_f} p_G(\nu_c, \nu_f) \frac{\mu_f}{\sigma} F(X_f) \,, \end{aligned} \tag{32}$$

where the second equality follows from setting $\{\nu\} = \nu_f$ in the general expression (15), while μ_f and X_f are given by

$$\mu_f(D_f) \equiv \langle \delta' | \nu_c, \nu_f \rangle \,, \quad X_f(D_f) \equiv \frac{\mu_f(D_f)}{\sqrt{{\rm Var}\,(\delta' | \nu_c, \nu_f)}} \,, \tag{33}$$

as specified by equation (16). The conditional mean $\langle \delta' | \nu_c, \nu_f \rangle$ and variance ${\rm Var}\,(\delta' | \nu_c, \nu_f)$ are computed in equations (F21) and (F22), which give

$$\mu_f(D_f) = \frac{\omega' \delta_c}{\sigma_{1/2} D_f} + \frac{\sigma - \omega' \omega}{\sigma^2 - \omega^2} \left(\delta_c - \frac{\omega \delta_c}{\sigma_{1/2} D_f}\right) \,, \tag{34}$$

$$X_f(D_f) = \mu_f(D_f) \Bigg/ \left[\langle \delta'^2 \rangle - \omega'^2 - \frac{(\sigma - \omega' \omega)^2}{\sigma^2 - \omega^2}\right]^{1/2} \,, \tag{35}$$

where $\omega = \langle \delta \nu_{1/2} \rangle$ and $\omega' = \langle \delta' \nu_{1/2} \rangle$ are given by equations (E14) and (E15), respectively.

The conditional probability of D_f given upcrossing at σ – the main result of this subsection – is obtained dividing equation (32) by equation (11)

$$\begin{aligned} f_{\rm up}(D_f|\sigma) &= \frac{\nu_f}{D_f} p_G(\nu_f|\nu_c) \frac{\mu_f F(X_f)}{\nu_c F(X)} \,, \\ &= \frac{\left(\delta_c/\sigma_{1/2} D_f^2\right) e^{-\nu_{f,c}^2/2}}{\sqrt{2\pi(1 - \langle \nu \nu_{1/2} \rangle^2)}} \frac{\mu_f F(X_f)}{\nu_c F(X)} \,, \end{aligned} \tag{36}$$

where $(\nu_f/D_f) p_G(\nu_f|\nu_c) = p(D_f|\nu_c)$, not surprisingly, is the conditional probability of the (non-Gaussian) variable D_f given ν_c, and

$$\nu_{f,c} \equiv \frac{\nu_f - \langle \nu \nu_{1/2} \rangle \nu_c}{\sqrt{1 - \langle \nu \nu_{1/2} \rangle^2}} = \frac{\delta_c}{\sigma_{1/2}} \frac{1/D_f - \langle \delta \delta_{1/2} \rangle / \sigma^2}{\sqrt{1 - \langle \nu \nu_{1/2} \rangle^2}} \,. \tag{37}$$

Recall also that $X = \Gamma \nu_c$. The conditional probability $f_{\rm up}(D_f|\sigma)$ depends on D_f directly, through $\nu_{f,c}$ and through μ_f (which appears also in X_f). As both $\nu_{f,c}$ and μ_f are proportional to $1/D_f$ in the small-D_f limit, equation (36) scales like $e^{-\nu_{f,c}^2/2}/D_f^3$. Hence, $f_{\rm up}(D_f|\sigma)$ is exponentially suppressed for small D_f, that is for large formation redshift z_f: it is exponentially unlikely for a halo to assemble half of its mass at very high redshift.

Like in the previous section, the Gaussian cut-off in equation (36) enables to define a characteristic value $D_\star(\sigma)$ of the formation time, below which $f_{\rm up}(D_f|\sigma)$ is exponentially suppressed, by requesting that $\nu_{f,c} = 1$. This definition corresponds to

$$D_\star(\sigma) = \frac{\delta_c/\sigma_{1/2}}{\langle \nu \nu_{1/2} \rangle \nu_c + \sqrt{1 - \langle \nu \nu_{1/2} \rangle^2}} \,, \tag{38}$$

which can then be solved for the typical formation redshift $z_\star$. Similarly, one may define the most likely formation time $D_{\rm max}$ by finding the value of D_f that maximizes equation (36). Because its expression is rather involved and not much more informative than $D_\star$, it is not reported here.

Expanding $D_\star$ in powers of $\Delta\sigma_{1/2} \equiv \sigma_{1/2} - \sigma$ (even though $\Delta\sigma_{1/2}/\sigma \simeq -(1/2) {\rm dlog}\,\sigma/{\rm dlog}\,M$ may not be small, in which case this expansion may just give a qualitative indication), one gets

$$D_\star \simeq 1 - \frac{\Delta\sigma_{1/2}}{\sigma} \left(1 + \frac{\sqrt{\langle \delta'^2 \rangle - 1}}{\nu_c}\right) \simeq 1 - \frac{1}{\alpha_\star} \frac{\Delta\sigma_{1/2}}{\sigma} \,, \tag{39}$$

confirming the intuitive relation between accretion rate and formation time. Haloes with smaller accretion rates today must have formed earlier, in order for their final mass to be the same. To derive this expression, $\langle \delta \delta_{1/2} \rangle$ was expanded up to second order in $\Delta\sigma$, using $\langle \delta \delta' \rangle = \sigma$ and $\langle \delta \delta'' \rangle = 1 - \langle \delta'^2 \rangle = \Gamma^{-2}$. Let us stress that, strictly speaking, the conditional probability $f_{\rm up}(D_f|\sigma)$ is not a well-defined probability distribution. For instance, just like $f_{\rm up}(\sigma)$, equation (36) is not normalized to unity when integrated over $0 < D_f < D$. This is an artefact introduced by the upcrossing approximation to the first-crossing problem, because equation (29) does not require trajectories to reach δ_c/D_f for the first time. As D_f gets close to D, most trajectories reaching δ_c/D_f do so with negative slope, or after one or more crossings, which leads to overcounting. For $D_f = D$, trajectories that first crossed δ_c/D_f at σ cannot first cross again at $\sigma_{1/2}$, since $\sigma_{1/2}-\sigma$ remains finite: the true distribution should then have $f(D_f|\sigma)=0$. This is clearly not the case for $f_{up}(D_f|\sigma)$. In spite of these shortcomings, equation (36) approximates well the true conditional PDF for $D_f \ll D_\star$, and the characteristic time $D_\star$ still provides a useful parametrization of the height of the tail.

A better approximation than equation (36) may be obtained by imposing an upcrossing condition at $\sigma_{1/2}$ as well

$$\frac{\delta_c}{D_f^2}\int_0^\infty \mathrm{d}\delta'\,\delta'\int_0^\infty \mathrm{d}\delta'_{1/2}\,p_G(\delta_c,\delta',\delta_c/D_f,\delta'_{1/2})\,. \tag{40}$$

Notice the absence in this expression of the Jacobian factor $\delta'_{1/2}$: this is because the constraint at $\sigma_{1/2}$ is not differentiated with respect to $\sigma_{1/2}$, but only with respect to D_f. This reformulation, which unfortunately does not admit a simple analytical expression, would improve the approximation for values of D_f closer to $D_\star$, but it would still not yield a formally well-defined PDF. Furthermore, the mean $\langle D_f|\sigma\rangle$ and all higher moments would still be infinite: these divergences are in fact a common feature of first passage statistics, which typically involve the inverse of Gaussian variables. For all these reasons, this calculation is not pursued further.

This section has formalized analytical predictions for accretion rates and formation times from the excursion set approach with correlated steps. It confirmed the tight correlation between the two quantities, according to which at fixed mass, early-forming haloes must have small accretion rates today. Because the focus is here on accounting for the presence of a saddle of the potential at finite distance, for simplicity and in order to isolate this effect we have restricted our analysis to the case of a constant threshold δ_c. More sophisticated models (e.g. scale-dependent barriers involving other stochastic variables that account for deviations from spherical collapse) could however be accommodated without extra conceptual effort (see Appendix G).

4 HALO STATISTICS NEAR SADDLES

Let us now quantify how the presence of a saddle of the large-scale gravitational potential affects the formation of haloes in its proximity. To do so, let us study the tracers introduced in the previous section (the distributions of upcrossing scale, accretion rate, and formation time) using conditional probabilities. The condition we enforce is that the upcrossing point (the centre of the excursion set trajectories) lies at a finite distance $\boldsymbol{r}$ from the saddle point. The focus will be on (filament-type) saddles of the potential that describe local configurations of the peculiar acceleration with two spatial directions of inflow (increasing potential) and one of outflow (decreasing potential). See Appendix C for other critical points. These initial regions will evolve into filaments (at least in the Zel'dovich approximation), where particles accumulate out of the neighbouring voids from two directions, and the saddle points filament centres, where the gravitational attraction of the two nodes balances out. A schematic representation of this configuration is given in Fig. 5.

The saddles are identified as points with null gradient of the gravitational potential, smoothed on a sphere of radius $R_\mathcal{S}$ (which is assumed to be larger than the halo's scale R). This condition guarantees that the mean peculiar acceleration of the sphere, which at first order is also the acceleration of its centre of mass, vanishes. That is, the null condition (for $i=1,\ldots,3$)

$$g_i \equiv \frac{1}{R_\star}\int\frac{\mathrm{d}^3k}{(2\pi)^3}\frac{ik_i}{k^2}\delta_m(\boldsymbol{k})\frac{W(kR_\mathcal{S})}{\sigma_\mathcal{S}}=0, \tag{41}$$

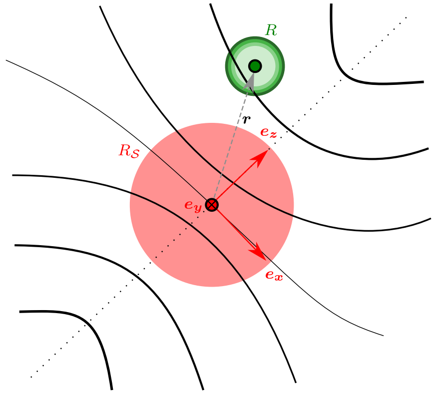

Figure 5. Illustration of the conditional excursion set smoothing on a few infinitesimally close scales around R (in green) at finite distance $\boldsymbol{r}$ from a saddle point of the gravitational potential smoothed on scale $R_\mathcal{S} \gg R$ (in red). The eigenvectors $\boldsymbol{e}_x$ and $\boldsymbol{e}_z$ of the tidal tensor at the saddle give the directions of steepest increase and decrease of the potential, corresponding to maximum inflow and outflow, respectively. The region is compressed along $\boldsymbol{e}_x$ and $\boldsymbol{e}_y$ and stretched along $\boldsymbol{e}_z$, thus creating a filament. The solid lines are isocontours of the mean density, the thickest the densest. The dotted line indicates a ridge of mean density (the filament), parallel to $\boldsymbol{e}_z$ near the saddle.

where $\sigma_\mathcal{S}\equiv\sigma(R_\mathcal{S})$, is imposed on the mean gradient of the potential smoothed with a Top-Hat filter on scale $R_\mathcal{S}$. This mean acceleration is normalized in such a way that $\langle g_i g_j\rangle=\delta_{ij}/3$ by introducing the characteristic length-scale[7]

$$R_\star^2 \equiv \int \mathrm{d}k\,\frac{P(k)}{2\pi^2}\frac{W^2(kR_\mathcal{S})}{\sigma_\mathcal{S}^2}\,. \tag{42}$$

Having null peculiar acceleration, the patch sits at the equilibrium point of the attractions of what will become the two nodes at the end of the filament.[8]

The configuration of the large-scale potential is locally described by the rank 2 tensor

$$q_{ij} \equiv \frac{1}{\sigma_\mathcal{S}}\int\frac{\mathrm{d}^3k}{(2\pi)^3}\frac{k_ik_j}{k^2}\delta_m(\boldsymbol{k})W(kR_\mathcal{S})\,, \tag{43}$$

which represents the Hessian of the perturbed potential smoothed on scale $R_\mathcal{S}$, normalized so that $\langle \mathrm{tr}^2(q)\rangle=1$. This tensor is the opposite of the so-called strain or deformation tensor. The peculiar gravitational acceleration at the surface of the sphere is proportional to $-q_{ij}r_j$. Thus, the trace $\mathrm{tr}(q)=\nu_\mathcal{S}$ of q_{ij} describes the

[7] This scale is similar, but not equivalent, to the scale often defined in peak theory. Calling σ_i^2 the variance of the density field filtered with $k^{2i}W(kR)$, the R_* defined here is σ_{-1}/σ_0, while the peak theory scale is $\sqrt{3}\sigma_1/\sigma_2$.

[8] The mean gravitational acceleration g_i includes an unobservable infinite wavelength mode, which should in principle be removed. A way to circumvent the problem would be to multiply $W(kR_\mathcal{S})$ by a high-pass filter on some large-scale R_0 to remove modes with $k\lesssim 1/R_0$. Because g_i is set to 0, it does not introduce any anisotropy, but simply affects the radial dependence of the conditional statistics through its covariance $\langle g_ig_j\rangle$, which however is not very sensitive to long wavelengths. For this reason, this minor complication is ignored.

available in RAMSES, and treated tracer particles just like standard particles (star or DM) with respect to code structure. In the following, the computation overhead will be expressed in terms of the number of tracer per initial cell: $N_t/N_{cell,i}$, where N_t is the number of tracer particles and $N_{cell,i}$ is the number of initial (gas) cells.

The runs with tracers show that the total run time starts increasing with the number of tracer particles per cell[10] when this number becomes of the order of ~0.1 tracer per initial cell. Above this threshold, the run time scales roughly linearly with the number of tracer per initial cell. We have run the simulation on the Occigen supercomputer with 672 cores (28 nodes of 24 cores). Each node is made of two Intel Haswell 12-Core E5-2690 V3s[11] running at a clock frequency of 2.6 GHz. The nodes are wired together with a DDR Infiniband network (20 Gbit s^{-1}). The code was compiled with the Intel Fortran compiler version 17.0 and OpenMPI 2.0.2. In this setup the overhead is 3% per tracer per initial cell. For example the run `t100` with 10 tracer per initial cell had a 40% overhead. Part of the overhead is due to the tracer particles themselves (moving, generating random numbers, etc.). Another part is due to the load balancing. Indeed, in this simulation, tracer particles are only found in the zoomed region, which is already the most CPU-intensive region. Our simulation can be seen as a worst-case scenario for the tracer particles. In general, let us write the conservative formula giving an estimate of the overhead induced by the tracer particles

$$\frac{\Delta t}{t}=0.03\left(\frac{N_t}{N_{cell,i}}\right)+0.1, \tag{23}$$

where t is the run time and Δt the extra cost induced by the tracer particles. Here, N_t and $N_{cell,i}$ are the total number of tracer particles and the total number of initial cells, respectively.

5. Conclusions

We present a new implementation of tracer particles in the RAMSES AMR code based on the Monte Carlo approach from Genel et al. (2013). It has been interfaced with the most common physical models used in cosmological simulations (star formation and stellar feedback, SMBH growth and AGN feedback). We have shown that the Lagrangian history of the gas is accurately reconstructed by testing the accuracy of the tracer distribution in an advection-dominated problem and in a diffusion-dominated problem. The gas tracer distribution matches that of the gas, even in complex situations that involve subgrid models. We have also provided a comparison of the new MC tracer particles to the previous velocity-based implementation and showed that the new version largely outperforms the accuracy of the previous one. We have made a detailed study of the distribution of tracer particles in a zoom-in cosmological simulation including state-of-the art subgrid model physics (cooling, star formation, SN feedback, SMBHs, and AGN feedback) and show that: (i) in each cell, the gas tracer distribution is given by a Poisson distribution with parameter $\lambda=M_{cell}/m_t$; and (ii) for each star, the number of star tracers can be approximated by a Poisson distribution with parameter $\lambda=M_\star/m_t$. The properties of the Poisson distribution give a simple rule to estimate the sampling noise of the tracer particle, as the noise can be represented by $1/\sqrt{\lambda}$. In turn this should allow users to quantify how many particles are needed to reach their sought accuracy. We have also shown that the gas tracer particles sample exactly the intrinsic numerical diffusion of the Godunov solver. To highlight the assets of tracer particles in a realistic setting, they were implemented in the problem of cold flow accretion at high redshift. The known bi-modality in the temperature of gas was recovered.

The performance of the algorithm was explored. In a zoom-in full physics cosmological simulation, the run time grows roughly linearly with the number of tracer particles per cell. The overall impact on computation time is estimated to be ~3% per tracer per initial cell plus a constant computation time overhead of 10%, regardless of the number of tracer particles. These figures should serve as upper limits on the computation time. The performance of the scheme could be optimised by using two separate linked lists for the tracer particles and the other particles, as is done in AREPO (Genel et al. 2013). Implementing these possible improvements will be the subject of future studies. Presently, the performance is significantly lower than that reported in the original paper of Genel et al. (2013): in addition to using a specific linked list for the tracer particles, the moving mesh of AREPO reduces the number of tracer movements and mitigates the cost of each tracer.

In comparison to the original paper by Genel et al. (2013), we provide an additional detailed description of the statistical properties of the ensemble of tracer particles not only in the gas but also in stars and in AGN jets. We also studied how their distributions behave when complex sub-grid models are involved (star formation and feedback, AGN feedback, BH accretion) and checked that their distribution is in agreement with the baryon distribution.

This implementation provides an efficient method to accurately track the evolution of the Lagrangian history in the Eulerian code RAMSES. It opens new perspectives to study how baryon flows interact in hydrodynamical simulations. For instance, tracer particles could be used to quantify the spatial and time evolution of the anisotropically accreted gas, its contribution to the spin of galaxies, and how these processes impact galactic morphology. Specifically, following Tillson et al. (2015), Danovich et al. (2015), and DeFelippis et al. (2017), one could address the following open questions: Where does the angular momentum go? Does it contribute to the spin-up of the galaxies or is it re-distributed before entering the disk? If it is, is it due to turbulent pressure, shock-heating or SN and AGN feedback?

Acknowledgements. We wish to thank J. Blaizot, J. Devriendt, R. Teyssier and M. Trebitsch for useful suggestions. CC wishes to acknowledge the valuable feedback provided by R. Beckmann and P. Mitchell. CC is sponsored by the Institut Lagrange de Paris fellowship. This work has made use of the Horizon Cluster hosted by Institut d'Astrophysique de Paris. We thank Stephane Rouberol for running smoothly this cluster for us. It has also made use of the Occigen Cluster hosted by the CINES on the A0040406955 GENCI grant. This work has extensively used YT, the open-source analysis and visualisation toolkit. The source code of the new tracer particles is available upon request.

[10] We note that here the number of cells is the one in the refined regions, not the initial number of cells.

[11] See Intel-Xeon-Processor- E5-2690.

References

Agertz, O., Lake, G., Teyssier, R., et al. 2009, MNRAS, 392, 294
Aubert, D., Pichon, C., & Colombi, S. 2004, MNRAS, 352, 376
Birnboim, Y., & Dekel, A. 2003, MNRAS, 345, 349
Booth, C. M., & Schaye, J. 2009, MNRAS, 398, 53
Bourne, M. A., & Sijacki, D. 2017, MNRAS, 472, 4707
Bryan, G. L., Norman, M. L., O'Shea, B. W., et al. 2014, ApJS, 211, 19
Danovich, M., Dekel, A., Hahn, O., Ceverino, D., & Primack, J. 2015, MNRAS, 449, 2087
DeFelippis, D., Genel, S., Bryan, G. L., & Fall, S. M. 2017, ApJ, 841, 16
Dubois, Y., & Teyssier, R. 2008, A&A, 477, 79
Dubois, Y., Pichon, C., Haehnelt, M., et al. 2012a, MNRAS, 423, 3616

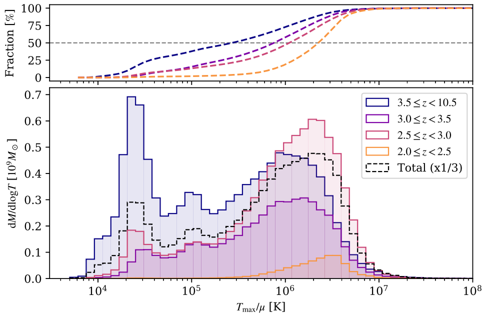

Fig. 16. *Bottom panel*: histogram of the maximum temperature of the gas accreted onto the central galaxy between different redshifts (from early accretion time in blue to late accretion time in yellow). *Top panel*: cumulative distribution of the gas temperature. Only the gas-forming stars within the virial radius are selected. The total distribution integrated over the total accretion time is shown with the black dashed line in the bottom panel. The total distribution has been rescaled by a factor of one third for visualisation. The halo has two modes of accretion: a cold and a hot mode. At high z the cold mode dominates and at low z the hot mode dominates.

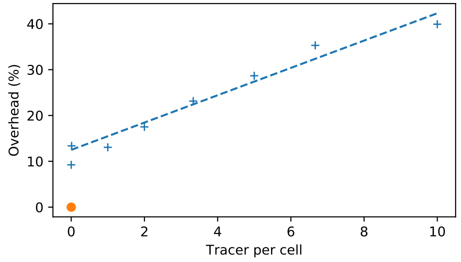

Fig. 17. Overhead as a function of the number of tracer particles per initial cell (symbols). The orange symbol is the simulation with the tracer deactivated. The data (excluding the run with the tracer deactivated) have been fitted with a linear function (dashed line). The estimated overhead (slope of the fit) is ~3% per tracer per initial cell with an extra constant of ~10%.

Table 1. Run time per coarse time step for the different runs.

Name	Absolute number	Tracer per cell	Run time (s)	Overhead (%)
`t100`	129325116	10	1310	39.9
`t67`	86214303	6.7	1270	35.3
`t20`	64656206	5	1210	28.7
`t33`	43104621	3.3	1160	23.1
`t20`	25861310	2	1100	17.5
`t10`	12929077	1	1060	13.1
`t0.1`	130250	0.01	1060	13.4
`t0`	0	0	1020	9.2
`not`	0	0	940	–

Notes. The run `notr` was performed with no tracer particles and with all the tracer particle routines deactivated. The column "Tracer per cell" is the number of tracer particles per initial cell in the zoomed region. The "Overhead" column contains the run-time overhead defined with respect to the `notr` run.

the gas are extracted from the local gas cell value. For each tracer particle, the maximum temperature $T_{\max}$ reached before falling into the virial radius is recorded. The infall time is defined as the last inward crossing of the virial radius. The merger tree is computed following Tweed et al. (2009). The procedure only selects tracer particles falling onto the galaxy in the gas phase. This excludes gas tracers tracking gas that formed stars in satellite galaxies but includes gas from wet mergers. Figure 16 presents the temperature distribution of the accreted gas for different bins of infall time. At early times (blue lines, $z \gtrsim 3$) the accretion is bi-modal. About 50% of the gas is accreted via the cold mode, as shown in the top panel of Fig. 16. At later redshifts ($z \lesssim 2.5$), the accretion becomes dominated by the hot mode. The relative importance of the cold accretion decreases and the distribution become less and less bimodal, until it is eventually entirely dominated by the hot mode. This is in qualitative agreement with the findings of Kereš et al. (2005) though the exact quantitative amount of cold versus hot accreted gas relies significantly on i) the numerical scheme to model gas dynamics (Nelson et al. 2013) and ii) the modelled feedback processes (Dubois et al. 2013).

Caution should be taken here: contrary to what was done in the original study, only the accretion onto a single galaxy is investigated. In particular, our results are sensitive to the particular accretion and merger history of that galaxy, which impact the temperature distribution of the gas. In order to achieve a fairer comparison, one would have to run a full cosmological simulation and study the gas accretion of the full population within the box. While this would now technically be possible thanks to the new tracer algorithm, it is nonetheless well beyond the scope of this paper.

4. Performance

To quantify the performance of the tracer particles and their associated CPU overhead (defined as the excess of computation time required by the tracer particles), we restarted the simulation of Sect. 3.2 at redshift $z = 2$, while varying the numbers of tracer particles to test the scaling of the algorithm. At restart, we decimate the tracer population to keep only 67, 50, 33, 20, 10, or 0.1% of the initial population (in the gas, star, and black holes). We also run a simulation with no tracer but all the tracer routines activated (`t0`) and a simulation with no tracer and the tracer routines deactivated (`notracer`). The parameters of the runs are presented in the first three columns of Table 1. The run time is defined as the total run time divided by the number of steps. The overhead is defined as the relative increase of the run time with respect to the run `not`. All the runs were stopped after two iterations of the coarse time step (about ~2000 s of run time, ~2.8 Myr of simulation time). The results are also plotted in Fig. 17.

By comparing the two runs `t0` and `notr`, we conclude that the tracer particle machinery adds a constant cost of about 10% to the computation. This is due to the fact that the tracer particles require the fluxes at the interface of each cell (six quantities per cell) to be stored, which then have to be communicated between CPUs. In addition, there are multiple loops that iterate over all the cells and all the particles (see Sect. 2 for more details). In principle, this could be optimised by setting tracer particles in their own linked list, but we exploited the particle machinery

average infall (or expansion, if negative) acceleration of the three axes with respect to the background, while the anisotropic shear is given by the traceless part $\bar{q}_{ij} \equiv q_{ij} - \delta_{ij}\nu_{\mathcal{S}}/3$, which deforms the region by slowing down or accelerating each axis. By construction, $\langle \nu_{\mathcal{S}}\bar{q}_{ij}\rangle = 0$.

For the initial spherical patch to evolve into a filament, the eigenvalues q_i of q_{ij} must obey $q_1 < 0 < q_2 < q_3$ (see also Fig. D1). In this configuration, the Zel'dovich flow of the patch has one expanding direction and two infalling ones. The non-linear evolution is unlikely to revert this behaviour, and the spherical region will end up in a filament (Zel'dovich 1970; Bond, Kofman & Pogosyan 1996). There is no clear consensus on what the initial density of a protofilament should be for the structure to form at $z = 0$ (see however Shen et al. 2006). The value $\nu_{\mathcal{S}} = 1.2$ was chosen here, corresponding to a mean density of 0.8 within a sphere of $R_{\mathcal{S}} = 10\,\mathrm{Mpc}h^{-1}$, which is about one standard deviation higher than the mean value for saddle points of this type (see Appendix D for details), and thus corresponds to a filament slightly more massive than the average (or to an average filament that has not completely collapsed yet). The qualitative results presented in this paper do not depend on the exact value of $\nu_{\mathcal{S}}$ (even though they obviously do at the quantitative level).

4.1 Expected impact of saddle tides

The mean and covariance of δ and δ' at $\boldsymbol{r}$ are modified by the presence of the saddle at the origin. The zero mean density field is replaced by $\delta - \langle\delta|\mathcal{S}\rangle$, where (using Einstein's convention as usual)

$$\langle\delta|\mathcal{S}\rangle = \langle\delta|\mathcal{S}\rangle\langle\delta\nu_{\mathcal{S}}\rangle\nu_{\mathcal{S}} + 3\langle\delta g_i\rangle g_i + \frac{15}{2}\langle\delta\bar{q}_{ij}\rangle\bar{q}_{ij}\,, \tag{44}$$

where the correlation functions are evaluated at finite separation. Here, $\mathcal{S}$ stands for a filament-type saddle condition of zero gradient and two positive eigenvalues of the tidal tensor, see Fig. 5. The slope δ' is replaced by the derivative of this whole expression with respect to σ, which gives $\delta' - \langle\delta'|\mathcal{S}\rangle$, since the correlation functions of δ' with the saddle quantities correspond to the derivatives of the δ correlations. These modified height and slope no longer correlate with any saddle quantity. Thus, the abundance of the various tracers at $\boldsymbol{r}$ can be inferred from standard excursion sets of this effective density field. The building blocks of this effective excursion set problem – the variance of the field and of its slope, height, and slope of the effective barrier – are derived in full in Appendix F. The main text of this section discusses how the saddle condition affects the upcrossing statistics, and the excursion set proxies for accretion rate and formation time.

For geometrical reasons, since statistical isotropy is broken only by the separation vector, any angular dependence of the correlation functions may arise only as r_i or r_ir_j. Let us thus write equation (44) as

$$\langle\delta|\mathcal{S}\rangle = \xi_{00}\nu_{\mathcal{S}} + 3\xi_{11}\frac{r}{R_\star}\hat{r}_i g_i - 5\xi_{20}\frac{3\hat{r}_i\bar{q}_{ij}\hat{r}_j}{2}\,, \tag{45}$$

where $\hat{r}_i \equiv r_i/r$ and the correlation functions $\xi_{\alpha\beta}(r, R, R_{\mathcal{S}})$ – whose exact form is given in equation (E11) – depend only on the radial separation $r = |\boldsymbol{r}|$ and the two smoothing scales, and have positive sign. Notice the presence of a minus sign in the shear term. In the frame of the saddle, oriented with the $\hat{z}$-axis in the direction of outflow,

$$\mathcal{Q} \equiv \hat{r}_i\bar{q}_{ij}\hat{r}_j = \bar{q}_3\sin^2\theta\cos^2\phi + \bar{q}_2\sin^2\theta\sin^2\phi + \bar{q}_1\cos^2\theta\,, \tag{46}$$

where θ and ϕ are the usual cylindrical coordinates in the frame of the eigenvectors $(\boldsymbol{e}_3, \boldsymbol{e}_2, \boldsymbol{e}_1)$ of $\bar{q}_{ij}$ with eigenvalues $\bar{q}_3 > \bar{q}_2 > \bar{q}_1$.

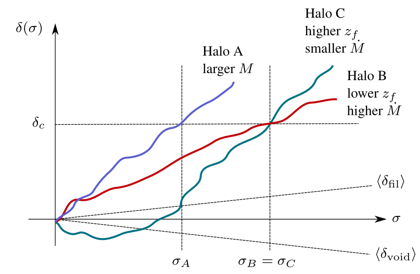

Figure 6. Pictorial representation of the effect of the presence of saddle point on the excursion set trajectories at a finite distance from it. Haloes A and B lie in the direction of the filament ($\mathcal{Q} \equiv \hat{r}_i\bar{q}_{ij}\hat{r}_j < 0$), where the mean density is higher than the average density. Halo C lies in the direction orthogonal to it ($\mathcal{Q} > 0$), where the mean density is lower. Haloes in the filament are likely to cross the collapsing threshold earlier, like halo A, than haloes in the voids. They thus tend to have larger mass. At fixed crossing scale $\sigma_{\mathrm{B}} = \sigma_{\mathrm{C}}$, haloes in the filament are likely to cross with shallower slopes, like halo B, than halo in the voids. At their half-mass scale $\sigma_{1/2} > \sigma_{\mathrm{A}}$, their trajectories tend to be lower. Hence, at fixed mass, haloes in the filaments tend to have larger accretion rates and to assemble half of their mass later. Conversely, haloes in the voids assemble their mass earlier, and then stop accreting.

When setting $g_i = 0$, an angular dependence can only appear as a functional dependence on $\mathcal{Q}(\hat{\boldsymbol{r}}) = \hat{r}_i\bar{q}_{ij}\hat{r}_j$. That is, a dependence on the direction $\hat{\boldsymbol{r}}$ with respect to the eigenvectors of the shear $\bar{q}_{ij}$. As shown by equation (45), a negative value of $\mathcal{Q}$ corresponds to a higher mean density, which makes it easier for δ to reach δ_{c} and for haloes to form. At fixed distance from the saddle point, halo formation is thus enhanced in the outflow direction with respect to the inflow direction: haloes are naturally more clustered in the filament than in the voids. Moreover, excursion set trajectories with a lower mean will tend to cross the barrier with steeper slopes than those crossing at the same scale but with a higher mean, and will reach higher densities at smaller scales. Hence, haloes of the same mass that form in the voids will form earlier and have a lower accretion rates. These trends are shown in Fig. 6.

To understand the radial dependence, one may expand equation (45) for small r away from the saddle, obtaining

$$\langle\delta|\mathcal{S}\rangle \simeq \langle\delta\nu_{\mathcal{S}}\rangle_{r=0}\nu_{\mathcal{S}} + \langle\delta\nabla^2\nu_{\mathcal{S}}\rangle_{r=0}\frac{r^2}{2}\hat{r}_i q_{ij}\hat{r}_j\,; \tag{47}$$

whether the mean density increases or decreases with r depends on the sign of the eigenvalues, i.e. the curvatures of the saddle, of the full $\boldsymbol{q}$ defined in equation (43). Since $\langle\delta\nabla^2\nu_{\mathcal{S}}\rangle < 0$, the mean density grows quadratically with r if $\hat{r}_i q_{ij}\hat{r}_j < 0$, and decreases otherwise. One thus expects the saddle point to be a maximum of halo number density, accretion rate, and formation time in the two directions perpendicular to the filament, and a minimum in the direction parallel to it (corresponding to the negative eigenvalue q_1).

4.2 Conditional halo counts

The conditional distribution of the upcrossing scale σ at finite distance $\boldsymbol{r}$ from a saddle point of the potential can be evaluated following the generic procedure described in Section 2.2, fixing

$$\{v_I\} = \{\nu_{\mathcal{S}}, 0, -\sqrt{5}(3\mathcal{Q}/2)\} \equiv \mathcal{S}(\boldsymbol{r}) \tag{48}$$

as the constraint. With this replacement, equation (15) divided by $p_{\rm G}(\mathcal{S})$ gives

$$f_{\rm up}(\sigma;\boldsymbol{r}) = \frac{{\rm e}^{-\nu_{{\rm c},\mathcal{S}}^2/2}}{\sqrt{2\pi{\rm Var}(\delta|\mathcal{S})}}\,\mu_{\mathcal{S}}\,F(X_{\mathcal{S}})\,, \tag{49}$$

which is the sought conditional distribution, with

$$\mu_{\mathcal{S}}(\boldsymbol{r}) \equiv \langle\delta'|\nu_{\rm c},\mathcal{S}\rangle\,,\quad X_{\mathcal{S}}(\boldsymbol{r}) \equiv \frac{\mu_{\mathcal{S}}(\boldsymbol{r})}{\sqrt{{\rm Var}(\delta'|\nu_{\rm c},\mathcal{S})}}\,, \tag{50}$$

as in equation (16). The effective threshold $\nu_{{\rm c},\mathcal{S}}$ given the saddle condition is obtained replacing the generic constraint v with $\mathcal{S}$ in equation (18).

The explicit calculation of the conditional quantities needed to compute $\nu_{{\rm c},\mathcal{S}}$, $\mu_{\mathcal{S}}$, and $X_{\mathcal{S}}$ is carried out in Appendix F. The results of Appendix F2 [namely, equation (F13)] give

$$\nu_{{\rm c},\mathcal{S}}(\boldsymbol{r}) \equiv \frac{\delta_{\rm c}-\langle\delta|\mathcal{S}\rangle}{\sqrt{{\rm Var}(\delta|\mathcal{S})}} = \frac{\delta_{\rm c}-\xi_{00}\nu_{\mathcal{S}}+\frac{15}{2}\xi_{20}\mathcal{Q}(\hat{\boldsymbol{r}})}{\sqrt{\sigma^2-\xi^2}}\,, \tag{51}$$

consistently with equation (45), where

$$\xi^2(r) \equiv \xi_{00}^2(r) + 3\xi_{11}^2(r)r^2/R_\star^2 + 5\xi_{20}^2(r)\,. \tag{52}$$

The effective slope parameters, obtained by replacing equations (F10) and (F11) into equation (50), are

$$\mu_{\mathcal{S}}(\boldsymbol{r}) = \xi_I'\mathcal{S}_I + \frac{\sigma-\xi_I'\xi_I}{\sqrt{\sigma^2-\xi^2}}\nu_{{\rm c},\mathcal{S}}(\boldsymbol{r})\,, \tag{53}$$

$$X_{\mathcal{S}}(\boldsymbol{r}) = \mu_{\mathcal{S}}(\boldsymbol{r})\Bigg/\left[\langle\delta'^2\rangle - \xi'^2 - \frac{(\sigma-\xi_I'\xi_I)^2}{\sigma^2-\xi^2}\right]^{1/2}\,, \tag{54}$$

in terms of the vectors

$$\xi(r) \equiv \{\xi_{00}(r), \sqrt{3}\xi_{11}(r)r/R_\star, \sqrt{5}\xi_{20}(r)\}\,, \tag{55}$$

$$\xi'(r) \equiv \{\xi_{00}'(r), \sqrt{3}\xi_{11}'(r)r/R_\star, \sqrt{5}\xi_{20}'(r)\}\,. \tag{56}$$

The correlation functions $\xi_{\alpha\beta}(r, R, R_S)$ and their derivatives $\xi_{\alpha\beta}' = {\rm d}\xi_{\alpha\beta}/{\rm d}\sigma$ are given in equations (E11) and (E12), respectively. Note that throughout the text, $\xi_{\alpha\beta}$ or $\xi_{\alpha\beta}(r)$ will be used as a shorthand for $\xi_{\alpha\beta}(r, R, R_S)$.

Equation (49), the main result of this subsection, is the conditional counterpart of equation (11), and is formally identical to it upon replacing $\nu_{\rm c}$, $\nu_{\rm c}'$, and X with $\nu_{{\rm c},\mathcal{S}}(\boldsymbol{r})$, $\nu_{{\rm c},\mathcal{S}}'(\boldsymbol{r}) = -\mu_{\mathcal{S}}(\boldsymbol{r})/\sqrt{\sigma^2-\xi^2}$ and $X_{\mathcal{S}}(\boldsymbol{r})$. The position-dependent threshold $\nu_{{\rm c},\mathcal{S}}(\boldsymbol{r})$ and the slope parameter $\mu_{\mathcal{S}}(\boldsymbol{r})$, given by equations (51) and (53), respectively, contain anisotropic terms proportional to $\mathcal{Q}$ These terms account for all the angular dependence of $f_{\rm up}(\sigma;\boldsymbol{r})$. In the large-mass regime, as $\{\xi_I'\} \simeq 0$, $X_{\mathcal{S}} \simeq \nu_{{\rm c},\mathcal{S}}/(1-\xi^2) \gg 1$ and $F(X_{\mathcal{S}}) \simeq 1$. The most relevant anisotropic contribution is thus the angular modulation of $\nu_{{\rm c},\mathcal{S}}$, which raises or lowers the exponential tail of $f_{\rm up}(\sigma;\boldsymbol{r})$ along or perpendicular to the filament. Upcrossing, and hence halo formation, will be most likely in the direction that makes the threshold $\nu_{{\rm c},\mathcal{S}}$ smallest, as this makes it easier for the stochastic process to reach it.

In analogy to the unconditional case, when a characteristic mass scale could be defined for which $\sigma = \delta_{\rm c}$, equation (49) suggests to define the characteristic mass scale $\sigma_\star = \sigma(M_\star)$ for haloes near the saddle as the one for which $\nu_{{\rm c},\mathcal{S}} = 1$ in equation (51). In the language of excursion sets, this request naturally sets the scale

$$\sigma_\star^2(\boldsymbol{r}) \equiv \left(\delta_{\rm c} - \xi_{00}\nu_{\mathcal{S}} + \frac{15}{2}\xi_{20}\mathcal{Q}\right)^2 + \xi^2(r)\,. \tag{57}$$

This is now an implicit equation for $\sigma_\star$, because the RHS has a residual dependence on $\sigma_\star$ through $\xi_{\alpha\beta}(r, R(\sigma_\star), R_S)$, as shown in

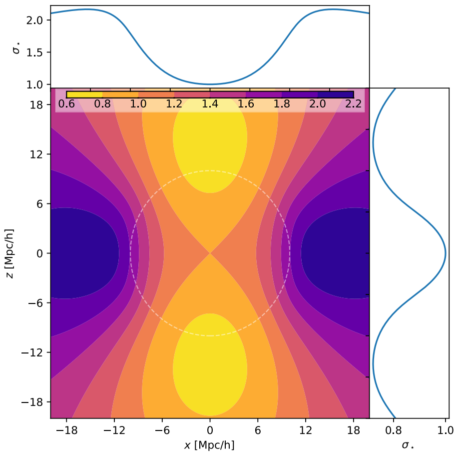

Figure 7. Isocontours in the x–z plane of the typical upcrossing scale $\sigma_\star$ around a saddle point [at (0, 0)]. The saddle point is defined using the values of Table D1. The profiles in the direction of the filament (z-direction) and of the void (x-direction) are plotted on the sides. The smoothing scale is $R = 1$ Mpc h^{-1}. They are obtained by solving equation (57) for $\sigma_\star$ at each point, with a ΛCDM power spectrum, and normalized to the value at the saddle point. In the filament, haloes form at a smaller σ (higher mass) and conversely in the void.

Appendix E. This equation can be solved numerically for $\sigma_\star$ and then for $M_\star$.

The angular dependence of $\sigma_\star(\boldsymbol{r})$ is entirely due to $\xi_{20}\mathcal{Q}$. Since the pre-factor of $\mathcal{Q} \equiv \hat{r}_i q_{ij}\hat{r}_j$ is positive, $\sigma_\star(\boldsymbol{r})$ will be smallest when $\boldsymbol{r}$ aligns with the eigenvector with the smallest eigenvalue, and $\mathcal{Q}$ is most negative. This happens when $\theta = 0$ in equation (46): that is, in the direction of positive outflow, along which a filament will form. Thus, in filaments haloes tend to be more massive than field haloes. The full radial and angular dependence of the characteristic mass scale $\sigma_\star$ is shown in Fig. 7.

4.3 Conditional accretion rate

The abundance of haloes of given mass and accretion rate at distance $\boldsymbol{r}$ from a saddle is obtained by replacing the probability distribution $p_{\rm G}(\nu_{\rm c}, \nu_{\rm c}' + \nu_{\rm c}/\sigma\alpha)$ in equation (23) with its conditional counterpart given the saddle constraint. As shown by equation (F12), this conditional distribution is equal to the distribution of the effective independent variables $\tilde{\nu}$ and $\delta' - \langle\delta'|\nu_{\rm c},\mathcal{S}\rangle$ introduced in Section 2.2, times a Jacobian factor of $\sigma/(1-\xi^2/\sigma^2)$. Furthermore, the relation (19) giving the excursion set slope in terms of the accretion rate reads in these new variables

$$\delta' - \langle\delta'|\nu_{\rm c},\mathcal{S}\rangle = \frac{\nu_{\rm c}}{\alpha} - \mu_{\rm S}\,. \tag{58}$$

Putting these two ingredients together, equation (23) becomes

$$f_{\rm up}(\sigma,\alpha;\boldsymbol{r}) = \frac{\nu_{\rm c}^2}{\sigma^2\alpha^3}p_{\rm G}(\nu_{\rm c}, \nu_{\rm c}'+\nu_{\rm c}/\sigma\alpha|\mathcal{S})\,,$$
$$= \frac{\nu_{\rm c}^2}{\alpha^3}\frac{{\rm e}^{-\left(\nu_{{\rm c},\mathcal{S}}^2+\gamma_{\alpha,\mathcal{S}}^2\right)/2}}{2\pi\sqrt{(\sigma^2-\xi^2){\rm Var}(\delta'|\nu_{\rm c},\mathcal{S})}}\,, \tag{59}$$

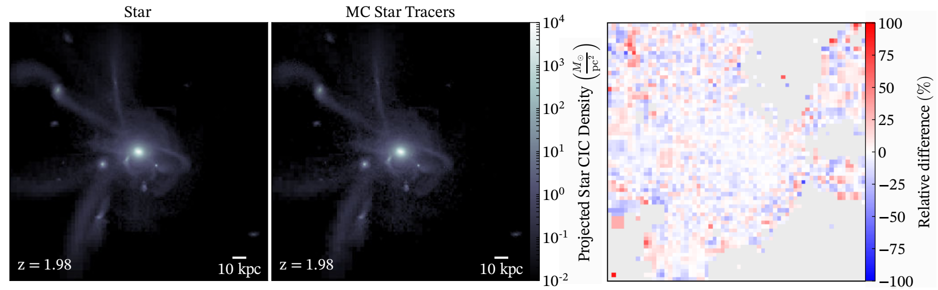

Fig. 13. Stellar surface density (*left panel*), star-tracer surface density (*centre panel*), and relative difference (*right panel*). The data are the same as in Fig. 10. In the difference map, regions where no stars are found are indicated in grey. The star and star-tracer distributions are in very good agreement; their difference shows no spatial dependence. The noise level is higher than in Fig. 10 at large radii where the star surface density is smaller than the gas surface density, hence the star mass distribution is less resolved than the gas.

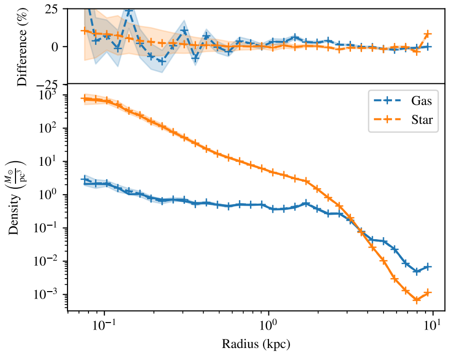

Fig. 14. *Bottom panel*: radial profile of the gas density (solid blue) and star density (solid orange) vs. the gas tracer density (blue cross) and the star-tracer density (orange cross). The error bars are given by a Poisson sampling noise. *Top panel*: relative difference between the baryon and the tracer profiles. The tracers match their baryon counterpart at a few percent level.

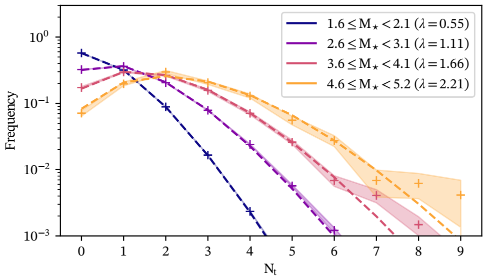

Fig. 15. Distribution of the number of star tracers per star for different star particle mass bins (in units of $10^4\,M_\odot$) as observed in the simulation (symbols and shaded surfaces) vs. as given by a Poisson distribution with parameter $\lambda = \langle M_\star\rangle/m_{\rm t}$ (dashed). The error bars have been estimated using a bootstrap method. For all stars, the distribution of the number of star tracers per star is approximated by a Poisson distribution with parameter λ.

3.3. Bi-modal accretion at high redshift: a science case for tracer particles

Low-mass galaxies (embedded in halos $M_{\rm h} \lessapprox 10^{11}\,M_\odot$) exhibit a significant amount of "cold-mode" cosmological accretion made of cold gas streaming in narrow filaments with a temperature typically below $T_{\rm max} \lessapprox 10^5$ K (Birnboim & Dekel 2003; Kereš et al. 2005; Ocvirk et al. 2008; Nelson et al. 2013, 2016). A "hot-mode" phase made of gas that was shock heated before entering the virial radius ($T_{\rm max} \sim 10^6$ K) appears in halos with higher mass. At early times ($z > 2.5$), the accretion is dominated by the cold mode. As time goes by, halos grow in mass so that an increasing fraction of the gas heats up before entering the halo. The outcome of this is a decrease of the relative importance of cold accretion compared to hot accretion. By $z \lessapprox 2$, most of the accreted material comes from the diffuse hot phase. Hence, getting access to the Lagrangian history of the stars and of the star-forming gas is key to pinning down the origin of gas acquisition in galaxies.

We revisit this result using RAMSES and the MC tracer particles. Using the cosmological simulation of Sect. 3.2, we study the accretion of gas as a function of time around the central galaxy. We select all the gas tracers that end up in star particles (not the star-forming gas) at $z = 2$ and $r < 0.1R_{\rm vir}$. The halos were detected using the AdaptaHOP halo finder (Aubert et al. 2004). For the positioning of the centre of the DM halo, we start from the first AdaptaHOP guess of the centre (densest particle in the halo) and from a sphere the size of the virial radius of the halo; we use a shrinking sphere (Power et al. 2003) by recursively finding the centre of mass of the DM within a sphere 10% smaller than the previous iteration. We stop the search once the sphere has a size smaller than ≃100 pc and take the densest particle in the final region. Twenty neighbours are used to compute the local density. Only structures with a density greater than 80 times the average total matter density and with more than 200 particles are taken into account. The original AdaptaHOP finder is applied to the stellar distribution in order to identify galaxies with more than 200 particles. Their Lagrangian history is reconstructed in post-processing from the 132 equally spaced (Δt = 25 Myr) outputs, and the thermodynamical properties of

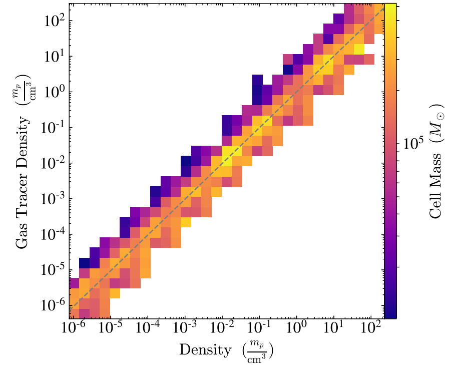

Fig. 11. Gas density vs. gas tracer density, colour coded by cell mass. The grey dashed line shows the one-to-one relation. The gas and gas tracer densities match on nine orders of magnitude.

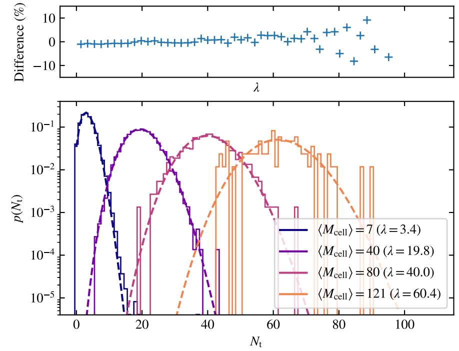

Fig. 12. *Bottom panel*: distribution of the number of gas tracers for different cell-mass bins as observed in the simulation (solid lines) vs. a Poisson distribution with parameter $\lambda = \langle M_{\rm cell}\rangle/m_{\rm t}$ (dashed lines, reported in the legend). *Top panel*: relative difference between the observed mean number of tracer particles and the expected one, λ, as a function of λ. For all cells, the distribution of the number of gas tracers per cell is given by a Poisson distribution with parameter λ.

particle is attached to the star particle and has a probability of $p_\star \equiv M_{\star,0}/M_{\rm cell}$ of becoming a "star tracer", where $M_{\star,0}$ is the mass of the newly created star particle[8]. Because $M_{\star,0} < M_{\rm cell}$ – a star particle cannot be formed with more material than what is available – this probability is well defined: $0 < p_\star < 1$. When the heavy stars in a star particle go into SN, they yield $\eta M_\star$, and the mass of the corresponding star particle becomes $M_\star = (1-\eta)M_{\star,0}$. The star tracers are then returned to the gas with a probability of η. Before the SNe explode, the distribution of tracers for an individual star particle is given by a binomial distribution with parameters N_i (the initial number of tracer in the cell where the star particle formed) and $p_\star$

$$p_{\rm form}(N_i; N_f = k) = \binom{N_i}{k} p_\star^k (1-p_\star)^{N_i-k}. \tag{20}$$

The number of tracer particles released in the SN event reads

$$p_{\rm SN}(N_f; N = k) = \binom{N_f}{k} \eta^k (1-\eta)^{N_f-k}, \tag{21}$$

where N_f is the number of star tracers in the star particle before the SN explosion. The number of tracers in the star particle after the SN has exploded is, thus, given by a binomial distribution of parameters N_i and $(1-\eta)p_\star$,

$$p_\star^{\rm f}(N_i; N = k) = \binom{N_i}{k} ((1-\eta)p_\star)^k (1-(1-\eta)p_\star)^{N_i-k}. \tag{22}$$

In the limit where the N_i becomes large and $(1-\eta)p_\star$ small, Eq. (22) converges mathematically to a Poisson distribution with parameter $N_i(1-\eta)p_\star$.

Now, we compare the expected distribution of tracer particles to the measured one. Figure 15 presents the distribution of the number of tracer particles per star particle for different star particle mass bins. The number of star tracers per star particle can be seen to be well approximated by a Poisson distribution with parameter $\lambda = \langle M_\star\rangle/m_{\rm t}$. There is a clear deviation at the tail of the distribution which displays an excess of probability. This is however expected as when a star forms in a cell, a significant part of the cell mass is converted into the star, so that $p_\star \approx 1$. Because usually $(1-\eta) \approx 0.9$, the product $p_\star(1-\eta)$ is also of order unity. At the same time, cells where stars form have a typical mass of $10^4 M_\odot \sim m_{\rm t}$, meaning that they contain only a few gas tracers at star formation. Therefore, we expect a significant deviation from a Poisson distribution, as the requirement for Eq. (22) to converge to a Poisson distribution is not met. This argument is reinforced by the fact that, compared to light stars (e.g. the blue curve of Fig. 15), the most massive stars have a more top-heavy distribution (e.g. the red curve) than a Poisson distribution. Indeed, these massive stars are relatively more massive than their parent cell, meaning that the parameter $p_\star$ is larger. In the simulation, star formation is only activated for cells above a given (fixed) density threshold. This is usually achieved at the maximum resolution, causing cells experiencing star formation to have typically the same mass, and therefore the same number of gas tracer particles, regardless of the mass of the forming stars. Consequently, the massive star particle distribution is indeed less Poissonian than that of the light stars, since their $p_\star$ is larger at fixed N_i. Figure 15 is in qualitative agreement with this.

3.2.4. SMBH evolution

Using our cosmological simulations, we have checked that the total mass of SMBH tracer particles ($M_{\rm t\,SMBH,tot} = (3.5 \pm 0.3) \times 10^6\,M_\odot$[9]) matches that of SMBH in the simulation ($M_{\rm SMBH,tot}/(1-\varepsilon_{\rm r}) = 3.1 \times 10^6\,M_\odot$) at the 10% level, up to an $\varepsilon_{\rm r}$ factor. This factor is due to the mass lost by the accreted material as it falls onto the black hole. This mass is radiated away and lost to the simulation. Because the tracer particles have a fixed mass in our implementation, they are unable to capture the mass energy that is radiated. However, one could store the value of $\varepsilon_{\rm r}$ at accretion time onto each tracer to be able to reconstruct the exact mass that the SMBH tracer represents.

[8] We note that in practice the star particles have a mass that is a multiple of the stellar mass resolution.

[9] The uncertainty has been estimated using a 1-σ Poissonian noise.

where $\mathrm{Var}\left(\delta'|\nu_{\rm c},\mathcal{S}\right)$ is given by equation (F17) and

$$Y_{\alpha,\mathcal{S}}(\boldsymbol{r}) \equiv \frac{\nu_{\rm c}/\alpha - \mu_{\mathcal{S}}(\boldsymbol{r})}{\sqrt{\mathrm{Var}\left(\delta'|\nu_{\rm c},\mathcal{S}\right)}}\,, \tag{60}$$

with $\mu_{\mathcal{S}}(\boldsymbol{r})$ given by equation (53). Again, like equation (23), this result could be obtained by taking $\langle\delta'|\nu_{\rm c},\alpha,\mathcal{S}\rangle = \nu_{\rm c}/\alpha$ and the limit $\mathrm{Var}\left(\delta'|\nu_{\rm c},\alpha,\mathcal{S}\right) \to 0$ in equation (16), which would give $F(X_{\alpha,\mathcal{S}}) = 1$.

To investigate the anisotropy of the accretion rate for haloes of the same mass, one needs the conditional probability of α given upcrossing at σ, that is the ratio of equations (59) and (49). This conditional probability reads

$$f_{\rm up}(\alpha|\sigma;\boldsymbol{r}) = \frac{\nu_{\rm c}\mathrm{e}^{-Y^2_{\alpha,\mathcal{S}}/2}}{\alpha^3\sqrt{2\pi\mathrm{Var}\left(\delta'|\nu_{\rm c},\mathcal{S}\right)}}\frac{\nu_{\rm c}}{\mu_{\mathcal{S}}F(X_{\mathcal{S}})}\,, \tag{61}$$

with $\mu_{\mathcal{S}}(\boldsymbol{r})$ and $X_{\mathcal{S}}(\boldsymbol{r})$ given by equations (53) and (54), respectively. The second fraction in this expression is thus a normalization factor that does not depend on α, and which tends to 1 when $\nu_{\rm c} \gg 1$ in the large-mass limit. Equation (61) is the main result of this subsection. It depends on the angular position $\hat{\boldsymbol{r}}$ through the terms $\xi'_{20}\mathcal{Q}$ and $\xi_{20}\mathcal{Q}$ contained in $\mu_{\mathcal{S}}(\boldsymbol{r})$, and thus also in $Y_{\alpha\mathcal{S}}$ and $X_{\mathcal{S}}$. The angular dependence is now weighted by two different functions $\xi_{20}(r)$ and $\xi'_{20}(r)$, whose relative amplitude matters to determine the overall effect.

To understand the angular variation of the exponential tail of this distribution, let us focus on how $Y_\alpha(\boldsymbol{r})$ depends on $\hat{\boldsymbol{r}}$. That is, on the anisotropic part of $-\mu_{\mathcal{S}}(\boldsymbol{r})$. In the large-mass limit, when $\sigma\xi'_{\alpha\beta}(r) \ll \xi_{\alpha\beta}(r)$, equation (53) tells us that the anisotropic part of $Y_\alpha(\boldsymbol{r})$ is proportional to $-\xi_{20}\mathcal{Q}$, with a proportionality factor that is always positive and $\mathcal{O}(1)$. Thus, the modulation has the opposite sign of the anisotropic part of $\nu_{\rm c,\mathcal{S}}$, given in equation (51): for trajectories with the same upcrossing scale, the probability of having a given accretion rate is lowest in the direction of the eigenvector of $\bar{q}_{ij}$ with the lowest (most negative) eigenvalue, for which Y_α is largest. That is, for haloes with the same mass, the probability of having a given accretion rate is lowest along the ridge of the potential saddle, which will become the filament.

The typical accretion rate $\alpha_\star$ of the excursion set haloes described by the distribution (61) corresponds to the condition $Y_{\alpha_\star,\mathcal{S}} = 1$. This definition transforms equation (27) into

$$\alpha_\star(\sigma,\boldsymbol{r}) \equiv \frac{\nu_{\rm c}}{\sqrt{\mathrm{Var}\left(\delta'|\nu_{\rm c},\mathcal{S}\right)} + \mu_{\mathcal{S}}(\boldsymbol{r})}\,, \tag{62}$$

where $\mathrm{Var}\left(\delta'|\nu_{\rm c},\mathcal{S}\right)$ and $\mu_{\mathcal{S}}(\boldsymbol{r})$ are given by equations (F17) and (53). In the limit of small anisotropy, the angular variation of the typical accretion rate is

$$\Delta\alpha_\star(\sigma,\boldsymbol{r}) = \frac{\alpha_\star^2|_{\bar{q}=0}}{\nu_{\rm c}}\frac{15}{2}\left[\xi'_{20} - \frac{\sigma - \xi'_I\xi_I}{\sigma^2 - \xi^2}\xi_{20}\right]\hat{r}_i\bar{q}_{ij}\hat{r}_j\,, \tag{63}$$

where $\alpha_\star|_{\bar{q}=0}$ – the value of $\alpha_\star(\sigma,\boldsymbol{r})$ when $\bar{q}_{ij} = 0$ – is function of r but not of the angles. Therefore, at a fixed distance r from the saddle, haloes that form in the direction of the filament tend to have higher accretion rates than haloes with the same mass that form in the orthogonal direction. The full dependence of the characteristic accretion rate $\alpha_\star$ for haloes of the same mass on the position with respect to the saddle point of the potential is shown in Fig. 8. The figure shows that the saddle point is a local minimum of the accretion rate along the direction connecting two regions with high density of final objects, which is two peaks of the final halo density field. This is consistent with the result that the accretion of haloes in filaments is suppressed by the effect of the tidal forces (as shown by, e.g. Hahn et al. 2009; Borzyszkowski et al. 2016). The threshold $\delta \lesssim \delta_{\rm c}$ is reached at smaller σ in filaments than in void, hence the slope is smaller at upcrossing. It is shown schematically in the top panel of Fig. B3. A verification with a constrained random field is shown in the bottom panel of Fig. B3. The details of the method used are given in Appendix B.

One can also evaluate the mean of the conditional distribution (61) following equation (26), integrating $\alpha\,f_{\rm up}(\alpha|\sigma,\mathcal{S})$ over the range of positive α. This conditional mean value is

$$\langle\alpha|\sigma\rangle(\boldsymbol{r}) = \frac{\nu_{\rm c}}{\mu_{\mathcal{S}}(\boldsymbol{r})}\frac{1+\mathrm{erf}(X_{\mathcal{S}}(\boldsymbol{r})/\sqrt{2})}{2F(X_{\mathcal{S}}(\boldsymbol{r}))}\,; \tag{64}$$

in the large-mass regime, where $X_{\mathcal{S}} \gg 1$ and the whole second fraction tends to 1, the position-dependent conditional mean $\langle\alpha|\sigma\rangle(\boldsymbol{r})$ is essentially the same as $\alpha_\star(\boldsymbol{r})$ defined in equation (62). As for $f_{\rm up}(\alpha|\sigma)$, all higher order moments are ill defined. One can also find useful information in the most likely accretion rate

$$\alpha_{\rm max}(\sigma,\boldsymbol{r}) = \frac{\nu_{\rm c}^2}{6\mathrm{Var}\left(\delta'|\nu_{\rm c},\mathcal{S}\right)}\left[\sqrt{1+\frac{12}{X^2_{\mathcal{S}}(\boldsymbol{r})}} - 1\right], \tag{65}$$

which generalizes equation (28) to the presence of a saddle point at distance $\boldsymbol{r}$. The same conclusion holds here namely the most likely accretion rate increases from voids to saddles and saddles to nodes. The following only considers maps of $\alpha_\star(\sigma,\boldsymbol{r})$, since the information encoded in $\alpha_{\rm max}(\sigma,\boldsymbol{r})$ and $\langle\alpha|\sigma\rangle(\boldsymbol{r})$ is somewhat redundant.

4.4 Conditional formation time

The formation time in the vicinity of a saddle is obtained by fixing the saddle parameters $\mathcal{S} = \{\nu_{\mathcal{S}}, \hat{r}_i g_i, \hat{r}_i\bar{q}_{ij}\hat{r}_j\}$, with $g_i = 0$, besides $\nu = \nu_{\rm c}$ and $\nu_{1/2} = \nu_{\rm f}$. A five-dimensional constraint on the Gaussian variables must now be dealt with, and mapped into $\{\sigma, D_{\rm f}, \mathcal{S}\}$. Since the mapping of the saddle parameters is the identity, the Jacobian of the transformation still gives $|\nu' - \nu'_{\rm c}|\nu_{\rm f}/D_{\rm f}$, like in Section 3.2 (where there was no saddle constraint). The formalism outlined in Section 2.2 still applies: the joint probability of upcrossing at σ with formation time $D_{\rm f}$ given the saddle is obtained replacing $\{\nu\}$ with $\{\nu_{\rm f},\mathcal{S}\}$ in equation (16), multiplying by the Jacobian $\nu_{\rm f}/D_{\rm f}$ and dividing by the probability $p_{\rm G}(\mathcal{S})$ of the saddle. The result is

$$f_{\rm up}(\sigma, D_{\rm f};\boldsymbol{r}) = \frac{\nu_{\rm f}}{D_{\rm f}}p_{\rm G}(\nu_{\rm c},\nu_{\rm f}|\mathcal{S})\frac{\mu_{\rm f,\mathcal{S}}}{\sigma}F(X_{\rm f,\mathcal{S}}) \tag{66}$$

which extends equation (32) by including the presence of a saddle point of the potential at distance $\boldsymbol{r}$, with

$$\mu_{\rm f,\mathcal{S}} \equiv \langle\delta'|\nu_{\rm f},\nu_{\rm c},\mathcal{S}\rangle\,,\quad X_{\rm f,\mathcal{S}} \equiv \frac{\mu_{\rm f,\mathcal{S}}}{\sqrt{\mathrm{Var}\left(\delta'|\nu_{\rm f},\nu_{\rm c},\mathcal{S}\right)}}\,. \tag{67}$$

The conditional mean and variance of δ' given $\{\nu_{\rm f},\nu_{\rm c},\mathcal{S}\}$ are explicitly computed in Appendix F4, equations (F30) and (F31).

The conditional probability of the formation time $D_{\rm f}$ given σ at a distance $\boldsymbol{r}$ from the saddle follows dividing equation (66) by $f_{\rm up}(\sigma|\boldsymbol{r})$, given by equation (49). This ratio – which is the main result of this section – gives

$$\begin{aligned} f_{\rm up}(D_{\rm f}|\sigma;\boldsymbol{r}) &= \frac{\nu_{\rm f}}{D_{\rm f}}p_{\rm G}(\nu_{\rm f}|\nu_{\rm c},\mathcal{S})\frac{\mu_{\rm f,\mathcal{S}}}{\mu_{\mathcal{S}}}\frac{F(X_{\rm f,\mathcal{S}})}{F(X_{\mathcal{S}})}\,, \\ &= \frac{(\delta_{\rm c}/D_{\rm f}^2)\mathrm{e}^{-\nu^2_{\rm f,c,\mathcal{S}}/2}}{\sqrt{2\pi\mathrm{Var}\left(\delta_{1/2}|\nu_{\rm c},\mathcal{S}\right)}}\frac{\mu_{\rm f,\mathcal{S}}}{\mu_{\mathcal{S}}}\frac{F(X_{\rm f,\mathcal{S}})}{F(X_{\mathcal{S}})}\,. \end{aligned} \tag{68}$$

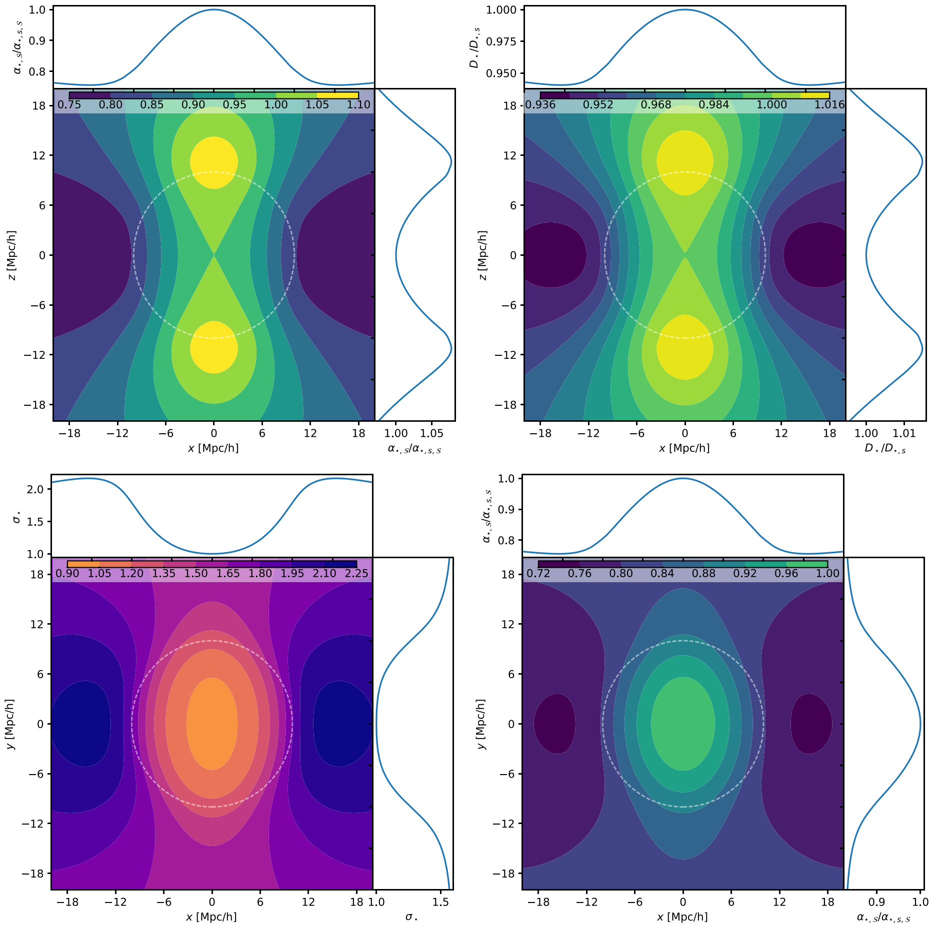

Figure 8. Isocontours in the x–z plane of the typical accretion rate $\alpha_\star$ (upper left) and formation time $D_\star$ (upper right) around a saddle point [at (0, 0)] and in the x–y plane of the characteristic upcrossing scale $\sigma_\star$ (lower left) and typical accretion rate (lower right). The saddle point is defined using the values of Table D1. The profiles going through the saddle point in the x–z (upper panels) and x–y (lower panels) planes are plotted on the sides. The smoothing scale is $R = 1\,\mathrm{Mpc}\,h^{-1}$. They were obtained with a ΛCDM power spectrum, and normalized to the value at the saddle point. Since the filament has higher mean density, excursion set trajectories upcrossing at a given σ have shallower slopes. Hence, typical haloes are more massive in filaments and at fixed mass, haloes forming in the filament have larger accretion rates at $z = 0$ and form later. The same hierarchy exists between the two perpendicular directions.

Equation (68) provides the counterpart of equation (36) near a saddle point, in terms of the effective threshold

$$\nu_{\mathrm{f,c},\mathcal{S}}(D_\mathrm{f}, \boldsymbol{r}) \equiv \frac{\delta_\mathrm{c}/D_\mathrm{f} - \langle\delta_{1/2}|\nu_\mathrm{c}, \mathcal{S}\rangle}{\sqrt{\mathrm{Var}\left(\delta_{1/2}|\nu_\mathrm{c}, \mathcal{S}\right)}}\,, \tag{69}$$

with

$$\langle\delta_{1/2}|\nu_\mathrm{c}, \mathcal{S}\rangle = \xi_{1/2}\cdot\mathcal{S} + \frac{\langle\delta\delta_{1/2}\rangle - \xi\cdot\xi_{1/2}}{\sigma^2 - \xi^2}(\delta_\mathrm{c} - \xi\cdot\mathcal{S})\,, \tag{70}$$

$$\mathrm{Var}\left(\delta_{1/2}|\nu_\mathrm{c}, \mathcal{S}\right) = \sigma^2_{1/2} - \xi^2_{1/2} - \frac{(\langle\delta\delta_{1/2}\rangle - \xi\cdot\xi_{1/2})^2}{\sigma^2 - \xi^2}\,. \tag{71}$$

It also depends on the effective upcrossing parameters $\mu_\mathcal{S}(\boldsymbol{r})$ and $X_\mathcal{S}(\boldsymbol{r})$, given in equations (50)–(53). The explicit forms of the functions $\mu_{\mathrm{f},\mathcal{S}}(D_\mathrm{f}, \boldsymbol{r})$ and $X_{\mathrm{f},\mathcal{S}}(D_\mathrm{f}, \boldsymbol{r})$ are reported in Appendix F4 for convenience [equations (F33) and (F34)].

Note that in equation (68), $f_\mathrm{up}(D_\mathrm{f}|\sigma;\boldsymbol{r})$ depends on D_f also through $\nu_{\mathrm{f,c},\mathcal{S}}$ and $\mu_{\mathrm{f},\mathcal{S}}$. For early formation times ($D_\mathrm{f} \ll 1$), the

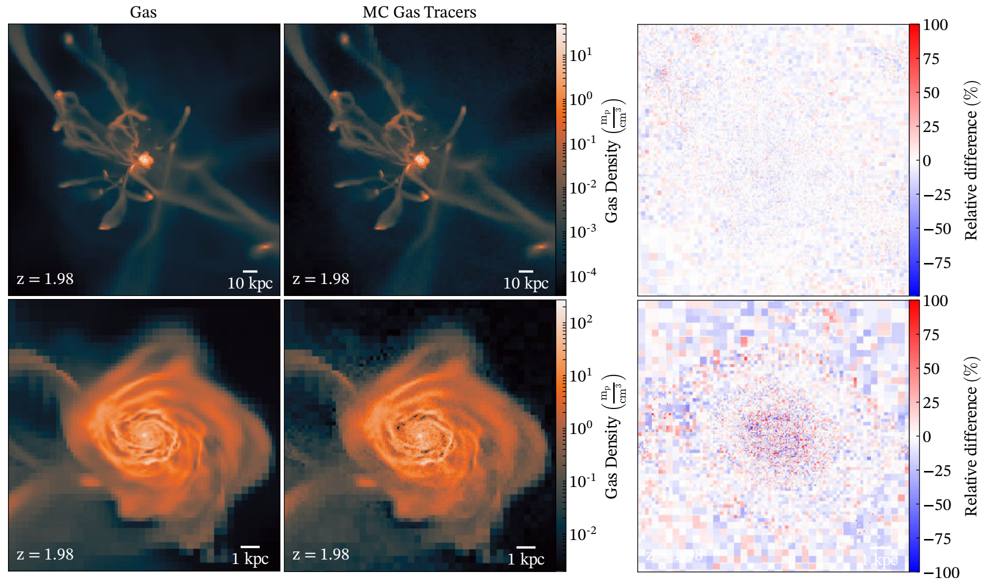

Fig. 10. Density-weighted projection of the gas density (*left panels*), of the gas tracer density (*centre panels*), and of their relative difference (*right panels*) along the x axis around the most massive galaxy of the cosmological simulation at $z = 2$. *Top panels*: large-scale structure of the gas; data have been selected within 200 kpc of the centre. *Bottom panels*: zoom on the central galaxy; data have been selected within 10 kpc of the centre of the galaxy. The MC tracer density is similar to that of the gas. The radial modulations are due to differences in cell mass at fixed cell resolution: massive cells (closer to the centre at fixed resolution) are best sampled by the MC tracers.

now continue to explore only the distribution of MC tracer particles with respect to the actual distribution of baryons. Figure 10 shows the density-weighted projected gas density and cloud-in-cell interpolated gas tracers around the zoomed galaxy of the simulation. Visual inspection reveals that the gas tracer distribution matches that of the gas with additional noise. All structures with a contrast above the noise level are reproduced by the gas tracers. More quantitatively, Fig. 11 shows the density of tracers versus the density of gas for the entire available range of gas densities (i.e. 9 orders of magnitude); the expected one-to-one relation is seen, with some scatter due to MC sampling noise.

More quantitative results can be obtained by computing the statistical properties of the gas tracer population. A cell of mass M_cell is expected to contain on average $M_\mathrm{cell}/m_\mathrm{t}$ tracers. For a sample of cells of similar masses, we expect the mean number of tracers per cell to be $\lambda \equiv \langle M_\mathrm{cell}\rangle/m_\mathrm{t}$. The distribution of the number of tracers per cell in the simulation is shown in Fig. 12 for different cell-mass bins. Within a cell-mass bin, the number of tracers N_t can be seen to be very well approximated by a Poisson distribution with parameter λ

$$p_\lambda(N_\mathrm{t} = k) = \frac{\lambda^k e^{-\lambda}}{k!}. \tag{19}$$

To confirm this observation, we compared the mean number of tracers per cell to the expected number λ in the top panel of Fig. 12. For all cell masses, the mean number of tracer particles per cell is accurately described by its expected Poisson distribution. At large values of gas mass within a cell (right of the plot), the scatter in the histogram count is due to the small number of massive cells in the simulation. Indeed, these cells can only be found in the most refined regions (otherwise they would be refined into smaller cells) where they also tend to be converted into stars.

In the following we assume that the gas tracer distribution is given by a Poisson distribution with parameter $\lambda = \langle M_\mathrm{cell}\rangle/m_\mathrm{t}$. This yields a simple rule of thumb to estimate the precision of the tracer scheme. The accuracy of the Eulerian distribution of the tracer can be written $1/\sqrt{\lambda} \sim \sqrt{m_\mathrm{t}/M_\mathrm{cell}}$.

3.2.3. Star formation and feedback

Figure 13 shows the integrated stellar mass and star-tracer mass around the zoomed galaxy of the cosmological simulation. Both distributions are visually in agreement and feature the same spatial distribution. At large radii where the star density is smaller than the gas density ($r \gtrsim 4$ kpc, see Fig. 14), the noise level of the star-tracer distribution is larger than that of the gas. This is due to the fact that small masses are poorly resolved by the MC tracers. Close to the galactic centre, the increasing star density induces a larger star-tracer density, and therefore, at fixed resolution, a smaller noise sampling. This is illustrated by the right panel of Fig. 13, where the centre of the plot shows smaller fluctuations than at large radii. More quantitative results are presented below.

We first present the analytical distribution of tracer particles for stars and for the number of tracers released in SN events, derived from first principles. When a star particle is formed, each tracer in the cell containing the newly created star

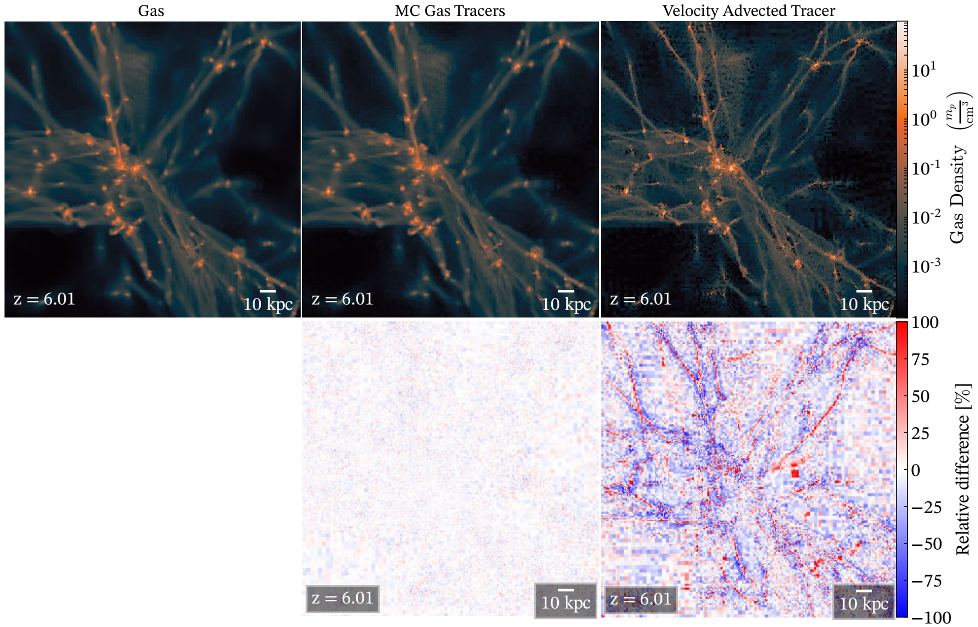

Fig. 9. *Top panels*: density weighted projection of the gas density in a cosmological simulation (*left*), of the velocity tracer distribution (*right*), and of the MC gas tracer distribution (*centre*). All the plots share the same colour map. *Bottom panels*: relative difference between the tracer and the gas. Velocity tracers accumulate in convergent regions (e.g. filaments, nodes). The MC gas tracer distribution reproduces more accurately that of the gas than velocity tracers.

($N_{\mathrm{tot}} \approx 1.3 \times 10^8$ particles). There is on average 0.55 tracers per star and 22 per initial cell. Cells of size 35 pc and density 20 cm^{-3} contain on average one tracer per cell.

3.2.1. Velocity tracers versus Monte Carlo tracers

In addition to the above simulation, we ran the exact same one replacing each MC tracer with a velocity-advected tracer. This simulation was performed down to $z = 6$ and compared to the fiducial one. Both have a similar gas distribution, confirming that the tracer particles are indeed passive[7]. At this redshift, 99% of the baryons are still in the gas phase (0.72% in stars and 8×10^{-5}% in SMBHs), meaning that the comparison between MC tracers (that can be transferred into stars) and velocity tracers is fair when looking at cosmological scales. Since the velocity tracers have not been linked to star formation or SMBHs, we expect significant discrepancies within galaxies, where the gas-to-star ratio is much smaller.

The top panels of Fig. 9 show projections of the density-weighted density of gas (top left panel), of MC tracers (top-centre panel), and of velocity-advected tracers (top-right panel). The distribution of the MC tracers resembles that of the gas with extra noise due to sampling noise. All the prominent structures in the gas are also present in the MC tracer distribution. On the other hand, the velocity tracer distribution is much sharper than that of the gas. The velocity tracers aggregate in converging flows (filaments and centres of galaxies) while MC tracers do not (they aggregate in high-mass regions, as expected). At such large scales, the origin of the discrepancy is an intrinsic issue of velocity tracers. This test shows that on a qualitative level, the MC tracers have a distribution that is in much better agreement with the gas distribution than the velocity advected tracers. The relative difference between the gas distribution and the tracer distribution is presented in the bottom panels of Fig. 9. The relative difference between the MC tracer density and the gas density (bottom central panel) is significantly smaller than the relative difference between the velocity advected tracer density and the gas density (bottom right panel). The latter is also much more biased: the velocity advected tracer density in convergent flows (e.g. filaments) can be up to an order of magnitude larger than the gas density, while in the vicinity of converging regions, the velocity advected tracer density is largely underestimated (e.g. around filaments). On the contrary, the MC tracer density is found to be in better agreement with the gas density and is not biased.

3.2.2. Gas tracers

As we have seen, velocity tracer particles are a less reliable tracer of the actual gas density compared to MC tracer particles, and this can already be seen on cosmological scales. Therefore, we

[7] They have however an indirect impact on stochastic processes such as star formation and SN feedback as they impact the random number generator (hence the outcome of these random processes will vary depending on how many and where the tracer particles are).

conditional mean $\langle \delta' | \nu_{\mathrm{f}}, \nu_{\mathrm{c}}, \mathcal{S} \rangle$ becomes large, since the trajectory must reach a very high value at $\sigma_{1/2}$. Hence, $\mu_{\mathrm{f},\mathcal{S}}(D_{\mathrm{f}}, \boldsymbol{r}) \propto 1/D_{\mathrm{f}}$. In this limit, the last ratio in equation (68) above tends to 1, and $f_{\mathrm{up}}(D_{\mathrm{f}}|\sigma; \boldsymbol{r}) \propto (1/D_{\mathrm{f}}^3)\exp(-\nu_{\mathrm{f,c},\mathcal{S}}^2/2)$, with a proportionality constant that does not depend on the angle. Then, the probability decays exponentially for small D_{f} as $\nu_{\mathrm{f,c},\mathcal{S}}$ grows. The typical formation time $D_\star = D(z_\star)$ can be defined as that value for which $\nu_{\mathrm{f,c},\mathcal{S}} = 1$ and this exponential cut-off stops being effective, that is

$$D_\star(\boldsymbol{r}, \sigma) \equiv \frac{\delta_{\mathrm{c}}}{\sqrt{\mathrm{Var}\left(\delta_{1/2}|\nu_{\mathrm{c}}, \mathcal{S}\right)} + \langle \delta_{1/2}|\nu_{\mathrm{c}}, \mathcal{S}\rangle}\,, \tag{72}$$

which provides the anisotropic generalization of the expression given in equation (38). The explicit expression for the conditional mean $\langle \delta_{1/2}|\nu_{\mathrm{c}}, \mathcal{S}\rangle$ and variance $\mathrm{Var}\left(\delta_{1/2}|\nu_{\mathrm{c}}, \mathcal{S}\right)$ are given by equations (70) and (71), respectively.

As the angular variation of $\langle \delta_{1/2}|\nu_{\mathrm{c}}, \mathcal{S}\rangle$ is approximately

$$\frac{15}{2}\Delta\sigma_{1/2}\xi_{20}(r)\mathcal{Q}(\hat{\boldsymbol{r}})\,, \tag{73}$$

where $\mathcal{Q}(\hat{r}) \equiv \hat{r}_i \bar{q}_{ij} \hat{r}_j$, $\Delta\sigma_{1/2} = \sigma_{1/2} - \sigma > 0$, the formation time $D_\star$ is larger when $\boldsymbol{r}$ is aligned with the eigenvector with the most negative eigenvalue, corresponding to the direction of the filament. One has in fact

$$\Delta D_\star(\boldsymbol{r}, \sigma) = -\frac{D_\star^2|_{\bar{q}=0}}{\delta_{\mathrm{c}}}\frac{15}{2}\Delta\sigma_{1/2}\xi_{20}(r)\mathcal{Q}(\hat{\boldsymbol{r}})\,, \tag{74}$$

where $D_\star$ depends only on the radial distance r, which shows that at a fixed distance from the saddle point, haloes in the direction of the filament tend to form later (larger $D_\star$). The saddle point is thus a minimum of the half-mass time $D_\star$ along the direction of the filament, that is a maximum of $z_\star$: haloes that form at the saddle point assemble most of their mass the earliest. Fig. 8 displays a cross-section of a map of $D_\star$ in the frame of the saddle.

5 ASTROPHYSICAL REFORMULATION

The joint and conditional PDFs derived in Sections 2–4 were expressed in terms of variables (σ, α, and D_{f}) that are best suited for the excursion set theory. Now, for the sake of connecting to observations and gathering a wider audience, let us write explicitly what the main results of those sections – equations (14), (25), and (36), and their constrained counterparts (49), (61), and (68) – imply in terms of astrophysically relevant quantities like the distribution of mass, accretion rate, and formation time of DM haloes.

5.1 Unconditional halo statistics

The upcrossing approximation provides an accurate analytical solution of the random walk problem formulated in the Extended Press–Schechter model, for a Top-Hat filter in real space and a realistic power spectrum. In this framework, the mass fraction in haloes of mass M is

$$\frac{M}{\bar{\rho}}\frac{\mathrm{d}n}{\mathrm{d}M} = \left|\frac{\mathrm{d}\sigma}{\mathrm{d}M}\right| f_{\mathrm{up}}(\sigma(M))\,, \tag{75}$$

with $f_{\mathrm{up}}(\sigma)$ given by equation (14) and is a function of mass via equation (1). For instance, for a power-law power spectrum $P(k) \propto k^{-n}$ with index $n = 2$ one has $M/M_\star = (\sigma/\sigma_\star)^{-6}$. The general power-law result $M \propto \sigma^{6/(n-3)}$ follows from equation (E17).

The excursion set approach also establishes a natural relation between the accretion rate of the halo and the slope of the trajectory at barrier crossing. One can thus predict the joint statistics of σ and of the excursion set proxy $\alpha \equiv \nu_{\mathrm{c}}/[\mathrm{d}(\delta - \delta_{\mathrm{c}})/\mathrm{d}\sigma]$ for the accretion rate. In order to get the joint mass fraction in haloes of mass M and accretion rate $\dot{M}$, one needs to introduce the Jacobian of the mapping from (σ, α) to $(M, \dot{M})$. Since $\sigma(M)$ does not depend on α, this Jacobian has the simple factorized form $|\mathrm{d}\sigma/\mathrm{d}M||\mathrm{d}\alpha/\mathrm{d}\dot{M}|$. Since $\mathrm{d}\alpha/\mathrm{d}\dot{M} = \alpha/\dot{M}$ from equation (20), one can write the joint analogue of equation (75) as

$$\frac{M\dot{M}}{\bar{\rho}}\frac{\mathrm{d}^2 n}{\mathrm{d}M\mathrm{d}\dot{M}} = \left|\frac{\mathrm{d}\log\sigma}{\mathrm{d}M}\right| \sigma\alpha f_{\mathrm{up}}(\sigma, \alpha)\,, \tag{76}$$

where $f_{\mathrm{up}}(\sigma, \alpha)$ is now given by equation (23), whereas $\sigma(M)$ and $\alpha(M, \dot{M})$ are functions of M and $\dot{M}$ via equations (1) and (20), respectively. From the ratio of equations (76) and (75), the expected mean density of haloes of given mass and accretion rate can be reformulated as

$$\dot{M}\frac{\mathrm{d}^2 n}{\mathrm{d}M\mathrm{d}\dot{M}} = \alpha f_{\mathrm{up}}(\alpha|\sigma)\frac{\mathrm{d}n}{\mathrm{d}M}\,, \tag{77}$$

where $f_{\mathrm{up}}(\alpha|\sigma)$ is given by equation (25). This expression relates analytically the number density of haloes binned by mass and accretion rate to the usual mass function.

Similarly, the joint mass fraction of haloes of mass M and formation time z_{f} (defined as the redshift at which the halo has assembled half of its mass) can be inferred from the joint statistics of σ and D_{f} $\equiv \delta_{\mathrm{c}}/\delta(\sigma_{1/2})$, where $\sigma_{1/2} \equiv \sigma(M/2)$ is the scale containing half of the initial volume. The redshift dependence of the growth function $D(z)$ is defined by equation (4). Hence, the mass fraction in haloes of given mass M and formation time z_{f} is

$$\frac{M}{\bar{\rho}}\frac{\mathrm{d}^2 n}{\mathrm{d}M\mathrm{d}z_{\mathrm{f}}} = \frac{\mathrm{d}\sigma}{\mathrm{d}M}\frac{\mathrm{d}D_{\mathrm{f}}}{\mathrm{d}z_{\mathrm{f}}} f_{\mathrm{up}}(\sigma, D_{\mathrm{f}})\,, \tag{78}$$

and its conditional is

$$\frac{\mathrm{d}^2 n}{\mathrm{d}M\mathrm{d}z_{\mathrm{f}}} = \frac{\mathrm{d}D_{\mathrm{f}}}{\mathrm{d}z_{\mathrm{f}}} f_{\mathrm{up}}(D_{\mathrm{f}}|\sigma)\frac{\mathrm{d}n}{\mathrm{d}M}\,, \tag{79}$$

where the joint and conditional distributions of D_{f} and σ are given by equations (32) and (36), respectively.

Interestingly, while the excursion set mass function is subject to the limitation of upcrossing theory, the conditional statistics of accretion rate, or formation redshift, at given mass should be considerably more accurate. This is because the main shortcoming of excursion sets is the lack of a prescription for where to centre in space each set of concentric spheres giving a trajectory. These spheres are placed at random locations, whereas they should insist on the centre of the protohalo. However, choosing a better theoretical model (e.g. the theory of peaks) to set correctly the location of the excursion set trajectories would not dramatically modify the conditional statistics. Changing the model would modify the function $F(x)$, defined in equation (13), that modulates each PDF. In conditional statistics, only ratios of this function appear, which are rather model independent, whereas the probability of the constraint does not appear. The relevant part for our analysis – the exponential cut-off of each conditional distribution given the constraint – would not change. Hence, even though equation (75) does not provide a good mass function $\mathrm{d}n/\mathrm{d}M$, one may argue that the relations (77) and (79) are still accurate in providing the joint abundance statistics of mass and accretion rate, or mass and formation redshift, once a better model – or even a numerical fit – is used to infer $\mathrm{d}n/\mathrm{d}M$.

5.2 Halo statistics in filamentary environments

In the tide of a saddle of given height and curvature, equations (75), (76), and (78) remain formally unchanged, except for the

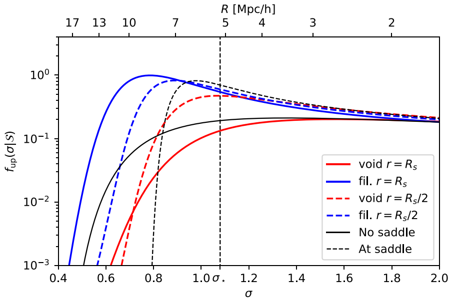

Figure 9. PDF of σ at upcrossing given the saddle point in the x (void, in red) and z (filament, in blue) directions at distance $r = 10\,\mathrm{Mpc}\,h^{-1}$ (solid lines) and $r = 5\,\mathrm{Mpc}\,h^{-1}$ (dashed lines). The saddle point is defined using the values of Table D1. The PDF without the saddle point is shown in black and at the saddle point in dashed black. The value of $\sigma_\star$ at the saddle point is shown by the vertical dashed line. In the filament, the PDF is boosted for small values of σ: there are more massive haloes in the filament. The opposite trend is seen in the void.

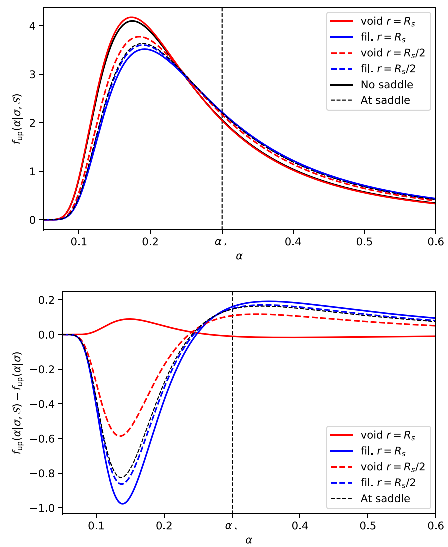

Figure 10. PDF of α at upcrossing given the smoothing scale and the saddle point in the x (void, in red) and z (filament, in blue) directions at distance $r = 10\,\mathrm{Mpc}\,h^{-1}$ (solid lines) and $r = 5\,\mathrm{Mpc}\,h^{-1}$ (dashed lines) (upper panel) compared to the PDF without the saddle point (lower panel). The saddle point is defined using the values of Table D1. The PDF with no saddle point is shown in solid black and the PDF at the saddle point in dashed black. In the filament, the PDF is boosted at its high end: haloes accrete more. The opposite trend is seen in the void.

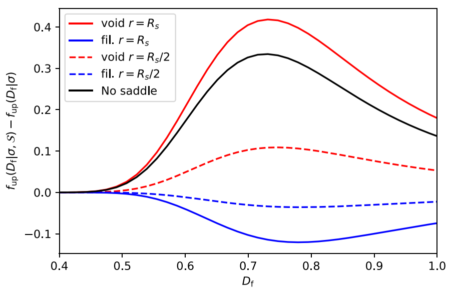

Figure 11. PDF of D_{f} at upcrossing given the smoothing scale and the saddle point in the x (void, in red) and z (filament, in blue) directions at distance $r = 10\,\mathrm{Mpc}\,h^{-1}$ (solid lines) and $r = 5\,\mathrm{Mpc}\,h^{-1}$ (dashed lines) and without saddle point (black) compared to the PDF at the saddle point. The saddle point is defined using the values of Table D1. In the filament, the PDF is boosted at the late formation end: haloes form later. The opposite trend is seen in the void.

replacement of $f_{\mathrm{up}}(\sigma)$, $f_{\mathrm{up}}(\sigma, \alpha)$, and $f_{\mathrm{up}}(\sigma, D_{\mathrm{f}})$ by their position-dependent counterparts $f_{\mathrm{up}}(\sigma; \boldsymbol{r})$, $f_{\mathrm{up}}(\sigma, \alpha; \boldsymbol{r})$, and $f_{\mathrm{up}}(\sigma, D_{\mathrm{f}}; \boldsymbol{r})$ conditioned to the presence of a saddle, given by equations (49), (59), and (66), respectively. Similarly, in equations (77) and (79), one should substitute the distribution $f_{\mathrm{up}}(\alpha|\sigma)$ and $f_{\mathrm{up}}(D_{\mathrm{f}}|\sigma)$ by their conditional counterparts $f_{\mathrm{up}}(\alpha|\sigma; \boldsymbol{r})$ and $f_{\mathrm{up}}(D_{\mathrm{f}}|\sigma; \boldsymbol{r})$ of accretion rate and formation time at fixed halo mass, given by equations (61) and (68).

These functions depend on the mass M, accretion rate $\dot{M}$, and formation time z_{f} of the halo through $\sigma(M)$, $\alpha(M, \dot{M})$, and $D_{\mathrm{f}}(z_{\mathrm{f}})$, as before. However, conditioning on $\mathcal{S}$ introduces a further dependence on the geometry of the environment (the height $\nu_{\mathcal{S}}$ of the saddle and its anisotropic shear $\bar{q}_{ij}$) and on the position $\boldsymbol{r}$ of the halo with respect to the saddle point. This dependence arises because the saddle-point condition modifies the mean and variance of the stochastic process (δ, δ') – the height and slope of the excursion set trajectories – in a position-dependent way, making it more or less likely to form haloes of given mass and assembly history within the environment set by $\mathcal{S}$. The mean becomes anisotropic through $\mathcal{Q} = \hat{r}_i \bar{q}_{ij} \hat{r}_j$, and both mean and variance acquire radial dependence through the correlation functions $\xi_{\alpha\beta}$ and $\xi'_{\alpha\beta}$, defined in equation (E12), which depend on r, $R_{\mathcal{S}}$, and R [the variance remains isotropic because the variance of $\bar{q}_{ij}$ is still isotropic, see e.g. equation (71) and Appendix E].

The relevant conditional distributions are displayed in Figs 9–11. The plots show that haloes in the outflowing direction (in which the filament will form) tend to be more massive, with larger accretion rates and forming later than haloes at the same distance from the saddle point, but located in the infalling direction (which will become a void). This trend strengthens as the distance from the centre increases. The saddle point is thus a minimum of the expected mass and accretion rate of haloes, and a maximum of formation redshift, as one moves along the filament. The opposite is true as one moves perpendicularly to it. This behaviour is consistent with the expectation that filamentary haloes have on average lower mass and accretion rate, and tend to form earlier, than haloes in peaks.

few kiloparsecs). This is chosen so that the jet reaches cells at different levels of refinement and in other CPU domains. Within 50 kpc of the AGN, there are 1200, 24 000, 12 000, 13 000 and 8000 cells at levels 2^8 to 2^{12} (Δx from 5 kpc to 0.3 kpc) so that the tracer particles are deposited in regions of different refinement level. This region also covers 8 of the 16 CPU domains used. This controlled test enables us to check that the distribution of tracers sent through the jet matches the expected distribution, in the presence of deep refinement and parallelism.

Let us first present the theoretical probability distribution function as a function of the distance to the jet and along the jet. We then compare theoretical figures to those of the simulation. The marginal probability density function (PDF) in the direction of the jet $r_\parallel$ is given by

$$p(r_\parallel) = \frac{1}{A} \begin{cases} \sqrt{e} - e^{r_\parallel^2/2r_{\mathrm{AGN}}^2}, & \text{if } |r_\parallel| < r_{\mathrm{AGN}}, \\ \sqrt{e} - 1, & \text{if } r_{\mathrm{AGN}} < |r_\parallel| < 2r_{\mathrm{AGN}}, \end{cases} \tag{16}$$

where

$$A = 2\sqrt{e} r_{\mathrm{AGN}} \left(2 + \sqrt{2} F\left(1/\sqrt{2}\right) - 1/\sqrt{e}\right). \tag{17}$$

Here F is Dawson's integral. The marginal PDF in the radial direction $r_\perp$ is

$$p(r_\perp) = \frac{r_\perp e^{-r_\perp^2/2r_{\mathrm{AGN}}^2}\left(1 + \sqrt{1 - r_\perp^2/r_{\mathrm{AGN}}^2}\right)}{r_{\mathrm{AGN}}^2\left(2 - \sqrt{2}F\left(1/\sqrt{2}\right) - 1/\sqrt{e}\right)}. \tag{18}$$

The marginal PDF in the radial distribution is similar to a χ distribution with two degrees of freedom with an extra factor due to the two spherical caps: more particles are found close to the centre of the jet since the capsule is more extended close to its centre.

Figure 8 presents the results from the comparison of the simulation to the expected distribution. The distribution in the radial direction has been rescaled by a factor of two to span the same range as in the parallel direction. Theoretical curves (Eqs. (16) and (18)) are in very good agreement with the observed distributions, confirming that the algorithm is distributing tracer particles correctly in jets. In addition we have also run the same idealised simulation without forcing the AGN efficiency. We report that the tracer mass flux is equal to the gas mass flux. This confirms that the physical model of the jet is accurately sampled by the tracer particles interacting with it, both in terms of its mass and for its spatial distribution.

3.2. Astrophysical test

We have run a 50 cMpc/h-wide cosmological simulation down to $z = 2$ zoomed on a group of mass $1 \times 10^{13}\,M_\odot$ at $z = 0$, where the size of the zoom in the Lagrangian volume of initial conditions is chosen to encapsulate a volume of two times the virial radius of the halo at $z = 0$. We start with a coarse grid of 128^3 (level 7) and several nested grids with increasing levels of refinement up to level 11. The adopted cosmology has a total matter density of $\Omega_{\mathrm{m}} = 0.3089$, a dark energy density of $\Omega_\Lambda = 0.6911$, a baryonic mass density of $\Omega_{\mathrm{b}} = 0.0486$, a Hubble constant of $H_0 = 67.74\,\mathrm{km\,s^{-1}\,Mpc^{-1}}$, a variance at $8\,\mathrm{Mpc}$ $\sigma_8 = 0.8159$, and a non-linear power spectrum index of $n_{\mathrm{s}} = 0.9667$, compatible with a Planck 2015 cosmology (Planck Collaboration XIII 2016).

The simulation includes a metal-dependant tabulated gas-cooling function following Sutherland & Dopita (1993) allowing the gas to cool down to $T \sim 10^4\,\mathrm{K}$ via Bremsstrahlung

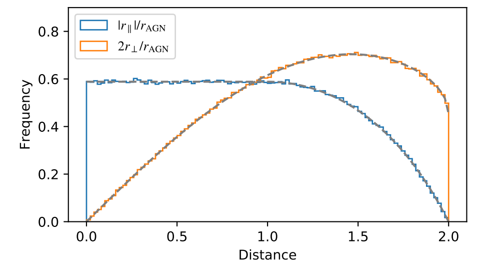

Fig. 8. Distribution of particles moved by a jet before any hydrodynamical time step has occurred. Shown is the parallel distribution marginalised over the plane of the jet (blue) and the radial distribution marginalised over the direction of the jet (orange) vs. the expected theoretical distributions from Eqs. (16) and (18) (dashed grey). The abscissa is in units of r_{AGN} in the parallel direction and in units of $r_{\mathrm{AGN}}/2$ in the radial direction. The distribution of gas tracers sent into the jet perfectly matches the expected one.

radiation (effective until $T \sim 10^6\,\mathrm{K}$), and via collisional and ionisation excitation followed by recombination (dominant for $10^4\,\mathrm{K} \leq T \leq 10^6\,\mathrm{K}$). The metallicity of the gas in the simulation is initialised to $Z_0 = 10^{-3}\,Z_\odot$ to allow further cooling below $10^4\,\mathrm{K}$ down to $T_{\mathrm{min}} = 10\,\mathrm{K}$. Reionisation occurs at $z = 8.5$ using the Haardt & Madau (1996) model and gas self-shielding above $10^{-2}\,\mathrm{m_p\,cm^{-3}}$. Star formation is allowed above a gas number density of $n_0 = 10\,\mathrm{H\,cm^{-3}}$ according to the Schmidt law and with an efficiency $\varepsilon_{\mathrm{ff}}$ that depends on the gravo-turbulent properties of the gas (for details, see Kimm et al. 2017; Trebitsch et al. 2017). The main distinction of this turbulent star-formation recipe with the traditional star formation in Ramses (Rasera & Teyssier 2006) is that the efficiency can approach and even exceed 100% (with $\varepsilon_{\mathrm{ff}} > 1$ meaning that stars are formed faster than in a free-fall time). The stellar population is sampled with a Kroupa (2001) initial mass function, where $\eta_{\mathrm{SN}} = 0.317$ and the yield (in terms of mass fraction released into metals) is 0.05. The stellar feedback model is the mechanical feedback model of Kimm et al. (2015) with a boost in momentum due to early UV pre-heating of the gas following Geen et al. (2015). The simulation also tracks the formation of SMBHs and the evolution of AGN feedback in jet mode (radio mode) and thermal mode (quasar mode) using the model of Dubois et al. (2012b). The jet is modelled in a self-consistent way by following the angular momentum of the accreted material and the spin of the black hole (Dubois et al. 2014b). The radiative efficiency and spin-up rate of the SMBH is then computed using the MAD results of McKinney et al. (2012).

We have a minimum roughly constant physical resolution of 35 pc (one additional maximum level of refinement at expansion factor 0.1, 0.2, and 0.4), a star particle mass resolution of $m_{\star,\mathrm{res}} = 1.1 \times 10^4\,M_\odot$, a dark matter (DM) particle mass resolution of $m_{\mathrm{DM,res}} = 1.5 \times 10^6\,M_\odot$, and gas mass resolution of $2.2 \times 10^5\,M_\odot$ in the refined region. A cell is refined according to a quasi-Lagrangian criterion: if $\rho_{\mathrm{DM}} + \rho_{\mathrm{b}}/f_{\mathrm{b/DM}} > 8 m_{\mathrm{DM,res}}/\Delta x^3$, where ρ_{DM} and ρ_{b} are respectively the DM and baryon density (including stars plus gas plus SMBHs), and where $f_{\mathrm{b/DM}}$ is the cosmic mean baryon-to-DM mass ratio. The max level of refinement is also enforced in all cells closer than $4\Delta x$ from any SMBH, where Δx is the minimum cell size. We add tracer particles in the refined region with a fixed mass of $m_{\mathrm{t}} = 2.0 \times 10^4\,M_\odot$

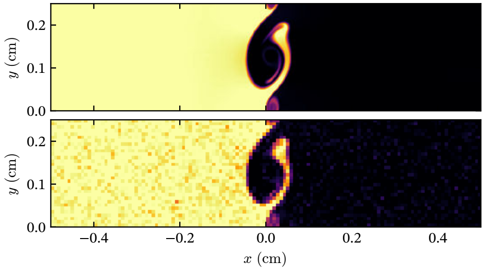

Fig. 6. Projection of the density (*top panel*) and of the gas tracer density (*bottom panel*) around a developing Kelvin–Helmoltz instability. To reduce the noise of the gas tracer projection, we have superposed the four projections of the forming rollers (each of size 0.25 cm). The gas tracer distribution resembles that of the gas with extra noise due to their stochastic nature.

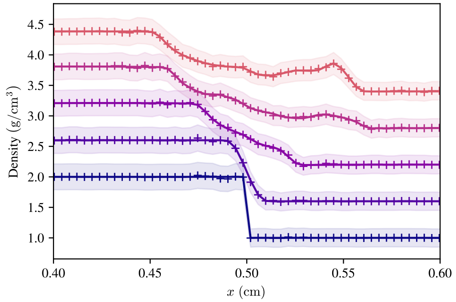

Fig. 7. Evolution of the cross-section of the gas density (solid lines) and the gas tracer density (symbols and shaded regions) for the Kelvin–Helmoltz instability at different times (from blue to red from the start to the end of the simulation at $t = 0.3$ s). The profiles have been shifted vertically (each by $0.6\,\mathrm{g\,cm^{-3}}$) so that one may easily distinguish them from one another. The shaded regions are $\pm 5\sigma$, where σ has been estimated using a Poisson sampling noise. The gas tracers are accurately following the diffusion of the gas.

The Sedov explosion is a reliable way of testing the ability of hydrodynamical codes to deal with shocks: more specifically it tests the ability of the code to capture the shock dynamics properly and also tests that the code resolves the shock interface with a few cells in a regime where the Mach number is largely above 1. Here, the gas tracer distribution has been shown to match that of the gas to a high degree of confidence, confirming that the gas tracers are correctly transported with the flow and are able to resolve shocks.

3.1.3. Kelvin–Helmholtz instability

We ran a classical Kelvin–Helmoltz (KH) instability in three dimensions to compare the gas density to the gas tracer density projected maps. The gas has an adiabatic index $\gamma = 7/5$[5]. The simulation is performed on a 128^3 grid with a physical size of 1 cm and a maximum level of refinement of 2^{10}. Cells are refined based on the relative variation of the density: a new level is triggered when the local relative variation of the density is larger than 1%. Only hydrodynamics is included. The instability is initialised with two regions of left and right density of $2\,\mathrm{g\,cm^{-3}}$ and $1\,\mathrm{g\,cm^{-3}}$, and of tangential velocity $u_{\mathrm{y,L}} = -1\,\mathrm{cm\,s^{-1}}$ (resp. $u_{\mathrm{y,R}} = 1\,\mathrm{cm\,s^{-1}}$). The instability was initially triggered by adding a small damped sinusoidal perturbation of the perpendicular velocity field $u_x = u_0 \cos(k(x - \lambda/2)) \exp(-k|x - x_0|)$, where $\lambda = 0.25$ cm, $k = 2\pi/\lambda$, $x_0 = 0.5$ cm and $v_0 = 0.1\,\mathrm{cm\,s^{-1}}$. Here 2 900 000 gas tracers were initially distributed in the box, so that their Eulerian distribution matched that of the gas.

Figure 6 shows a projection of the gas density and of the tracer density at time $t = 0.3$ s, when the Kelvin–Helmoltz was already settled. The gas tracer distribution reproduces well the vortices found in the gas distribution, with extra noise due to the reduced number of tracer particles.

The largest k wave numbers of the perturbation are the first to grow following a KH growth timescale of $\tau_{\mathrm{KH}} = 2\pi \mathcal{R}^{1/2}/(|\Delta u| k)$, with $\pm\mathcal{R} = \rho_{\mathrm{R}}/\rho_{\mathrm{L}}$, and $\Delta u = u_{\mathrm{y,R}} - u_{\mathrm{y,L}}$. Therefore, as time proceeds, larger rollers develop in the shear interface between the two phases of gas, and hence, the mixing layer spreads further. We computed the evolution of the cross-section profile of the density at different times. The results are presented in Fig. 7. The phase-mixing region grows as a function of time and the growth is correctly captured by the tracer particles that are able to track it within their intrinsic noise level. Therefore, the gas tracer particles are able to correctly capture the KH shear instability leading to mixing of two gas phases. Interestingly, the present algorithm does not lead to any relative diffusion between the gas and the tracers, as is illustrated quantitatively in Sect. 3.1.1.

3.1.4. AGN feedback

We subsequently tested the accuracy of the mass transfer for the jet mode of AGN feedback, which transfers part of the gas of the central cell to the surrounding cells within a "capsule" region (see Sect. 2.5 for details). We ran an idealised simulation of a halo with an AGN at its centre. The simulation is performed on a coarse grid of 128^3, refined according to a quasi-Lagrangian refinement criterion: a cell is refined/derefined wherever the mass resolution is above/below $1.4 \times 10^7\,M_\odot$ up to a maximum level of refinement of 12. The box size is 1.2 Mpc, hence with a minimum cell size of 300 pc. The max level of refinement is also enforced in all the cells closer than $4\Delta x$ from the SMBH, where Δx is the minimum cell size. The gas distribution follows a NFW (Navarro et al. 1997) gas density profile, while the dark matter part follows a similar NFW profile modelled with a static gravitational profile (no back reaction of gas onto dark matter). The NFW profile has parameters $V_{200} = 200\,\mathrm{km\,s^{-1}}$ (at 200 times the critical density of a $H_0 = 70\,\mathrm{km\,s^{-1}\,Mpc^{-1}}$ Universe), a concentration of $c = 6.8$, and is 10% gas. The gas is initially put at rest and at hydrostatic equilibrium. A SMBH of mass $M_{\mathrm{SMBH,0}} = 3.5 \times 10^{10}\,M_\odot$[6] is set at the centre of the box and 10^6 tracers are set in the cell containing the black hole. We force the AGN to be in jet mode with a fixed direction in space and boost its efficiency so that all the tracer particles are sent into the jet in one time step. The radius and height of the jet is $r_{\mathrm{AGN}} = 50$ kpc. This value is much larger than usual values which are usually a few times the cell resolution (here typical values would be a

[5] This value is consistent with the adiabatic index of air at 20°.

[6] We note that the SMBH mass is taken anomalously high for a typical halo mass of $M_{200} \simeq 3 \times 10^{12}\,M_\odot$. This is chosen simply to get a sufficient power of the jet through the Bondi accretion rate given the NFW distribution of gas.

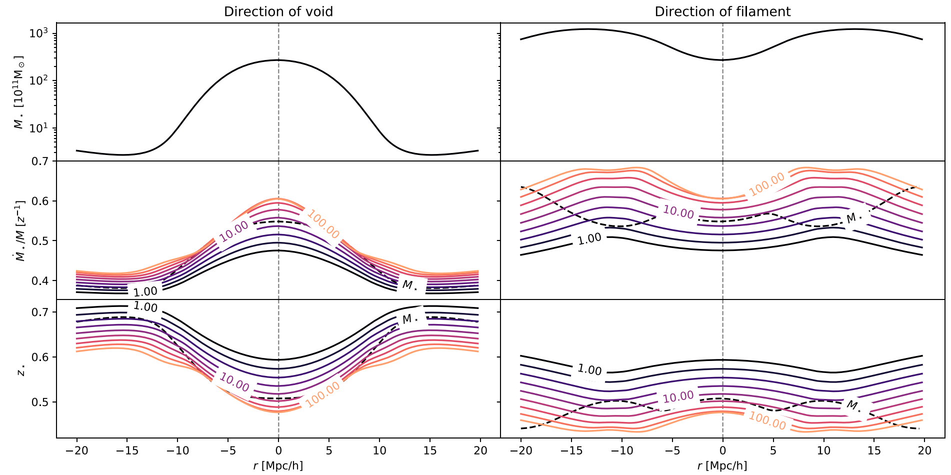

Figure 12. Top: plot of the typical mass $M_\star$, middle: the typical specific accretion rates $\dot{M}/M$, and bottom: the formation redshifts $z_\star$ for different masses as a function of the distance to the saddle point, left: in the direction of the void and right: in the direction of the filament. The colour of each line encodes the smoothing scale (hence the mass), from dark to light $M = 10^{11}\,\mathrm{M_\odot}\,h^{-1}$ ($R = 0.8\,\mathrm{Mpc}\,h^{-1}$) to $M = 10^{13}\,\mathrm{M_\odot}\,h^{-1}$ ($R = 3.7\,\mathrm{Mpc}\,h^{-1}$) logarithmically spaced; the dashed line is evaluated at $M = M_\star$. Labels are given in unit of $10^{11}\,\mathrm{M_\odot}\,h^{-1}$. The saddle point has been defined using the values given in Table D1. More massive haloes accrete more and form later than less massive ones. At the typical mass, the space variation of the specific accretion rate and the formation redshift is smaller in the direction of the filament than in the direction of the void.

To better quantify these trends let us define the tidally modified characteristic quantities

$$M_\star(\boldsymbol{r}) = M(\sigma_\star(\boldsymbol{r}))\,, \tag{80}$$

$$\dot{M}_\star(\boldsymbol{r}, M) = -\frac{\mathrm{d}\log D}{\mathrm{d}z}\frac{\mathrm{d}M}{\mathrm{d}\log\sigma}\alpha_\star(\boldsymbol{r}, \sigma)\,, \tag{81}$$

$$z_\star(\boldsymbol{r}, M) = z(D_\star(\boldsymbol{r})) \simeq 1/D_\star(\boldsymbol{r}, \sigma) - 1\,, \tag{82}$$

giving the typical mass and the accretion rate and formation time at given mass as a function of the position with respect to the centre of the saddle.

The last approximation holds for haloes that assemble half of their mass before $z \sim 2$, since at early times $D \simeq (1+z)^{-1}$. These typical quantities are known functions of the position-dependent typical values of the excursion set parameters $\sigma_\star(\boldsymbol{r})$, $\alpha_\star(\boldsymbol{r}, \sigma)$, and $D_\star(\boldsymbol{r}, \sigma)$ given by equations (57), (62), and (72), respectively. They generalize the corresponding characteristic quantities obtained without conditioning on the saddle, given by $\sigma_\star = \delta_{\mathrm{c}}$, and by the functions $\alpha_\star(\sigma)$ and $D_\star(\sigma)$ defined in equations (27) and (38).

Taylor expanding equation (57) in the anisotropy gives the first-order angular variation of $M_\star$ at fixed distance r from the saddle

$$\Delta M_\star(\boldsymbol{r}) = -\frac{15}{2}\frac{\delta_{\mathrm{c}}\,\xi_{20}(r)}{|(\mathrm{d}\sigma/\mathrm{d}M)_{M_\star}|}\mathcal{Q}(\hat{\boldsymbol{r}})\,, \tag{83}$$

where $\xi_{20}(r)$ is the radial part of the shear-height correlation function at finite separation. Since ξ_{20} is positive, this variation is largest when $\boldsymbol{r}$ is parallel to the eigenvector with the smallest eigenvalue. That is, in the direction of positive outflow (with negative $\mathcal{Q} = \hat{r}_i \bar{q}_{ij} \hat{r}_j$), along which a filament will form. Thus, in filaments haloes tend to be more massive, and haloes of large mass are more likely.

The full dependence of the characteristic mass $M_\star$ as a function of the position with respect to the saddle point of the potential is shown in Fig. 12.

Similarly, like equations (63) and (74) for $\alpha_\star$ and $D_\star$, the first-order angular variations of $\dot{M}_\star$ and $z_\star$ are

$$\Delta \dot{M}_\star(\boldsymbol{r}, M) = -\frac{\mathrm{d}\log D}{\mathrm{d}z}\frac{\mathrm{d}M}{\mathrm{d}\log\sigma}\frac{\alpha_\star^2|_{\bar{q}=0}}{\nu_{\mathrm{c}}} \times \frac{15}{2}\left[\xi_{20}' - \frac{\sigma - \xi_l'\xi_l}{\sigma^2 - \xi^2}\xi_{20}\right]\mathcal{Q}(\hat{\boldsymbol{r}})\,, \tag{84}$$

$$\Delta z_\star(\boldsymbol{r}, M) = \left|\frac{\mathrm{d}z}{\mathrm{d}D}\right|\frac{D_\star^2|_{\bar{q}=0}}{\delta_{\mathrm{c}}}\frac{15}{2}\left|\frac{\mathrm{d}\sigma}{\mathrm{d}M}\right|\frac{M}{2}\xi_{20}(r)\mathcal{Q}(\hat{\boldsymbol{r}})\,. \tag{85}$$

These results confirm that in the direction of the filament, haloes have on average larger mass accretion rates and smaller formation redshifts than haloes of the same mass that form at the same distance from the saddle point, but in the direction perpendicular to it. The space variation becomes larger with growing halo mass and fixed R_S, as shown in Fig. 12, because the correlations become stronger as the difference between the two scales gets smaller. Conversely, for smaller masses haloes have on average smaller accretion rates (like in the unconditional case, see Fig. 3) and later formation times, but also less prominent space variations.

Note that two estimators of delayed mass assembly, $\Delta\dot{M}_\star$ and $\Delta z_\star$ do not rely on the same property of the excursion set trajectory and do not lead to the same physical interpretation. In particular, when extending the implication of delayed mass assembly to galaxies and their induced feedback, one should distinguish between the instantaneous accretion rate, and the integrated half-mass time as they trace different components of the excursion hence different epochs.

5.3 Expected differences between the isocontours

In order to investigate whether the assembly bias generated by the cosmic web and described in this work is purely an effect due to the local density (itself driven by the presence of the filament), this section studies the difference between the isocontours of the local density field and any other statistics (mass accretion rate for instance). The latter will be shown not to follow exactly the isodensity surfaces, but to intersect each other. This misalignment may only appear if spherical symmetry is broken (all isocontours would otherwise be spherical). However, it also shows that halo properties do not depend only on the local density, indicating that the role of the anisotropy of the nearby filament in the formation of structures goes beyond the simple creation of an anisotropic density field.

The normals to the level surfaces of $\dot M_\star(\boldsymbol{r},M)$, $M_\star(\boldsymbol{r})$, $z_\star(\boldsymbol{r},M)$, and $\langle\rho\rangle(\boldsymbol{r})\equiv\bar\rho(1+\langle\delta|\mathcal{S}\rangle)$ scale like the gradients of these functions. First note that any mixed product (or determinant) such as $\nabla\dot M_\star\cdot(\nabla M_\star\times\nabla\langle\rho\rangle)$ will be null by symmetry; i.e. all gradients are coplanar. This happens because the present theory focuses on scalar quantities (mediated, in our case, by the excursion set density and slope). In this context, all fields vary as a function of only two variables, r and $\mathcal{Q}=\hat r_i\bar q_{ij}\hat r_j$, hence the gradients of the fields will all lie in the plane of the gradients of r and $\mathcal{Q}$.[9] Ultimately, if one focuses on a given spherically symmetric peak, then $\mathcal{Q}$ vanishes, so all gradients are proportional to each other and radial. Let us now quantify the misalignments between two normals within that plane. In spherical coordinates, the Nabla operator reads

$$\nabla=\left(\frac{\partial}{\partial r},\frac{1}{r}\frac{\partial}{\partial\theta},\frac{1}{r\sin\theta}\frac{\partial}{\partial\phi}\right)\equiv\left(\frac{\partial}{\partial r},\frac{1}{r}\tilde\nabla\right), \tag{86}$$

so that for instance

$$\nabla\dot M_\star\propto\left(\frac{\partial\dot M_\star}{\partial r},\frac{1}{r}\frac{\partial\dot M_\star}{\partial\mathcal{Q}}\tilde\nabla\mathcal{Q}\right),$$

where equation (46) implies that

$$\tilde\nabla\mathcal{Q}=\begin{pmatrix}\sin2\theta\left(\bar q_3\cos^2\phi+\bar q_2\sin^2\phi-\bar q_1\right)\\ \sin\theta(\bar q_2-\bar q_3)\sin2\phi\end{pmatrix}. \tag{87}$$

Hence, for instance the cross product $\nabla M_\star\times\nabla\dot M_\star$ reads

$$\left(\frac{\partial\dot M_\star}{\partial r}\frac{\partial M_\star}{\partial\mathcal{Q}}-\frac{\partial\dot M_\star}{\partial\mathcal{Q}}\frac{\partial M_\star}{\partial r}\right)\tilde\nabla\mathcal{Q}. \tag{88}$$

It follows that the two normals are not aligned, since the pre-factor in equation (88) does not vanish: the fields are explicit distinct and independent functions of both r and $\mathcal{Q}$. The origin of the misalignment lies in the relative amplitude of the radial and 'polar' derivatives (with respect to $\mathcal{Q}$) of the field. For instance, even at linear order in the anisotropy, since $\Delta M_\star$ in equation (84) has a radial dependence in ξ_{20}' as a pre-factor to $\mathcal{Q}$, whereas $M_\star$ has only ξ_{20} as a pre-factor in equation (83), the bracket in equation (88) will involve the Wronskian $\xi_{20}'\partial\xi_{20}/\partial r-\xi_{20}\partial\xi_{20}'/\partial r$ which is non-zero because ξ_{20} and its derivative with respect to filtering are linearly independent. This misalignment does not hold for $M_\star$ and $\langle\rho\rangle$ at linear order, since $\Delta M_\star$ (equation 83) and $\langle\rho\rangle$ (equation 45) are proportional in this limit. Yet it does arises when accounting for the fact that the contribution to the conditional variance in $M_\star$ also depends additively on $\xi^2(r)$ in equation (57) [with $\xi^2(r)$ given by equation (52) as a function of the finite separation correlation functions $\xi_{\alpha\beta}$ computed in equation (E12) for a given underlying power spectrum]. Indeed, one should keep in mind that the saddle condition not only shifts the mean of the observables but also changes their variances. Since the critical 'star' observables ($M_\star$, $z_\star$, etc.) involve rarity, hence ratio of the shifted means to their variances (e.g. entering equation 60), both impact the corresponding normals. It is therefore a clear specific prediction of conditional excursion set theory relying on upcrossing that the level sets of density, mass density, and accretion rates are distinct.

Physically, the distinct contours could correspond to an excess of bluer or reddened galactic hosts at fixed mass along preferred directions depending on how feedback translate inflow into colour as a function of redshift. Indeed feedback from active galactic nuclei (AGNs), triggered during merger events, regulates gas inflows (Dubois et al. 2016), which in turn impacts star formation: when it is active, at intermediate and low redshift, it may reverse the naive expectation (see Appendix H). This would be in agreement with the recent excess transverse gradients (at fixed mass and density) measured both in cosmological hydrodynamical simulation Horizon-AGN (Dubois et al. 2014) and those observed in spectroscopic (e.g. VIPERS or GAMA, Malavasi et al. 2017; Kraljic et al. 2018) and photometric (e.g. COSMOS, Laigle et al. 2017) surveys: bluer central galaxies at high redshifts when AGN feedback is not efficient and redder central galaxies at lower redshift.

Our predictions are formulated in the initial conditions. However, one should take into account a Zel'dovich boost to get the observable contours of the quantities derived in the paper. Regions that will collapse into a filament are expected to have a convergent Zel'dovich flow in the plane perpendicular to the filament and a diverging flow in the filament's direction. As such, the contours of the different quantities will be advected along with the flow and will become more and more parallel along the filament. This effect is clearly seen in Fig. 13 which shows the contours of both the typical density and the accretion rate[10] (bottom panel) after the Zel'dovich boost (having chosen the amplitude of the boost corresponding to the formation of the filamentary structure). The contours are compressed towards the filament and become more and more parallel. Hence, the stronger the non-linearity, the more parallel the contours. This is consistent with the findings of Kraljic et al. (2018), whose colour and (stellar) mass gradients follow the underlying mean density, when the density is averaged on sufficiently small scales.

6 ASSEMBLY BIAS

The bias of DM haloes (see Desjacques, Jeong & Schmidt 2016, for a recent review) encodes the response of the mass function to variations of the matter density field. In particular, the Lagrangian bias function b_1 describes the linear response to variations of the initial matter density field. For Gaussian initial conditions, the

[9] In order to break this degeneracy, one would need to look at the statistics of higher spin quantities. For instance, the angular momentum of the halo would depend on the spin-one coupling $\varepsilon_{ijk}\hat r_j\bar q_{kl}\hat r_l$, with ε_{ijk} the totally anti-symmetric tensor (see e.g. Codis, Pichon & Pogosyan 2015), or to consider a barrier that depends on the local shear at $\boldsymbol{r}$ filtered on scale R (e.g. Castorina et al. 2016), like e.g. $\delta_c+\beta\sigma\bar q_{ij}(\boldsymbol{r},R)\bar q_{ij}(\boldsymbol{r},R)$ with some constant β.

[10] Interactive versions can be found online https://cphyc.github.io/research/assembly/with_boost.html and https://cphyc.github.io/research/assembly/no_boost.html.

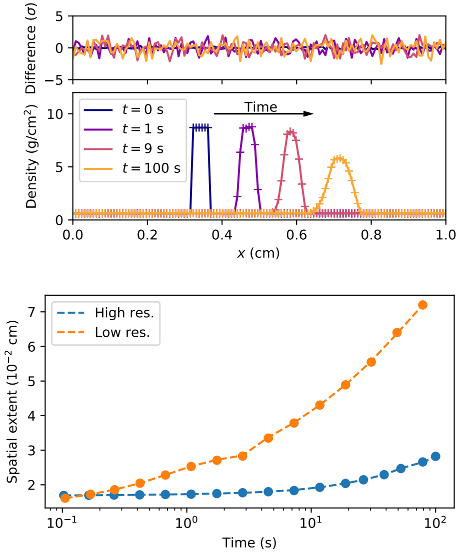

Fig. 4. *Top panel (bottom):*: gas density profile (solid line) and gas density profile (plus symbols) at different times (reported in the legend). The profiles have been recentred and shifted horizontally by −0.12 cm, 0, 0.12 cm, and 0.24 cm for t = 0, 1, 9, and 100 s, respectively. *Top panel (top):*: relative difference between the gas and gas tracer density profiles in units of the expected noise level $\sigma = 1/\sqrt{M_{\rm cell}/m_{\rm t}}$. *Bottom panel*: evolution of the spatial extent of an advected overdensity as a function of time for the gas (dashed) and the gas tracer particles (dot symbols) for a high-resolution run (blue) and a low-resolution run (orange, see text for details). The difference shows no spatial dependence. The gas tracers diffuse exactly as the gas.

no spatial modulation. Their distributions are the same with an extra factor that is entirely due to sampling noise, which in turn depends only on the local cell mass and the (constant) tracer mass.

In more quantitative terms, let us compare the time evolution of the spatial extent of the gas tracer overdensity to that of the gas. We rerun the simulation on a 32^2 grid (low resolution) in addition to the previous run (high resolution). We compute the spatial extent by fitting a Gaussian function $\rho(x) = \rho_0 + H\exp(-(x-x_0)^2/(2\sigma_\rho^2))$ to the gas and gas tracer profiles, with free parameters ρ_0 the base density, H the amplitude of the overdensity, x_0 the position of the overdensity, and σ_ρ its spatial extent. The results are shown in the bottom panel of Fig. 4. As expected due to the numerical diffusion, the spatial extent of the overdensity increases as a function of time and the diffusion becomes larger when the resolution is decreased. In both cases, the Eulerian distribution of tracer particles is diffused exactly as much as the gas[4].

[4] This result complements that of Genel et al. (2013). Indeed we study here the diffusion of the Eulerian distribution of the tracer particles, while the original paper presents the Lagrangian diffusion of the tracer particles.

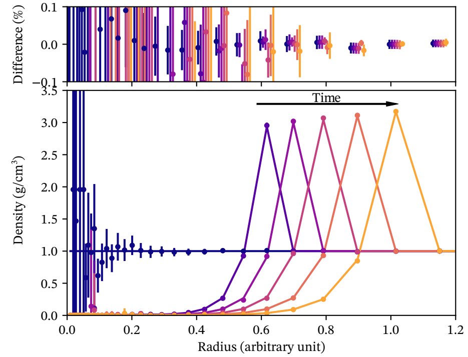

Fig. 5. *Bottom panel*: radial profile at different times of a Sedov explosion (from blue to yellow) for the gas (solid lines) and the gas tracer (dots). The error bars are 2σ errors. *Top panel*: relative difference between the gas profile and the gas tracer profile. Data have been shifted by −0.25, −0.125, 0, 0.125 and 0.25 radius units respectively (from blue to yellow) so that one may easily distinguish the different data points. Details of the simulation are discussed in the text. The gas tracer particles are accurately advected with the gas.

3.1.2. Sedov-Taylor explosion

We ran a classical Sedov-Taylor explosion in three dimensions and compare the gas density radial profile to the density profile of gas tracer particle. The simulation was performed on a coarse grid of 128^3, refined on the relative variation of the density and of the pressure: a new level is triggered when the local relative variation of one of these quantities is larger than 1% with up to two levels of refinement. The simulation was initialised with a uniform density and pressure of 1 g cm^{-3} and 10^{-5} dyne cm^{-2}, respectively, and an over-pressure in the central cell of the box of 6.7×10^6 dyne cm^{-2}. 2 900 000 tracers, statistically uniformly distributed initially in the box, hence, with around ~1.4 tracer per initial cell.

The evolution of the spherically averaged radial density profile of the gas and of the tracers is shown in Fig. 5. The tracer density has been computed by deposing the gas tracer mass in the nearest cell. The axes have been normalised so that the radius of the blast is one at the latest output. The error bars have been estimated assuming that the number of tracers per radial bin is given by a Poisson distribution. This assumption is discussed in more detail in Sect. 3.2.2.

At all stages of the blast, the tracer particles radial profile matches that of the gas at percent levels. This is more easily seen in the top panel of Fig. 5 where the relative difference between the gas tracer density and the gas density is plotted. The errors are all within a few percent and consistent with random fluctuations. As the explosion expands, the swept-up mass of gas in the shocked region increases. This is well tracked by the tracer distribution. Because the mass increases, the total number of tracer particles in the shock increases proportionally, causing the sample noise to decrease. In this particular test, the tracer distribution accurately reproduces that of the gas in the pre- (which is trivially that of the initial distribution) and post-shocked regions (shocked shell plus hot bubble interior). The noise level is a function of the number of tracer particles; its expected value is proportional to the total gas mass only.

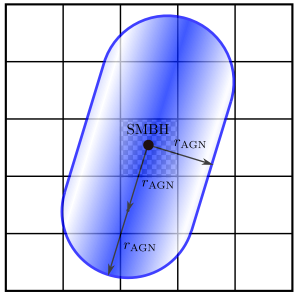

Fig. 3. Schematic representation of the jet model. Gas is transported from the central cell (hatched region) containing the SMBH (black dot) into the jet (blue shaded region). The radial profile of the jet is a Gaussian of scale $r_{\rm AGN}$. The shape of the jet is a "capsule" (a cylinder capped with two half spheres).

match the BH-to-galaxy mass relation; Dubois et al. 2012b) is released as thermal energy in all cells within a sphere of size $R_{\rm AGN}$ and the mass of the gas is left untouched. This feedback mode has only an indirect effect on the gas mass distribution (and hence on tracer particles), turning some fraction of the released thermal energy into kinetic energy and launching a quasar-like wind.

In radio mode, a jet is launched from the AGN. The jet moves mass from the central cell only and spreads it into the jet and injects linear momentum, and energy. The released energy (and hence, momentum within the jet), as for the quasar mode, is proportional to the rest-mass accreted energy with an efficiency of $\varepsilon_{\rm f,R}$, which is either taken as a constant value of 1 (to match the SMBH-to-galaxy mass relation; Dubois et al. 2012b) or a varying function of the spin of the SMBH following the results of magnetically arrested discs (MADs) from McKinney et al. 2012; see Dubois et al., in prep. for details). The jet is modelled by a "capsule" (a cylinder with spherical caps) of size $r_{\rm AGN}$, as illustrated in Fig. 3. The radius of the jet $r_{\rm AGN}$ is usually set to a few times the cell resolution. The mass sent through the jet is proportional to the accreted mass onto the SMBH

$$\dot{M}_{\rm jet} = f_{\rm Load}\dot{M}_{\rm SMBH}, \tag{13}$$

where $f_{\rm Load}$ is a mass-loading factor, usually 100. The mass transported by the jet is distributed to all the cells intersecting with the capsule. Each cell i receives a relative fraction ψ_i of the mass (and of the injected linear momentum)

$$\psi_i = \frac{\rho_i \int_{\mathcal{I}} e^{-r^2/2r^2_{\rm AGN}}{\rm d}^3V}{\sum_j \rho_j \int_{\mathcal{J}} e^{-r^2/2r^2_{\rm AGN}}{\rm d}^3V}, \tag{14}$$

where $\mathcal{I}$ (resp. $\mathcal{J}$) is the volume of the intersection between the AGN capsule and the cell i (resp. j) and ρ_i is the cell mean density. The radius r in Eq. (14) is the polar radius in the cylindrical frame centred on the AGN and aligned with its direction (it is the distance to the jet centre). This integral is computed approximately, using a numerical integration scheme.

The tracer particles are interfaced with the jet model as follows. Each gas tracer particle in the cell i containing the SMBH is moved into the jet volume with a probability of

$$p_{\rm jet} = \frac{\dot{M}_{\rm jet}\Delta t}{M_i}. \tag{15}$$

For each of these particles a random number r is drawn from a uniform distribution between 0 and 1. If $r < p_{\rm jet}$, the tracer is selected and moved into the jet. The new position of the tracer (x, y, z) is drawn randomly, z being the coordinate in the direction of the jet; x and y are drawn from a normal distribution of variance $r_{\rm AGN}$ and z is drawn uniformly between $-2r_{\rm AGN}$ and $2r_{\rm AGN}$. The algorithm uses a draw-and-reject method until one position inside the capsule is found. We note that the gas tracer distribution (as given by Eq. (15)) is consistent with the distribution of the gas sent through the jet (as given by Eq. (14))[3].

More details about the algorithm are given in Appendix A.

3. Validations and tests

Let us now present various validation tests of the algorithm. Section 3.1 presents the results of idealised tests for gas-only tracer particles. Section 3.2 presents the results obtained from a cosmological zoom-in simulation of a galaxy with its SMBH at $z = 2$ and provides the details of the observed distribution of tracer particles. Unless stated otherwise, the gas hydrodynamics is solved with an adiabatic index of $\gamma = 5/3$ and the HLLC approximate Riemann solver (Toro 2009), applying the MinMod slope limiter on the linearly reconstructed states.

3.1. *Idealised tests*

In this section, we introduce different idealised tests to confirm that the evolution of the gas is correctly tracked by gas tracers. Section 3.1.1 presents a simple two-dimensional (2D) advection of an overdensity to quantify diffusion effects. Sections 3.1.2 and 3.1.3 present a Sedov–Taylor explosion and a Kelvin–Helmoltz instability and confirm that the gas tracers are able to accurately follow the motion of the gas for a strong shock case and a mixing layer of gas, respectively. Section 3.1.4 presents an idealised halo with an AGN at its centre to confirm that the gas tracers correctly track the evolution of the gas in AGN jets.

3.1.1. Uniform advection

In order to quantify the level of diffusion of MC tracers, we run a simulation similar to that run for Fig. 6 of Genel et al. (2013). The simulation is a region of 1 cm in size with a constant density of $1\,{\rm g\,cm^{-3}}$ and a velocity of $0.01\,{\rm cm\,s^{-1}}$. An overdensity of $14\,{\rm g\,cm^{-3}}$ is set at $0 < x < 0.05\,{\rm cm}$. The sound speed is $c_{\rm s} = 1.3\,{\rm cm\,s^{-1}}$ in the under-dense region and $0.35\,{\rm cm\,s^{-1}}$ in the over-dense region. The simulation is performed on a uniform 2D 128^2 grid including 250 000 tracer particles, initially distributed in the same way as the gas. Due to the intrinsic numerical diffusion (advection error) of the hydrodynamical solver, the spatial extent of the overdensity increases as a function of time as it is advected away. This is illustrated in the central panel of Fig. 4. We note that the density profiles have each been shifted along their x coordinate for visualisation purposes and do not reflect their real absolute position (in fact the rightmost peak travelled 5 cm in 100 s). The top panel of Fig. 4 shows that, when rescaled by the expected noise level $\sigma \equiv 1/\sqrt{M_{\rm cell}/m_{\rm t}} = 1/\sqrt{N}$ (N is the expected number of tracer particles in the cell), the relative error between the gas tracers and the gas distributions shows

[3] In practice, the numerical evaluation of the integrals of Eq. (14) may lead to small yet undetected discrepancies between the gas tracer and the gas distributions.

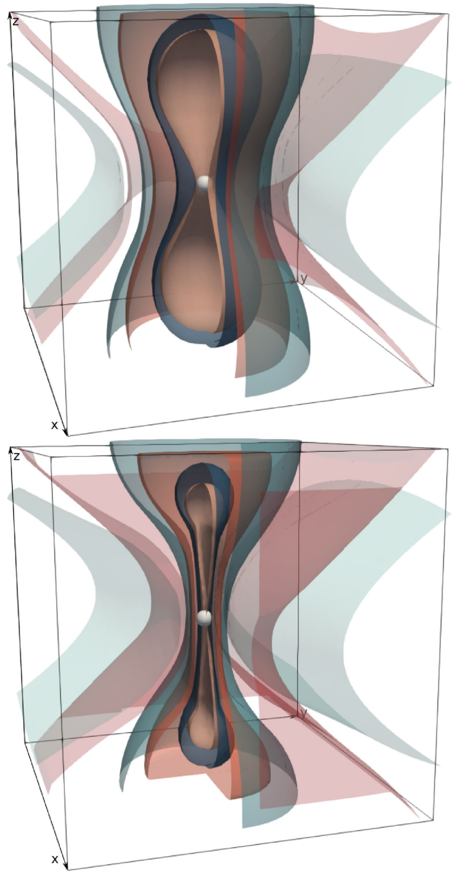

Figure 13. Level surfaces of the typical density $\rho_\star$ (light to dark blue) and of the accretion rate $\alpha_\star$ (light to dark red) with no Zel'dovich boost (upper panel and with a Zel'dovich boost (lower panel). The saddle is represented by a ball. Once boosted, the structure of the filament in the z-direction is clearly seen and the isocontours align one with each other.

correlation of the halo overdensity with an infinite wavelength matter overdensity δ_0 is then (Fry & Gaztanaga 1993),

$$\langle\delta_0\delta_{\rm h}(\boldsymbol{r}, M)\rangle = \int {\rm d}\boldsymbol{r}_1\langle\delta_0\delta_{\rm m}(\boldsymbol{r}_1)\rangle b_1(\boldsymbol{r}, \boldsymbol{r}_1, M)\,, \tag{89}$$

where formally $b_1(\boldsymbol{r}, \boldsymbol{r}_1, M) \equiv \langle\partial[\delta_{\rm h}(\boldsymbol{r}, M)]/\partial[\delta_{\rm m}(\boldsymbol{r}_1)]\rangle$ is the expectation value of the functional derivative of the local halo overdensity with respect to the (unsmoothed) matter density field $\delta_{\rm m}(\boldsymbol{r})$ (Bernardeau, Crocce & Scoccimarro 2008). In the standard setup, because of translational invariance (which does not hold here), it is only a function of the separation $|\boldsymbol{r} - \boldsymbol{r}_1|$.

The dependence of the halo field on the matter density field can be parametrized with a potentially infinite number of variables constructed in terms of the matter density field, evaluated at the same point. With a simple chain rule applied to the functional derivative, equation (89) can be written as the sum of the cross-correlation of δ_0 with each variable, times the expectation value of the ordinary partial derivative of the halo point process with respect to the same variable. The latter are the so-called bias coefficients, and are mathematically equivalent to ordinary partial derivatives of the mass function with respect to the expectation value of each variable.

The most important of these variables is usually assumed to be the density $\delta(\boldsymbol{r}, R)$ filtered on the mass scale of the haloes, which mediates the response to the variation of an infinite wavelength mode of the density field, the so-called large-scale bias. Because the smoothed density correlates with the $k = 0$ mode of the density field, this returns the peak-background split bias. Its bias coefficient is also equal to (minus) the derivative with respect to $\delta_{\rm c}$.

Excursion sets make the ansatz that the next variable that matters is the slope $\delta'(\boldsymbol{r}, R)$ (Musso, Paranjape & Sheth 2012). In the simplest excursion set models with correlated steps and a constant density threshold, trajectories crossing $\delta_{\rm c}$ with steeper slopes have a lower mean density on larger scales (Zentner 2007). They are thus unavoidably associated with less strongly clustered haloes. This prediction is in agreement with N-body simulations for large-mass haloes, but the trend is known to invert for smaller masses (Sheth & Tormen 2004; Gao et al. 2005; Wechsler et al. 2006; Dalal et al. 2008). Although more sophisticated models are certainly needed in order to account for the dynamics of gravitational collapse, we will see that the presence of a saddle point contributes to explaining this inversion.

None of the concepts outlined above changes in the presence of a saddle point: the bias coefficients are derivatives of ${\rm d}n/{\rm d}M$, that is of the upcrossing probability through equation (75). Because we are interested in the bias of the joint saddle-halo system, we must differentiate the joint probability $f_{\rm up}(\sigma; \boldsymbol{r})p(\mathcal{S})$, rather than just $f_{\rm up}(\sigma; \boldsymbol{r})$, and divide by the same afterwards. Of course, the result picks up a dependence on the position within the frame of the saddle. The relevant uncorrelated variables are $\delta - \langle\delta|\mathcal{S}\rangle$, $\delta' - \langle\delta'|\nu, \mathcal{S}\rangle$, $\nu_{\mathcal{S}}$, $\hat{r}_i g_i = 0$, and $\mathcal{Q} = \hat{r}_i\bar{q}_{ij}\hat{r}_j$. Differentiating equation (49), the bias coefficients of the halo are

$$b_{10}(M; \boldsymbol{r}) \equiv \frac{\partial \log\left[f_{\rm up}(\sigma; \boldsymbol{r})\right]}{\partial\langle\delta|\mathcal{S}\rangle} = \frac{\delta_{\rm c} - \xi_I\mathcal{S}_I}{\sigma^2 - \xi^2}\,, \tag{90}$$

$$b_{01}(M; \boldsymbol{r}) \equiv \frac{\partial \log\left[f_{\rm up}(\sigma; \boldsymbol{r})\right]}{\partial\langle\delta'|\nu_{\rm c}, \mathcal{S}\rangle} = \frac{1 + {\rm erf}(X_{\mathcal{S}}(\boldsymbol{r})/\sqrt{2})}{2\mu_{\mathcal{S}}(\boldsymbol{r})F(X_{\mathcal{S}}(\boldsymbol{r}))}\,, \tag{91}$$

which without saddle reduce to (a linear combination of) those defined by Musso et al. (2012). The coefficients of the saddle are

$$b^{(\mathcal{S})}_{100} \equiv -\frac{\partial}{\partial\delta_{\rm s}}\log p_{\rm G}(\mathcal{S}) = \frac{\nu_{\mathcal{S}}}{\sigma_{\mathcal{S}}}\,, \tag{92}$$

$$b^{(\mathcal{S})}_{010} \equiv -\frac{\partial}{\partial(\hat{r}_i g_i)}\log p_{\rm G}(\mathcal{S})\bigg|_{g_i=0} = 0\,, \tag{93}$$

$$b^{(\mathcal{S})}_{001} \equiv -\frac{\partial}{\partial\mathcal{Q}}\log p_{\rm G}(\mathcal{S}) = \frac{15}{2}\frac{3\mathcal{Q}}{2}\,. \tag{94}$$

A constant δ_0 does not correlate with $\bar{q}_{ij}$, since there is no zero mode of the anisotropy. One can see this explicitly by noting that $\xi_{20}(R_0, R_{\mathcal{S}}, r) \to 0$ as $R_0 \to \infty$. The only coefficients that survive in the cross-correlation with δ_0 are thus b_{10}, b_{01} and $b^{(\mathcal{S})}_{100}$, so that equation (89) becomes

$$\langle\delta_0\delta_h(\boldsymbol{r}, M)\rangle = b^{(\mathcal{S})}_{100}\langle\delta_0\delta_{\rm s}\rangle + b_{10}{\rm Cov}\left(\delta_0, \delta|\mathcal{S}\right) + b_{01}{\rm Cov}\left(\delta_0, \delta'|\nu_{\rm c}, \mathcal{S}\right)\,. \tag{95}$$

Similarly, in this limit δ_0 does not correlate with g_i either, while $\langle\delta_0\delta\rangle$ becomes independent of R. Thus, $\langle\delta_0\delta\rangle \simeq \langle\delta_0\delta_s\rangle$ and $\langle\delta_0\delta'\rangle \simeq 0$. Hence,

$$\frac{\langle\delta_0\delta_h\rangle}{\langle\delta_0\nu_{\mathcal{S}}\rangle} \simeq \nu_{\mathcal{S}} + \frac{\delta_c - \xi_I \mathcal{S}_I}{\sigma^2 - \xi^2}(\sigma_s - \xi_{00}) - b_{01}\left[\xi'_{00} + \frac{\sigma - \xi'_I\xi_I}{\sigma^2 - \xi^2}(\sigma_s - \xi_{00})\right]. \qquad (96)$$

Setting $\nu_{\mathcal{S}} = \xi_{\alpha\beta} = \xi'_{\alpha\beta} = 0$ recovers Musso et al.'s (2012) results.

The anisotropic effect of the saddle is easier to understand looking at the sign of the terms in the round and square brackets, corresponding to $\mathrm{Cov}\left(\delta_0, \delta|\mathcal{S}\right)$ and $-\mathrm{Cov}\left(\delta_0, \delta'|\nu_c, \mathcal{S}\right)$ respectively. One can check that for $R = 1\ \mathrm{Mpc}\,h^{-1}$ and $R_{\mathcal{S}} = 10\ \mathrm{Mpc}\,h^{-1}$ both terms are negative near $r = 0$, but become positive at $r \simeq 0.75R_{\mathcal{S}}$. This separation marks an inversion of the trend of the bias with $\nu_{c,\mathcal{S}}$, the parameter measuring how rare haloes are given the saddle environment. Far from the saddle, haloes with higher $\nu_{c,\mathcal{S}}$ are *more biased*, which recovers the standard behaviour since $\nu_{c,\mathcal{S}} \to \nu_c$ as $r \to \infty$. However, as $r/R_{\mathcal{S}} \lesssim 0.75$, the trend inverts and haloes with higher $\nu_{c,\mathcal{S}}$ become *less biased*. Therefore, one expects that at fixed mass and distance from the saddle-point haloes in the direction of the filament are less biased far from the saddle, but become more biased near the saddle point. The upper panel of Fig. 14, displaying the exact result of equation (96), confirms these trends and their inversion at $r \simeq 0.75R_{\mathcal{S}}$. The height of the curves at $r = 0$ depends on the chosen value for $\nu_{\mathcal{S}}$, but the inversion at $r \simeq 0.75R_{\mathcal{S}}$ and the behaviour at large r do not. Fig. 14 also shows that a saddle point of the potential need not be a saddle point of the bias (in the present case, it is in fact a maximum).

The inversion can be interpreted in terms of excursion sets. Near the saddle, fixing $\nu_{\mathcal{S}}$ at $\boldsymbol{r} = 0$ puts a constraint on the trajectories at $\boldsymbol{r}$ that becomes more and more stringent as the separation gets small. At $r = 0$, the value of the trajectory at $R_{\mathcal{S}}$ is completely fixed. Therefore, trajectories constrained to have the same height at both $R_{\mathcal{S}}$ and R, but lower $\langle\delta|\mathcal{S}\rangle$ at R, will tend to drift towards lower values between $R_{\mathcal{S}}$ and R, and thus towards higher values for $R_0 \gg R_{\mathcal{S}}$. This effect vanishes far enough from the saddle point, since the constraint on the density at $R_{\mathcal{S}}$ becomes looser as the conditional variance grows. Hence, trajectories with lower $\langle\delta|\mathcal{S}\rangle$ at R will remain lower all the way to R_0. Note however that interpreting these trends in terms of clustering is not straightforward, because the variations happen on a scale $R_{\mathcal{S}} \ll R_0$ (they are thus an explicit source of scale-dependent bias). The most appropriate way to understand the variations of clustering strength is looking at the position dependence of $\mathrm{d}n/\mathrm{d}M$, which is predicted explicitly through $f_{\mathrm{up}}(\sigma; \boldsymbol{r})$ in equation (49).

When one bins haloes also by mass and accretion rate, the bias is given by the response of the mass function at fixed accretion rate. That is, to get the bias coefficients one should now differentiate the joint probability $f_{\mathrm{up}}(\sigma, \alpha; \boldsymbol{r})p_{\mathrm{G}}(\mathcal{S})$ with respect to mean values of the different variables, with $f_{\mathrm{up}}(\sigma, \alpha; \boldsymbol{r})$ given by equation (59). The only bias coefficient that changes is b_{01}, the derivative with respect to $\langle\delta'|\nu_c, \mathcal{S}\rangle$, which becomes

$$b_{01}(M, \dot{M}, \boldsymbol{r}) \equiv \frac{\partial \log\left[f_{\mathrm{up}}(\sigma, \alpha; \boldsymbol{r})\right]}{\partial\langle\delta'|\nu_c, \mathcal{S}\rangle} = \frac{\nu_c/\alpha - \mu_{\mathcal{S}}(\boldsymbol{r})}{\mathrm{Var}\left(\delta'|\nu_c, \mathcal{S}\right)}, \qquad (97)$$

with α defined by equation (20). Inserting this expression in equation (96), returns the predicted large-scale bias at fixed accretion rate. Notice that in this simple model, the coefficient multiplying the $1/\alpha$ term is purely radial. The asymptotic behaviour of the bias at small accretion rates will then always be divergent and isotropic, with a sign depending on that of the square bracket in equation (96). If this term is positive, the bias decreases as α gets smaller, and vice versa. Clearly, the value of α for which the divergent behaviour becomes dominant depends on the size of all the other terms, and is therefore anisotropic.

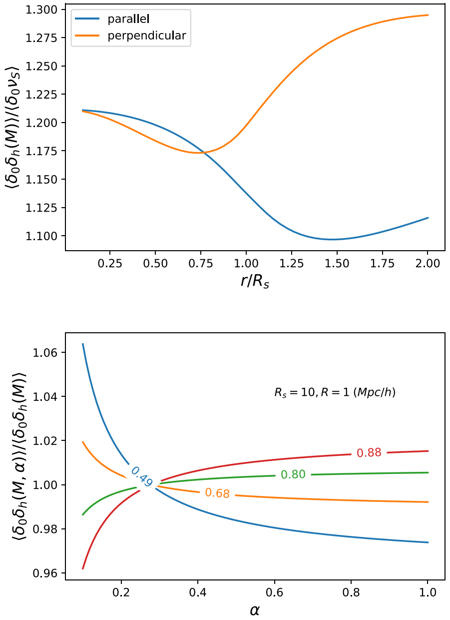

Figure 14. Upper panel: large-scale Lagrangian bias as a function of the distance from the saddle point, along the filament and perpendicularly to it, for haloes of mass $M = 2.0 \times 10^{11}\ \mathrm{M}_\odot\,h^{-1}$ ($R = 1\ \mathrm{Mpc}\,h^{-1}$). Haloes in the perpendicular direction are less biased at small separation, but the trend inverts at $r/R_{\mathcal{S}} \simeq 0.75$. Lower panel: bias as a function of accretion rate, for different values of the separation $r/R_{\mathcal{S}}$ in the direction of the filament. For haloes closer to the centre, bias decreases with accretion rate, but the trend inverts at $r/R_{\mathcal{S}} \simeq 0.75$. In the perpendicular direction, the effect is 30 per cent smaller, but the relative amplitudes and the inversion point do not change appreciably. As discussed in the main text, both inversions depend on the fact that $\delta - \langle\delta|\mathcal{S}\rangle$ and δ_0 correlate at large distance from the saddle, but they anticorrelate at small separation.

As one can see from Fig. 14, the sign of the small-α divergence depends on the distance from the saddle point. It is negative for $r \gtrsim 0.75R_{\mathcal{S}}$, but it reverses closer to the centre. This effect is again a consequence of the constraint on the excursion set trajectories at $R_{\mathcal{S}}$. Trajectories with steeper slopes at R will sink to lower values between $R_{\mathcal{S}}$ and R, then turn upwards to pass through $\delta(R_{\mathcal{S}})$, and reach higher values for $R_0 \gg R_{\mathcal{S}}$. The haloes they are associated with are thus *more biased*. This trend is represented in Fig. 15. This inversion effect is lost as the separation increases, and the constraint on the density at $R_{\mathcal{S}}$ becomes loose, and trajectories that reach R with steeper slopes are likely to have low (or even negative) values at very large scales. These haloes are thus *less biased*, or even antibiased.

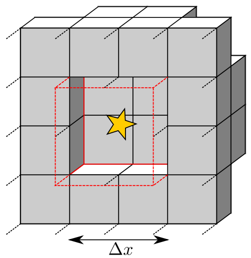

Fig. 2. Scheme of the 48 neighbouring virtual cells (only the 24 rear ones are shown) where mass and momentum are deposed during a SN event. The cell containing the SN has a size of Δx and is outlined in red.

distribution between 0 and 1. If $r < p_{\mathrm{SN}}$, the star-tracer particle is released in the gas and turned into a gas tracer particle. Otherwise, the tracer is left attached to the stellar remnant.

The transfer of star-tracer particles to the gas by SNII is described here for the so-called mechanical feedback model of (Kimm & Cen 2014; see also Kimm et al. 2015)[2]. In this model, the gas is released in the neighbouring cells. The mechanical feedback scheme is designed to overcome the consequences of radiative losses in SN bubbles due to the lack of resolution. Where the cooling time of the SN-heated gas is shorter than the hydrodynamical time step, the energy-conserving phase (with Sedov-Taylor solution), during which the momentum is growing by the pressure work of the bubble, cannot be captured properly, and leads to spurious energy and momentum loss. To circumvent this problem, Kimm & Cen (2014) introduced a model that correctly accounts for the momentum injection according to the Sedov-Taylor or snow-plough solution (Thornton et al. 1998), which depends on the cooling rate of the gas, or more precisely on the energy release, local gas density, and metallicity. The cell containing the exploding star particle is virtually represented by 8 cells refined by an additional level, which are equivalently surrounded by 48 such virtual neighbouring cells, as illustrated in Fig. 2 (Kimm & Cen 2014). The mass ejecta together with the mass of the swept-up gas of the central true cell is released evenly in all the virtual cells, and is attributed back accordingly to the true existing cells.

The tracer particles are interfaced with this feedback model as follows: For each released star to gas tracer particle, a random integer number $l \in [1, 48]$ is drawn uniformly. The star tracer is then moved to the centre of the lth virtual cell and attributed to the corresponding true existing cell as a new gas tracer particle.

2.4. SMBH formation and gas accretion

Supermassive black holes are modelled as sink particles that can form out of the dense star-forming gas, grow by accretion of gas, and coalesce following the implementation described in Dubois et al. (2012b).

[2] We have extended this implementation to i) simple thermal pulses of energy (with or without delayed cooling; Teyssier et al. 2013), where the mass is released to the central cell only, and ii) to the so-called kinetic model of (Dubois & Teyssier 2008; in its more recent form described in Rosdahl et al. 2017) where "debris" particles are replaced by a bubble injection region of energy, momentum, and mass according to the Sedov-Taylor solution.

A SMBH forms according to several user-defined criteria, typically above a given gas density threshold ρ_0 and outside an exclusion distance radius r_{ex} within which SMBH is artificially prevented if any other SMBH already exists (in order to prevent creation of multiple SMBHs within the same galaxy). When a SMBH forms with an initial seed mass $M_{\mathrm{SMBH,0}}$, gas tracer particles in the cell of mass M_i containing the SMBH are attached to the SMBH and become SMBH tracer particles according to a probability

$$p_{\mathrm{SMBH}} = \frac{M_{\mathrm{SMBH,0}}}{M_i}. \qquad (8)$$

SMBHs can continuously accrete gas according to the Bondi–Hoyle–Littleton accretion rate, capped at Eddington with

$$\dot{M}_{\mathrm{SMBH}} = (1 - \varepsilon_{\mathrm{r}})\,\dot{M}_{\mathrm{acc}} = (1 - \varepsilon_{\mathrm{r}})\,\min(\dot{M}_{\mathrm{B}}, \dot{M}_{\mathrm{Edd}}), \qquad (9)$$

$$\dot{M}_{\mathrm{B}} = \frac{4\pi\rho G^2 M_{\mathrm{SMBH}}^2}{(c_{\mathrm{s}}^2 + u^2)^{3/2}}\left(\frac{\rho}{\rho_{\mathrm{boost}}}\right)^{\alpha}, \qquad (10)$$

$$\dot{M}_{\mathrm{Edd}} = \frac{4\pi G m_{\mathrm{p}} M_{\mathrm{SMBH}}}{\sigma_T \varepsilon_{\mathrm{r}} c}, \qquad (11)$$

where $\dot{M}_{\mathrm{acc}}$, $\dot{M}_{\mathrm{SMBH}}$, $\dot{M}_{\mathrm{B}}$, and $\dot{M}_{\mathrm{Edd}}$ are the disc, SMBH, Bondi–Hoyle–Littleton, and Eddington accretion rates, respectively, m_{p} is the mass of a proton, G the gravitational constant, σ_{T} the Thomson cross-section, ε_{r} the radiative efficiency, c_{s} the speed sound, u the mean velocity of the gas with respect to the SMBH, and c the speed of light. ρ_{boost} and α are free parameters set, here, to $\rho_{\mathrm{boost}} = 8m_{\mathrm{p}}\,\mathrm{cm}^{-3}$ and $\alpha = 2$ introduced to boost the accretion rate due to unresolved small-scale larger densities (Booth & Schaye 2009). The value of ε_{r} is either chosen as a constant value equal to 0.1, or, here, as a varying function of the spin of SMBH, whose evolution is governed by gas accretion and BH coalescence (see Dubois et al. 2014a,b, and Dubois et al., in prep., for details).

The mass taken from the gas cell in one time step is $\Delta M_{\mathrm{acc}} \equiv \Delta t\,\min(\dot{M}_{\mathrm{BH}}, \dot{M}_{\mathrm{Edd}})$. We note that $\Delta M_{\mathrm{acc}} > \dot{M}_{\mathrm{SMBH}}\Delta t$ as part of the accreted mass is radiated away due to relativistic effect (and lost to the simulation). Each gas tracer in the cell containing the SMBH at a given time is accreted into the black hole with a probability of

$$p_{\mathrm{acc}} = \frac{\Delta M_{\mathrm{acc}}}{M_i}. \qquad (12)$$

Tracer particles also model SMBH merger events. All the tracer particles attached to the two parent SMBHs are moved to the newly formed SMBH. There is no mechanism to extract tracers from the SMBH (reflecting the fact that there is no way to extract matter from a BH). One should also note that the total mass of SMBH tracers is larger than the total mass of SMBHs, as part of the energy-mass has been radiated away during accretion (and tracers have a fixed mass).

2.5. AGN feedback

In Dubois et al. (2012b), there are two modes of AGN feedback: a quasar/heating mode and a radio/jet mode. The mode is selected based on the ratio of the Bondi–Hoyle–Littleton accretion rate to the Eddington accretion rate $\chi = \dot{M}_{\mathrm{B}}/\dot{M}_{\mathrm{Edd}}$. If $\chi < 0.01$, the AGN is in jet mode, and, otherwise, it is in quasar mode (Merloni & Heinz 2008).

In quasar mode, all the energy of the AGN proportional to $E_{\mathrm{AGN},Q} = \varepsilon_{\mathrm{f},Q}\varepsilon_{\mathrm{r}}\dot{M}_{\mathrm{acc}}c^2\Delta t$ (the value $\varepsilon_{\mathrm{f},Q} = 0.15$ is calibrated to

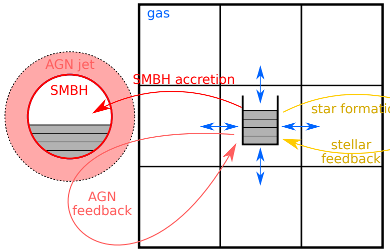

Fig. 1. Scheme of the different "buckets" that can hold tracer particles and the process that moves them around. The three buckets are gas cells, stars, and SMBHs. Arrows indicate outgoing mass fluxes between buckets and the physical process associated, and grey squares represent tracer particles. The jet mode feedback from AGNs (around SMBHs) is able to move gas tracer particles from the central cell to the surrounding cells. The particles have no spatial distribution within the buckets or any phase-space distribution. Tracer particles are exchanged probabilistically between buckets based on the mass fluxes. For example, for the gas, they are exchanged based on the mass fluxes at the boundary of the cells.

to be the probability of displacing a gas tracer particle from one cell to any other of its neighbouring cell, and

$$p_j = \max\left(\frac{\Delta M_{ij}}{\Delta M}, 0\right), \tag{3}$$

to be the probability of moving this tracer particle into cell j. For each tracer particle in cell i, a random number r is drawn from a uniform distribution between 0 and 1. If $r < p_{\rm gas}$, the tracer is selected. For each selected tracer, another random number r' is drawn. For each neighbouring cell j with a positive flux (such that $\Delta M_{ij} > 0$), if $r' < p_j$ the tracer particle is moved into cell j and the algorithm proceeds to the next particle; else, r' is decreased so that $r' \leftarrow r' - p_j$ and the algorithm proceeds to the next neighbouring cell. Because the sum of all the p_j is 1, this procedure will assign the tracer to a single cell.

When a cell of mass M_0 is refined between two time steps, all its tracers are distributed randomly to one of the eight newly created cells, the probability for a tracer particle to be attached to the new cell i being $p = M_i/M_0$ (refined density can be interpolated from neighbouring values or equally distributed amongst new cells). Conversely when a cell is derefined all its tracers are attached to the parent cell.

2.2. Star formation

This part of the algorithm involves moving tracers from the gas phase into star particles, and moving the star-tracer particles along with their star particles.

We first recall that the star formation process in Ramses is usually modelled by a Schmidt law, where the star formation rate density is non-zero and

$$\frac{d\rho_\star}{dt} = \epsilon_\star \frac{\rho_g}{t_{\rm ff}}, \tag{4}$$

when $\rho_g > \rho_0$, and where ρ_g is the gas density, ρ_0 a gas density threshold, $t_{\rm ff} = (3\pi/(32G\rho_g))^{1/2}$ the gas free-fall time, and $\epsilon_\star$ the efficiency of star formation, which can be taken as an ad hoc constant, or as a function of the local gravo-turbulent properties of the gas (Krumholz & McKee 2005; Hennebelle & Chabrier 2011; Padoan & Nordlund 2011). A single star particle made of $N_\star$ stars of mass resolution $M_{\star,0}$ is created, where $N_\star$ is drawn according to random Poisson process (Rasera & Teyssier 2006):

$$P_{\rm sf} = \frac{\lambda^{N_\star}}{N_\star!} \exp(-\lambda), \tag{5}$$

where $P_{\rm sf}$ is the probability of creating $N_\star$ particles from the gas (and accordingly removing $M_\star \equiv N_\star M_{\star,0}$ mass from the gas cell), and

$$\lambda = \frac{\rho_g \Delta x^3}{M_{\star,0}} \frac{\Delta t}{\epsilon_\star^{-1} t_{\rm ff}}. \tag{6}$$

Finally, the transfer of gas tracer particles to star-tracer particles at time of creation t of $M_\star$ is given by the probability

$$p_\star = \frac{M_\star}{M_i}. \tag{7}$$

In more details, we loop over all the gas tracer particles contained in the cell where the new star is created. For each of them, a random number r is drawn from a uniform distribution between 0 and 1. If $r < p_\star$, the gas tracer particle is turned into a star-tracer particle at the same position as that of the star particle (i.e. at the centre of the cell). The star-tracer particle is "attached" to the star particle by moving along with the star particle, which is done through a classic leap-frog integration of its motion. Therefore, at all time steps, the position of the tracer is updated to match the position of its star. The index of the star is also recorded on the tracer for convenience.

The implementation also comes with two alternatives to initialise the tracer particles. One can feed in a list of positions to the code; one tracer will be created at each location. Alternatively, we developed an initialisation scheme that takes as input the mass that each tracer particle represents, m_t. The scheme is called "in-place initialisation" as it is performed directly within the code: the scheme is called once at startup, after the AMR grid has been built. It loops over all cells, and for each of them computes the number of tracer particles to create. The expected number of tracers created in a cell of mass $M_{\rm cell}$ is $N = m_t/M_{\rm cell}$. Let us write $N_0 = \lfloor N \rfloor$. The scheme creates $N_0 \equiv \lfloor N \rfloor$ particles in the cell and then creates an additional one with probability $N - N_0$. In the end, the expected number of tracer particles created in the cell is N, meaning that on average each cell is populated with the correct number of tracer particles. In the following, unless stated otherwise, the tracer particle distribution is always initialised using the in-place method.

2.3. Supernova feedback

Let us describe the transfer of mass of a star particle to the gas according to type II SN explosions (referred to henceforth as SNII) and their associated tracer particles. This can be trivially extended to the more complete description of the evolution of stellar mass loss.

When a star particle sampling an initial mass function (IMF) of mass $M_\star$ explodes into type II SNe, it releases a mass $\eta_{\rm SN} M_\star$, where $\eta_{\rm SN}$ can be crudely approximated by the mass fraction of the IMF going SNII. The probability of releasing a star-tracer particle into the gas is $p_{\rm SN} = \eta_{\rm SN}$. For each star particle turning into SNe, we loop over all the star-tracer particles attached to it. For each of these, a random number r is drawn from a uniform

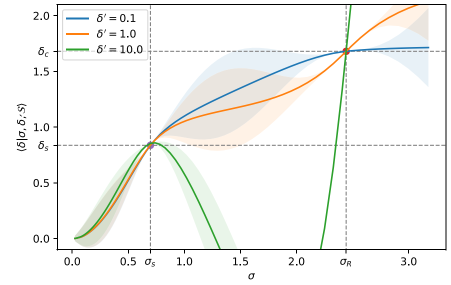

Figure 15. Plot of the mean of density given the saddle point, the upcrossing condition and the slope at R for different slopes. The saddle point was defined using the values of Table D1. The details of the calculation are provided in Appendix B. For steep slopes (small accretion rate), the mean of the density overshoots at small σ, resulting in a larger bias.

It follows that the bias of haloes far from structures grows with accretion rate (the usual behaviour expected from excursion sets), while the trend inverts for haloes near the centre of the filament. Because typical mass of haloes also depends on the position along the filament, with haloes towards the nodes being more massive, the different curves of Fig. 14 correlate with haloes of different mass. This effect explains why low-mass haloes with small accretion rate (or early formation time, or high concentration) are more biased, when measuring halo bias as a function of mass and accretion rate (or formation time or concentration, which strictly correlate with accretion rate), without knowledge of the position in the cosmic web. Conversely, the high-mass ones are less biased (Sheth & Tormen 2004; Gao et al. 2005; Wechsler et al. 2006; Dalal et al. 2008; Faltenbacher & White 2010; Paranjape & Padmanabhan 2017). It is also intriguing to compare this result with the measurements by Lazeyras et al. (2017, , namely their fig. 7) which show the same trends (although their masses are not small enough to clearly see the inversion).

Note in closing that the conditional bias theory presented here does not capture changes in accretion rate and formation time presented in Sections 4.3 and 4.4.

7 CONCLUSION AND DISCUSSION

7.1 Conclusion

With the advent of modern surveys, assembly bias has become the focus of renewed interest as a process which could explain some of the diversity of galactic morphology and clustering at fixed mass. It is also investigated as a mean to mitigate intrinsic alignments in weak-lensing survey such as *Euclid* or LSST. Both observations and simulations have hinted that the large-scale anisotropy of the cosmic web could be responsible for stalling and quenching. This paper investigated this aspect in Lagrangian space within the framework of excursion set theory. As a measure of infall, we computed quantities related to the slope of the contrast conditioned to the relative position of the collapsing halo with respect to a critical point of the large-scale field. We focused here on mass accretion rate and half-mass redshift and found that their expectation vary with the orientation and distance from saddle points, demonstrating that assembly bias is indeed influenced by the geometry of the tides imposed by the cosmic web.

More specifically, we derived the Press–Schechter typical mass, typical accretion rate, and formation time of dark haloes in the vicinity of cosmic saddles by means of an extension of excursion set theory accounting for the effect of their large-scale tides. Our principal findings are the following: we have computed the (i) *upcrossing PDF* for halo mass, accretion rate, and formation time; they are given by equations (14), (23), and (32), and their constrained-by-saddles counterparts equations (49), (61), and (68). These PDFs allowed us to identify the (ii) *typical halo mass*, and *typical accretion rate and formation time at given mass* as functions of the position within the frame of the saddle via equations (83)–(85). All quantities are expressed as a function of the geometry of the saddle for an arbitrary cosmology encoded in the underlying power spectrum via the correlations $\xi_{\alpha\beta}$ and $\xi'_{\alpha\beta}$ given by equations (E11) and (E12). In turn, this has allowed us to compute and explain the corresponding (iii) *distinct gradients* for the three typical quantities and for the local mean density (Section 5.3). The misalignment of the gradients, defined as the normals to the their isosurfaces, arises because the saddle condition is anisotropic and because it does not only shift the local mean density and the mean density profile (the excursion set slope) but also their variances, affecting different observables in different way. Finally, we have presented (iv) *an extension of classical large-scale bias theory* to account for the saddle (Section 6).

Our simple conditional excursion set model subject to filamentary tides makes intuitive predictions in agreement with the trends found in N-body simulations: haloes in filaments are less massive than haloes in nodes, and at equal mass they have earlier formation times and smaller accretion rates today. The same hierarchy exists for haloes in walls with respect to filaments. For the configuration we examined, the effect is stronger as one moves perpendicularly to the filament. The typical mass changes by a factor of 5 along the filament, and by two orders of magnitude perpendicularly. The relative variation of accretion rates and formation times is of about 5–10 per cent along the filament, and of about 20–30 per cent in the perpendicular direction, for haloes of $10^{11}\,{\rm M}_\odot\,h^{-1}$. Furthermore, our model predicts that at fixed halo mass, the trend of the large-scale bias with accretion rate depends on the distance from the centre of the filament. Far from the centre, the large-scale bias grows with accretion rate (which is the naive expectation from excursion sets), while near the centre the trend inverts and haloes with smaller accretion rates become more biased. Since haloes near the centre are also on average less massive, this effect should contribute to explaining why the trend of bias with accretion rate (or formation time) inverts at masses much smaller than the typical mass.

These findings conflict with the simplistic assumption that the properties of galaxies of a given mass are uniquely determined by the density of the environment. The presence of distinct space gradients for the different typical quantities is also part and parcel of the conditional excursion set theory, simply because the statistics of the excursion set proxies for halo mass, accretion rate, and formation time (the first-crossing scale and slope, and the height at the scale corresponding to $M/2$) are different functions of the position with respect to the saddle point. They have thus different level surfaces. At the technical level, the contours depend on the presence of the conditional variance of $\delta(\boldsymbol{r})$, besides its conditional mean, and of the correlation functions of $\delta'(\boldsymbol{r})$. At finite separation, the traceless shear of the large-scale environment modifies in an anisotropic way the statistics of the local mean density $\delta(\boldsymbol{r})$ (and of its derivative $\delta'(\boldsymbol{r})$ with respect to scale). The variations are modulated by $\mathcal{Q} = \hat{r}_i \bar{q}_{ij} \hat{r}_j$,

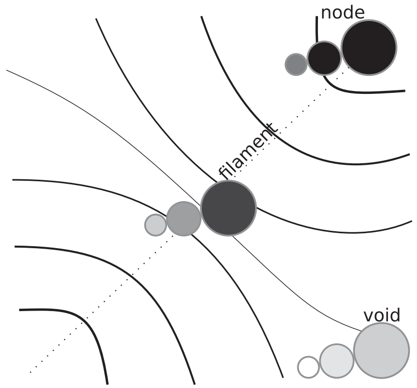

Figure 16. Scheme of the intensity of the accretion rate at different locations near a filament-type saddle for different final halo masses. The darkness of the colour encodes the intensity of the accretion rate (darker is more accretion). At fixed mass, the accretion rate increases from voids to saddle points and from saddle points to nodes (along dotted line which marks the filament's direction). At a given location, the accretion rate increases with mass.

i.e. the relative orientation of the separation vector in the frame set by the tidal tensor of the saddle. This angular modulation enters different quantities with different radial weights, which results in different angular variations of the local statistics of density, mass, and accretion rate/formation time. It provides a supplementary vector space, $\bar{\nabla}\mathcal{Q}$, beyond the radial direction over which to project the gradients, whose statistical weight depend on each specific observable. These quantities have thus different isosurfaces from each other and from the local mean density, a genuine signature of the traceless part of the tidal tensor. The qualitative differences in terms of mass accretion rate and galactic colour is sketched in Fig. 16.

7.2 Discussion and perspectives

In contrast to the findings of Alonso et al. (2015), Tramonte et al. (2017), and von Braun-Bates et al. (2017), we focused our attention on variations of *mass accretion rates* with respect to the cosmic web rather than mass functions. We have found that, even in a very simple model like excursion sets, halo properties are indeed affected by the anisotropic tides of the environment (involving the traceless part of the tidal tensor), and not just by its density (involving the trace of the tidal tensor). This effect cannot be explained by a simple rescaling of the local mean density (the average density in a sphere of radius of the order of the Lagrangian radius, centred around the halo). Our predictions are in qualitative agreement with the observational results of Kraljic et al. (2018), who detect a misalignment between the isocontours of mass, secondary halo property (type/colour in their case), and local mean density averaged on sufficiently large scales. This misalignment tends to disappear as the scale of the smoothing becomes small, and the signal is increasingly driven by the density alone: this can be interpreted as a consequence of the dynamical stretching of all contours as the filament forms.

Although the excursion set approach is rather crude, and additional constraints (e.g. peaks) would be needed to pinpoint the exact location of halo formation in the initial conditions, we argued that the effect we are investigating does not strongly depend on the presence of these additional constraints. The underlying reason is that the extra constraints usually involve vector or tensor quantities evaluated *at the same location* $\boldsymbol{r}$ *as the excursion set sphere*, which do not directly correlate with the scalars considered here (they only do so through their correlation with the saddle point). They may add polynomial corrections to the conditional distributions, but will not strongly affect the exponential cut-offs on which we built our analysis. Our formalism may thus not predict exactly whether a halo will form (hence, the mass function), but it can soundly describe the secondary properties and the assembly bias of haloes that actually form. A more careful treatment would change our results only at the quantitative level. For this reason, we chose to prefer the simplicity of the simple excursion set approach. Furthermore, in order to describe the cosmic web, we focused on saddle points of the initial gravitational potential, rather than of the density field, as these are more suitable to trace the *dynamical* impact of filamentary structures in connection to the spherical collapse model.

The present Lagrangian formalism only aims at describing the behaviour of the central galaxy: it cannot claim to capture the strongly non-linear process of dynamical friction of subclumps within dark haloes, nor strong deviations from spherical collapse. We refer to Hahn et al. (2009) which captures the effect on satellite galaxies, and to Ludlow et al. (2014), Castorina et al. (2016), and Borzyszkowski et al. (2016) which study the effect of the local shear on haloes forming in filamentary structures. Incorporating these effects would require adopting a threshold for collapse that depends on the local shear, as discussed in the Introduction. Such a barrier would not pose a conceptual problem to our treatment;[11] technically, however it requires two extra integrations (over the amplitude of the local shear and its derivative with respect to scale), and cannot be done analytically. The shear-dependent part of the critical density (and its derivative) would correlate with the shear of the saddle at $\boldsymbol{r} = 0$, and introduce an additional anisotropic effect on top of the change of mean values and variances of density and slope we accounted for. Evaluating this effect will be the topic of future investigation.

Our analysis demonstrated that the large-scale tidal field alone can induce specific accretion gradients, distinct from mass and density ones. One would now like to translate those distinct DM gradients into colour and specific star formation rate (SFR) gradients. At high redshift, the stronger the accretion, the bluer the central galaxy. Conversely at low redshift, one can expect that the stronger the accretion, the stronger the AGN feedback, the stronger the quenching of the central. Should this scaling hold true, the net effect in terms of gradients would be that colour gradients differ from mass and density ones. The transition between these two regimes (and in general, the inclusion of baryonic effects) is beyond the scope of this paper, but see Appendix H for a brief discussion.

Beyond the DM-driven processes described in this paper, different explanations have been recently put forward to explain filamentary colour gradients. On the one hand, it has been argued (Aragon-Calvo, Neyrinck & Silk 2016) that the large-scale turbulent flow within filaments may explain the environment dependence in observed physical properties. Conversely, the vorticity of gas inflow within filaments (Laigle et al. 2015) may be prevalent in feeding galactic discs coherently (Pichon et al. 2011; Stewart et al. 2011). Both processes will have distinct signatures in terms of the efficiency and stochasticity of star formation. A mixture of both may

[11] The details of the impact on the present derivation are given in Appendix G.

can also impact the modelling itself (e.g. Federrath et al. 2008; Silvia et al. 2010).

In this paper we present a new implementation of tracer particles in the AMR Ramses code (Teyssier 2002). This implementation is based on the one developed by Genel et al. (2013) for the moving mesh arepo code (Springel 2010). It has been extended to track the full Lagrangian history of baryons in any phase, including their conversion from gas to stars, from stars back into the gas via supernova feedback, their interaction with feedback from black holes, and their accretion onto them. This Monte Carlo (MC) tracer particle implementation improves the previous implementation, velocity-advected tracers. With the velocity-based approach, tracer particles are moved based on the interpolated local values of the gas velocity field. While this yields qualitative results, it suffers from systematic effects: tracer particles over-condensate in regions of converging flows (Genel et al. 2013). Monte Carlo tracer particles follow a different idea. They are moved such that the tracer particle mass flux at each cell interface is statistically equal to that of the gas. Thanks to this property, the Eulerian distribution of tracers converge to that of the gas when the number of tracer particles goes to infinity. In addition to matching the gas distribution, the implementation of tracer particles here is also able to match the distribution of baryons in stars and in black holes.

The paper is structured as follows. Section 2 details the implemented algorithm. Section 3 presents tests and validations of the new implementation. In particular, Sect. 3.1 presents the results from idealised tests and Sect. 3.2 presents an analysis of the properties of tracers in a real astrophysical simulation. Using the same simulation, Sect. 3.3 illustrates the efficiency of the scheme applied to a specific science case – the bimodal accretion of gas onto galaxies at high redshift. Section 4 assesses the performance of the scheme. Section 5 provides a discussion of our results and our conclusions. Appendix A provides more details about the algorithm.

2. Implementation

The Ramses code (Teyssier 2002) solves the full set of Euler equations by formulating the equations in terms of finite-volume, that is, by calculating fluxes at the interfaces of cells of the adaptive mesh. This is done by using a MUSCL-Hancock method with a second-order Godunov solver calculating the fluxes from linearly interpolated values at cell faces from the cell-centred values limited by a total-variation-diminishing scheme. Such a Eulerian-based method has proven efficient at capturing shock discontinuities and achieves efficient mixing of shear layers of gas; however, its main drawback is that it does not naturally provide the Lagrangian trajectories of gas elements.

To address this problem, it is possible to introduce the so-called tracer particles of the flow that should follow the flow lines of the gas. A naive approach to track the motion of the gas is to use the velocity of the gas itself, assign it to tracer particles, and move them accordingly. This is done with a cloud-in-cell interpolation of the velocity values of the overlapped cells where the volume of the cloud is that of the host cell, though the level of the interpolation is not particularly important (nearest grid point or triangular shape cloud; Federrath et al. 2008). Such a velocity-based approach was implemented in Ramses (Dubois et al. 2012a) and used to probe the link between cosmic gas infall and galactic gas feeding, and its acquisition of angular momentum (Pichon et al. 2011; Dubois et al. 2012a; Tillson et al. 2015). While this approach yields smooth trajectories, it falls short of reproducing the gas density distribution accurately in regions with strong convergence of the velocity field (Genel et al. 2013).

To address this shortcoming, we have implemented in Ramses the MC approach of tracer particles introduced by Genel et al. (2013) for arepo (Springel 2010). Instead of having proper velocities and positions, MC tracers are attached to individual cells and are allowed to "jump" from the centre of one cell to the centre of another according to the mass fluxes obtained through the Godunov solver.

We have generalised the MC method to track exchanges of baryons between gas, star particles, and supermassive black hole (SMBH) particles, and in the following we refer to them as "buckets". At each time step, tracers are allowed to jump from any bucket i to any bucket j with a probability (gas→gas, gas↔star, gas→black hole) of

$$p_{ij} = \begin{cases} \dfrac{\Delta M_{ij}}{M_i}, & \text{if } \Delta M_{ij} \geq 0, \\ 0, & \text{if } \Delta M_{ij} < 0, \end{cases} \tag{1}$$

where ΔM_{ij} is the mass flowing from bucket i to bucket j between t and $t + \Delta t$ and M_i is the mass of the depleted bucket i at time t. This probability is also the fraction of baryons flowing from one bucket to another. If the initial Eulerian distributions of tracers and baryons are equal, then in the limit where the number of tracers becomes large, satisfying Eq. (1) is sufficient for the Eulerian distributions to remain equal at all times. Here is an outline of the proof. For any bucket i containing N_t tracers of equal mass m_t, let the total tracer mass read $M_\mathrm{t} \equiv N_\mathrm{t} m_\mathrm{t}$. Because tracers are moved stochastically, the tracer mass flux $\Delta M_{\mathrm{t},ij}$ is a random variable. If at time t, $M_\mathrm{t} = M_i$ (i.e. the Eulerian distributions are the same), then the expected tracer flux is $\mathrm{E}\left[\Delta M_{\mathrm{t},ij}\right] = N_\mathrm{t} \times p_{ij} m_\mathrm{t} = M_i p_{ij} = \Delta M_{ij}$. When the number of tracers becomes large, the tracer mass flux converges to the baryon flux, $\Delta M_{\mathrm{t},ij} \to \Delta M_{ij}$. The buckets have the same initial mass and are updated with the same mass fluxes, so they remain equal at the next time step, $t + \Delta t$. Therefore, if the initial Eulerian distributions are equal, by induction they remain equal at all times (in the limit of a large number of tracers)[1].

All the processes that are able to move tracers from bucket to bucket are summarised in Fig. 1. Tracers can move from one gas cell to another through gas dynamics, and the jet mode of AGN feedback from SMBHs, from gas to stars via star formation, from stars to gas via supernova (SN) feedback, and from gas to SMBHs via black hole accretion. Below, we present the different algorithms used for each of these processes.

2.1. Gas dynamics

The algorithm moving tracer particles from one gas cell to another is the following. For each level of refinement, all the unrefined leaf cells are iterated over. For each leaf cell i containing tracer particles, the total outgoing mass is computed as $\Delta M \equiv \sum_{j=1}^{2N_\mathrm{d}} \max(\Delta M_{ij}, 0)$, where j runs over the index of the neighbouring cells, N_d is the number of dimensions, and ΔM_{ij} is the mass transferred between cell i and cell j in one time step and obtained from the Godunov flux of mass $F_{m,\mathrm{ij}}$, that is, $\Delta M_\mathrm{ij} = F_{m,\mathrm{ij}} \Delta t$. We take

$$p_\mathrm{gas} = \frac{\Delta M}{M_i}, \tag{2}$$

[1] In general, any stochastic scheme for which the expected tracer flux equals that of the baryons is able to track the Eulerian distribution at all times.

A&A 621, A96 (2019)
https://doi.org/10.1051/0004-6361/201834496

Astronomy & Astrophysics

Accurate tracer particles of baryon dynamics in the adaptive mesh refinement code Ramses

Corentin Cadiou[1], Yohan Dubois[1], and Christophe Pichon[1,2]

[1] Institut d'Astrophysique de Paris, CNRS & UPMC, UMR 7095, 98 bis Boulevard Arago, 75014 Paris, France
e-mail: corentin.cadiou@iap.fr
[2] Korea Institute of Advanced Studies (KIAS), 85 Hoegiro, Dongdaemun-gu 02455, Seoul, Republic of Korea

Received 23 October 2018 / Accepted 9 November 2018

ABSTRACT

We present a new implementation of the tracer particles algorithm based on a Monte Carlo approach for the Eulerian adaptive mesh refinement code RAMSES. The purpose of tracer particles is to keep track of where fluid elements originate in Eulerian mesh codes, so as to follow their Lagrangian trajectories and re-processing history. We provide a comparison to the more commonly used velocity-based tracer particles, and show that the Monte Carlo approach reproduces the gas distribution much more accurately. We present a detailed statistical analysis of the properties of the distribution of tracer particles in the gas and report that it follows a Poisson law. We extend these Monte Carlo gas tracer particles to tracer particles for the stars and black holes, so that they can exchange mass back and forth between themselves. With such a scheme, we can follow the full cycle of baryons, that is, from gas-forming stars to the release of mass back to the surrounding gas multiple times, or accretion of gas onto black holes. The overall impact on computation time is ~3% per tracer per initial cell. As a proof of concept, we study an astrophysical science case – the dual accretion modes of galaxies at high redshifts –, which highlights how the scheme yields information hitherto unavailable. These tracer particles will allow us to study complex astrophysical systems where both efficiency of shock-capturing Godunov schemes and a Lagrangian follow-up of the fluid are required simultaneously.

Key words. hydrodynamics – methods: numerical – cosmology: theory – Galaxy: formation

1. Introduction

Many astrophysical problems of interest require us to solve equations of hydrodynamics on very different timescales and physical scales. Two main methods have been developed to solve these equations. On the one hand, one can study the motion of the gas by following the evolution of interacting particles. This Lagrangian approach is the one used by smooth particle hydrodynamics (SPH, e.g. Springel 2005; Wadsley et al. 2004; Price et al. 2018) codes. These codes sample the gas distribution using a set of fixed-mass macro-particles smoothed with a given kernel, and move particles accordingly. By construction, this approach provides the Lagrangian evolution of the gas. This property is also one of its shortcomings: low-density regions are populated by large particles and hence lack resolution. On the other hand, gas hydrodynamics can also be described on a grid, where gas distribution is sampled on finite volumes, and solved with efficient shock-capturing Godunov solvers. Adaptive mesh refinement (AMR, e.g. Kravtsov et al. 1997; Teyssier 2002; Springel 2010; Bryan et al. 2014) codes follow this approach and allow for a dynamical refinement of the mesh. Though quasi-Lagrangian refinement is most commonly adopted in situations addressing galaxy formation problems, super-Lagrangian resolutions can also be achieved by refining the grid based on gas quantities such as the Jeans length to follow gravitationaly unstable star-forming regions (Agertz et al. 2009), the vorticity to follow the seeding of turbulence (e.g. Iapichino & Niemeyer 2008), the relative variation of any hydro quantity (such as e.g. the ionised fraction of hydrogen; Rosdahl & Blaizot 2012), or using a passive scalar to keep track of a particular gas phase (such as for jets, see, e.g. Bourne & Sijacki 2017), among others. While super-Lagrangian refinement provides a very flexible method to trigger refinement, it falls short of providing the Lagrangian history of the gas.

To overcome this issue, AMR codes have been equipped with "tracer" particles. Tracer particles are passively displaced with the gas flow, and hence track its Lagrangian evolution. Each tracer can also be used to record instantaneous quantities, such as the thermodynamical properties of the gas or any other property. Many astrophysical problems can can benefit greatly from this Lagrangian information. For example, when studying galaxy formation, the past Lagrangian history of the gas is crucial to understand how gas has been accreted and how it has been ejected in large-scale galactic outflows. Tracer particles can be used to study the density and temperature evolution of the gas (e.g. Nelson et al. 2013; Tillson et al. 2015) that will eventually form stars. For example, one could use tracer particles to study the temperature evolution of the gas as it falls onto galaxies, to study the number of dynamical times before it becomes star forming or to quantity the number of time gas is recycled in stars or sent in galactic fountains. Another problem that requires the use of tracer particles is the study of mixing. Particularly in turbulent environments, such as the interstellar or the intergalactic medium, the Lagrangian information provides information about, for example, mixing timescale (e.g. Federrath et al. 2008), the origin of turbulence (e.g. Vazza et al. 2011, 2012), or how it contributes to core buildup Mitchell et al. (2009). In addition to this, the past Lagrangian evolution of a parcel of fluid

in fact be taking place, given that the kinematic of the large-scale flow is neither strictly coherent nor fully turbulent. Yet, even if ram-pressure stripping in filaments operate as efficiently as in clusters, it will remain that the anisotropy of the tides will also impact the consistency of angular momentum advection, which is deemed important at least for early-type galaxies. The amplitude of thermodynamical processes depends on the equation of state of the gas and on the amplitude of feedback which are not fully calibrated today. Recall that shock heating, AGN and stellar feedback are driven by cold gas infall, which in turn is set by gravity (as the dominant dynamical force). Since gravity has a direct effect through its tides, unless one can convincingly argue that its direct impact is negligible on galactic scales, it should be taken into account.

Codis et al. (2015), following a formally related route, investigated the orientation of the spin of dark haloes in relation to their position with respect to the saddle points of the (density) cosmic web (see also Wang & Kang 2018, for a slightly different approach). Together with their predictions on spin orientation, this work could be extended to model galaxy colours based on both spin and mass accretion. It could also guide models aiming at mitigating the effect of intrinsic alignments (Joachimi et al. 2011) impacting weak-lensing studies, while relying on colour gradients. More generally, galactic evolution as captured by semi-analytical models will undoubtedly gain from a joint description of involving both mass and spin acquisition as relevant dynamical ingredients. Indeed, it has been recently shown in hydrodynamical simulation (e.g. Zavala et al. 2016) that the assembly of the inner DM halo and its history of specific angular momentum loss is correlated to the morphology of galaxies today. One should attempt to explain the observed diversity at a given mass driven by anisotropic large-scale tides, which will impact gas inflow towards galaxies, hence their properties. An improved model for galaxy properties should eventually explicitly integrate the geometry of the large environment (following, e.g. Hanami 2001) and quantify the impact of its anisotropy on galactic mass assembly history.

Thanks to significant observational, numerical, and theoretical advances, the subtle connection between the cosmic web and galactic evolution is on the verge of being understood.

ACKNOWLEDGEMENTS

Simulations were carried on the Horizon Cluster hosted by Institut d'Astrophysique de Paris. We thank S. Rouberol for running it smoothly for us. This research is part of Spin(e) (ANR-13-BS05-0005, http://cosmicorigin.org). We are thankful to Stephane Arnouts, Francis Bernardeau, Oliver Hahn, Clotilde Laigle, Aseem Paranjape, Dmitri Pogosyan, Ravi Sheth, Marie Treyer, and Didier Vibert for helpful discussions. MM is partially supported by the Programme Visiteur of the Institut d'Astrophysique de Paris. CC is supported by the Institut Lagrange de Paris LABEX (under reference ANR-10-LABX-63 and ANR-11-IDEX-0004-02).

REFERENCES

Alonso D., Eardley E., Peacock J. A., 2015, MNRAS, 447, 2683
Alpaslan M. et al., 2016, MNRAS, 457, 2287
Aragon-Calvo M. A., Neyrinck M. C., Silk J., 2016, preprint (arXiv:1607.07881)
Bernardeau F., Crocce M., Scoccimarro R., 2008, Phys. Rev. D, 78, 103521
Bond J. R., Myers S. T., 1996, ApJS, 103, 1
Bond J. R., Cole S., Efstathiou G., Kaiser N., 1991, ApJ, 379, 440
Bond J. R., Kofman L., Pogosyan D., 1996, Nature, 380, 603
Borzyszkowski M., Porciani C., Romano-Diaz E., Garaldi E., 2016, MNRAS, 469, 594
Castorina E., Paranjape A., Hahn O., Sheth R. K., 2016, preprint (arXiv:1611.0361)
Chen Y.-C. et al., 2017, MNRAS, 466, 1880
Codis S., Pichon C., Pogosyan D., 2015, MNRAS, 452, 3369
Corasaniti P. S., Achitouv I., 2011, Phys. Rev. D, 84, 023009
Dalal N., White M., Bond J. R., Shirokov A., 2008, ApJ, 687, 12
Del Popolo A., Ercan E. N., Gambera M., 2001, Balt. Astron., 10, 629
Desjacques V., Jeong D., Schmidt F., 2016, preprint (arXiv:1611.09787)
Doroshkevich A. G., 1970, Astrophysics, 6, 320
Dubois Y., Devriendt J., Slyz A., Teyssier R., 2010, MNRAS, 409, 985
Dubois Y., Pichon C., Devriendt J., Silk J., Haehnelt M., Kimm T., Slyz A., 2013, MNRAS, 428, 2885
Dubois Y. et al., 2014, MNRAS, 444, 1453
Dubois Y., Peirani S., Pichon C., Devriendt J., Gavazzi R., Welker C., Volonteri M., 2016, MNRAS, 463, 3948
Efstathiou G., Frenk C. S., White S. D. M., Davis M., 1988, MNRAS, 235, 715
Faltenbacher A., White S. D. M., 2010, ApJ, 708, 469
Fry J. N., Gaztanaga E., 1993, ApJ, 413, 447
Gao L., Springel V., White S. D. M., 2005, MNRAS, 363, L66
Gradshteyn I. S., Ryzhik I. M., 2007, Table of Integrals, Series, and Products, Seventh edn. Elsevier/Academic Press, Amsterdam
Hahn O., Porciani C., Dekel A., Carollo C. M., 2009, MNRAS, 398, 1742
Hanami H., 2001, MNRAS, 327, 721
Joachimi B., Mandelbaum R., Abdalla F. B., Bridle S. L., 2011, A&A, 527, A26
Kaiser N., 1984, ApJ, 284, L9
Kauffmann G., Li C., Zhang W., Weinmann S., 2013, MNRAS, 430, 1447
Kawinwanichakij L. et al., 2016, ApJ, 817, 9
Kraljic K. et al., 2018, MNRAS, 474, 547
Lacey C. G., Cole S., 1993, MNRAS, 262, 627
Laigle C. et al., 2015, MNRAS, 446, 2744
Laigle C. et al., 2017, MNRAS, 474, 5437
Lazeyras T., Musso M., Schmidt F., 2017, J. Cosmol. Astropart. Phys., 3, 059
Ludlow A. D., Borzyszkowski M., Porciani C., 2014, MNRAS, 445, 4110
Maggiore M., Riotto A., 2010, ApJ, 711, 907
Malavasi N. et al., 2017, MNRAS, 465, 3817
Martínez H. J., Muriel H., Coenda V., 2016, MNRAS, 455, 127
Musso M., Sheth R. K., 2012, MNRAS, 423, L102
Musso M., Sheth R. K., 2014a, MNRAS, 438, 2683
Musso M., Sheth R. K., 2014b, MNRAS, 443, 1601
Musso M., Sheth R. K., 2014c, MNRAS, 443, 1601
Musso M., Paranjape A., Sheth R. K., 2012, MNRAS, 427, 3145
Oemler A., Jr, 1974, ApJ, 194, 1
Paranjape A., Padmanabhan N., 2017, MNRAS, 468, 2984
Paranjape A., Hahn O., Sheth R. K., 2017, preprint (arXiv:1706.09906)
Pichon C., Pogosyan D., Kimm T., Slyz A., Devriendt J., Dubois Y., 2011, MNRAS, 1739
Pogosyan D., Bond J. R., Kofman L., Wadsley J., 1998, in Colombi S., Mellier Y., Raban B., eds, Wide Field Surveys in Cosmology. Editions Frontieres, Dreux, p. 61
Poudel A., Heinämäki P., Tempel E., Einasto M., Lietzen H., Nurmi P., 2017, A&A, 597, A86
Press W. H., Schechter P., 1974, ApJ, 187, 425
Redner S., 2001, A Guide to First-Passage Processes. Cambridge University Press, Cambridge
Shen J., Abel T., Mo H. J., Sheth R. K., 2006, ApJ, 645, 783
Sheth R. K., Tormen G., 2004, MNRAS, 350, 1385
Sheth R. K., Mo H. J., Tormen G., 2001, MNRAS, 323, 1
Sheth R. K., Chan K. C., Scoccimarro R., 2013, Phys. Rev. D, 87, 083002
Sousbie T., Pichon C., Colombi S., Pogosyan D., 2008, MNRAS, 383, 1655
Stewart K. R., Kaufmann T., Bullock J. S., Barton E. J., Maller A. H., Diemand J., Wadsley J., 2011, ApJ, 738, 39
Tramonte D., Rubino-Martin J. A., Betancort-Rijo J., Dalla Vecchia C., 2017, MNRAS, 467, 3424

at high redshift. I have underlined that AM acquisition is dominated by the interaction between the inner halo, the outer halo, the disk, cold flows and hot-accreted material. Cold flows are able to reach the inner halo and the disk while hot-accreted gas interacts mostly with the outer halo.

4.6 "Accurate tracer particles of baryon dynamics in the adaptive mesh refinement code Ramses" (article)

This section presents the results obtained using the new tracer particle scheme developed during my thesis. These results have been published in Cadiou et al., 2019 and have already been presented in section 4.2.3.

von Braun-Bates F., Winther H. A., Alonso D., Devriendt J., 2017, J. Cosmol. Astropart. Phys., 3, 012
Wang P., Kang X., 2018, MNRAS, 473, 1562
Wang J. et al., 2011, MNRAS, 413, 1373
Wechsler R. H., Zentner A. R., Bullock J. S., Kravtsov A. V., Allgood B., 2006, ApJ, 652, 71
Weinmann S. M., van den Bosch F. C., Yang X., Mo H. J., 2006, MNRAS, 366, 2
Yan H., Fan Z., White S. D. M., 2013, MNRAS, 430, 3432
Zavala J. et al., 2016, MNRAS, 460, 4466
Zel'dovich Y. B., 1970, A&A, 5, 84
Zentner A. R., 2007, Int. J. Mod. Phys. D, 16, 763

APPENDIX A: DEFINITIONS AND NOTATIONS

Table A1 presents all the definitions introduced in the paper. Table 1 gives also the motivation behind the choice of variables. The following conventions is used throughout:

(i) unless stated otherwise, all the quantities evaluated at (halo) scale R have their dependence on R omitted (e.g. $\sigma = \sigma(R)$);
(ii) the quantities that have a radial dependence are evaluated at a distance r when the radius is omitted. Sometimes, the full form is used to emphasize the dependence on this variable;
(iii) unless stated otherwise, the quantities are evaluated at $z = 0$ and $D(z) = 1$ (e.g. $\delta_c = 1.686$);
(iv) a prime denotes a derivative with respect to σ of the excursion set (e.g. $\delta' = \mathrm{d}\delta/\mathrm{d}\sigma$);
(v) variables carrying a hat have unit norm (e.g. $|\hat{\boldsymbol{r}}| = 1$), matrices carrying an overbar are traceless (e.g. $\mathrm{tr}(\bar{q}_{ij}) = 0$);
(vi) the *Einstein*'s convention on repeated indexes is used throughout, except in Appendix F2.

APPENDIX B: VALIDATION WITH GRFS

Let us first compare the prediction of Section 4 to statistics derived from realization of GRF, while imposing a saddle-point condition. The values used at the saddle point are reported in Table D1. We further imposed the saddle point's eigenframe to coincide with the x, y, z frame, which in practice has been done by imposing $\bar{q}_{ij}$ to be diagonal. We have used two different methods to validate our results, by generating random density cubes (Appendix B1) and by computing the statistics of a constrained field (Appendix B2).

B1 Validation for $\sigma_\star$

The procedure is the following: (i) 4000 cubes of size $(128)^3$ and width $L_{\mathrm{box}} = 200\ \mathrm{Mpc}\,h^{-1}$ centred on a saddle point were generated following a ΛCDM power spectrum; (ii) each cube has been smoothed using a Top-Hat filter at 25 different scales ranging from 0.5 to 20 $\mathrm{Mpc}\,h^{-1}$; (iii) for each point of each cube, the *first-crossing* point σ_{first} was computed; and (iv) the 4000 realizations were stacked to get a distribution of σ_{first} and to compute the median value. It is worth noting that the value of $\Gamma(\sigma(R))$ in the GRF is not the same as in theory. This is a well-known effect (see e.g. Sousbie et al. 2008) that arise on small scales due to the finite resolution of the grid and on large scale because of the finite size of the box. The Γ measured in a GRF is correct at scales verifying $\Delta L \lesssim R \ll L_{\mathrm{box}}$, where ΔL is the grid spacing. In our case, the largest smoothing scale is $20\ \mathrm{Mpc}\,h^{-1} = L_{\mathrm{box}}/10$. However, the smallest scale is comparable to the grid spacing. To attenuate the effect of finite resolution, we have measured $\Gamma(\sigma(R))$ in the GRF and used its value to compute the theoretical cumulative distribution function (CDF). The results of the measured CDF F_{first} and

Table A1. Summary of the variables used throughout the paper.

Variable	Definition	Comment
$\bar{\rho}_{\mathrm{m}}$	$(2.8\times10^{11}\ \mathrm{h^2 M_\odot/Mpc^3})\times\Omega_{\mathrm{M}}$	Uniform matter background density
$R, M, M_\star$	$M = 4/3\pi R^3\bar{\rho}_{\mathrm{m}}$	Smoothing scale, mass, and typical mass
δ_{m}	$(\rho_{\mathrm{m}}-\bar{\rho}_{\mathrm{m}})/\bar{\rho}_{\mathrm{m}}$	Linear matter overdensity
$W(x)$	$3j_1(x)/x$	Real-space Top-Hat filter (Fourier representation)
δ	$\int \frac{\mathrm{d}^3k}{(2\pi)^3}\delta_{\mathrm{m}}(\boldsymbol{k})W(kR)\mathrm{e}^{i\boldsymbol{k}\cdot\boldsymbol{r}}$	Linear matter overdensity smoothed at scale R, position $\boldsymbol{r}$
σ^2	$\mathrm{Var}(\delta)$	Variance of the overdensity at scale R
ν	δ/σ	Rescaled overdensity
$\delta_{\mathrm{c}}, \nu_{\mathrm{c}}$	$1.68, \delta_{\mathrm{c}}/\sigma$	Critical overdensity
δ', ν'	$\mathrm{d}\delta/\mathrm{d}\sigma, \mathrm{d}\nu/\mathrm{d}\sigma$	Slope of the E.S. trajectories
Γ^{-2}	$\mathrm{Var}(\delta')-1=\langle(\sigma\nu')^2\rangle=\mathrm{Var}\left(\delta'\vert\nu\right)$	Conditional variance of δ' at fixed ν
$R_{\mathcal{S}}, \sigma_{\mathcal{S}}$	$\sigma_{\mathcal{S}}=\sigma(R_{\mathcal{S}})$	Smoothing scale used at the saddle point
$R_\star^2$	(42) $\int \mathrm{d}k\frac{P(k)}{2\pi^2}\frac{W^2(kR_{\mathcal{S}})}{\sigma_{\mathcal{S}}^2}$.	Characteristic length-scale of the saddle (squared)
$g_i, q_{ij}, \nu_{\mathcal{S}}$	(41) and (43)	Mean acceleration, tidal tensor, and overdensity at saddle (see Table D1 for their value)
$\bar{q}_{ij}, \mathcal{Q}$	$\bar{q}_{ij}=q_{ij}-\nu_{\mathcal{S}}\delta_{ij}/3, \hat{r}_i\bar{q}_{ij}\hat{r}_j$	Traceless tidal tensor and anisotropy ellipsoidal-hyperbolic coordinate
$\xi_{\alpha\beta}, \xi'_{\alpha\beta}$	(E11) and (E12); $\xi'_{\alpha\beta}=\mathrm{d}\xi_{\alpha\beta}/\mathrm{d}\sigma$	Two-point correlation functions at separation r and scales R, $R_{\mathcal{S}}$
$\alpha, \alpha_\star$	$\nu_{\mathrm{c}}/[\sigma(\nu'-\nu'_{\mathrm{c}})]$; (27) and (62)	Accretion rate and typical accretion rate
$R_{1/2}, \sigma_{1/2}$	$R/2^{1/3}, \sigma(R_{1/2})$	Half-mass radius and variance
$\delta_{1/2}, \nu_{1/2}$	$\delta(\sigma_{1/2}), \delta_{1/2}/\sigma_{1/2}$	Overdensity at half-mass
$D_{\mathrm{f}}, D_\star$	$\delta_{\mathrm{c}}/\delta_{1/2}$; (38) and (72)	Formation time and typical formation time
ν_{f}	$\delta_c/(\sigma_{1/2}D_{\mathrm{f}})$	Density threshold at formation time
ω, ω'	(E14) and (E15); $\omega'=\mathrm{d}\omega/\mathrm{d}\sigma$	Zero-distance correlation functions between scales R and $R_{1/2}$
Ω, Ω'	(F27) and (F32); $\Omega'=\mathrm{d}\Omega/\mathrm{d}\sigma$	Zero-distance conditional covariance between scales R and $R_{1/2}$ given the saddle point
δ_0	$\delta(R_0 \gg R)$	Large-scale overdensity
δ_{h}		Local halo number density contrast

4.5 Conclusion

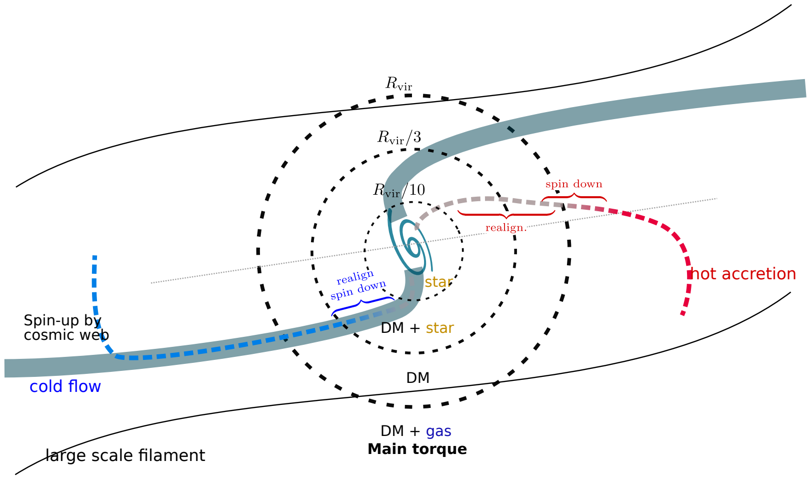

Figure 4.23: Sketch of the evolution of the AM at large z (not to scale). hot gas (red dashed line) is spun-up by the cosmic web and loses most of its AM at the virial radius in the shock. Cold gas (blue dashed line) is spun-up by the cosmic web and retains its AM down to the inner halo. Between the inner halo and the disk, most of the AM is lost due to interactions with the DM halo and the disk.

Using a set of high-resolution zoom-in simulations, I have studied the evolution of the AM of gas accreted via the cold and the hot mode around six group progenitors at $z \gtrsim 2$. I also presented new numerical methods to extract the contributions of the different forces and torques (gravitational and pressure torques). My findings are the following:

1. the magnitude of the sAM of the cold gas is conserved down to the inner halo, the magnitude of the sAM of the hot gas is lost outside the halo,
2. the orientation of the sAM of the cold gas is conserved down to the inner halo and,
3. the sAM of the hot gas is significantly less aligned to the large scale environment,
4. the dominant local forces in the cold gas are pressure forces and DM gravitational forces in the outer halo, and DM gravitational and star gravitational forces in the inner halo and the disk,
5. the pressure forces lack a spatial structure, so that their net contribute averages out in the cold gas,
6. the dominant torques in the cold cold gas are gravitational torques: DM gravitational torques dominate in the outer halo, star gravitational torques dominate in the disk.

The results on the major torques are sketched on figure 4.23. My findings indicate that the acquisition of the AM for group progenitors at $z \gtrsim 2$ is driven by the AM acquired at large-scale, consistent with the findings that the spin of galaxies is aligned with their environment. Most of the AM is able to flow down to the inner halo where gravitational torques redistribute it to the DM and the disk component, effectively transporting AM from the scales of the cosmic web to the scales involved in disk formation. These findings indicate that galaxy formation models aimed at understanding AM acquisition should take into account the cold accretion mode, at least

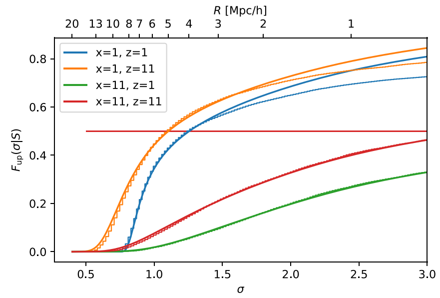

Figure B1. Theoretical CDF of σ at upcrossing (bold lines) and numerical CDF (steps) at first-crossing at four locations around the saddle point (the distances are in Mpc h^{-1} in the x (void) and z (filament) directions). The CDF have been normalized to share the same 50˜ per cent quantile (the horizontal line). See the text for the details of the normalization.

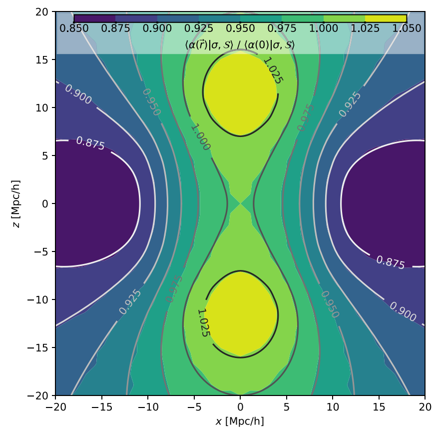

Figure B2. Mean value of α using a numerical method (purple to yellow) versus its theoretical value (grey contours). Both are normalized by the theoretical value at the saddle point.

theoretical CDF $F_{\rm up}$ (with the measured Γ) at four different positions are shown on Fig. B1. The measured CDFs have been normalized so that $F_{\rm first}^{-1}(0.5) = F_{\rm up}^{-1}(0.5)$: we impose that the CDF match at the 'median' (defined as the σ such that $F(\sigma) = 0.5$[12]). As shown on Fig. B2, the abscissa of the peak of the PDF in the direction of the void is around $\sigma \approx 2.7$. As $\sigma(R_{\rm min}) \approx 3$, it means that in the direction of the void, the PDF is only sampled up to its peak. The experimental CDF at such location is hence only probing less than 50˜ per cent of the distribution and the median is not reached. In this case, we are normalizing the experimental CDF to have the same value at the largest σ as the theoretical CDF. As shown on Fig. B1, the experimental and theoretical CDFs start diverging at $F \gtrsim 0.5$. At larger σ, the upcrossing approximation used in the theory breaks as more and more trajectories cross multiple time the barrier (they are counted once for the first crossing and multiple times for up-crossing). The orange and blue lines, in the direction of the filament show this clearly as they diverge one from each other at large σ. As $\sigma_\star$ is a measure of the location of the peak of the PDF (which is where the CDF is the steepest), it is sufficient that the experimental and theoretical CDF match up to their flat end to have the same $\sigma_\star$ values.

[12] This definition matches the classical one for distributions that have a normalized CDF, which is not true for $F_{\rm up}$.

B2 Validation for $\alpha_\star$ using constrained fields

A second check was implemented on the accretion rate as follows: (i) for each location, the covariance matrix of ν, δ', ν_S, $\bar{q}_{ij}$, g_i was computed at finite distance. These quantities all have a null mean; (ii) the covariance matrix and the mean of ν, δ' conditioned to the value at the saddle point was computed using the values of Table D1; (iii) the variance and mean of ν, δ' were computed given $\nu = \nu_c$ and the saddle point; and (iv) a sample of 10^6 points were then drawn from the distribution of $\delta' > 0$ (upcrossing). (v) The values of $\alpha \propto 1/\delta'$ were computed to obtain a sample of α. Each draw was weighted by $1/\alpha$ (the Jacobian of the transform from δ' to α). Finally, the numerical value of $\langle\alpha|\sigma, \mathcal{S}\rangle$ was estimated from the samples and compared with the theoretical value. The results are shown on Fig. B2 and are found to be in very good agreement.

We computed Fig. B3 by following steps (i)–(iii) at 10 Mpc h^{-1} in the direction of the filament (blue) and of the void (orange) and plotting the mean and standard deviation of δ given the saddle and the threshold. Fig. 15 was computed by following steps (i)–(iii) at the saddle point ($r = 0$). An extra constrain on the value of δ' was then added to compute the different curves.

APPENDIX C: OTHER CRITICAL POINTS

For the sake of generality, let us discuss here the conditional excursion set expectations in the vicinity of other critical points of the potential. At the technical level, all the formulae we derived in Section 4 depend on the eigenvalues of q_{ij} with no a priori assumption on their sign. The expressions will thus remain formally the same, with all information about the environment being channelled through the values of ν_S and $\hat{r}_i\bar{q}_{ij}\hat{r}_j$. For instance, the typical quantities $M_\star$, $\dot{M}_\star$, and $z_\star$ parametrizing the PDFs of interest will be defined in exactly the same way as in equations (80)–(82). However, their level curves will have different profiles in different environments.

As physical intuition suggests, and equation (47) explicitly shows, the dependence of the various halo statistics on the distance from the stationary point (whether the probability of a given halo property increases or decreases with separation) is encoded in the signs of the eigenvalues q_i of q_{ij}. Besides filaments (having two positive eigenvalues), one may thus be interested in wall-type saddles (one positive eigenvalue), maxima (all negative), and minima (all positive), corresponding to voids and nodes, respectively. In general, $q_1 + q_2 + q_3 = \nu_S$ parametrizes the mean variation with distance (averaged over the angles), whereas the traceless shear $\bar{q}_{ij}$ is responsible for the angular variation at fixed distance.

In all cases, however, for a given direction $M_\star$, $\dot{M}_\star$, and $-z_\star$ will either all increase (if $r_iq_{ij}r_j < 0$) or all decrease (if $r_iq_{ij}r_j > 0$).

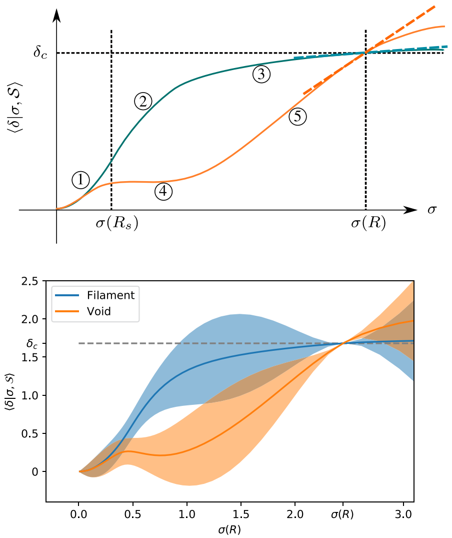

Figure B3. Top: scheme of the mean value of the density in the direction of a filament (red) and void (blue) close to a saddle point smoothed at $\sigma = \sigma_{\mathcal{S}}$ with the constrain that $\delta(\sigma(R)) = \delta_c$. (1) The value of the density imposed at the saddle point forces both mean densities to increase. (2) In the direction of the filament, a large-scale overdensity, the mean density at a given point increases quickly, but (3) the constrain $\delta(\sigma) = \delta_c$ prevents any further increase at $\sigma \lesssim \sigma(R)$, hence the slope δ' is small at upcrossing. (4) In the direction of the void, a large-scale underdensity, the mean density at a given point cannot increase with σ. (5) At $\sigma \lesssim \sigma(R)$, the upcrossing constrain forces a sharp increase of the density to reach $\delta(R) = \delta_c$, hence the slope is high at upcrossing. Bottom: a validation using constrained GRF at a distance of 10 Mpc h^{-1} in the direction of the filament (blue) and of the void (orange). See the text for the details.

Their increase will be fastest (or their decrease slowest) in the direction of $\bar{q}_3$, the least negative eigenvalue, and slowest in that of $\bar{q}_1$. The rationale of this behaviour will always be that an increase of the conditional mean density will make it easier for excursion set trajectories to reach the threshold. Upcrossing will happen preferentially at smaller σ, corresponding to the formation of haloes of bigger mass. At fixed mass (fixed crossing scale σ), the crossing will happen preferentially with shallower slopes, corresponding to higher accretion rates and more recent formation (i.e. assembly of half-mass).

C1 Walls

A wall will form in correspondence of a saddle point of the potential filtered on scale $R_{\mathcal{S}}$, for which $q_1 < q_2 < 0 < q_3$. This combination of eigenvalue signs generates collapse in one spatial direction and expansion in the other two. As argued, a saddle point of the potential induces a saddle point of the opposite type in $M_\star$, $\dot{M}_\star$, and $-z_\star$, which will increase along two space directions following the increase of the mean density, and decrease along one. Since for walls (like for filaments), the value of $\nu_{\mathcal{S}}$ is likely to be smaller than $\sqrt{\mathrm{tr}(\bar{q}^2)}$, they will tend to have an angular modulation larger

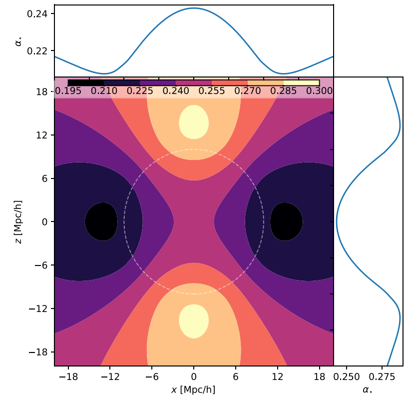

Figure C1. Isocontours in the x–z plane of the typical accretion rate $\alpha_\star$ around a wall-type saddle point [at (0, 0)]. The saddle point is defined using the values of Table D1. The profiles in the main direction of the wall (z-direction) and of the void (x-direction) are plotted on the sides. The smoothing scale is $R = 1$ Mpc h^{-1}. The typical accretion rate is computed using a ΛCDM power spectrum. Similarly to what happens in filaments, haloes accrete more in the direction of the wall than in the direction of the void.

than the radial angle-averaged variation. Walls are thus likely to be highly anisotropic configurations also of the accretion rate and of the formation time. This is illustrated for example in Fig. C1 for the accretion rate. On average, $\nu_{\mathcal{S}}$ will be smaller for a wall-type saddle (which has two negative eigenvalues) than for a filament-type one. Thus, haloes in walls tend to be less massive, and at fixed mass, they tend to have smaller accretion rates and earlier assembly times.

C2 Voids

A void will eventually form (although not necessarily by $z = 0$) when $\boldsymbol{r} = 0$ is a local maximum of the potential filtered on scale $R_{\mathcal{S}}$ (from which matter flows away), for which $q_1 < q_2 < q_3 < 0$. The centre of the void is a minimum of $M_\star$, $\dot{M}_\star$, and $-z_\star$. All these quantities will gradually increase with the separation. As $|\nu_{\mathcal{S}}|$ may be large (in particular for a large, early-forming void), halo statistics in voids may not show a large anisotropy relative to their radial variation. However, because voids have the most negative $\nu_{\mathcal{S}}$, they are the environment with the least massive haloes, the smallest accretion rates and the earliest formation times (at fixed mass).

C3 Nodes

Nodes form out of local minima of the gravitational potential, for which $0 < q_1 < q_2 < q_3$ (corresponding to three directions of infall). The centre of the node is thus a maximum of $M_\star$, $\dot{M}_\star$, and $-z_\star$, all of which decrease with radial separation. Like voids, large early-forming nodes (whose density $\nu_{\mathcal{S}}$ must reach ν_c when $\sigma_{\mathcal{S}}$ is very small) are relatively less anisotropic, since the relative amplitude of the angular variation induced by $\bar{q}_{ij}$ is likely to be small compared to the radial variation. Since $\nu_{\mathcal{S}}$ is the largest for nodes, they host the most massive haloes, and at fixed mass, those with the largest accretion rates and the latest formation times.

radius of the halo at $z = 2$.

Interestingly, I find that, even though most of the AM has been lost before entering the halo, the orientation of the AM of the hot gas is well-conserved between R_{vir} and $R_{\mathrm{vir}}/3$. This can be explained either by the fact that the spin of the halo, which has been reported to be well aligned with the first axis of the large scale tides (Danovich et al., 2012) do not reorient significantly the AM of hot gas, or that the infall of the hot gas coincides with the loss of most, but not all, of its angular momentum. In this scenario, the hot gas starts infalling at the sweet spot where most of the angular momentum has been lost, but before all of it has been removed.

As reported in (Rosdahl and Blaizot, 2012), the trajectory the cold gas is different and follows a mostly radial (with a non-null impact parameters) free-fall trajectory. In our simulation, the cold gas typically takes one (500 ± 350) Myr to go from $3R_{\mathrm{vir}}$ to $R_{\mathrm{vir}}/3$, so that the halo gravitational torques are not large enough to reduce the AM of the cold gas. As the cold gas plunge into the halo, the influence of the disk increases up to the point where torques become dominated by stars. I report here that most of the AM of the cold gas is lost at the same location as where the disk component become important. While the AM loss seem to be a combination of the torques of the inner halo and, to a smaller extent, the disk, most of the realignment of the gas before it actually settles in the disk is due to gravitational torques of the disk, reaching a similar conclusion as Danovich et al., 2015. Most of the AM of the cold gas, that was acquired at large scales and conserved down to the inner regions, is lost to the inner halo and the disk. One can then suggest that both the inner halo and the disk will then tend to be aligned to the mean orientation of the inflowing material in a similar way, resulting. This may explain why galactic spin is well aligned with the internal halo's, while being only mildly aligned with the global halo spin.

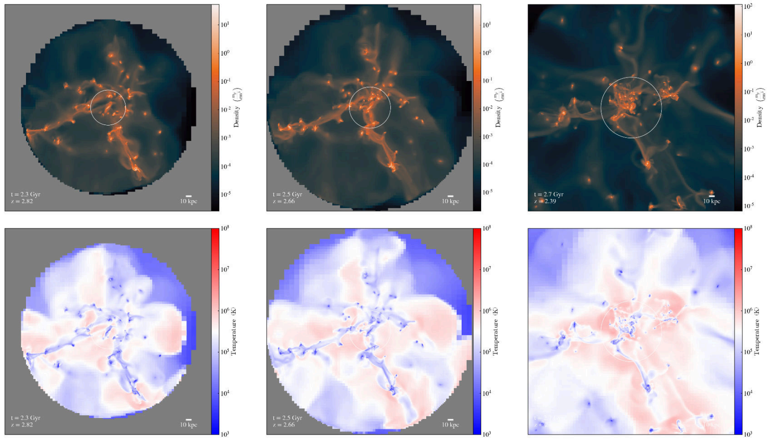

Figure 4.22: *Top:* Mass weighted density projections around $t = 2.5$ Gyr for halo D and *bottom:* mass weighted temperature projections. The central halo (with virial radius shown in white) has a lot of mergers that are able to disrupt the cold gas accretion.

work, I find that the pressure forces are dominant in the hot phase and are as important as the DM gravitational forces in the outer halo, in particular in the ortho-radial direction. In the inner halo, a transition occurs so that the dominant forces become star gravitational forces. I also report a significant "pressure ring" in the inner halo that may affect the kinematics of the infalling gas in which pressure forces dominate over all forces in both the cold- and hot-accreted gas. This pressure ring may have significant implications on the thermodynamical evolution of the gas, as well as to contribute to mixing the cold-accreted material to the hot gas, effectively blurring the line between hot- and cold-accreted material. The study of this pressure ring will be the topic of future work.

While pressure forces can act locally as the dominant forces, I report that their net contribution to the evolution of the cold gas is negligible. Indeed, pressure forces do not possess any structure over hundreds of parsecs, so that their individual contribution to the evolution of the cold gas cancel out. On the contrary, gravitational forces, that depend on the distribution of matter on larger scales, are able to coherently apply torques on the infalling material, resulting in most of the spin-down signal.

The net effect of the gravitational forces is reported to be a spin-down of the accreted gas, as a result of dynamical friction and gravitational torques. Most of the spin-down of the hot gas happens before entering the halo and is due to DM torques. One possible reason for this is the following: under the effect of gas infall, the DM halo become slightly polarised which in turn creates a tidal field that will torque the hot gas down. Using the ortho-radial gravitational forces reported in figure 4.10, the typical angular momentum of the gas upon its entry in the halo ($\sim 10^4\,\mathrm{km/s\,kpc}$) would be depleted in a time $t_{\mathrm{torque}}(R = 100\,\mathrm{kpc}) = |\boldsymbol{l}|/|\boldsymbol{\tau}| \approx 10^4\,\mathrm{km/s\,kpc}/10^{-1}\,\mathrm{km/s/Myr} \times 80\,\mathrm{kpc} \approx 1\,250\,\mathrm{Gyr}$, which is about twice the free-fall time of the halo $t_{\mathrm{ff}}(z = 2) = 500\,\mathrm{Myr}$ at $z = 2$. If the hot gas lingers in the outskirts of the outer halo during two free-fall times, the DM gravitational torques are large enough to get rid of most of the angular momentum before accretion. In our simulations, hot gas takes on average (10.0 ± 0.5) Gyr to fall from $3R_{\mathrm{vir}}(z = 2)$ to $R_{\mathrm{vir}}(z = 2)/3$ where $R_{\mathrm{vir}}(z = 2)$ is the final virial

APPENDIX D: PDF OF SADDLES

This section presents the distribution of the eigenvalues of the anisotropic (i.e traceless) part of the tidal tensor at critical points of the potential field. By definition, a critical point is such that $g_i = 0$ and its kind is given by the signature (the signs of the eigenvalues of the hessian of the potential, q_{ij}): $+++$ for a peak, $-++$ for a filament-type saddle point, $--+$ for a wall-type saddle point, and $---$ for a void. Because the anisotropic tidal tensor reads $\bar{q}_{ij} = q_{ij} - \delta_{ij}\nu_S/3$, the type of the critical point is then given by the number of eigenvalues of $\bar{q}_{ij}$ above $-\nu_S/3$.

The distribution of the eigenvalues of the (normalized) tidal tensor denoted $q_1 < q_2 < q_3$ is described by the Doroshkevich formula (Doroshkevich 1970; Pogosyan et al. 1998)

$$p(q_i) = \frac{675\sqrt{5}}{8\pi}\exp\left[\frac{15}{2}I_2 - 3I_1^2\right](q_3 - q_1)(q_3 - q_2)(q_2 - q_1), \tag{D1}$$

where $\{I_n\}$ denotes the rotational invariants which define the characteristic polynomial of q_{ij}, namely its trace $I_1 = q_1 + q_2 + q_3$, trace of the comatrix $I_2 = q_1q_2 + q_2q_3 + q_1q_3$, and determinant $I_3 = q_1q_2q_3$. Subject to a filament-type saddle-point constraint, this PDF becomes

$$p(q_i|-++) = \frac{540\sqrt{5\pi}}{29\sqrt{2} + 12\sqrt{3}} q_1q_2q_3\vartheta(q_2)\vartheta(-q_1)p(q_i), \tag{D2}$$

after imposing the condition of a saddle $|\det q_{ij}|\delta_D(g_i)\vartheta(q_2)\vartheta(-q_1)$ for which as the acceleration is decoupled from the tidal tensor, only the condition on the sign of the eigenvalues and the determinant contribute. From this PDF, it is straightforward to compute the distribution of saddles of heights $\nu_S = q_1 + q_2 + q_3$

$$p(\nu_S|-++) = p^+(\nu_S)\vartheta(\nu_S) + p^-(\nu_S)\vartheta(-\nu_S), \tag{D3}$$

with

$$p^+(\nu_S) = \frac{5\sqrt{10\pi}e^{-\frac{\nu_S^2}{2}}\left(3\nu_S - \nu_s^3\right)\mathrm{Erfc}\left(\frac{\sqrt{5}\nu_S}{2\sqrt{2}}\right) + e^{-\frac{9\nu_S^2}{8}}\left(32 + 155\nu_s^2\right)}{\left(29\sqrt{2} + 12\sqrt{3}\right)\sqrt{\pi}},$$

$$p^-(\nu_S) = \frac{5\sqrt{10\pi}e^{-\frac{\nu_S^2}{2}}\left(3\nu_S - \nu_s^3\right)\mathrm{Erfc}\left(\frac{-\sqrt{5}\nu_S}{\sqrt{2}}\right) + e^{-3\nu_s^2}\left(32 - 10\nu_S^2\right)}{(29\sqrt{2} + 12\sqrt{3})\sqrt{\pi}}.$$

In particular, the height of filament-type saddles has mean and standard deviation given by

$$\langle\nu_S|-++\rangle = 250\left(3(29\sqrt{2} + 12\sqrt{3})\sqrt{\pi}\right)^{-1} \approx 0.76,$$

$$\mathrm{Std}\,(\nu_S|-++) = \frac{\sqrt{696\sqrt{6} + 75\pi(10 - 3\sqrt{6}) - 2114}}{15\sqrt{\pi}} \approx 0.55.$$

For other types of critical points, a similar calculation can be done. As expected, the heights of wall-type saddle points follow the same distribution as $-\nu_S$. Peak and void heights have mean $\pm\sqrt{2114 + 696\sqrt{6}/15\sqrt{\pi}} \approx \pm 2.3$ and standard deviation $\sqrt{75\pi(10 + 3\sqrt{6}) - (2114 + 696\sqrt{6})/15\sqrt{\pi}} \approx 0.62$.

This work picks a typical value for the filament-type saddle at roughly 1σ from the mean $\nu_S = 1.2$. For wall-type saddles, $\nu_S = 0$ is chosen. The distribution of eigenvalues of the anisotropic tidal tensor $\bar{q}_i$ for a filament-type saddle point with a given positive[13] height can then be easily obtained from equation (D2)

$$p(\bar{q}_1|\nu_S) = \frac{15(3\bar{q}_1 + \nu_S)\left[a_1 e^{-\frac{4\nu_S^2}{3} + \frac{5}{2}\bar{q}_1\nu_S - \frac{15\bar{q}_1^2}{2}} - a_2 e^{-\frac{\nu_S^2}{2} - \frac{45\bar{q}_1^2}{8}}\right]}{16(29\sqrt{2} + 12\sqrt{3})\sqrt{\pi}\mathcal{P}^+(\nu_S)},$$

where $\bar{q}_1 < -\nu_S/3$ and a_1 and a_2 are two polynomials of $\bar{q}_1$ and ν_S given by

$$a_1(\bar{q}_1, \nu_S) = 32\left[5|\nu_S - 6\bar{q}_1|(3\bar{q}_1 + \nu_S) + 12\right],$$

and

$$a_2 = 6075\bar{q}_1^4 - 8100\bar{q}_1^3\nu_S + 900\bar{q}_1^2\left(3\nu_S^2 - 4\right) + 480\bar{q}_1\nu_S - 160\nu_S^2 + 384.$$

Similarly, the PDF of the intermediate and major eigenvalues are, respectively, given by

$$p(\bar{q}_2|\nu_S) = \frac{15(3\bar{q}_2 + \nu_S)a_1 e^{-\frac{11}{12}\nu_S^2 + \frac{5}{4}\bar{q}_2\nu_S - 15\bar{q}_2^2 - \frac{5}{12}(\nu_S + 3\bar{q}_2)|\nu_S - 6\bar{q}_2|}}{16(29\sqrt{2} + 12\sqrt{3})\sqrt{\pi}\mathcal{P}^+(\nu_S)}$$

where $\bar{q}_2 > -\nu_S/3$ and $a_1 = a_1(\bar{q}_2, \nu_S)$, and

$$p(\bar{q}_3|\nu_S) = \frac{15(3\bar{q}_3 + \nu_S)\left[a_1 e^{-\frac{\nu_S^2}{2} - \frac{45\bar{q}_3^2}{8}} + \bar{a}_1 e^{-\frac{4\nu_S^2}{3} + \frac{5}{2}\bar{q}_3\nu_S - \frac{15\bar{q}_3^2}{2}}\right]}{16(29\sqrt{2} + 12\sqrt{3})\sqrt{\pi}\mathcal{P}^+(\nu_S)}$$

where $\bar{q}_3 > \nu_S/6$, having defined $a_1 = a_1(\bar{q}_3, \nu_S)$ and $\bar{a}_1(\bar{q}_3, \nu_S) = -a_1(-\bar{q}_3, -\nu_S)$. Similar expressions can be obtained for wall-type saddles (together with peaks and voids). The top panel of Fig. D1 shows the distribution of eigenvalues for a filament-type saddle point of height $\nu_S = 1.2$ and the bottom panel shows the distribution for a wall-type saddle point of height $\nu_S = 0$. Typical values of $\bar{q}_{ij}$ were selected to correspond roughly to the maximum of the above-mentioned distributions of $\bar{q}_1, \bar{q}_2, \bar{q}_3$ and are reported in Table D1. Note that all the results obtained in this section are independent of the power spectrum. The only assumption is that the density is a GRF.

APPENDIX E: COVARIANCE MATRICES

Let us present here the covariance matrix of all variables introduced in the main text. The density δ and slope δ' are evaluated at position $\boldsymbol{r}$ and smoothed on the halo scale R, the half-mass density $\delta_{1/2}$ is also evaluated at the halo position $\boldsymbol{r}$ but smoothed on $R_{1/2} = 2^{-1/3}R$, while the saddle rareness ν_S, acceleration g_i, and detraced tidal tensor $\bar{q}_{ij}$ are evaluated at the origin and smoothed on a scale $R_S \gg R$. The correlation matrix of $\boldsymbol{X} \equiv \{\delta, \delta', \nu_{1/2}, \nu_S, g_i, \bar{q}_{ij}\}$, a vector with 12 Gaussian components, is

$$\boldsymbol{C} = \begin{pmatrix} \sigma^2 & \sigma & \omega & \boldsymbol{C}_{14} & \boldsymbol{C}_{15} & \boldsymbol{C}_{16} \\ \sigma & \langle\delta'^2\rangle & \omega' & \boldsymbol{C}_{24} & \boldsymbol{C}_{25} & \boldsymbol{C}_{26} \\ \omega & \omega' & \sigma_{1/2}^2 & \boldsymbol{C}_{34} & \boldsymbol{C}_{35} & \boldsymbol{C}_{36} \\ \boldsymbol{C}_{14} & \boldsymbol{C}_{24} & \boldsymbol{C}_{34} & 1 & 0 & 0 \\ \boldsymbol{C}_{15}^T & \boldsymbol{C}_{25}^T & \boldsymbol{C}_{35}^T & 0 & \boldsymbol{C}_{55} & 0 \\ \boldsymbol{C}_{16}^T & \boldsymbol{C}_{26}^T & \boldsymbol{C}_{36}^T & 0 & 0 & \boldsymbol{C}_{66} \end{pmatrix}, \tag{E1}$$

with $\omega = \langle\delta\nu_{1/2}\rangle$, $\omega' = \langle\delta'\nu_{1/2}\rangle$, and

$$\boldsymbol{C}_{14} = \langle\delta\nu_S\rangle = \xi_{00}, \quad \boldsymbol{C}_{15} = \langle\delta g_i\rangle = \frac{r_i}{R_\star}\xi_{11}, \tag{E2}$$

$$\boldsymbol{C}_{16} = \langle\delta\bar{q}_{ij}\rangle = \left(\frac{\delta_{ij}}{3} - \hat{r}_i\hat{r}_j\right)\xi_{20}, \tag{E3}$$

[13] A similar expression can be obtained for negative heights.

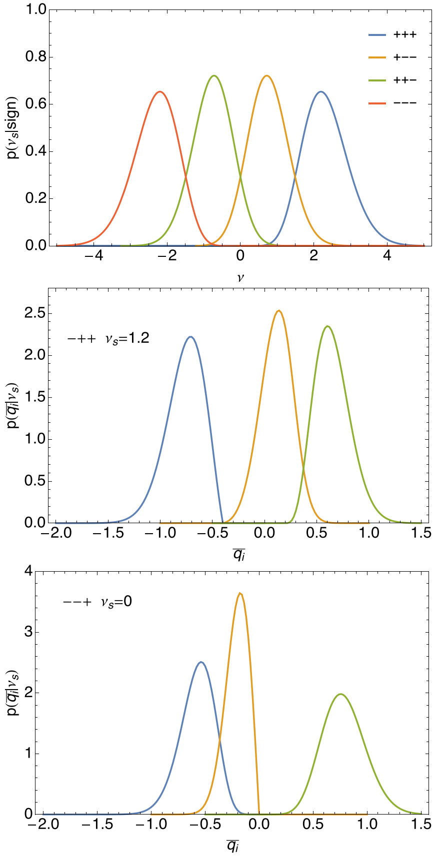

Figure D1. Top panel: distribution of heights of critical points of various signatures (peaks, filament-type saddles, wall-type saddles, and voids) for GRF with any power spectrum. Middle panel: PDF of the eigenvalues, $\bar{q}_1$ (blue), $\bar{q}_2$ (yellow), and $\bar{q}_3$ (green), of the anisotropic tidal tensor given a filament-type constraint at $\nu_{\mathcal{S}} = 1.2$. Bottom panel: same as middle panel for a wall-type constraint at $\nu_{\mathcal{S}} = 0$.

Table D1. Eigenvalues $\bar{q}_i = q_i - \nu_{\mathcal{S}}/3$ of the traceless tidal tensor $\bar{q}_{ij}$, height $\nu_{\mathcal{S}}$, and smoothing scale used to define the saddle points. See Appendix D for details.

	Traceless tide			Height	Scale	Saddle type
Quantity	$\bar{q}_1$	$\bar{q}_2$	$\bar{q}_3$	$\nu_{\mathcal{S}}$	$R_{\mathcal{S}}$	
Value	−0.7	0.1	0.6	1.2	10 Mpc h^{-1}	Filament-type
Value	−0.6	−0.2	0.8	0	10 Mpc h^{-1}	Wall-type

$$\boldsymbol{C}_{24} = \langle \delta' \nu_{\mathcal{S}} \rangle = \xi'_{00}, \quad \boldsymbol{C}_{25} = \langle \delta' g_i \rangle = \frac{r_i}{R_\star} \xi'_{11}, \tag{E4}$$

$$\boldsymbol{C}_{26} = \langle \delta' \bar{q}_{ij} \rangle = \left(\frac{\delta_{ij}}{3} - \hat{r}_i \hat{r}_j \right) \xi'_{20}, \tag{E5}$$

$$\boldsymbol{C}_{34} = \langle \nu_{1/2} \nu_{\mathcal{S}} \rangle = \frac{\xi_{00}^{(1/2)}}{\sigma_{1/2}}, \ \boldsymbol{C}_{35} = \langle \delta_{1/2} g_i \rangle = \frac{r_i}{R_\star} \frac{\xi_{11}^{(1/2)}}{\sigma_{1/2}}, \tag{E6}$$

$$\boldsymbol{C}_{36} = \langle \delta_{1/2} \bar{q}_{ij} \rangle = \left(\frac{\delta_{ij}}{3} - \hat{r}_i \hat{r}_j \right) \frac{\xi_{20}^{(1/2)}}{\sigma_{1/2}}, \tag{E7}$$

$$\boldsymbol{C}_{55} = \langle g_i g_j \rangle = \frac{\delta_{ij}}{3}, \quad \boldsymbol{C}_{66} = \langle \bar{q}_{ij} \bar{q}_{kl} \rangle = \frac{2 P_{ij,kl}}{15} \, . \tag{E8}$$

Hence, $\boldsymbol{C}_{14}$, $\boldsymbol{C}_{24}$, and $\boldsymbol{C}_{34}$ are scalars, $\boldsymbol{C}_{15}$, $\boldsymbol{C}_{25}$, and $\boldsymbol{C}_{35}$ are three vectors, $\boldsymbol{C}_{16}$, $\boldsymbol{C}_{26}$, and $\boldsymbol{C}_{36}$ are 3×3 traceless matrices (or five vectors in the space of symmetric traceless matrices), $\boldsymbol{C}_{55}$ is a 3×3 matrix, and $\boldsymbol{C}_{66}$ is a 5×5 matrix. The matrix $\boldsymbol{C}_{66}$ involves

$$P_{ij,kl} \equiv \frac{\delta_{ik}\delta_{jl} + \delta_{il}\delta_{jk}}{2} - \frac{\delta_{ij}\delta_{kl}}{3} \, , \tag{E9}$$

a projector that removes the trace and the antisymmetric part from a matrix. Since $P_{ij,\,ab} P_{ab,\,mn} = P_{ij,\,mn}$ and so $P^{-1}_{ij,mn} = P_{ij,mn}$, it acts as the identity in the space of symmetric traceless matrices. $P_{ij,\,kl}$ can be written in its matrix form by numbering the pairs {(1, 1), (2, 2), (1, 2), (1, 3), (2, 3)} from 1 to 5, the dimensionality of the space, resulting in a 5×5 matrix. The element (3, 3) has been dropped because it is linearly linked to (1, 1) and (2, 2). The explicit value of $\boldsymbol{C}_{66}$ is therefore

$$\boldsymbol{C}_{66} = \frac{1}{45} \begin{pmatrix} 4 & -2 & 0 & 0 & 0 \\ -2 & 4 & 0 & 0 & 0 \\ 0 & 0 & 3 & 0 & 0 \\ 0 & 0 & 0 & 3 & 0 \\ 0 & 0 & 0 & 0 & 3 \end{pmatrix}. \tag{E10}$$

The finite separation correlation functions $\xi_{\alpha\beta}(r, R, R_{\mathcal{S}})$ and $\xi'_{\alpha\beta}(r, R, R_{\mathcal{S}})$ are defined as

$$\xi_{\alpha\beta} \equiv \int \mathrm{d}k \frac{k^2 P(k)}{2\pi^2} W(kR) \frac{W(kR_{\mathcal{S}})}{\sigma_{\mathcal{S}}} \frac{j_\alpha(kr)}{(kr)^\beta}, \tag{E11}$$

$$\xi'_{\alpha\beta} \equiv \int \mathrm{d}k \frac{k^2 P(k)}{2\pi^2} W'(kR) \frac{W(kR_{\mathcal{S}})}{\sigma_{\mathcal{S}}} \frac{j_\alpha(kr)}{(kr)^\beta}, \tag{E12}$$

where $W'(kR) = [\mathrm{d}W(kR)/\mathrm{d}R]/(\mathrm{d}\sigma/\mathrm{d}R)$. Similarly, the correlation functions at the two different mass scales M and $M/2$ are

$$\xi_{\alpha\beta}^{(1/2)} \equiv \xi_{\alpha\beta}(r, R_{1/2}, R_{\mathcal{S}}) \, , \tag{E13}$$

where $R_{1/2} \equiv R/2^{1/3}$. At null separation ($r = 0$), it yields

$$\omega = \frac{\langle \delta\delta_{1/2} \rangle}{\sigma_{1/2}} = \int \mathrm{d}k \frac{k^2 P(k)}{2\pi^2} W(kR) \frac{W(kR_{1/2})}{\sigma_{1/2}} \, , \tag{E14}$$

$$\omega' = \frac{\langle \delta'\delta_{1/2} \rangle}{\sigma_{1/2}} = \int \mathrm{d}k \frac{k^2 P(k)}{2\pi^2} W'(kR) \frac{W(kR_{1/2})}{\sigma_{1/2}} \, . \tag{E15}$$

Recall that for a Top-Hat filter, one has

$$W(kR) = \frac{3 j_1(kR)}{kR} \quad \text{and} \quad W'(kR) = \frac{3 j_2(kR)}{R|\mathrm{d}\sigma/\mathrm{d}R|} \, , \tag{E16}$$

and notice that $W'(kR)$ is suppressed by a factor of k^2R^2 with respect to $W(kR)/\sigma$ when $k \ll 1/R$. In fact, in this limit $j_{\mathrm{n}}(kR) \sim (kR)^n/(2n+1)!!$. Hence, the action of $\mathrm{d}/\mathrm{d}\sigma$ is proportional to that of $R^2\nabla^2$, and $\sigma\xi'_{\alpha\beta} \propto R^2\nabla^2\xi_{\alpha\beta} \sim (R/R_{\mathcal{S}})^2\xi_{\alpha\beta}$. It follows that for $R \ll R_{\mathcal{S}}$ one has $\sigma\xi'_{\alpha\beta} \ll \xi_{\alpha\beta}$. In presence of a strong hierarchy of scales, the terms containing $\xi'_{\alpha\beta}$ are negligible (see Fig. E1).

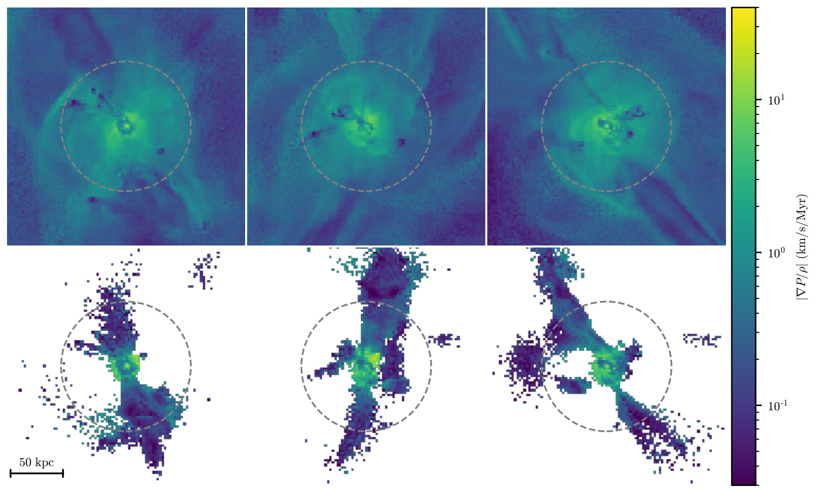

(a) Pressure gradients

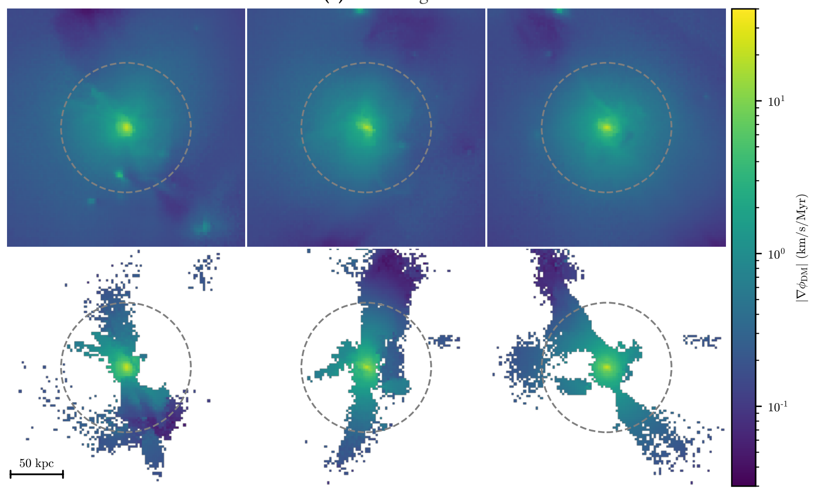

(b) DM gravitational forces

Figure 4.21: Projection of the pressure gradients (*top panel*) and of the DM gravitational force (*bottom panel*) for the hot gas (top rows) and the cold gas (bottom rows) in simulation A. From left to right in the xy, xz and yz plane. Pressure forces have a smaller magnitude in the cold gas than in the hot gas. DM gravitational forces have comparable magnitude in the cold and hot gas.

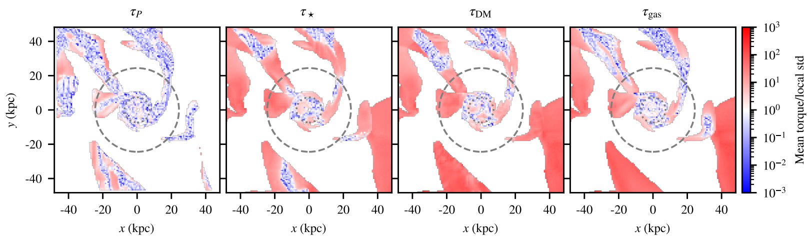

Figure 4.20: Mass-weighted projection of the ratio between the magnitude of the torques and the local standard deviation of the torques in halo A at $z = 2$ from left to right, for pressure torques, star gravitational torques, DM gravitational torques and gas torques. The local standard deviation is computed using the value of the torque in the 8 nearest cells. Blue regions indicate regions where torques are distributed randomly and red regions indicate where torques have a smooth and coherent distribution. The inner halo ($R_{\rm vir}/3$) is indicated by the gray dashed circle, while the dotted gray circle indicates $R_{\rm vir}/10$. In all regions, pressure torques have no spatial coherence on kpc scales. All gravitational sources have a much larger coherence scale, apart in a few regions in the filaments and in the disk.

Note that due to the the definition, ratios can exceed one[3]. The figure shows that after a settling time of about 1 Gyr ($z = 5.7$), the ratios of each torques are constant at all radii, with the DM gravitational forces dominating in the outer halo and star gravitational dominating around the disk. At early times, the potential of the halo is dominated by DM, so that torques are also dominated by the DM component. Interestingly, I report that pressure torques can sporadically contribute to the torque of the cold gas, in particular at late times. This is particularly the case in halo D, which at about 2.5 Gyr shows a spike in the importance of the pressure torques. This coincides with a number of merger events that are able to disrupt the cold gas structure, as illustrated on figure 4.22.

4.4 Discussion

At large radii, the evolution of the AM follows the tides imposed by the cosmic web, as explained by the TTT (e.g. Codis et al., 2012). The gas then flows on the forming galaxy *via* two different channels: the hot and cold accretion, in particular for massive enough galaxies at $z \gtrsim 2$ (Birnboim and Dekel, 2003; Dekel and Birnboim, 2006; Nelson et al., 2013; Pichon et al., 2011). The predominance of one or the other channel of accretion can be used to understand the formation of disky galaxies and the internal evolution of the galaxy. Indeed, in cold flows that result from cold accretion, the gas is able to penetrate deep in the halo and can feed the galaxy with fresh gas, with at steady AM orientation (Danovich et al., 2015). In numerical simulations, it has however been observed that cold gas has a higher AM at larger radii, as measured by their spin parameter (Danovich et al., 2015; Kimm et al., 2011; Tillson et al., 2015) which is up to one order of magnitude larger than that of the DM. In the inner halo and the disk however, the spin parameter of the cold-accreted gas is found to be only three times larger than that of the DM at the same location. The nature of the torques acting to reduce the AM of the gas is still debated today. While Danovich et al., 2015 argue that the dominant torques gravitational forces regardless of the distance to the galaxy, Prieto et al., 2017 instead found that the dominant torques were pressure torques. In this

[3] This can happen if two torques have similar magnitudes but opposite directions.

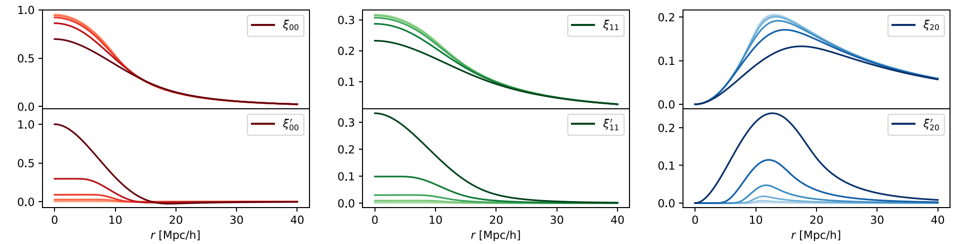

Figure E1. Plot as a function of r of the correlation functions defined in equation (E12). From left to right on the top row ξ_{00}, ξ_{11}, and ξ_{20}. The bottom row shows the same quantities derived with respect to σ. The correlation functions are evaluated at $R_{\mathcal{S}} = 10\,{\rm Mpc}\,h^{-1}$ for different values of R logarithmically spaced between 10^{-1} Mpc h^{-1} (light colour) and 10 Mpc h^{-1} (dark colours) with a ΛCDM power spectrum and plotted as a function of the distance r.

For a scale invariant power spectrum $P(k) = A(k/k_0)^{-n}$, $\xi_{\alpha\beta}$ and $\xi'_{\alpha\beta}$ have an analytical expression that depends on the relation between r, $R_{\mathcal{S}}$, and R. For example, when $R_{\mathcal{S}} > r + R$:

$$\frac{\xi_{\alpha\beta}(r, R, R_{\mathcal{S}})}{\sigma_{\mathcal{S}}} = BF_4\left(\frac{\alpha-\beta-n}{2}, \frac{3+\alpha-\beta-n}{2}; \frac{5}{2}, \alpha+\frac{3}{2}; \frac{R^2}{R_{\mathcal{S}}^2}, \frac{r^2}{R_{\mathcal{S}}^2}\right)$$

and

$$\xi'_{\alpha\beta}(r, R, R_{\mathcal{S}}) = \frac{2(\alpha-\beta-n+3)(n-\alpha+\beta)}{5(n-3)}\left(\frac{R}{R_{\mathcal{S}}}\right)^{\frac{7-n}{2}} B \times F_4\left(\frac{2+\alpha-\beta-n}{2}, \frac{5+\alpha-\beta-n}{2}; \frac{7}{2}, \alpha+\frac{3}{2}; \frac{R^2}{R_{\mathcal{S}}^2}, \frac{r^2}{R_{\mathcal{S}}^2}\right),$$

where F_4 is the Appell Hypergeometric function of the fourth kind (Gradshteyn & Ryzhik 2007, p. 677),[14] while

$$B = -\left(\frac{r}{R_{\mathcal{S}}}\right)^{\alpha-\beta} \times \frac{\pi(n+3)\csc\left(\frac{n\pi}{2}\right)\Gamma\left(\frac{3+\alpha-\beta-n}{2}\right)}{2^{\beta+2n+2}3(n-1)\Gamma\left(\frac{3+2\alpha}{2}\right)\Gamma(-n-1)\Gamma\left(\frac{n-\alpha+\beta+2}{2}\right)}$$

and

$$\sigma^2(R) = \sigma_8^2\left(\frac{R}{R_8}\right)^{n-3}, \quad \frac{{\rm d}\log\sigma^2}{{\rm d}\log R} = n-3, \tag{E17}$$

where $R_8 = 8$ Mpc h^{-1} and $\sigma_8 = \sigma(R_8)$ are normalization factors. For the same power-law power spectrum, setting $\alpha = 1 + n$ and $\beta = R_{1/2}/R = 2^{-1/3}$, ω and ω' defined in equations (E14) and (E15) have the analytical expressions

$$\frac{\omega}{\sigma} = \frac{(1+\beta)^\alpha\left(\beta^2-\alpha\beta+1\right) - (1-\beta)^\alpha\left(\beta^2+\alpha\beta+1\right)}{2^\alpha(2-\alpha)\beta^{\frac{\alpha+2}{2}}}, \tag{E18}$$

and

$$\omega' = \frac{\left(3\beta^3+\beta n^2+3\beta^2 n+n\right)(1-\beta)^n}{2^n\beta^{\frac{n+3}{2}}(n-3)(n-1)} + \frac{\left(3\beta^3+\beta n^2-3\beta^2 n-n\right)(1+\beta)^n}{2^n\beta^{\frac{n+3}{2}}(n-3)(n-1)}. \tag{E19}$$

[14] http://mathworld.wolfram.com/AppellHypergeometricFunction.html

APPENDIX F: CONDITIONAL STATISTICS

The goal of this section is to derive explicitly the conditional statistics needed in the paper. Assuming that the underlying density field obeys Gaussian statistics, the PDF of the 12-dimensional vector $\boldsymbol{X} \equiv \left\{\delta(\boldsymbol{r}), \delta'(\boldsymbol{r}), \nu_{1/2}(\boldsymbol{r}), \nu_{\mathcal{S}}, g_i, \bar{q}_{ij}\right\}$ already defined in Appendix E involves inverting the 12 × 12 covariance matrix $\boldsymbol{C} \equiv \langle \boldsymbol{X}\cdot\boldsymbol{X}^{\rm T}\rangle$, given by equation (E1). Since however the focus here is on conditioning heights and slopes, which are scalar quantities, their correlation with the saddle is the correlation with the three unit-variance Gaussian components

$$\mathcal{S}(\hat{\boldsymbol{r}}) \equiv \{\nu_{\mathcal{S}}, \sqrt{3}\hat{r}_i g_i r/R_\star, -\sqrt{5}(3\hat{r}_i\bar{q}_{ij}\hat{r}_j/2)\}. \tag{F1}$$

Hence, the six-dimensional vector $\tilde{\boldsymbol{X}} \equiv \{\delta(\boldsymbol{r}), \delta'(\boldsymbol{r}), \nu_{1/2}(\boldsymbol{r}), \mathcal{S}\}$ is sufficient, and has a 6×6 covariance matrix given by

$$\tilde{\boldsymbol{C}}(r) = \begin{pmatrix} \sigma^2 & \sigma & \omega & \xi(r) \\ \sigma & \langle\delta'^2\rangle & \omega' & \xi'(r) \\ \omega & \omega' & \sigma_{1/2}^2 & \xi_{1/2}(r) \\ \xi^T(r) & \xi'^T(r) & \xi_{1/2}^T(r) & \mathbb{1}_{3\times3} \end{pmatrix}, \tag{F2}$$

where

$$\xi(r) \equiv \left\{\xi_{00}, \sqrt{3}\xi_{11}r/R_\star, \sqrt{5}\xi_{20}\right\},$$
$$\xi'(r) \equiv \left\{\xi'_{00}, \sqrt{3}\xi'_{11}r/R_\star, \sqrt{5}\xi'_{20}\right\},$$
$$\xi_{1/2}(r) \equiv \left\{\xi_{00}^{(1/2)}, \sqrt{3}r/R_\star\xi_{10}^{(1/2)}, \sqrt{5}\xi_{20}^{(1/2)}\right\}/\sigma_{1/2}. \tag{F3}$$

The PDF of $\tilde{\boldsymbol{X}}$ is the six-variate Gaussian

$$p_{\rm G}(\tilde{\boldsymbol{X}}) = \frac{1}{(2\pi)^3\sqrt{\det\tilde{\boldsymbol{C}}}}\exp\left(-\frac{1}{2}\tilde{\boldsymbol{X}}\cdot\tilde{\boldsymbol{C}}^{-1}\cdot\tilde{\boldsymbol{X}}\right), \tag{F4}$$

so that in each case, the task is to invert the appropriate section of the covariance matrix $\tilde{\boldsymbol{C}} \equiv \langle\tilde{\boldsymbol{X}}\cdot\tilde{\boldsymbol{X}}^{\rm T}\rangle$, marginalizing over the variables that are not involved.

F1 The general conditional case

To speed up the computation of conditional statistics, rather than doing a brute force block inversion of $\tilde{\boldsymbol{C}}$, it is best to use the decorrelated variables

$$\nu_v \equiv \frac{\delta - \langle\delta|\{v\}\rangle}{\sqrt{{\rm Var}(\delta|\{v\})}}, \quad \text{and} \quad \nu'_v \equiv \frac{{\rm d}\nu_v}{{\rm d}\sigma}, \tag{F5}$$

where the possible $\{v\}$ considered in this work are $\nu_{1/2}$, $\mathcal{S}$ or $\{\nu_{1/2}, \mathcal{S}\}$. By construction, ν_v and ν'_v are uncorrelated, because ν_v has unit variance. Furthermore, if each ν_1 is independent of σ (as it will be the case in the following), ν_v' does not correlate with the constraint either, since $\langle \nu_v' \nu_I \rangle = \langle \nu_v \nu_I \rangle' = 0$. Then, being a linear combination of δ', ν, and $\{v\}$ that does not correlate with ν nor ν_I, ν_v' must be proportional to $\delta' - \langle \delta' | \nu, \{v\} \rangle$ (the only such linear combination by definition), and $\langle \nu_v'^2 \rangle$ to $\mathrm{Var}\left(\delta' | \nu, \{v\}\right)$. That is,

$$\langle \delta' | \nu, \{v\} \rangle = \delta' - \sqrt{\mathrm{Var}\left(\delta | \{v\}\right)}\, \nu_v' \,,$$
$$= \langle \delta' | \{v\} \rangle + \frac{[\mathrm{Var}\left(\delta | \{v\}\right)]'}{2\mathrm{Var}\left(\delta | \{v\}\right)} \left(\delta - \langle \delta | \{v\} \rangle\right), \quad \text{(F6)}$$

$$\mathrm{Var}\left(\delta' | \nu, \{v\}\right) = \mathrm{Var}\left(\delta | \{v\}\right) \langle \nu_v'^2 \rangle \,,$$
$$= \mathrm{Var}\left(\delta' | \{v\}\right) - \frac{[\mathrm{Var}\left(\delta | \{v\}\right)]'^2}{4\mathrm{Var}\left(\delta | \{v\}\right)}\,, \quad \text{(F7)}$$

providing the conditional statistics of δ' given ν and $\{v\}$ in terms of those of δ and δ' given $\{v\}$ alone. Since $[\mathrm{Var}\left(\delta | \{v\}\right)]' = 2\mathrm{Cov}\left(\delta, \delta' | \{v\}\right)$, these formulae reduce to the standard results for constrained Gaussian variables, but taking derivatives makes their calculation easier.

To compute ν_v and ν_v' explicitly, one needs to insert (using Einstein's convention on repeated indices)

$$\langle \delta | \{v\} \rangle = \psi_I C_{IJ}^{-1} v_J \,, \quad \text{(F8)}$$

$$\mathrm{Var}\left(\delta | \{v\}\right) = \sigma^2 - \psi_I C_{IJ}^{-1} \psi_J \,, \quad \text{(F9)}$$

in equation (F5), where $C_{IJ} \equiv \langle v_I v_J \rangle$ is the covariance matrix of the constraint, and $\psi_I \equiv \langle \delta v_I \rangle$ is the mixed covariance. The conditional statistics obtained from equations (F6) and (F7) are then

$$\langle \delta' | \nu, \{v\} \rangle = \psi_I' C_{IJ}^{-1} v_J + \frac{\sigma - \psi_I' C_{IJ}^{-1} \psi_J}{\sqrt{\sigma^2 - \psi_I C_{IJ}^{-1} \psi_J}} \nu_v, \quad \text{(F10)}$$

$$\mathrm{Var}\left(\delta' | \nu, \{v\}\right) = \langle \delta'^2 \rangle - \psi_I' C_{IJ}^{-1} \psi_J' - \frac{(\sigma - \psi_I' C_{IJ}^{-1} \psi_J)^2}{\sigma^2 - \psi_I C_{IJ}^{-1} \psi_J}, \quad \text{(F11)}$$

[where ν_v is given by equation (F5)] from which one can evaluate equations (15) and (16), after setting $\delta = \delta_c$. Since $\langle \delta' | \nu_c \rangle = \nu_c$ and $\mathrm{Var}\left(\delta' | \nu_c\right) = 1/\Gamma^2$, equation (11) is recovered in the unconstrained case. For later convenience, let us also note that the conditional probability of ν and ν' given the constraint $\{v\}$ is

$$p_G(\nu, \nu' | \{v\}) = \sigma \frac{p_G(\nu_v)\, p_G(\delta' - \langle \delta' | \nu_c, \{v\} \rangle)}{\sqrt{1 - \psi_I C_{IJ}^{-1} \psi_J / \sigma^2}}\,, \quad \text{(F12)}$$

since by construction ν_v and $\delta' - \langle \delta' | \nu_c, \{v\} \rangle \propto \nu_v'$ are independent.

F2 Conditioning to the saddle

Equation (F8) and its derivative guarantee that conditioning on the values of $\mathcal{S}$ (that is, fixing the geometry of the saddle) returns

$$\langle \delta | \mathcal{S} \rangle = \xi \cdot \mathcal{S} \,, \quad \mathrm{Var}\left(\delta | \mathcal{S}\right) = \sigma^2 - \xi^2 \,,$$
$$\langle \delta' | \mathcal{S} \rangle = \xi' \cdot \mathcal{S} \,, \quad \mathrm{Var}\left(\delta' | \mathcal{S}\right) = \langle \delta'^2 \rangle - \xi'^2 \,,$$
$$\langle \nu_{1/2} | \mathcal{S} \rangle = \xi_{1/2} \cdot \mathcal{S} \,, \quad \mathrm{Var}\left(\nu_{1/2} | \mathcal{S}\right) = 1 - \xi_{1/2}^2 . \quad \text{(F13)}$$

To make the equations less cluttered, here and in the following, scalar products of these vectors are denoted with a dot, rather than in *Einstein*'s notation. Equation (F13) effectively amounts to replacing in all unconditional expressions

$$\delta \to \delta - \xi \cdot \mathcal{S},$$
$$\delta' \to \delta' - \xi' \cdot \mathcal{S},$$
$$\nu_{1/2} \to \nu_{1/2} - \xi_{1/2} \cdot \mathcal{S}, \quad \text{(F14)}$$

reducing the problem to three zero-mean variables that no longer correlate with $\mathcal{S}$ (but still do with each other!). The covariance of δ, δ' and $\nu_{1/2}$ at fixed $\mathcal{S}$ reads

$$\mathrm{Cov}\left(\delta, \delta' | \mathcal{S}\right) = \sigma - \xi \cdot \xi',$$
$$\mathrm{Cov}\left(\delta, \nu_{1/2} | \mathcal{S}\right) = \omega - \xi \cdot \xi_{1/2},$$
$$\mathrm{Cov}\left(\delta', \nu_{1/2} | \mathcal{S}\right) = \omega' - \xi' \cdot \xi_{1/2}, \quad \text{(F15)}$$

with ω and its derivative ω' given by equations (E14) and (E15). The first equation in (F15) is one half the derivative of $\mathrm{Var}\left(\delta | \mathcal{S}\right)$ with respect to σ from equation (F13), consistently with taking the conditional expectation value of the relation $\delta\delta' = (1/2)\mathrm{d}\delta^2/\mathrm{d}\sigma$. The third is the derivative of the second, since $\xi_{1/2}$ depends on $\sigma_{1/2}$ and not on σ (the relation between the two scales arising since $\sigma_{1/2} = \sigma(M/2)$ should be imposed after taking the derivative).

F3 Slope given height at distance r from the saddle

The saddle point being fixed, it can now be assumed that the excursion set point is at the critical overdensity $\nu = \nu_c$. The conditional mean and variance of the slope are then

$$\langle \delta' | \nu_c, \mathcal{S} \rangle = \langle \delta' | \mathcal{S} \rangle + \frac{\mathrm{Cov}\left(\delta', \delta | \mathcal{S}\right)}{\mathrm{Var}\left(\delta | \mathcal{S}\right)} \left(\delta_c - \langle \delta | \mathcal{S} \rangle\right)$$
$$= \xi' \cdot \mathcal{S} + \frac{\sigma - \xi \cdot \xi'}{\sigma^2 - \xi^2} \left(\delta_c - \xi \cdot \mathcal{S}\right), \quad \text{(F16)}$$

after using equations (F13) and (F15), and

$$\mathrm{Var}\left(\delta' | \nu_c, \mathcal{S}\right) = \mathrm{Var}\left(\delta' | \mathcal{S}\right) - \frac{\mathrm{Cov}\left(\delta', \nu | \mathcal{S}\right)^2}{\mathrm{Var}\left(\nu | \mathcal{S}\right)},$$
$$= \langle \delta'^2 \rangle - \xi'^2 - \frac{(\sigma - \xi \cdot \xi')^2}{\sigma^2 - \xi^2}, \quad \text{(F17)}$$

respectively. This result is equivalent to decorrelating the effective variables $\delta - \xi \cdot \mathcal{S}$ and $\delta' - \xi' \cdot \mathcal{S}$ introduced in equation (F14), whose covariance is in fact $\sigma - \xi' \cdot \xi$.

Equation (F16) contains an angle-dependent offset $\hat{r}_i \bar{q}_{ij} \hat{r}_j \xi_{20}$ and a density dependent one $\xi_{00} \nu_{\mathcal{S}}$, entering through $\mathcal{S}$. On the contrary, the conditional variance does not depend on the angle nor the height of the saddle. At large distance from the saddle, when $\xi = \xi' = 0$, equations (F16) and (F17) tend as expected to the unconditional mean ν_c and variance $1/\Gamma^2 = \langle \delta'^2 \rangle - 1$.

From equations (F16) and (F17), one can compute the effective upcrossing parameters presented in the main text

$$\mu_{\mathcal{S}}(\boldsymbol{r}) = \xi' \cdot \mathcal{S} + \frac{\sigma - \xi' \cdot \xi}{\sigma^2 - \xi^2} (\delta_c - \xi \cdot \mathcal{S})\,, \quad \text{(F18)}$$

$$X_{\mathcal{S}}(\boldsymbol{r}) = \mu_{\mathrm{S}}(\boldsymbol{r}) / \sqrt{\mathrm{Var}\left(\delta' | \nu_c, \mathcal{S}\right)}\,. \quad \text{(F19)}$$

F4 Upcrossing at σ with given formation time but no saddle

Recalling that $\omega = \langle \delta\delta_{1/2} \rangle / \sigma_{1/2}$ and $\omega' = \langle \delta'\delta_{1/2} \rangle / \sigma_{1/2}$, as defined by equations (E14) and (E15), the conditional statistics of δ and δ' given that $\nu_{1/2} = \nu_f$ are

$$\langle \delta | \nu_f \rangle = \omega \nu_f \,, \quad \mathrm{Var}\left(\delta | \nu_f\right) = \sigma^2 - \omega^2 \,,$$
$$\langle \delta' | \nu_f \rangle = \omega' \nu_f \,, \quad \mathrm{Var}\left(\delta' | \nu_f\right) = \langle \delta'^2 \rangle - \omega'^2 \,,$$
$$\mathrm{Cov}\left(\delta, \delta' | \nu_f\right) = \sigma - \omega\omega' \,. \quad \text{(F20)}$$

Hence, the conditional mean and variance of δ' given $\nu_c = \delta_c / \sigma$ and ν_f are

$$\langle \delta' | \nu_c, \nu_f \rangle = \omega' \nu_f + \frac{\sigma - \omega'\omega}{\sigma^2 - \omega^2} \left(\delta_c - \omega \nu_f\right), \quad \text{(F21)}$$

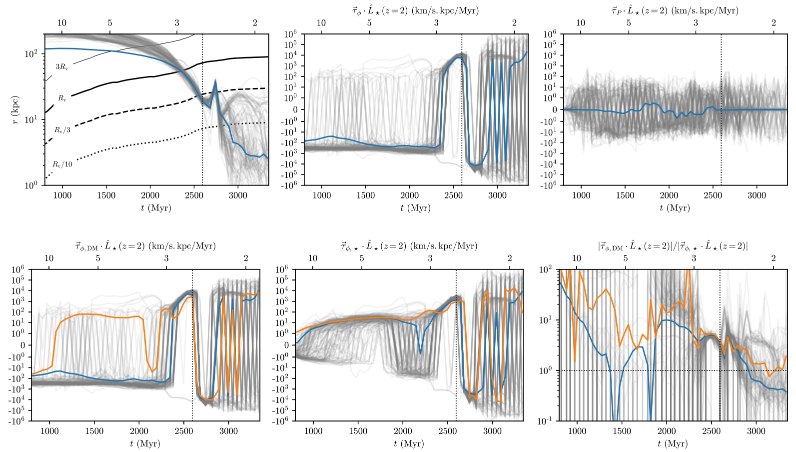

Figure 4.19: Same as figure 4.17 for halo C.

using the mean sAM of the gas or the individual value of the sAM of each tracer particle lead to similar results.

Figure 4.16 shows that, once averaged over the entire cold phase, pressure forces do not contribute significantly to the variation of the sAM of the gas. Indeed, I have seen on figure 4.20 that pressure forces are noise-dominated, with a signal-to-noise ratio of the order of 10^{-3}. While the magnitude of the pressure forces are comparable to the DM gravitational forces, their net contribution to the torque budget is shown to be at least three order of magnitude smaller. As gas falls towards the galaxy, gravitational forces exert increasing torques resulting in a spin-down of the gas. In the inner halo down, torques become weakly coupled with the mean sAM of the gas at R_{vir}, so that their projection can either contribute to the spin-up or spin-down in this specific frame. Similar results can be found if one project the torques on the axis of the AM vector of the galaxy at the end of the simulation, $L_\star(z = 2)$, as shown for halos A, B and C on figures 4.17 to 4.19. These plots also feature individual Lagrangian trajectories of the gas and illustrate the pressure torques spin the gas up as much as they spin it down. Instead, gravitational torques are coherent over the Lagrangian evolution of the gas, so that their contribution add up to spin the cold gas down. The bottom-right panels of figures 4.17 to 4.19 show the ratio of the DM gravitational torques to the star gravitational torques. Similarly to the results presented in figure 4.16, star gravitational torques are negligible in the outer halo but become dominant in the inner halo and in the disk.

The hierarchy between the different torques can, in principle evolve with redshift. In order to study their relative importance, I have computed the total pressure torques, DM gravitational torques and star torques and compared the magnitude of each torques to the total torques from all sources $\boldsymbol{\tau}_{\mathrm{all}} = \boldsymbol{\tau}_{\mathrm{P}} + \boldsymbol{\tau}_{\mathrm{DM}} + \boldsymbol{\tau}_\star$. The ratio r is then defined as

$$r_i = \frac{|\sum_{\mathrm{particles}} \boldsymbol{\tau}_i|}{|\sum_{\mathrm{particles}} \boldsymbol{\tau}_{\mathrm{all}}|}. \quad (4.11)$$

Here i can be any of P, DM, $\star$ and sums run over all cold gas particles. The results are presented on figure 4.12, where torque ratios are presented as a function of the radial distance to the galaxy.

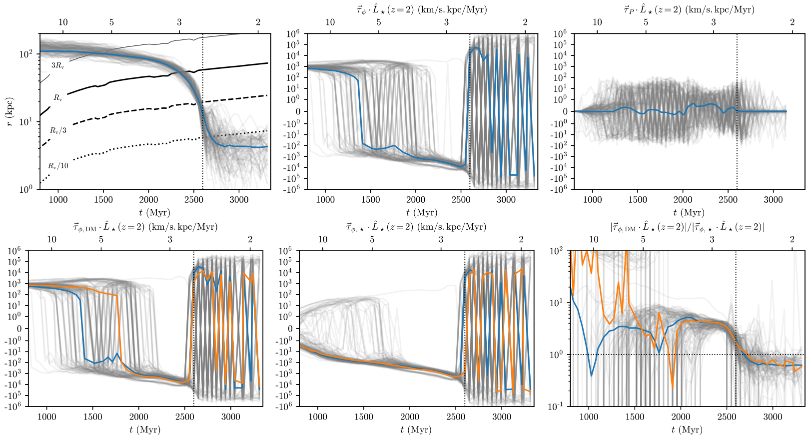

Figure 4.17: Trajectories (grey lines) of cold accreted gas particles with a first infall at $z = 2.5$ (vertical dotted line) in halo A. *Upper left:* The radial distance to the galaxy, *upper centre:* The total gravitational torque, *upper right:* the pressure torques, *bottom left:* the DM gravitational torques, *bottom centre:* the star gravitational torques and *bottom right:* the ratio of the DM to star gravitational torques. All the torques are projected onto the normalised AM vector of the galaxy $\hat{L}_\star$. Median (blue) and mean (orange) values are shown as a function of time. DM is responsible to sAM acquisition at large radii. Stars and DM are responsible for the decrease of sAM at $\sim 2R_{\rm vir} > r > R_{\rm vir}/3$. In the inner halo, torques become dominated by stars.

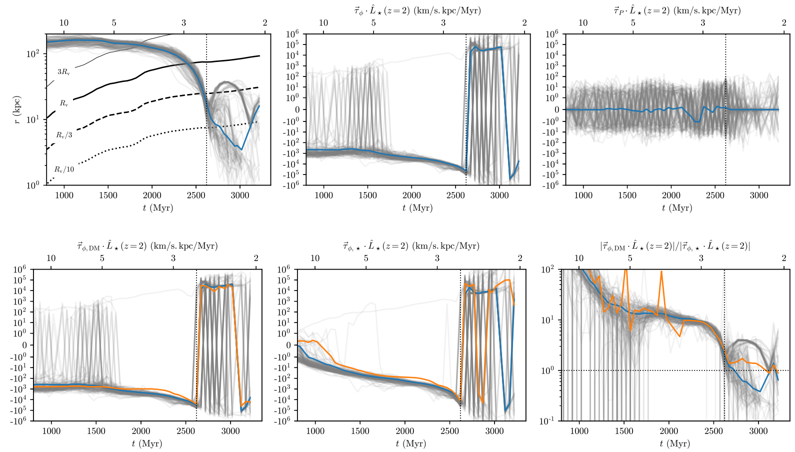

Figure 4.18: Same as figure 4.17 for halo B.

$$\mathrm{Var}\left(\delta'|\nu_{\rm c},\nu_{\rm f}\right) = \langle\delta'^2\rangle - \omega'^2 - \frac{(\sigma-\omega'\omega)^2}{\sigma^2-\omega^2}\,. \tag{F22}$$

which is equivalent to decorrelating the zero-mean effective variables $\delta - \omega\nu_{\rm f}$ and $\delta' - \omega'\nu_{\rm f}$, whose covariance is $\sigma - \omega'\omega$. From equations (F21) and (F22), one can compute the parameters of the effective upcrossing problem

$$\mu_{\rm f}(D_{\rm f}) = \langle\delta'|\nu_{\rm c},\nu_{\rm f}\rangle\,, \tag{F23}$$

$$X_{\rm f}(D_{\rm f}) = \mu_{\rm f}(D_{\rm f})/\sqrt{\mathrm{Var}\left(\delta'|\nu_{\rm c},\nu_{\rm f}\right)}\,, \tag{F24}$$

introduced in Section 2.2.

F5 Upcrossing at σ given formation time and the saddle

Similarly, thanks to equations (F13) and (F15), the mean and covariance of $p_{\rm G}(\nu|\nu_{\rm f},\mathcal{S})$ are

$$\langle\delta|\nu_{\rm f},\mathcal{S}\rangle = \langle\delta|\mathcal{S}\rangle + \frac{\mathrm{Cov}\left(\delta,\nu_{1/2}|\mathcal{S}\right)}{\mathrm{Var}\left(\nu_{1/2}|\mathcal{S}\right)}\left(\nu_{\rm f} - \langle\nu_{1/2}|\mathcal{S}\rangle\right)\,,$$
$$= \xi\cdot\mathcal{S} + \Omega\,\nu_{{\rm f},\mathcal{S}}\,, \tag{F25}$$

$$\mathrm{Var}\left(\delta|\nu_{\rm c},\mathcal{S}\right) = \mathrm{Var}\left(\delta|\mathcal{S}\right) - \frac{\mathrm{Cov}\left(\delta,\nu_{1/2}|\mathcal{S}\right)^2}{\mathrm{Var}\left(\nu_{1/2}|\mathcal{S}\right)}\,,$$
$$= \sigma^2 - \xi^2 - \Omega^2\,, \tag{F26}$$

where [recalling that ξ has the dimensions of δ but $\xi_{1/2}$ has those of ν, see equation (F3)]

$$\nu_{{\rm f},\mathcal{S}} \equiv \frac{(\nu_{\rm f} - \xi_{1/2}\cdot\mathcal{S})}{\sqrt{1-\xi_{1/2}^2}}\,,\quad \Omega \equiv \frac{\omega - \xi\cdot\xi_{1/2}}{\sqrt{1-\xi_{1/2}^2}}\,. \tag{F27}$$

As discussed in Appendix F1, the statistics of $p_{\rm G}(\delta'|\nu_{\rm c},\nu_{\rm f},\mathcal{S})$ can be derived from those of $p_{\rm G}(\delta|\nu_{\rm f},\mathcal{S})$ as follows:

$$\langle\delta'|\nu_{\rm c},\nu_{\rm f},\mathcal{S}\rangle = \langle\delta|\nu_{\rm f},\mathcal{S}\rangle' + \frac{\mathrm{Var}\left(\delta|\nu_{\rm f},\mathcal{S}\right)'}{2\mathrm{Var}\left(\delta|\nu_{\rm f},\mathcal{S}\right)}\left(\delta_{\rm c} - \langle\delta|\nu_{\rm f},\mathcal{S}\rangle\right) \tag{F28}$$

thanks to the relations $\langle\delta|\nu_{\rm f},\mathcal{S}\rangle' = \langle\delta'|\nu_{\rm f},\mathcal{S}\rangle$ and $\mathrm{Var}\left(\delta|\nu_{\rm f},\mathcal{S}\right)' = 2\mathrm{Cov}\left(\delta\delta'|\nu_{\rm f},\mathcal{S}\right)$, and

$$\mathrm{Var}\left(\delta'|\nu_{\rm c},\nu_{\rm f},\mathcal{S}\right) = \mathrm{Var}\left(\delta'|\nu_{\rm f},\mathcal{S}\right) - \frac{[\mathrm{Var}\left(\delta|\nu_{\rm f},\mathcal{S}\right)']^2}{4\mathrm{Var}\left(\delta|\nu_{\rm f},\mathcal{S}\right)}\,. \tag{F29}$$

Hence, taking derivatives of equations (F25) and (F26) give

$$\langle\delta'|\nu_{\rm c},\nu_{\rm f},\mathcal{S}\rangle = \xi'\cdot\mathcal{S} + \Omega'\nu_{{\rm f},\mathcal{S}}$$
$$+ \frac{\sigma - \xi'\cdot\xi - \Omega'\Omega}{\sigma^2 - \xi^2 - \Omega^2}\left(\delta_{\rm c} - \xi\cdot\mathcal{S} - \Omega\,\nu_{{\rm f},\mathcal{S}}\right)\,, \tag{F30}$$

and

$$\mathrm{Var}\left(\delta'|\nu_{\rm c},\nu_{\rm f},\mathcal{S}\right) = \langle\delta'^2\rangle - \xi'^2 - \Omega'^2$$
$$-\frac{(\sigma - \xi'\cdot\xi - \Omega'\Omega)^2}{\sigma^2 - \xi^2 - \Omega^2}\,, \tag{F31}$$

where

$$\Omega' = \frac{\omega' - \xi'\cdot\xi_{1/2}}{\sqrt{1-\xi_{1/2}^2}}\,, \tag{F32}$$

which can finally be used to compute the effective slope parameters

$$\mu_{{\rm f},\mathcal{S}}(D_{\rm f},\boldsymbol{r}) = \langle\delta'|\nu_{\rm c},\nu_{\rm f},\mathcal{S}\rangle\,, \tag{F33}$$

$$X_{{\rm f},\mathcal{S}}(D_{\rm f},\boldsymbol{r}) = \mu_{{\rm f},\mathcal{S}}(D_{\rm f},\boldsymbol{r})/\sqrt{\mathrm{Var}\left(\delta'|\nu_{\rm c},\nu_{\rm f},\mathcal{S}\right)}\,. \tag{F34}$$

APPENDIX G: GENERIC AND MOVING BARRIER

The results presented hereby hold for a constant barrier, however, one can easily recover the results for a non-constant one – where the upcrossing conditions becomes $\delta_{\rm c} > \delta_{\rm c}'$ – by replacing μ_ν by $\mu_\upsilon - \delta_{\rm c}'$ in the general formula of equations (15) and (16), yielding

$$\mu_\upsilon \equiv \langle\delta'|\nu_{\rm c},\{\upsilon\}\rangle - \delta_{\rm c}'\,, \tag{G1}$$

and by taking into account contributions from $\delta_{\rm c}'$ in $\nu_{\rm c}'$

$$\nu_{\rm c}' = \frac{\delta_{\rm c}'}{\sigma} - \frac{\delta_{\rm c}}{\sigma^2}\,, \tag{G2}$$

and in the definition of accretion rate

$$\alpha = \frac{\delta_{\rm c}}{\sigma(\delta' - \delta_{\rm c}')} \tag{G3}$$

in equation (19). In practical terms, dealing with a moving barrier simply amounts to replacing

$$\mu \to \langle\delta'|\nu_{\rm c}\rangle - \delta_{\rm c}'\,, \tag{G4}$$

$$\mu_{\rm f} \to \langle\delta'|\nu_{\rm c},\nu_{\rm f}\rangle - \delta_{\rm c}'\,, \tag{G5}$$

$$\mu_{\mathcal{S}} \to \langle\delta'|\nu_{\rm c},\mathcal{S}\rangle - \delta_{\rm c}'\,, \tag{G6}$$

$$\mu_{{\rm f},\mathcal{S}} \to \langle\delta'|\nu_{\rm c},\nu_{\rm f},\mathcal{S}\rangle - \delta_{\rm c}'\,, \tag{G7}$$

in equations (12), (33), (50), and (67), which automatically affects also the corresponding X, $X_{\rm f}$, $X_{\mathcal{S}}$, and $X_{{\rm f},\mathcal{S}}$, as well as Y_α and $Y_{\alpha,\mathcal{S}}$ in equations (24) and (60).

For instance, for a barrier of the type $\delta_{\rm c} + \beta\sigma\bar{q}_{ij,R}\bar{q}_{ij,R}$ (Castorina et al. 2016), where $\bar{q}_{ij,R}$ is the traceless tidal tensor smoothed on scale R, and β is some constant, one would use

$$\delta_{\rm c}' \to \beta(\bar{q}_{ij,R}\bar{q}_{ij,R} + 2\sigma\bar{q}_{ij,R}'\bar{q}_{ij,R})\,. \tag{G8}$$

More generally, barriers should involve $\{I_{\rm n}\}$, the rotationally invariants of $\bar{q}_{ij,R}$ defined in Appendix D.

APPENDIX H: IMPLIED GALACTIC COLOURS

Let us in closing attempt to convert the position-dependent accretion rates, computed in the main text, in terms of colour modulo some reasonable assumption on the respective role of AGN and how star formation proceeds at low and high redshifts. Galaxy colours are proportional to the amount of recent star formation, which in turn is driven by the recently accreted gas from cosmic infall. One complication comes from the impact of feedback on heating the gas to be accreted on to galaxies. Cosmological hydrodynamical simulations, which include the feedback of supermassive black holes, suggest that, at intermediate and low redshift, mass accretion through mergers triggers AGN feedback in massive galaxies. This in turn heats up the circumgalactic medium and prevents subsequent smooth gas accretion from feeding central galaxies efficiently (e.g. Dubois et al. 2010), quenching star formation and reddening massive galaxies (hosted in haloes with mass of $10^{12}\,{\rm M}_\odot\,h^{-1}$ or more). Conversely, at higher redshift, cold flows are less impacted by galactic feedback and reach the centre of dark haloes unimpaired, so that matter infall translates into bluer galaxies (though it has been suggested that in massive haloes, the disruption of cold flows can be significant, Dubois et al. 2013). Fig. H1 sketches these ideas, while distinguishing low- and high-mass haloes. As argued in the main text, this

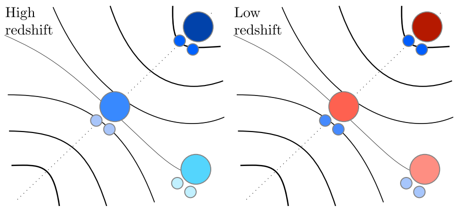

Figure H1. Scheme of the intensity of expected colour/SFR at different location near a filament-type saddle for different final halo mass. The displayed colour encodes galactic colour (or equivalently sSFR from high blue to low red). Massive galaxies in the filament (respectively, nodes) are expected to accrete more cold baryonic matter at high redshift and be bluer than less massive ones and than their counterparts in voids (respectively, filaments). At lower redshifts, AGN feedback is expected to quench cold gas accretion, thus reddening the massive ones – they are more likely to be central ones. The impact on lower mass satellite galaxies may also depend on the efficiency of processes such as starvation or ram-pressure stripping.

scenario remains speculative, if only because the impact of AGN feedback is still a fairly debated topic. For instance ram-pressure stripping on satellites plunging into clusters is known to induce reddening, but its efficiency within filaments is unclear. Fig. 16 encodes the robust result of the present investigation.

This paper has been typeset from a TEX/LATEX file prepared by the author.

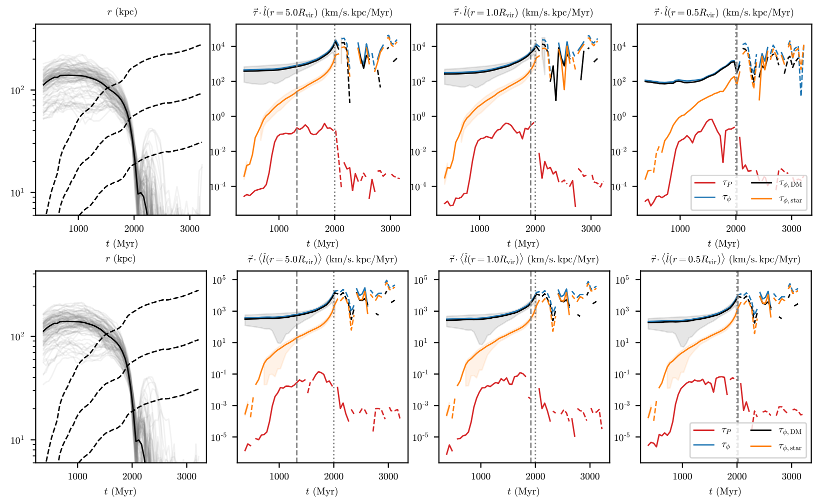

Figure 4.16: Evolution of the radius (*left panel*) and the specific torques projected (*top:*) onto the direction of the sAM of the gas at $r = 5R_{\rm vir}$, $r = R_{\rm vir}$ and $r = R_{\rm vir}/2$ and (*bottom:*) on the mean direction of the sAM at the same radii. Solid lines indicate negative values (spin down) and dashed lines positive values (spin up). Particle are selected to cross $R_{\rm vir}/3$ at $t = 2\,{\rm Gyr}$ ($z = 3.2$) (vertical dotted lines). The mean time at which the sAM is measured is shown as vertical dashed lines. In all regions, pressure torques are negligible

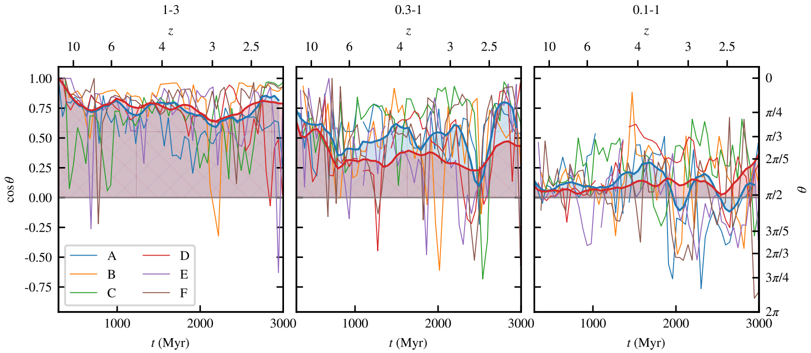

Figure 4.15: *Left:* Relative orientation of the sAM of the cold gas at $R_{\rm vir}$ compared to its value at $3R_{\rm vir}$ (*left*), $R_{\rm vir}/3$ (*middle*) and $R_{\rm vir}/10$ (*right*) for each halo (thin lines). The blue thick line shows the median value for the cold gas, smoothed over 11 consecutive outputs (550 Myr) using a fourth-order Savgol filter and the red thick line shows the median value for the hot gas smoothed in a similar way. In all simulations, the orientation of the sAM of the cold gas is conserved down to $\sim R_{\rm vir}/3$. Upon the entry in the disk, the sAM is reoriented and loses its connection to the large scale. The sAM of the hot gas start decoupling at larger radii.

scales similar or smaller than the size of filamentary structures, so that the net contribution of the pressure torque on a slab of filament cancels out. Gravitational torques have a net (positive or negative) contribution thanks to their large-scale coherence, so that their effect adds up. More quantitatively, the coherence of the torques can be estimated by comparing the local torque value to the local torque standard deviation. This is similar to computing the "signal to noise" ratio, where the signal is the torque magnitude and the noise is its local deviation. Large values of this quantity are found in regions where torque have a coherent structures while small values are found in regions with no structure. In figure 4.20, I present mass-weighted projections of the signal to noise ratio, where the local standard deviation is computed using the 3^3 nearest cells in the cold gas. This illustrates that pressure torques have no spatial coherence, so that they may spin the gas up and then immediately down at the next timestep. On the contrary, large patches of the cold flows undergo coherent gravitational torques that can add up. Interestingly, gas gravitational torques seem to have more fluctuations than other gravitational torques, so that their net effect is small, even though they may contribute to the local force budget in the inner halo. In the disk, all torque sources lose their long-range spatial coherence and appear noisy. This ratio for pressure torques is of the order of 10^{-3}, so that it is expected that the net contribution of pressure torques can be decreased by three order of magnitudes compared to their mean magnitude.

In order to go one step further, let us study the evolution of the cold gas by computing the contributions of the different torques to the spin-up or spin-down of the gas, projected on the axis of the mean sAM at a given radius. This is done on figure 4.16, which presents the Lagrangian evolution of the projection of the torques on the sAM at $5R_{\rm vir}$ (left panel), $R_{\rm vir}$ (center panel) and $R_{\rm vir}/2$ (right panel) for halo A. In this plot, the cold gas has been selected to cross $r = R_{\rm vir}/3$ at $t = 2\,\rm Gyr$ ($z = 3.2$). The results presented are not sensible to the radius at which the sAM has been measured. Indeed, in figure 4.15 I have shown that the sAM of the cold gas is well-aligned between large scales and the inner halo, so that the orientation is conserved. I also report that

3.3 A theory of merger events in the large scale structures

[♠ citer confluence + rossi+?] The value of science lays in its predictive power. Hence, in the context of structure formation, a central question that theoretical cosmology must address is the following: to what extent can today's properties of galaxies be predicted from the initial Gaussian random field from which they emerge? More specifically, can we identify special sets of points via a multi-scale analysis of the initial conditions as a mean of predicting their fate and compressing the relevant information content of the initial field?

Within the paradigm of the spherical collapse, one can draw a relationship between the time of collapse of a given over density and the scale at which its initial patch must be smoothed so as to pass a given threshold. In this sense, the fate of a given region is encoded in its initial condition and is captured by the multi-scale properties of the corresponding Gaussian random field (Bond et al., 1996). The topology of this field at a given smoothing scale is encoded in the position and height of its critical points. The drift of these critical points with smoothing define the so-called skeleton tree (Hanami, 2001) which captures the variation of this topology with scale, hence time. One can identify special scales at which two such points coalesce, which via the aforementioned duality corresponds to special events. It is the sequence and geometry of these special events which will shape the fate of its host galaxy. In Hanami, 2001; Manrique and Salvador-Sole, 1995 the focus was on the coalescence of filament saddles with maxima which the author identified as slopping saddles (as they are vanishing saddle points on the slope of peaks), which are proxy for merging events. More generally here we will consider the coalescence of minima with wall-saddles and wall-saddles with filament-saddles corresponding respectively to the disappearance of a tunnel and a void. Indeed these coalescence impact the geometry of cosmic web (in particular the filaments) which in turn define preferred directions along which galaxies are fed cold gas and acquire their spin. Merger events are also known to play an important role in triggering AGN feedback, which in turn impacts gas inflow and therefore galactic morphology. Hence we will extend Hanami, 2001 by studying the clustering of these other critical events in the multi-scale landscape.

In recent years the concept of persistence has played a central role in identifying special pairing between critical points (Sousbie et al., 2011b). Here the focus is on singular points in 4D smoothing-position space, which occur at the scale where these critically paired points merge, i.e. when the persistence level tends to zero as a function of smoothing. Using the duality between scale and cosmic time provided by the spherical collapse model, these can be matched to special structurally important times which modify the topology of the density field. For instance, when two halos merge, the topology of the excursion set of the density field is changed, because it decrements the number of components above a given threshold. Mapping the geometry of the Gaussian random field to the knowledge of these singular events only is a very efficient and useful compression of the information encoded in the field. It is efficient because it maps a 3D space into a finite set of points in 4D. It is useful because astronomers know how to characterise the corresponding point process in terms of the properties of the underlying initial Gaussian field. Since these points bear significance in terms of galaxy formation we can therefore relate this process to the underlying power spectrum. Our motivations are many-fold:

i) Study the generalised history of accretion: what kind of mergers happens when, and where?
ii) Quantify the conditional rate of filament and wall disappearance in conjunction to that of an existing larger scale peaks,
iii) connect multiscale landscape of initial conditions to the morphology of a given galaxy. Identify the distribution of critical events within its past lightcone. Study how the anisotropic large scales modes bias its assembly history;
iv) Understand the origin of void disappearance and its usefulness as a cosmic probe.

In order to achieve these goals, we will re-derive the condition for a critical event in an

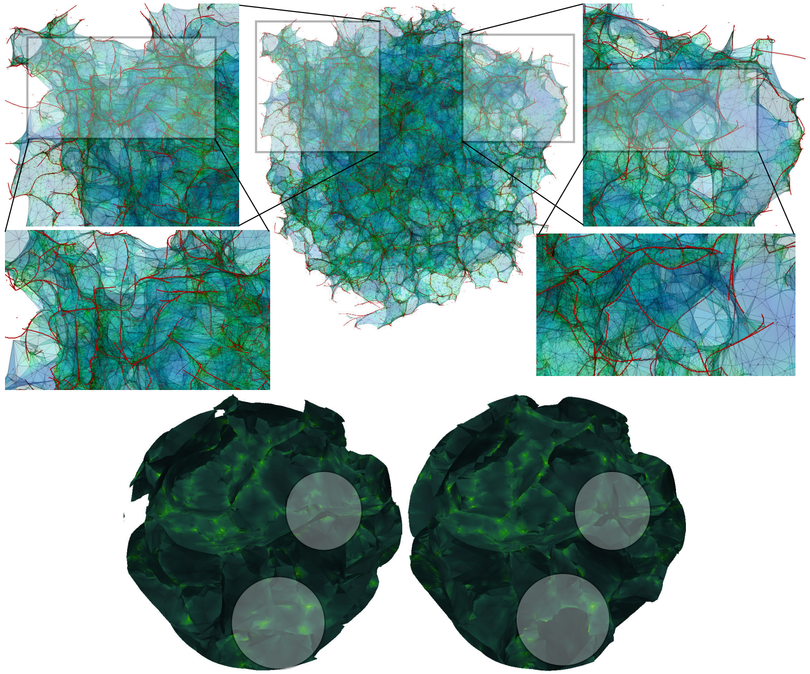

Figure 3.1: *Top:* Snapshot and zooms of a hydrodynamical simulation showing filaments (in red) walls (in shades of blue to green) and peaks (at the node of the filament network) as traced by DISPERSE. The cosmic evolution of these large scale structure features impacts the geometry of infall, the size of voids. As this simulation forms galaxies their properties reflect partially the corresponding tides and the funnelling of cold gas along the filamentary structure. Understanding when and how the topology of this network changes is therefore of interest in this context. *Bottom:* The walls w1 and w2 within the centre of the simulation identified in two consecutive snapshots. The colour coding scales with the log density of dark matter on the walls. Note the change in topology in the set of walls, highlighted in particular by the four spheres.

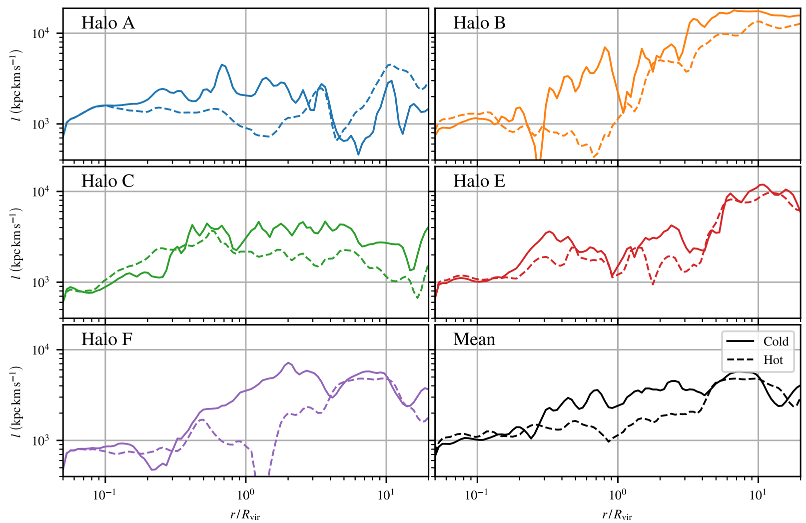

Figure 4.14: Evolution of the magnitudes of the mean sAM of the cold gas (solid lines) and of the hot gas (dashed lines) as a function of the distance to the halo center for all halos. *Bottom right:* Mean value of the sAM averaged over all halos. The gas has been selected to cross the virial radius inward for the first time at $t = 2.2\,\mathrm{Gyr}$ ($z = 2.9$). In the outskirts of the halos ($r \sim 3R_{\rm vir}$), hot gas starts loosing sAM while cold gas conserves it down to the inner halo ($r \sim R_{\rm vir}/3$).

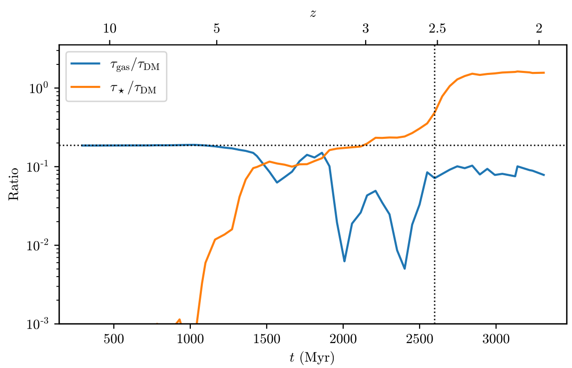

Figure 4.13: Evolution of the ratio of the gas gravitational torques to the DM gravitational torques (blue) and of the ratio of the star gravitational torques to the DM gravitational torques (orange) for gas crossing a $R_{\rm vir}/3$ at $z = 2.5$ in halo A. The ratio $\Omega_{\rm b}/\Omega_{\rm DM}$ (horizontal dotted line) corresponds to the initial gas-to-DM density ratio. Star torques become important in the inner halo $r \lessapprox R_{\rm vir}/3$ (vertical dotted line).

results, together figure 4.10, suggest that the spin-down of the gas happens due to the interaction with the inner DM halo and the stellar disk.

4.3.4 The orientation of the angular momentum

So far, I have only described the evolution of the magnitude of the sAM of the gas. In practice, the evolution of the orientation of the sAM evolves slightly differently. In order to quantify the evolution of the sAM orientation, a relevant quantity is the relative angle between the sAM at radius R_1, R_2, defined as

$$\cos\theta = \frac{\boldsymbol{l}(R_1)\cdot\boldsymbol{l}(R_2)}{\|\boldsymbol{l}(R_1)\|\|\boldsymbol{l}(R_2)\|}. \tag{4.10}$$

If the sAM orientation is conserved, equation (4.10) should have values close to one, whereas random reorientations yield values close to zeros. Values close to -1 are found in anti-aligned cases. The evolution of $\cos\theta$ is shown on figure 4.15, which presents the relative alignment of the sAM between its value at $R_{\rm vir}$ and its past value at $3R_{\rm vir}$ (left panel) and its value at the interface between the outer and inner halo ($0.3R_{\rm vir}$, center panel) and between the inner halo and the disk ($0.1R_{\rm vir}$, right panel). The alignment angle is computed at crossing time ($r = R_{\rm vir}$) for all six halos. The sAM of the cold gas stays mostly aligned from $3R_{\rm vir}$ to $0.3R_{\rm vir}$ with typical misalignments of the order of $\pi/3$ ($\sim 60°$) or less. At its entry in the disk, most of the original orientation has been lost. I however report a weak yet non-null alignment. Before entering the halo, the evolution of the hot gas is similar to the cold gas: the orientation is conserved from $3R_{\rm vir}$ to $R_{\rm vir}$ but it becomes significantly less aligned between $R_{\rm vir}$ and $R_{\rm vir}/3$, where the misalignment is typically of the order of $2\pi/5$ ($\sim 70°$). I do not report any significant evolution of the sAM orientation with redshift.

4.3.5 Dominant torques in the cold and hot phase

Figure 4.9 shows a 3D representation of the sAM, pressure torques and gravitational torques acting on the cold gas of halo A at $z = 3$. The figure illustrates that both sAM and gravitational torques have a coherent long-range spatial structure. On the contrary, pressure torques vary on

arbitrary frame, and quantify its one- and two-point statistics in 2 and 3 dimensions (main text) and higher dimensions (Appendix). We will proceed as follows.
Section 3.4 forecasts special events through the coalescence of critical points in the multi-scale landscape. Section 3.5 predicts the clustering properties of these special events. Section 3.6 compares the predictions to realisations of Gaussian random fields. Section 3.7 discusses possible applications. Finally section 3.8 wraps up. Section 3.A presents the joint PDF of a Gaussian random field up to the third derivative of the field. Section 3.B presents the counts in arbitrary dimensions and illustrates them in up to 6D. Section 3.C explains how the critical events are measured in random field maps and cubes. Section 3.C.3 presents an algorithm to generate gaussian random fields satisfying a set of given "event" at some scale and position.

3.4 Theory: one point statistics

In this work we consider the overdensity field $\delta = (\rho - \bar\rho)/\bar\rho$ to be a homogeneous and isotropic Gaussian random field of zero mean, described by its power spectrum $P(k)$, as defined in section 2.1.1.3. In this section, we will focus on one point statistics associated with merger rates. In section 3.4.1 we define and derive the number counts of critical events in smoothing-position space. Then section 3.4.2 presents the number counts of critical events, counted together and by type (peak, filament and wall mergers), while section 3.4.3 presents the differential event type as a function of event height. section 3.4.4 sketches the corresponding theory for projected maps, while section 3.4.5 presents its extension to non-Gaussian fields.

3.4.1 Critical events definition

When studying the time evolution of the density field, the spherical collapse model has shown that one can establish a mapping between collapse time and overdensity – high overdensity regions collapse earlier in the history of the Universe than underdense ones. At the same time, larger overdensities enclose more mass and will hence give birth to more massive structures. These relations mathematically read

$$\delta(R) = \frac{\delta_{\rm c}}{\sigma(R)D(z)}, \quad M = \frac{4\pi}{3}\bar\rho R^3, \tag{3.1}$$

where R is the smoothing scale of the Top-Hat filter, $\delta_{\rm c} = 1.69$ is the spherical collapse critical overdensity (see section 2.1.2.2), $D(z)$ is the linear matter growth function at redshift z (see section 2.1.2.1) and $\bar\rho$ is the mean matter density of the Universe. The spherical collapse threshold can also be adapted to study the formation of voids (Jennings et al., 2013; R. K. Sheth and van de Weygaert, 2004) with $\delta_{\rm v} = -2.7$. From a theoretical perspective, the action of smoothing the density field δ enables to probe the time-evolution of spherical proto-halos by following the density evolution of peaks as smoothing scale increases. In order to match the results of equation (3.1) with a Gaussian filter, as is the case in the following of this work, one need to establish a mapping of the smoothing scales between Top-Hat filtering and Gaussian filtering. This is usually achieved by matching the variance of the field $\sigma_{\rm G}(R/\alpha) = \sigma_{\rm TH}(R)$. At scales of a few Mpc/h, the scale ratio is of the order of $\alpha \approx 2.1$ for a ΛCDM power spectrum (see section 2.1.6.2) so that equation (3.1) becomes

$$M = \frac{4\pi}{3\alpha^3}\bar\rho R^3. \tag{3.2}$$

Let us now define critical events associated to mergers. These events are defined in smoothing-position space and correspond to mergers of critical *points* (peaks, saddle points and minima). The slopping saddle defined in Hanami, 2001 are particular critical events that correspond to mergers between a peak and a saddle point. In this chapter, we will instead focus on all critical events as they are of interest to study the evolution of the geometry of the cosmic web. The formation and location of critical events is illustrated for a 1D field on figure 3.2: critical events are found at the tip of critical point lines and represent the disappearance of a critical point into another critical point of another kind (e.g. a maximum and a minimum in 1D, a maximum and a saddle point in 2 or 3D). They encode locations where the topology of the field is changed by removing a pair of critical points.

Let us emphasize here that critical points are a compact encoding of the proto-structures: each proto-filament has at its center a filament-type saddle-point, while proto-walls have at their center a wall-type saddle-point. Using an analogy with a mountainous landscape, one can describe a given mountain range by giving the set of its peaks and passes. In practice, we have compressed the continuous information about the height of the mountains into a discrete set of critical points. A similar approach can be used to describe the skeleton of the cosmic web as a set of its critical events.

The concept of critical events can be presented using the same analogy. Let us illustrate the concept of critical events using an analogy with a mountainous landscape, the latter being restricted to 2D space, see figures 3.3 and 3.4. A mountainous landscape is made of peaks analogous to proto-halos. Each pair of neighbour peaks is linked via a pass, analogous to a proto-filamentary structure. Following the ridge from one peak to another one is analogous to following a filamentary structure between two proto-halos. On each downhill side of a pass there are two valleys whose faces are analogous to proto-walls in the cosmic web while their depth (hence their geometry) is described by their lowest point. With the action of time, the mountains will erode until eventually no peak will subsist – this is analogous to the smoothing operation. In the process, a disappearing peak will see its height (the density) decrease with time. If the peak is not prominent enough, it will eventually be smoothed to the point where it no longer is a peak but a shoulder on another peak's slope. Just before the peak disappears, it is still linked to its neighbour via a pass. When the peak disappears so does the pass – indeed a pass is always located between *two* peaks ; when one disappears, so does the pass. This particular event is what we define as a critical *event*. It encodes the moment when two critical points (here a peak and a saddle point) annihilate. This can also be interpreted as the moment a peak disappears on the slope of its nearest neighbour – the two peaks merged and the most prominent subsisted. Critical events have hence a dual interpretation: in the initial Lagrangian space, critical points are found at the location where a critical event merges into another critical event of another kind (e.g. a peak with a filament saddle-point). In the Eulerian physical space, critical points spot the merger of two similar structures, for example two halos merging into a single one (squashing the filament in between them).

Since the primordial density field is a 3D field, the density landscape is made of peaks (proto-halos), saddle-points (proto-filaments and proto-walls) and minima (proto-voids). Critical events record the merger of peaks into proto-filaments (PF critical events), of proto-filaments into proto-walls (FW critical events) and of proto-walls into proto-voids (WV critical events).

Using the duality discussed above, they also encode halo mergers (PF critical events), filament mergers (FW critical events) and wall mergers (WV critical events). This is illustrated on figure 3.5. PF critical events (top panel) encode the merger of two halos separated by a filament. After the merger, the most prominent peak subsists, while the other proto-halo and the proto-filament have annihilated. FW critical events (center panel) encode the merger of two filaments separated by a wall. After the merger, the most prominent filament subsists, while the other proto-filament and the proto-wall have annihilated. WV critical events (bottom panel) encode the merger of two walls separated by a void. After the merger, the most prominent wall subsists, while the other proto-wall and the proto-void have annihilated.

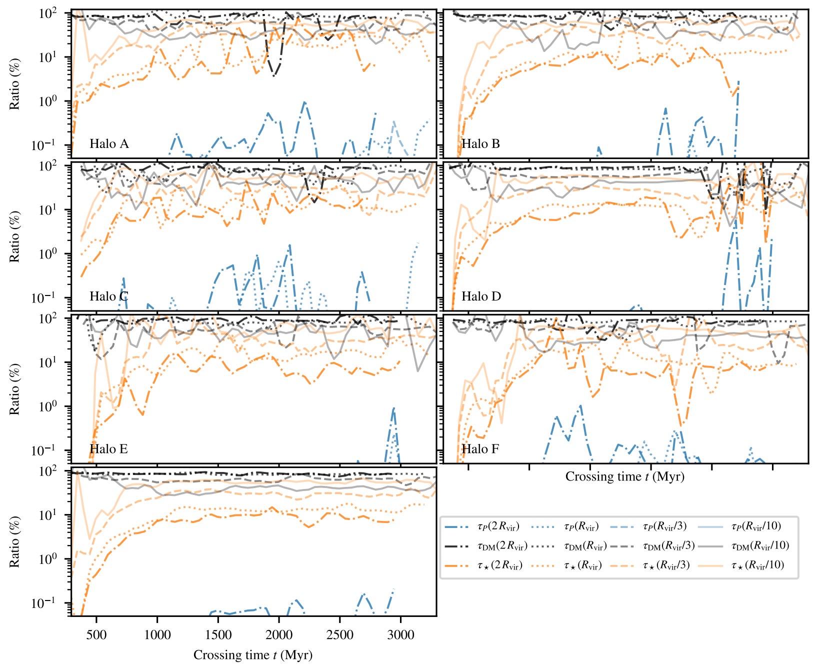

Figure 4.12: Absolute value of the torque ratios r_i measured in the cold gas (see text for details) as a function of time in different halos for different radial distance, as labelled. *Bottom left:* Mean value of the torque ratios, averaged over all six halos. After 1 Gyr, there is no average evolution of the torque ratios at any radius.

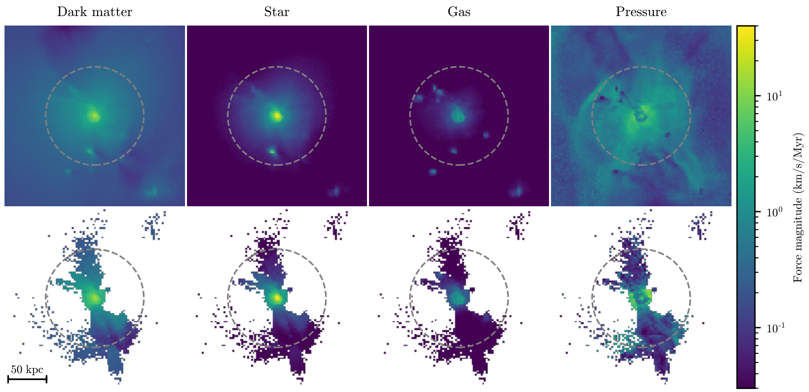

Figure 4.10: From left to right, mass-weighted projection of the magnitude of the DM gravitational forces, star gravitational forces, gas gravitational forces and gas pressure gradients, *top panel:* for all the gas but the cold one and *bottom panel:* only the cold gas in halo A at $z = 2.7$. In the hot phase outside the halo, gas pressure and DM gravitational forces have similar magnitudes. In the inner halo star and DM gravitational forces have a magnitude comparable to pressure forces. In the cold phase, the pressure forces are significantly weaker. The gas gravitational forces are negligible everywhere in both the cold and hot phases.

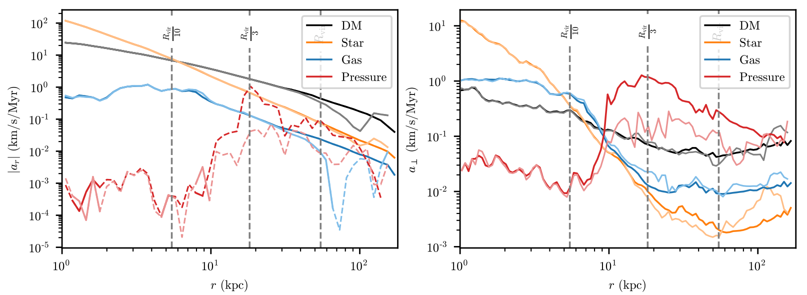

Figure 4.11: *Left:* Radial profile of the radial component and *right:* of the ortho-radial component of the different forces around halo A at $z = 2.7$: DM gravitational forces (black), star gravitational forces (orange), gas gravitational forces (blue) and pressure forces (red). Inward radial accelerations are shown as solid lines and outward accelerations are shown as dashed lines. Dark lines show the profiles for the hot gas and light lines for the cold gas. The virial radius $R_{\rm vir}$, $R_{\rm vir}/3$ and $R_{\rm vir}/10$ are shown as vertical dashed gray lines. Gravitational forces have a similar action on cold gas. The ortho-radial component of pressure forces is significantly smaller in the cold gas outside the inner halo.

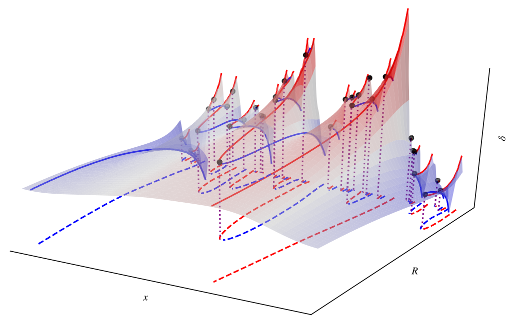

Figure 3.2: 2D "landscape" of a 1D field smoothed at a scale R in smoothing-position space. Here R is the smoothing scale, while δ is the density smoothed at the given scale. Solid lines indicate maxima (red) and minima (blue). Critical point lines end at critical events (black dots). The projections of the critical point lines are shown as red and blue dashed lines, while vertical dotted purple lines indicate the projection of critical events to illustrate that critical events are found at the location where two critical points merge.

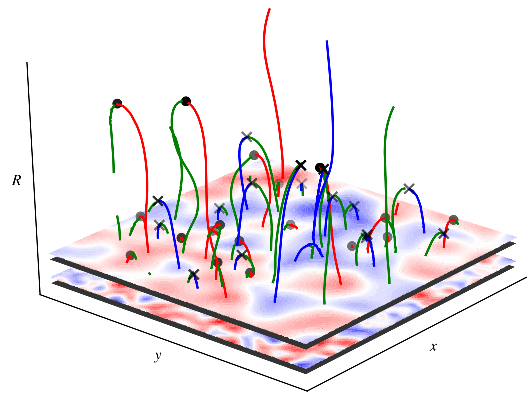

Figure 3.3: 3D "landscape" of a 2D field smoothed at a scale R in smoothing-position space. The density field (blue to red map) is smoothed at increasing R. For each scale, the critical points (red lines: peaks, green lines: saddle points, blue lines: minima) are found. At the tip of each branch a critical event is found (●: peak-saddle critical events, ×: saddle-minima). Lines near the boundaries have been hidden for the sake of clarity.

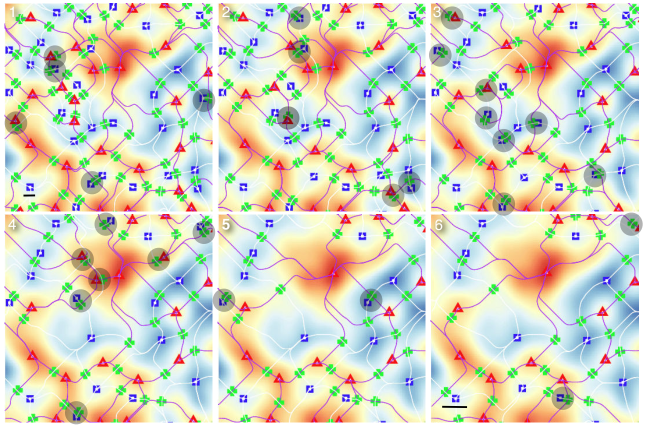

Figure 3.4: From left to right and top to bottom, a smoothing sequence of a Gaussian random field, whose density is colour coded from blue to red as a function of height (analogous to the slices shown on figure 3.3). The skeleton tracing the ridges is shown in purple, while the anti-skeleton tracing the trough is shown in white. The saddles shown as green crosses lay at the intersection. The Maxima are shown as red triangles while the minima as blue squares. As one smooths the field, these critical points drift towards each other along the skeletons, until they vanish in pairs. The upcoming coalescence are identified with gray circles. Note that as saddle points vanish, the two corresponding skeletons do too. Note also that the direction of coalescence is typically set by the skeleton's just before coalescence. In this two dimensional example, the ratio of peak+saddle to void+saddle event is one. The black segment in the bottom left of the first and last image represents the amount of smoothing. This work is concerned with studying the one and two point statistics of these gray circles. Note that these events are indeed proxy for mergers of the peaks of the underlying field: for instance, between snapshot 3 and 5 the central four peaks have merged into one. Similarly, between 1 and 4 the central four voids have merged into one. We provides an interactive tool to follow such events in 2D and 3D.

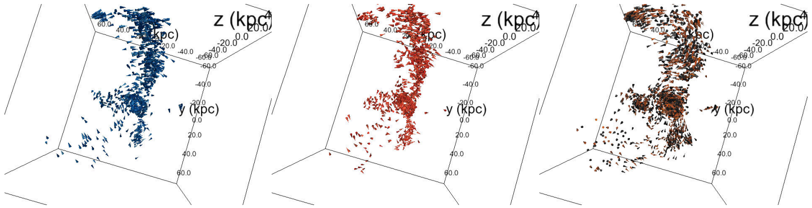

Figure 4.9: 3D representation of the sAM (left panel), pressure torques (central panel) and DM gravitational torques (right panel, black) and star gravitational torques (right panel, yellow) of the cold gas being accreted onto the central galaxy of halo A at $z = 2.7$. An interactive version can be found online. Pressure torques applied to the cold gas are mostly directed radially with respect to the filamentary structure, so that their net impact averages to zero. Gravitational torques are spatially coherent and contribute to a non-null net torque on the cold gas.

acceleration is due to both the DM and the pressure forces. The ortho-radial acceleration stays pressure-dominated in the hot phase up to a few Virial radii. Interestingly, both components of the gravitational forces have similar magnitudes in the cold and hot phase. I also notice that in the outer halo, the magnitude of both components of the pressure forces are comparable, indicating that pressure forces do not have a preferred direction. Pressure forces form a "pressure-ring" in the inner halo, as shown clearly in figure 4.10, right panel.

4.3.3 The magnitude of the angular momentum

Before turn-around, gas acquires AM *via* torque with the cosmic web as explained by the TTT (Catelan and Theuns, 1996; Hoyle, 1949; Peebles, 1969; S. D. M. White, 1984). At these scales, the torque magnitudes are proportional to the mean density of the gas and DM component. Indeed, when the gas is far from the halo, the density ratio sourcing the gravitational torques is given $\Omega_\mathrm{b}/\Omega_\mathrm{DM} \approx 0.19$. As a consequence, a similar ratio is expected on the torque ratio, as shown on figure 4.13. The figure presents the evolution of the torque for cold gas falling in halo A at $z = 2.5$.

The sAM of the hot and cold gas follows a different path. In order to study how the sAM evolves, one can study the Lagrangian evolution the sAM of all the gas accreted at the same time as a function of its radius, as shown on figure 4.14. The figure presents the Lagrangian evolution of the sAM as a function of radius for the cold (solid lines) and hot gas (dashed lines). In all halos, the sAM of the cold gas is conserved down to smaller radii, typically $r \sim R_\mathrm{vir}/3$ than in the hot gas.

For the hot gas, the virial shock is able to efficiently mix the pristine, freshly-accreted high-sAM gas with the gas already in the halo. In the process, most of the AM is either radiated away as thermal energy or transferred to the hot halo. This picture is consistent with the results of section 4.3.2 and figure 4.10, where I showed that the dominant forces in the outer halo and up to the outskirts of the halo in the hot gas are pressure forces.

The fate of cold gas is significantly different. On average in all our halos, the cold gas has a sAM ~ 3 times larger than the warm gas throughout its accretion in the outer halo down to the inner halo. The cold gas is mostly in free-fall (Rosdahl and Blaizot, 2012) up to the inner halo, where the cold gas shocks and the sAM quickly drops down to values comparable to the hot gas. While significant deviations are found from halo to halo, see the different panels of figure 4.14, the mean Lagrangian history of the sAM is clearly different between the cold and the warm gas. Our

4.3 Results

In the following of this chapter, I will adopt the same naming conventions as Danovich et al., 2015. I will write $R_{\mathrm{vir}}$the virial radius of a halo. The outer halo is defined as the region between $R_{\mathrm{vir}}$and $R_{\mathrm{vir}}/3$. The inner halo is defined as the region between $R_{\mathrm{vir}}/3$ and $R_{\mathrm{vir}}/10$. The "disk" is the region at radius $r < R_{\mathrm{vir}}/10$ where the galaxy is found.

4.3.1 Specific angular momentum vs. angular momentum per unit volume

?? differs from Eq. 9 of Danovich et al., 2015. Indeed, **??** is an equation on the *sAM* instead of the AM per unit volume. The rate of change of AM per volume includes a dependence to the cell volume, which is itself highly sensible to the compression and decompression of the gas. This is particularly important in astrophysical flows that are highly compressible. Contrary to what Danovich et al., 2015 reported, I find that the divergence term dominates over the gravitational and pressure terms. Inflowing gas typically moves at $100\,\mathrm{km/s}$ with typical variation scales of a few kpc. An order of magnitude of the divergence is then $\approx 100\,\mathrm{km\,s^{-1}}/1\,\mathrm{kpc} \approx 100\,\mathrm{Gyr^{-1}}$, with larger values found in shocked and highly compressed regions. These values are comparable or larger than pressure and gravitational torques, highlighting their importance in the study of the evolution of the AM per unit volume.

In the following of the dissertation, I will use the sAM, its evolution being described by **??**. I will hence *not* consider the divergence term in our study, as it does not enter the equation of evolution of the sAM. In addition to neglecting this term, following the Lagrangian evolution of the sAM has the advantage of interfacing naturally with tracer particles. Indeed, Lagrangian tracer particles have a fixed mass, so that their sAM is linked to their AM via a constant factor (their mass).

4.3.2 Dominant forces in the cold and hot phase

The different accretion mode for the cold and the hot phase of the gas leads to a spatial segregation of the cold phase into thin collimated filamentary structures, as shown on figure 4.2. In addition, their thermodynamical properties differ: the cold phase is made of a quite homogenous gas, so that the internal pressure gradients are weak. As a result, strong pressure gradients are found at their interface, as shown by Danovich et al., 2015. On the contrary the hot gas is less homogenous, so that pressure forces may be locally dominant. **[♡ reorder figures]** Figure 4.10 presents projected maps of the magnitude of the gravitational forces and pressure forces around one halo at $z = 2.7$ for the hot gas (top panel) and the cold gas (bottom panel), while figures 4.21a and 4.21b presents similar maps in the three directions (x, y and z). In the hot gas, the two dominant forces are qualitatively DM gravitational forces and pressure forces, with star gravitational forces being important only in the inner halo. In the cold phase, pressure forces are significantly smaller, while gravitational forces are mostly unimpaired. In the inner halo, a notable "pressure-ring" is clearly visible in the cold gas, as shown in the bottom right panel of figure 4.10.

In order to better disentangle the different contributions to the dynamical evolution of the gas, one needs to distinguish the radial component of the forces — that is responsible for the infall of the gas — and the ortho-radial component — that is mostly responsible for the sAM variation. This is shown on figure 4.11 the presents radial profiles of the two components of each (specific) forces (pressure forces, gravitational forces) in one if the simulated halo. In the disk, the dominant forces in the radial and ortho-radial directions are star gravitational forces due to the disk. The forces are mostly radial, with their ortho-radial component one order of magnitude smaller than the radial one. In the inner halo, star gravitational forces become less dominant. The radial acceleration become DM-dominated, while the ortho-radial component is dominated by pressure torques. This is in particular the case for the hot gas, where ortho-radial pressure forces are one order of magnitude larger than DM gravitational forces. In the cold phase, the ortho-radial

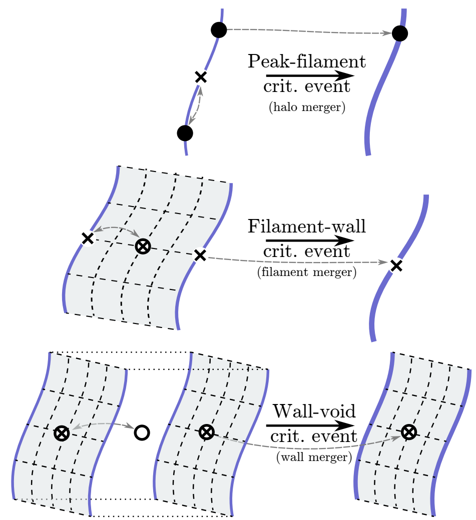

Figure 3.5: Illustration of critical events in a 3D random fields and their physical meaning. ● symbols are peaks, × symbols are filament-type saddle points (filament centres), ⊗ symbols are wall-type saddle points (wall centres) and ○ symbols are minima (void centres). *Top:* Peak-filament critical events encode the merger of two halos and the disappearance of their shared filament. After the merger, only one peak subsists and the filament disappears. *Middle:* Filament-wall critical events encode the merger of two filaments and the disappearance of their shared wall. After the merger, only one filament subsists. *Bottom:* Wall-void critical events encode the merger of two walls and the disappearance of their joint void (surrounded by the two walls and the dotted lines). After the merger, only one wall-type saddle-point subsists and the void has disappeared. Halo mergers are encoded by peak-filament critical events, filament mergers. Alternatively, one could have chosen to describe these events as resp. filament, wall and void disappearances.

3.4.2 3D critical events number counts

In this section, we will present the derivation of the number count of critical events in smoothing-position space in 3D. In section 3.4.2.1, we present how one can express the critical event constrain as a function of the local properties of the field and its derivatives. We then express the condition in the frame of the Hessian of the field in section 3.4.2.2 where it takes a simpler expression. In section 3.4.2.3, we extend the previous formula to distinguish between different critical event types (halo mergers, filament mergers, wall mergers).

3.4.2.1 General formulation

Following Hanami, 2001, the number density of critical events in smoothing-position space is given by

$$\frac{\partial^4 \mathcal{N}}{\partial r^3 \partial R} \equiv \langle \delta_{\rm D}^{(3)}(\boldsymbol{r}-\boldsymbol{r}_0)\delta_{\rm D}(R-R_0)\rangle \,, \tag{3.3}$$

where $\boldsymbol{r}_0$ is the position of a critical event (i.e. a critical point with a degenerate direction) in real space and R_0 its associated smoothing scale. Following the definition of section 3.4.1, critical events are found at the smoothing-position location where two critical points of different types (maximum, saddle points or minimum) merge. The nature of a critical point (occurring where $\boldsymbol{\nabla}\delta = 0$) is characterised by its index, that is to say the number of negative eigenvalues of the density Hessian matrix at this point. Critical *events* can then be defined as critical points for which one of the eigenvalues vanishes, which is also equivalent to having a vanishing determinant. By definition, only critical points whose indices differ by one can merge (peak–filament type saddle point, filament–wall type saddles, wall type saddle–void).

Let us therefore first define the determinant of the Hessian $d(\delta) \equiv \det(\boldsymbol{\nabla\nabla}\delta) = \sigma_2^3\lambda_1\lambda_2\lambda_3$, $\lambda_1 \leq \lambda_2 \leq \lambda_3$ being the ordered eigenvalues of the Hessian matrix $\boldsymbol{\nabla\nabla}\delta/\sigma_2$. In the following, we will use ∂_R to denote derivatives with respect to scale R. Since critical events are found where $d = 0$ and $\boldsymbol{\nabla}\delta = 0$, let us rewrite equation (3.3) in terms of the properties of the field, using the coordinate transformation from $\boldsymbol{r}, R$ to $\boldsymbol{\nabla}\delta, d$. This involves the 4D Jacobian of the transformation[1]

$$J(d, \boldsymbol{\nabla}\delta) = \begin{vmatrix} \partial_R d & \boldsymbol{\nabla} d \\ \partial_R \boldsymbol{\nabla}\delta^T & \boldsymbol{\nabla\nabla}\delta \end{vmatrix} = \begin{vmatrix} \partial_R d & \boldsymbol{\nabla} d \\ -R\boldsymbol{\nabla}\nabla^2\delta^T & \boldsymbol{\nabla\nabla}\delta \end{vmatrix} \,, \tag{3.4}$$

using the fact that for a Gaussian filter (see Table 2.2)

$$\partial_R \delta = -R\nabla^2\delta, \tag{3.5}$$

with ∇^2 the Laplacian operator. The fully covariant formulation of the number density of critical events is then

$$\frac{\partial^4 \mathcal{N}}{\partial r^3 \partial R} = \Big\langle |J|\, \delta_{\rm D}^{(3)}(\boldsymbol{\nabla}\delta)\, \delta_{\rm D}(d) \Big\rangle \,. \tag{3.6}$$

The expectation value in equation (3.6) can be evaluated using the joint distribution of the field and its successive derivatives up to third order, $P(x, x_i, x_{ij}, x_{ijk})$ which involves 20 variables, see section 3.A for the PDF for Gaussian random fields. One difficulty in evaluating equation (3.6) spans from $\delta_{\rm D}(d)$. In practice, it can for instance be dealt with numerically by 'broadening' the Dirac delta function: this method is used for validation and when considering two point statistics in the next section. Alternatively, we can go to the Hessian's eigenframe as described in the next section.

[1] Note that the determinant can be developed along the first line or the first column of the Jacobian matrix to find out – as shown by the simplifications in the next section – that the final result in our case does not depend on $\partial_R d$, thanks to the zero determinant constraint $\det \boldsymbol{\nabla\nabla}\delta = 0$.

Table 4.2: Cold gas fraction in the six halos at $z = 2$ and $z = 4$, comparing the cold gas mass to the total baryon mass within two virial radii (left columns) or within the inner halo (right columns).

	$z = 2$		$z = 4$	
Simulation	$r < 2R_{\rm vir}$ (%)	$r < 0.3R_{\rm vir}$ (%)	$r < 2R_{\rm vir}$ (%)	$r < 0.3R_{\rm vir}$ (%)
A	26	37	33	52
B	7	16	32	55
C	1	1	1	1
D	22	74	2.2	7.4
E	16	26	32	55
F	9	22	33	58

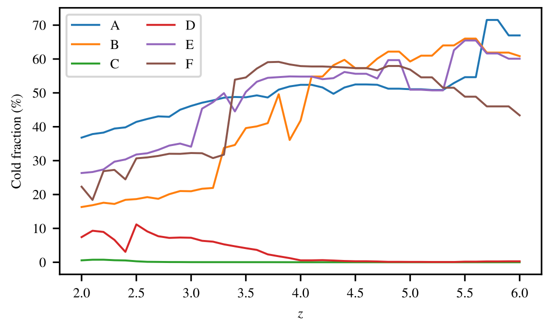

Figure 4.8: Cold gas fraction with respect to the total baryon mass in the inner halo as a function of redshift for the six halos. With increasing time, most of the gas is converted to star so that the cold gas fraction decreases.

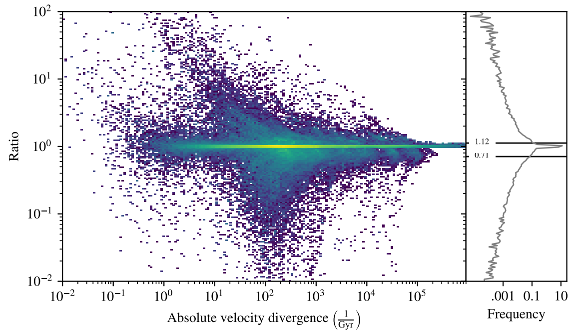

Figure 4.6: *Left panel:* Plot of the velocity divergence as computed by RAMSES vs. the ratio of the value computed in post-processing to RAMSES's one. *Right panel:* PDF of the ratio. 95 % of the distribution falls between the two horizontal lines. 95 % of the cells have a value between 0.71 and 1.12 times the value computed internally by RAMSES.

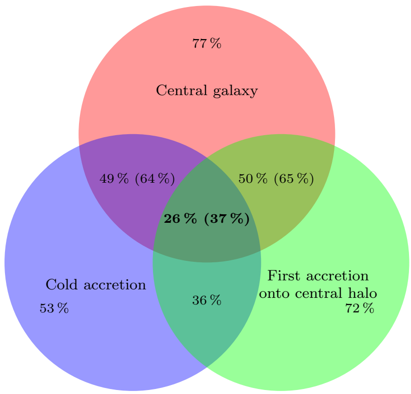

Figure 4.7: Venn diagram of the ensembles of tracer particles used to define the cold-accreted tracer particles. Direct cold-accreted tracer particles are the intersection of the tracer particles accreted cold between 1.5 and $0.5R_{\rm vir}$ (blue) that end up in the central galaxy at $z = 2$ (red) and that were first accreted onto the central halo (green). See the text for details on how each of these ensembles are defined. Percentages indicate the fraction in simulation A of all the particles within $2R_{\rm vir}$ found in each part of the diagram. Percentages within parenthesis indicate the fraction of tracer in the inner halo ($r < 0.3R_{\rm vir}$) found in each part of the diagram. Direct cold-accreted baryons represent 26 % of the baryons that end up within $2R_{\rm vir}$ and 37 % of the baryons within $0.3R_{\rm vir}$.

3.4.2.2 Expression in the frame of the Hessian

The Jacobian is by construction invariant under rotation, so we can rewrite it in the frame of the eigenvalues of the Hessian (which will be denoted with tildas) without loss of generality. Developing d into $\sigma_2^3\tilde{x}_{11}\tilde{x}_{22}\tilde{x}_{33}$ and assuming (arbitrarily) that direction 3 is the degenerate one, the Jacobian can be rewritten as follows

$$\frac{J(D,\delta)}{\sigma_1\sigma_2^4\sigma_3} = |\tilde{x}_{11}\tilde{x}_{22}|\begin{vmatrix}\partial_R\tilde{x}_{33} & \tilde{x}_{33i}\\ \partial_R\tilde{x}_i & \tilde{x}_{ij}\end{vmatrix}, \tag{3.7}$$

$$= |\tilde{x}_{11}\tilde{x}_{22}|\begin{vmatrix}\partial_R\tilde{x}_{33} & \tilde{x}_{133} & \tilde{x}_{233} & \tilde{x}_{333}\\ \partial_R\tilde{x}_1 & \tilde{x}_{11} & 0 & 0\\ \partial_R\tilde{x}_2 & 0 & \tilde{x}_{22} & 0\\ \partial_R\tilde{x}_3 & 0 & 0 & 0\end{vmatrix}, \tag{3.8}$$

$$= |\tilde{x}_{11}\tilde{x}_{22}|^2|\partial_R\tilde{x}_3||\tilde{x}_{333}|, \tag{3.9}$$

where the factorisation with $|\tilde{x}_{11}\tilde{x}_{22}|$ along the first line in equation (3.7) is a consequence of $\tilde{x}_{33}$ being zero – which also nulls the last component of equation (3.8). Using equation (3.5) again to re-express the derivative w.r.t. smoothing in terms of the Laplacian of the field, we can rewrite the number density of critical events using the typical scales of equation (2.90) as [2]

$$\frac{\partial n}{\partial R} = \frac{2\pi^2 R}{\tilde{R}^2 R_*^3}\left\langle |\textstyle\sum_i\tilde{x}_{3ii}||\tilde{x}_{333}|\delta_{\rm D}^{(3)}(\tilde{x}_i)\,|\tilde{x}_{11}\tilde{x}_{22}|\delta_{\rm D}(\tilde{x}_{33})\right\rangle, \tag{3.10}$$

where we introduced $n = \partial^3\mathcal{N}/\partial r^3$ the volume density of critical events (that does not depend on the spatial location $\boldsymbol{r}$ as the field is assumed to be stationary). Let us stress that the distribution of the fields expressed in the frame of the Hessian matrix differs from the original ones. The statistics of x and x_i and x_{ijk} are left unchanged and we therefore drop the tildes for the field and its first and third derivatives . However, going from cartesian coordinates to the Hessian eigenframe modifies the distribution of the second derivatives that we choose here to order (such that the Doroshkevich formula is recovered)

$$\begin{aligned}\tilde{P}(\tilde{x}_{11},\tilde{x}_{22},\tilde{x}_{33}) = 2\pi^2(\tilde{x}_{33}-\tilde{x}_{22})(\tilde{x}_{22}-\tilde{x}_{11})(\tilde{x}_{33}-\tilde{x}_{11})\times\\ P(x_{11}=\tilde{x}_{11}, x_{22}=\tilde{x}_{22}, x_{33}=\tilde{x}_{33}, x_{12}=0, x_{23}=0, x_{13}=0),\end{aligned}$$

where $\tilde{x}_{11} < \tilde{x}_{22} < \tilde{x}_{33}$ are distributed according to $\tilde{P}$ and fields in cartesian coordinates follow the distribution $\mathcal{P}$. Note that the factor $2\pi^2$ is due to the integration over the Euler angles. Equation (3.10) therefore introduces a jacobian $2\pi^2|x_{11}x_{22}(x_{11}-x_{22})|$, as x_{33} is null, when going from the Hessian eigenframe to cartesian coordinates and the differential number count of critical events becomes

$$\begin{aligned}\frac{\partial n}{\partial R} = \frac{2\pi^2 R}{\tilde{R}^2 R_*^3}\Big\langle |\textstyle\sum_i x_{3ii}||x_{333}|\delta_{\rm D}^{(3)}(x_i)\,|x_{11}x_{22}|^2\times\\ |x_{11}-x_{22}|\delta_{\rm D}(x_{33})\,\delta_{\rm D}^{(3)}(x_{i\neq k})\Big\rangle,\end{aligned} \tag{3.11}$$

where $\delta_{\rm D}^{(3)}(x_{i\neq k})$ must be understood as a product of Dirac delta functions of all the off-diagonal components of the Hessian matrix. Here R_* and $\tilde{R}$ are the typical inter critical point separation

[2] One factor of $|\tilde{x}_{11}\tilde{x}_{22}|$ drops between equation (3.9) and (3.10) because of the Dirac of D in equation (3.6).

and inter inflection point separation introduced in equation (2.90). The novelty of equation (3.11) w.r.t. the classical BBKS formula is the weight $|\sum_i x_{3ii}||x_{333}|$ which requires the knowledge of the statistics of the 3rd order derivative of the field. The expectations in equation (3.11) can be evaluated with the joint statistics of the field and its successive derivatives, $P(x_{113}, x_{223}, x_{333}, x_{11}, x_{22})$ which now only involves 5 variables. Interestingly, because the dominant contribution to the expectation value of $\langle|\sum_i x_{3ii}||x_{333}|\rangle$ comes from $\langle x_{333}^2\rangle$ with very good accuracy (at the percent level), equation (3.11) is very well approximated by

$$\frac{\partial n}{\partial R} \approx \frac{2\pi^2 R}{\tilde{R}^2 R_*^3} \Big\langle x_{333}^2 \delta_{\rm D}^{(3)}(x_i)\,|x_{11}x_{22}|^2 \times |x_{11} - x_{22}|\delta_{\rm D}(x_{33})\,\delta_{\rm D}^{(3)}(x_{i\neq k})\Big\rangle\,. \tag{3.12}$$

Note that this equation closely resembles the equation giving the flux of critical lines per unit surface presented in Pogosyan et al., 1998, up to the delta function on the third eigenvalue in the present context. This is in fact expected since we require here that along the filament's direction the curvature should be flat, whereas they marginalised over all possible longitudinal curvature. The similarity reflects the fact that critical points essentially slide along critical lines as one smooths the field, see figure 3.4. In some sense the 3D event count can be approximatively recast into a 1D event count along the ridges. The expectation involves the product of the transverse curvatures because the larger those curvature the larger the flux of such lines per unit transverse surface.

3.4.2.3 Gaussian number density of critical events per type

The aforementioned formalism makes no assumption on the type of the merging critical points. While the coalescence of peaks and filaments (PF critical events, the slopping saddles of Hanami, 2001) are clearly central to the theory of mass assembly, the filament-saddle to wall-saddle (FW critical events) and wall-saddle to minima coalescence (WV critical events) also impact the topology of galactic infall, as they destroy tunnels and voids within the surrounding cosmic web.

Let us therefore compute the number density of critical events of each type of mergers ($\mathcal{P} \equiv$ PF, $\mathcal{F} \equiv$ FW and $\mathcal{W} \equiv$ WV). Using the fact that for Gaussian random fields, equation (3.11) can be split into odd- and even-derivative terms, one can write

$$\frac{\partial n_j}{\partial R} = \frac{2\pi^2 R}{\tilde{R}^2 R_*^3} \overbrace{\left\langle \left|\sum_i x_{jii}\right| |x_{jjj}| \delta_{\rm D}^{(3)}(x_i) \right\rangle}^{C_{\rm odd}} \times \underbrace{\left\langle \vartheta_{\rm H}(x_{33}-x_{22})\,\vartheta_{\rm H}(x_{22}-x_{11})\,\delta_{\rm D}(x_{jj})\,\delta_{\rm D}^{(3)}(x_{k\neq l}) \left|\sum_{kl} \frac{\varepsilon^{jkl}}{2} x_{kk}^2 x_{ll}^2 (x_{kk}-x_{ll})\right| \right\rangle}_{C_{j,\rm even}} \tag{3.13}$$

where ε is the completely antisymmetric Levi-Civita tensor, ϑ the Heaviside function, and $j = 1, 2, 3$ for peak ($\mathcal{P}$), filament ($\mathcal{F}$) and wall ($\mathcal{W}$) mergers respectively. Note that equation (3.13) for a given value of j is essentially the same as equation (3.11), modulo a choice of null eigenvalue and the requirement that the eigenvalues are sorted. In 3D, $C_{\rm odd}$ and $C_{j,\rm even}$ have analytical expressions given by

$$C_{2,\rm even} = \langle\lambda_1\lambda_3\delta_{\rm D}(\lambda_2)\rangle = \frac{2}{\sqrt{15\pi}}\,,$$

$$C_{1,\rm even} = C_{3,\rm even} = \langle\lambda_1\lambda_2\delta_{\rm D}(\lambda_3)\rangle = \frac{29-6\sqrt{6}}{18\sqrt{10\pi}}\,, \tag{3.14}$$

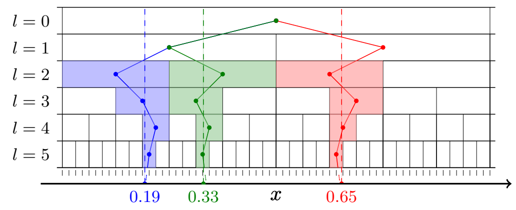

(a) Binary search in 1D

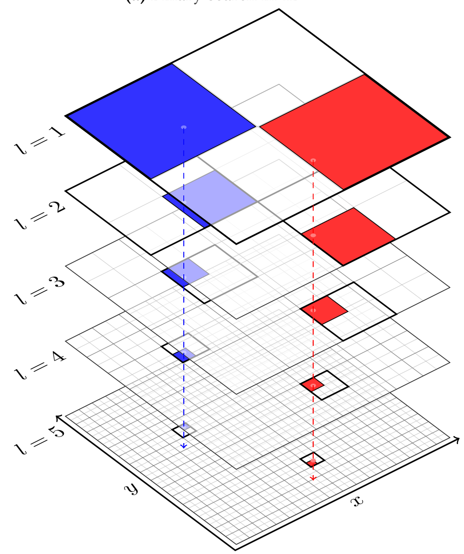

(b) Binary search in 2D

Figure 4.5: (a) Scheme of a binary search in an oct structure in 1D. The requested points are shown as red and blue dashed lines. The algorithm starts at the root level $l = 0$ and goes down the structure ; at each level, it picks the cell that contains the requested point. (b) A similar illustration in 2D, the algorithm works in the same way. At each level, it selects one of the four cells (red and blue squares) from the oct (thick line). The algorithm can be easily generalised to three or more dimensions. It is able to find any cell containing a given point in $l_{\rm max}$ iterations exactly. If the grid is sparse, as is the case for an AMR structure, $l_{\rm max}$ becomes an upper boundary.

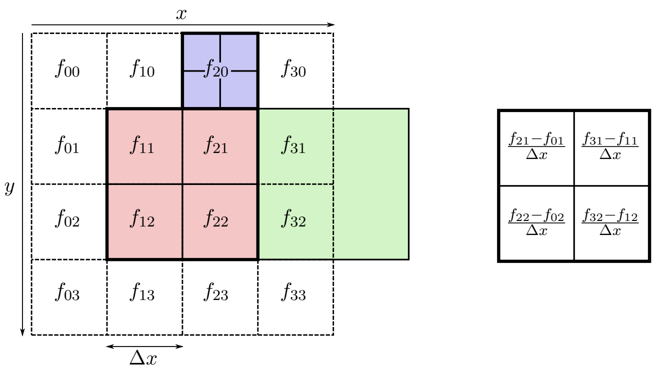

Figure 4.4: Scheme of the AMR structure used to estimate the gradient of a quantity f in the central oct (red). Octs are represented in thick lines, cells in thin lines and virtual cells in dashed lines. *Left panel:* The virtual cell values on a 4^3 grid are interpolated from the nearest cell in the AMR grid. If the nearest cell is at the same level, its value is directly used. If the cell is at a coarser level, its value is directly used (for example f_{31} and f_{32} have the value of the green cell). If the cell is refined, the mean of its children is used (for example f_{20} is the mean of all the *blue* cells). *Right panel:* Gradients are estimated using a first-order finite difference centred scheme on the 4^3 virtual cells.

history of all the baryons (gas and star) that end up within $2R_{\rm vir}$ of the central galaxy. This ensemble of particle in the vicinity of the galaxy are then grouped in three sets.

1. the baryons that end up in the inner halo $r < 0.3R_{\rm vir}$ at the end of the simulation. I will refer to this subset as "baryons in the galaxy".
2. the baryons that never heated above the threshold temperature $T \leq T_{\rm max}$ from $1.5R_{\rm vir}$ to $0.3R_{\rm vir}$. I will refer to this subset as "cold baryons".
3. the baryons that were never accreted on a satellite galaxies. I will refer to this subset as "directly accreted baryons". This effectively selects gas whose first accretion is onto the main halo. In practice, this is done by excluding any tracer found at any time at less than a third of the virial radius of any halo other than the main one.

The repartition of the gas in halo A at $z = 2$ is shown on figure 4.7 where baryons in the galaxy are represented in the red ensemble, cold-accreted baryons in blue and directly accreted baryons in green. In the following of the chapter, the subset of interest is the intersection of the three ensembles: this is the gas that was accreted cold onto the galaxy, that end up in the inner halo at $z = 2$ and that was not accreted *via* mergers. In the remaining of the paper, I will refer to this subset as the "cold gas" while I will use "hot gas" to describe gas that was not accreted via mergers but which eventually heated up above the temperature threshold.

I have checked that the fraction presented on figure 4.7 are robust to changes of the threshold radius for first-accretion detection: using $R_{\rm thresh} = 0.5R_{\rm vir}$ instead of $0.3R_{\rm vir}$ only leads to percent differences. Indeed, most of the gas already within $0.5R_{\rm vir}$ of a halo is likely to later fall into the inner part of the galaxy.

The cold gas fractions in the different halos are presented in Table 4.2 and their evolution is shown on figure 4.8. **[♡ remove this if I don't talk about it and also if I don't undertand it.]**

and

$$C_{\rm odd}=\frac{\sqrt{27}(1-\tilde\gamma^2)}{\sqrt{50\pi^5}}\left(\frac{2}{\sqrt{21(1-\tilde\gamma^2)}}+\tan^{-1}\frac{\sqrt{21(1-\tilde\gamma^2)}}{2}\right), \tag{3.15}$$

which can also be computed in arbitrary dimensions as shown in section 3.B. **[♡ Explicitly state the PDF of the λ_i]** From this we can compute the ratio of peak to filament mergers $r_{\mathcal{P}/\mathcal{F}} = C_{2,\rm even}/C_{1,\rm even}$. Interestingly, the event ratio is independent of the spectral index of the field and is given by

$$r_{\mathcal{P}/\mathcal{F}} = \frac{24\sqrt{3}}{29\sqrt{2}-12\sqrt{3}} \approx 2.05508 \approx \frac{37}{18}, \tag{3.16}$$

which is nothing but the ratio between the mean number of wall-type saddles and peaks minus 1, a relationship which is valid in arbitrary dimension. This equation shows that there are twice more filament disappearing in filament merger events ($\mathcal{F}$ events) than in halo merger events ($\mathcal{P}$ events). Similarly, we can compute $r_{\mathcal{F}/\mathcal{W}}$ to deduce that there are twice more walls disappearing due to filament mergers ($\mathcal{F}$ events) than due to void mergers ($\mathcal{W}$ events). Section 3.B also presents these ratios in dimension 4 to 6.

3.4.3 3D differential event counts of a given height

Introducing $\delta_{\rm D}(x-\nu)$ in the expectation of equation (3.13) allows us to write the density of critical events as a function of height, hence make the distinction between mergers of important critical points and less significant ones.

For Gaussian random fields, the field only correlates with its even derivatives (second in our case). Imposing the height of the critical events we consider therefore only modifies the term $C_{j,\rm even}$ while $C_{\rm odd}$ is left unchanged, following

$$C_{j,\rm even}(\nu)=\Big\langle \vartheta_{\rm H}(x_{33}-x_{22})\,\vartheta_{\rm H}(x_{22}-x_{11})\,\delta_{\rm D}(x_{jj})\delta_{\rm D}^{(3)}(x_{k\neq l})\,\delta_{\rm D}(x-\nu) \times\left|\sum_{kl}\frac{\varepsilon^{jkl}}{2}x_{kk}^2x_{ll}^2(x_{kk}-x_{ll})\right|\Big\rangle\,. \tag{3.17}$$

Interestingly, $C_{j,\rm even}(\nu)$ appears to have an analytical expression once rotational invariants are used to evaluate the expectations. Following the formalism described first in (Pogosyan et al., 2009), we introduce the variables

$$J_1 = I_1\,,\quad J_2 = I_1^2 - 3I_2\,, \tag{3.18}$$

$$J_3 = \frac{27}{2}I_3 - \frac{9}{2}I_1I_2 + I_1^3\,,\quad \zeta = \frac{x+\gamma J_1}{\sqrt{1-\gamma^2}}\,, \tag{3.19}$$

that are linear combinations of the density field x and rotational invariants of its second derivatives namely the trace $I_1 = \operatorname{tr}\mathbf{H} = \lambda_1+\lambda_2+\lambda_3$, minor $I_2 = 1/2((\operatorname{tr}\mathbf{H})^2 - \operatorname{tr}\mathbf{H}\cdot\mathbf{H}) = \lambda_1\lambda_2+\lambda_2\lambda_3+\lambda_3\lambda_1$ and determinant $I_3 = \det\mathbf{H} = \lambda_1\lambda_2\lambda_3$ of the Hessian matrix $\mathbf{H} = (x_{ij})$. The distribution of these variables is given by

$$P(\zeta, J_1, J_2, J_3) = \frac{25\sqrt{10\pi}}{24\pi^2}\exp\left(-\frac{1}{2}\zeta^2 - \frac{1}{2}J_1^2 - \frac{5}{2}J_2\right), \tag{3.20}$$

where J_3 is uniformly distributed between $-J_2^{3/2}$ and $J_2^{3/2}$ and J_2 is positive. Using these rotational invariants, one can rewrite equation (3.17) for each type of critical event

$$
\begin{aligned}
C_{1,\mathrm{even}}(\nu) &= \left\langle |I_2| \delta_D(x-\nu) \delta_D(I_3) \mathcal{B}(-2J_2^{1/2} < J_1 < -J_2^{1/2}) \right\rangle, \\
C_{2,\mathrm{even}}(\nu) &= \left\langle |I_2| \delta_D(x-\nu) \delta_D(I_3) \mathcal{B}(-J_2^{1/2} < J_1 < J_2^{1/2}) \right\rangle, \\
C_{3,\mathrm{even}}(\nu) &= \left\langle |I_2| \delta_D(x-\nu) \delta_D(I_3) \mathcal{B}(J_2^{1/2} < J_1 < 2J_2^{1/2}) \right\rangle = C_{1,\mathrm{even}},
\end{aligned}
\tag{3.21}
$$

with

$$
\delta_{\mathrm{D}}(I_3) = \frac{27}{2} \delta_{\mathrm{D}} \left(J_3 - \frac{3J_1J_2 - J_1^3}{2} \right), \tag{3.22}
$$

$$
\delta_{\mathrm{D}}(x-\nu) = \frac{1}{\sqrt{1-\gamma^2}} \delta_{\mathrm{D}} \left(\zeta - \frac{\nu + \gamma J_1}{\sqrt{1-\gamma^2}} \right), \tag{3.23}
$$

and the condition that the determinant is null due to λ_j being zero is enforced by restricted the range of J_1 according to the Boolean specified in equations (3.21). Eventually, the integration in equation (3.21) can be done symbolically and an analytical expression for $C_{j,\mathrm{even}}(\nu)$ follows

$$
C_{1,\mathrm{even}}(\nu) = \sum_{i=1,6,9} c_{1,i} \exp\left[-\frac{\nu^2}{2(1-\gamma^2/i)} \right], \tag{3.24}
$$

$$
C_{2,\mathrm{even}}(\nu) = c_{2,6} \exp\left[-\frac{\nu^2}{2(1-5\gamma^2/6)} \right], \tag{3.25}
$$

with

$$
c_{1,1} = \frac{3\sqrt{\frac{5}{2}}\gamma\sqrt{1-\gamma^2}\nu\left(275\gamma^4 + 30\gamma^2\left(2\nu^2-23\right)+351\right)}{\pi^{3/2}\left(9-5\gamma^2\right)^4},
$$

$$
c_{1,6} = -\frac{\operatorname{erf}\left(\frac{\gamma\nu}{\sqrt{2}\sqrt{5\gamma^4-11\gamma^2+6}}\right)+1}{\sqrt{5}\pi\sqrt{6-5\gamma^2}}, \quad c_{2,6} = \frac{2}{\pi\sqrt{30-25\gamma^2}},
$$

$$
c_{1,9} = \frac{\operatorname{erf}\left(\frac{\sqrt{2}\gamma\nu}{\sqrt{5\gamma^4-14\gamma^2+9}}\right)+1}{4\pi\sqrt{5}\left(9-5\gamma^2\right)^{5/2}} \times \left(\frac{3600\gamma^4\nu^4}{(9-5\gamma^2)^2} + \frac{120\gamma^2(27-35\gamma^2)\nu^2}{9-5\gamma^2} + 575\gamma^4 - 1230\gamma^2 + 783 \right),
$$

The resulting counts of critical events as a function of their height ν is plotted in figure 3.9 for different values of the spectral index n_{s}. Note that $\partial^2 n/\partial R \partial \nu$ scales like $1/R^4$ but is also a function of R via the spectral parameters γ and $\tilde{\gamma}$.

3.4.4 2D event counts and differential counts

Since the formalism is very similar, let us also briefly present the analogues of equation (3.13) for 2D fields. It reads

$$
\frac{\partial^2 n}{\partial R \partial \nu} = \frac{2\pi R}{\tilde{R}^2 R_*^2} \langle |x_{211} + x_{222}||x_{222}| \delta_{\mathrm{D}}(x_1)\, \delta_{\mathrm{D}}(x_2) \rangle \times \langle \vartheta_{\mathrm{H}}(x_{22} - x_{11})\, \delta_{\mathrm{D}}(x_{22}) \delta_{\mathrm{D}}(x_{12})\, \delta_{\mathrm{D}}(x-\nu) |x_{11} - x_{22}| \rangle , \tag{3.26}
$$

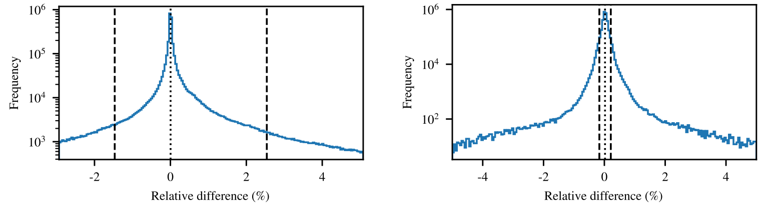

(a) Error on evolution rate computation **(b)** Error on acceleration computation

Figure 4.3: (a): Relative difference between the sum of the sAM evolution rate due to stars, DM and gas gravitational forces (as computed with the method presented in the text) and the rate due the total gravitational torques (as computed by Ramses). (b): Same, but with the total gravitational accelerations. Vertical dashed line indicate 5 % and 95 % quantiles. The vertical dotted line indicates the median value. The two methods yield similar results within a few percent.

quantity using a centred finite-difference scheme on the 4^3 grid, as illustrated on figure 4.4, right panel. (e) Store the value of the gradient in the central 2^3 cells.

This approach aims at providing results as close as possible to the values used internally by Ramses. In practice, most AMR post-processing tools compute gradients on a fixed regular grid. Even though this approach yields sensible results at scales comparable to the (arbitrary) grid spacing, any information at finer scales is lost while values at coarser levels have to be interpolated, eventually leading to spurious gradients. In the case of the study of accretion onto galaxies, the fixed-grid approach fails at providing a precise description of the gradients at play (pressure and potential gradients), as shocks may form over a large region of size $\sim R_{\mathrm{vir}}^3$. In order to capture all of them on a regular grid, one would then require $\sim (R_{\mathrm{vir}}/\Delta x)^3 \approx (100\,\mathrm{kpc}/30\,\mathrm{pc})^3 \approx 3 \times 10^{10}$ cells, which is in practice too large to fit in memory. In practice, it is much more efficient and consistent to directly work on the AMR structure dumped alongside the physical information of the simulation. Using a tree search algorithm, as illustrated on figure 4.5, I have developed a post-processing tool that is able to compute finite difference gradients directly on the AMR grid. It is worth noting that this approach is exactly consistent with the internal approach of Ramses, except at the interface between different grid levels where a linear interpolation is used by Ramses, whereas our method uses a simple average. One way to check the consistency is to compare gradients computed by the post-processing tool to the ones computed internally by Ramses. This is for example done using the velocity divergence, as shown on figure 4.6. The figure shows that the post-processing method recovers the velocity divergence within a few percent, while most of the scatter is attributed to the fact that Ramses uses a linear interpolation at the interface between coarse and fine cells.

4.2.6 Cold gas selection

The ratio of the total accreted mass with a maximum temperature below a given threshold $T_{\max}$ to the total gas mass — the cold fraction — is a widely reported quantity in the study of the cosmological gas accretion, dating back to Kereš et al., 2005. The cold fraction is made of cold flows that remain cold throughout their infall into the galaxy. In this study, a temperature cut $T \lesssim T_{\max} = 2.5 \times 10^5\,\mathrm{K}$ (see e.g. Nelson et al., 2013, for a discussion on the effect of the threshold) is used. In order to study the sAM evolution of the cold gas, I use the Lagrangian

Instead of providing smooth trajectories, tracer particles provide a statistical sample whose mean accurately tracks the properties of baryons in the simulation. I have then used them to track the temperature of the gas, so that one can distinguish cold gas from hot gas, but also other quantities such the sAM of the gas or the different torques.

4.2.4 Torque extraction

I have modified the code RAMSES to extract in post-processing the gravitational acceleration due to the different matter components (DM, gas, stars). This was performed by stripping down RAMSES to keep only the Poisson solver, applied to the density of each individual component[2] with exactly the same parameters as the full run. For each output I have computed the gravitational force of the stars, gas and dark matter. For each component (star, gas and DM), I have also computed the rate of change of sAM of the gas as

$$f_i = \frac{\boldsymbol{\tau}_i \cdot \boldsymbol{l}}{\|\boldsymbol{l}\|^2}, \tag{4.8}$$

where $\boldsymbol{\tau}_i \equiv \boldsymbol{r} \times \boldsymbol{a_i}$ is the specific torque due to the star ($\star$), gas or DM component and $\boldsymbol{l} = \boldsymbol{r} \times \boldsymbol{v}$ is the gas sAM. Using equation (4.5) and after some algebra, one gets that the total rate of change $f = \mathrm{d}\log l/\mathrm{d}t$. Equation (4.8) is therefore a measure of the inverse e-folding time along the Lagrangian trajectory of a particle. Both positions and velocities are evaluated for the gas in the frame of the central halo. f_i is positive and large where torques are efficient at increasing the sAM and negative where torques are efficient at decreasing the sAM. Figure 4.3a shows the relative difference between the sum of the evolution rates $f_\star + f_{\mathrm{DM}} + f_{\mathrm{gas}}$ extracted individually in post-processing and the total evolution rate $f = \boldsymbol{\tau} \cdot \boldsymbol{l}/\|\boldsymbol{l}\|^2$ computed on-the-fly by RAMSES. Figure 4.3b shows the relative difference between the gravitational accelerations computed using the two methods. The agreement is of the order of less than a percent in 90% of the cells. Note that a perfect agreement is not expected, as the potential from the SMBHs has been neglected in the post-processing method. In addition, RAMSES' Poisson solver has an accuracy of 10^{-4}, consistent with the median error obtained in the gravitational accelerations ($0.02\,\%$). Overall, the agreement between the computed rates are within a few percent. The errors on the evolution rate are slightly larger, albeit still small, as a result of the division by l that skews the distribution and spreads assigns larger weights in regions where $\boldsymbol{l}$ is small. This confirms that the post-processing decomposition yields results consistent with the on-the-fly-computed gravitational field used internally to evolve the simulation. Using equation (4.8), one can also compute torque timescales using

$$t_{\tau,i} = \frac{1}{f_i}. \tag{4.9}$$

These timescales measure the typical time over which a given torque will remove all the sAM from the gas.

4.2.5 Gradient estimation

In order to compute the torques due to pressure, I have extended the yt code (Turk et al., 2011) to enable computation of gradients on an oct-based AMR grid. The algorithm works as follow. (a) Loop over all octs in the tree. (b) Compute the positions of the $4^3 = 64$ virtual cells centred on the oct and extending in $\pm 2\Delta x$ in all three directions, as illustrated on figure 4.4, left panel. (c) Interpolate the value of interest at the centre of each virtual cell from the AMR grid. If the virtual cell exists on the grid or is contained in a coarser cell, the value on the grid is directly used. If the virtual cell contains leaf cells, the mean of these cells is used. (d) Compute the gradient of the

[2]The fiducial implementation solves the Poisson equation directly on the total matter density (gas + stars + DM + SMBHs).

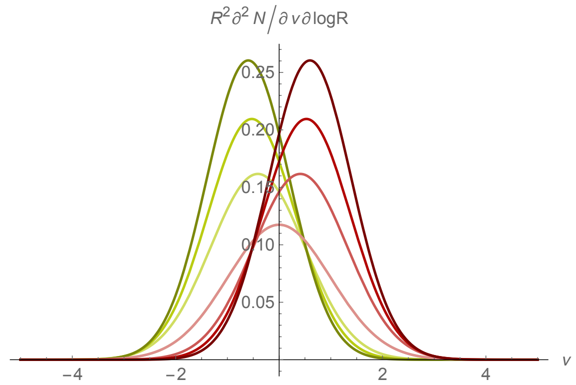

Figure 3.6: The PDF of critical events of the various types $(\mathcal{P}, \mathcal{F})$ in 2D for $n_s = -2, -3/2, -1, -1/2$ from light to dark. Note that the dominant change with spectral index is in the amplitude which scales like $1/\tilde{R}^2/R_\star^d$. The rest of the shape variation comes from the weaker γ and $\tilde{\gamma}$ dependence of C_{odd} and C_{even}.

which after some algebra, given the knowledge of the 2D PDF given in section 3.A, yields for the peak merger rate

$$\frac{\partial^2 n}{\partial R \partial \nu} = \frac{R C_{\mathrm{odd}}}{\tilde{R}^2 R_*^2}\left[\frac{4\gamma\nu\sqrt{1-\gamma^2}}{(3-2\gamma^2)^2}\exp\left(-\frac{\nu^2}{2(1-\gamma^2)}\right) + \frac{\sqrt{8\pi}(2\gamma^4+\gamma^2(\nu^2-5)+3)}{(3-2\gamma^2)^{5/2}}\mathrm{erfc}\left(\frac{-\gamma\nu}{\sqrt{4\gamma^4-10\gamma^2+6}}\right)\exp\left(-\frac{3\nu^2}{6-4\gamma^2}\right)\right],$$

with

$$C_{\mathrm{odd}} = \frac{\hat{\gamma}+3\hat{\gamma}^2\tan^{-1}(3\hat{\gamma})}{4\pi^2}, \text{ given } \hat{\gamma} = \sqrt{1-\tilde{\gamma}^2}.$$

The wall merger rate is obtained by swapping ν to $-\nu$ in this expression. The two rates are plotted in figure 3.6 and validated against Gaussian random fields in figure 3.10. The counts, $\partial n/\partial R = 2C_{\mathrm{odd}}R/(3\sqrt{3}\tilde{R}^2R_*^2)$ follows by integration over ν.

Section 3.B also presents differential counts in dimension 4 to 6, together with asymptotic expressions in the large dimension limit for the integrated count ratios. As expected, for any dimension the number counts per unit log-volume is logarithmically scale invariant (up to the slow variation in the spectral parameters), i.e. $R^d\,\partial^2 n^d/\partial\log R\partial\nu$ is a function of γ, $\tilde{\gamma}$ and ν only.

3.4.5 Beyond gaussian statistics

Let us finally compute the one point statistics for close to Gaussian fields. The Edgeworth expansion joint statistics of the field at x, $P(x, x_i, x_{ij}, x_{ijk})$, involving the hierarchy of cumulants obeys

$$P(\mathbf{x}) = P_{\mathrm{G}}(\mathbf{x})\left(1 + \sum_{k=3}^{\infty}\sigma^{k-2}\frac{\langle\mathbf{H}_k(\boldsymbol{x})\rangle}{\sigma^{2k-2}}\cdot\mathbf{H}_k(\boldsymbol{x})\right), \tag{3.27}$$

where $\mathbf{H}_k$ is a vector of orthogonal polynomials w.r.t. to the Kernel $P_{\rm G}$ obeying $\mathbf{H}_k = (-1)^k \partial^k P_{\rm G}/\partial \boldsymbol{x}^k / P_{\rm G}$ while at tree order in Perturbation Theory (Bernardeau et al., 2002), $\langle \mathbf{H}_k(\boldsymbol{x}) \rangle / \sigma^{2k-2}$ is independent of the variance $\sigma^2(z)$ below $k = 6$. Cumulants such as $\langle x_1^2 x_{113} \rangle$ entering equation (3.27) could in the context of a given cosmological model involve a parametrisation of modified gravity (via e.g. a parametrisation of $F_2(\boldsymbol{k}_1, \boldsymbol{k}_2)$), and/or primordial non-gaussianities (via e.g. $f_{\rm NL}$). From this expansion, or relying on the connection between event ratio and connectivity discussed in section 3.B.6, we can for instance compute the non-Gaussian correction to the ratio of critical events, defined in equation (3.16) as

$$\frac{r_{\mathcal{P}/\mathcal{F}}}{r_{\mathcal{P}/\mathcal{F},\rm G}} = \left(1 + c_r \left(8 \left\langle J_1^3 \right\rangle - 10 \left\langle J_1 J_2 \right\rangle - 21 \left\langle q^2 J_1 \right\rangle \right)\right). \tag{3.28}$$

where $c_r = \left(29\sqrt{2} + 12\sqrt{3}\right)/210/\sqrt{\pi}$, while $\sigma_1^2 q^2 = |\nabla \rho|^2$ the modulus square of the gradient, J_1 and J_2 are defined in equation (3.19) via the trace and minor of the Hessian. These extended skewness parameters are isotropic moments of the underlying Bispectrum which, when gravity drives the evolution, scale with σ at tree order in perturbation theory (e.g. $\left\langle J_1^3 \right\rangle / \sigma$ is independent of σ). The correction to one entering equation (3.28) is negative (approximately equal to $-\sigma(1/7 - \log(L)/5)$ for a ΛCDM spectra smoothed over L Mpc$/h$), suggesting that gravitational clustering reduces the relative number of peak mergers compared to filament mergers. When astronomers constrain the equation of state of dark energy using the cosmic evolution of voids disappearance they effectively measure σ in equation (3.28). Conversely, for primordial non Gaussianities, the extended skewness parameters must be updated accordingly (see Codis et al., 2013; Gay et al., 2012). For instance, $\langle J_1 q^2 \rangle = \langle J_1 q^2 \rangle_{\rm grav} - 2 f_{\rm NL} \sqrt{1 + f_{\rm NL}^2}/(1 + 4 f_{\rm NL}^2)$.

Since the computation of the expectation (3.13) with the Edgeworth expansion (3.27) is beyond the scope of this work, let us investigate an alternative proxy for the event rate. Figure 3.7 makes use of the perturbative prediction of Gay et al., 2012 to first order in σ for the gravitationally-driven non-gaussian differential extrema counts to compute the product of such counts as a proxy for the events, namely $\mathcal{P}(\nu) \propto P(\nu) \times F(\nu)$, $\mathcal{F}(\nu) \propto F(\nu) \times W(\nu)$, and $\mathcal{W}(\nu) \propto W(\nu) \times V(\nu)$. This Ansatz is reasonable, since for a merger to occur, two critical points of the same height must exist beforehand. We use the Gaussian PDF as a reference, to recalibrate the relative amplitude of the filament to peak merger counts. Since Gay et al., 2012 provide fits to the critical PDFs as a function of σ, it is straightforward to compute their product.

From figure 3.7, we see that gravitational clustering shifts the peak event counts to lower contrast, as it should. Let trivially, the filament merger rates also shift towards negative contrasts. From these PDFs we can re-compute the cosmic evolution of the ratio of critical events: its scales like $r_{\mathcal{P}/\mathcal{F}} = 7/34(1 - \sigma/7)$ (for $n = -1$) in good agreement with equation (3.28), suggesting that this approximation indeed captures the main features of gravitational clustering.

3.5 Theory: two point statistics

Let us now present a method to compute the two-point statistics of critical events. Such statistics is of interest e.g. to study the cosmic evolution of the connectivity of peaks, or to understand how large scale tides bias mass accretion (the so-called assembly bias). Section 3.5.1 presents the two-point statistics of merger events in 3D, while section 3.5.2 provides analytical approximations while assuming mergers occur along a straight filament. Section 3.5.3 computes the conditional merger rates subject to larger scale tides. We match these predictions to simulations in section 3.6 below.

3.5.1 Clustering of critical events in $R, \boldsymbol{r}$ space

We cannot generally assume that the orientation of the two critical events are aligned w.r.t. the vector separation, so the covariant condition for critical event of type $j \in \{\mathcal{P}, \mathcal{F}, \mathcal{W}\}$, cond_j, is

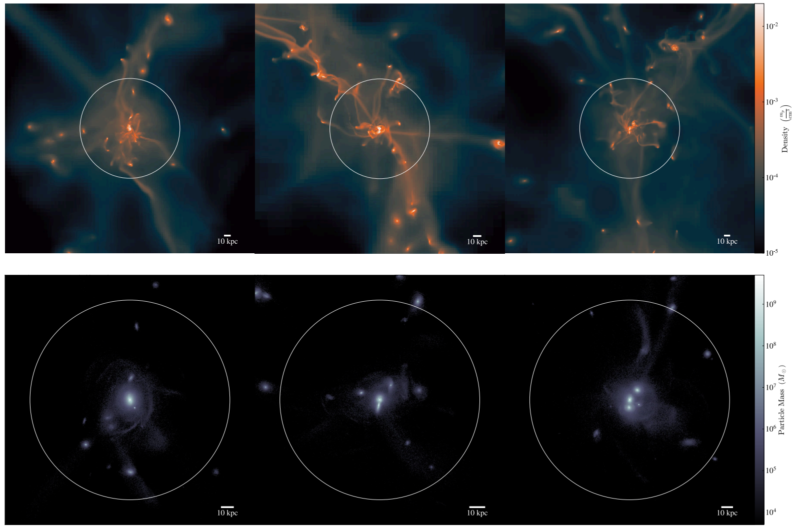

Figure 4.2: *Upper panel:* Projection of the gas density around the halos A (left), B (centre) and C (right) at $z = 2$. *Lower panel:* Line-of-sight integrated star density.

short of providing the Lagrangian history of the gas. To overcome this issue, AMR codes have been equipped with "tracer" particles. Tracer particles are passively displaced with the gas flow and hence track its Lagrangian evolution. Each tracer can also record instantaneous quantities, in particular the temperature of the gas it tracks and density. Using the approach described by Genel et al., 2013, I have implemented tracer particles for the code Ramses. While a more detailed discussion of the scheme are presented in section 4.6, let me present here a short description of the tracer particle scheme.

One of the constrain on tracer particle is their ability to accurately reproduce the Eulerian distribution of the gas. A naive approach to track the motion of the gas is to use the velocity of the gas itself. This is usually done with a cloud-in-cell interpolation (first order interpolation), where the value of the velocity is interpolated from the 8 closest cells. Such a velocity-based approach was implemented in Ramses (Dubois et al., 2012) and used to probe the link between cosmic gas infall and galactic gas feeding. While this approach yields smooth trajectories, it falls short of reproducing the gas density distribution accurately in regions of converging flows (Cadiou et al., 2019). Using a different approach, Genel et al., 2013 suggested to instead sample mass fluxes using a Monte-Carlo approach. In this approach, the mass flux between cells, which is readily computed by the Riemann solver of the code, is reproduced by moving particles across the cells interface. Each particle is assigned a transition probability

$$p_{ij} = \frac{\Delta M_{ij}}{M_i}, \tag{4.7}$$

where ΔM_{ij} is the transferred mass (as computed by the Riemann solver) and M_i is the mass of the cell originally containing the particle. The scheme can be easily generalised to any baryonic mass transfers between gas, stars, SMBHs *via* star formation and SN and AGN feedbacks.

Table 4.1: Properties of the halos at $z = 2$.

Name	Simulation	$M_{\rm vir}/10^{11}\,{\rm M}_\odot$	$M_\star/10^{10}\,{\rm M}_\odot$
A	S1	3.66	6.07
B	S2	7.82	9.20
C	S3	6.64	5.09
D	S1	7.29	4.18
E	S1	5.23	7.84
F	S3	4.63	3.49

the simulation is initialised to $Z_0 = 10^{-3}\,{\rm Z}_\odot$ to allow further cooing below $10^4\,{\rm K}$ down to $T_{\rm min} = 10\,{\rm K}$. Reionisation occurs at $z = 8.5$ using the Haardt and Madau, 1996 model and gas self-shielding above $10^{-2}\,{\rm m_p\,cm^{-3}}$. Star formation is allowed above a gas number density of $n_0 = 10\,{\rm m_p\,cm^{-3}}$ and with efficiency $\epsilon_{\rm ff}$ that depends on the gravoturbulent properties of the gas (for details, see Kimm et al., 2017; Trebitsch et al., 2017). The main distinction of this turbulent star-formation recipe with the traditional star formation in Ramses (Rasera and Teyssier, 2006) is that the efficiency can approach and even exceed 100 % (with $\epsilon_{\rm ff} > 1$ meaning that stars are formed faster than in a free-fall time). The stellar population is sampled with a Kroupa, 2001 initial mass function, where $\eta_{\rm SN} = 0.317$ and the yield (in terms of mass fraction released into metals) is 0.05. The stellar feedback model is the mechanical feedback model of Kimm et al., 2015 with a boost in momentum due to early UV pre-heating of the gas following Geen et al., 2015. The simulation also tracks the formation of SMBHs and the evolution of AGN feedback in jet mode (radio mode) and thermal mode (quasar mode) using the model of Dubois et al., 2012. The jet is modelled in a self-consistent way by following the AM of the accreted material and the spin of the black hole (Dubois et al., 2014). The radiative efficiency and spin-up rate of the SMBH is then computed using the MAD results of McKinney et al., 2012. SMBHs are created with a seed mass of $10^4\,{\rm M}_\odot$ for S1 and $10^5\,{\rm M}_\odot$ for S2 and S3.

The simulations have a roughly constant physical resolution of 35 pc (one additional maximum level of refinement at expansion factor 0.1 and 0.2), a star particle mass resolution of $m_{\star,\rm res} = 1.1\times10^4\,{\rm M}_\odot$, a dark matter (DM) particle mass resolution of $m_{\rm DM,res} = 1.5\times10^6\,{\rm M}_\odot$, and gas mass resolution of $2.2\times10^5\,{\rm M}_\odot$ in the refined region. A cell is refined according to a quasi-Lagrangian criterion: if $\rho_{\rm DM} + \rho_{\rm b}/f_{\rm b/DM} > 8m_{\rm DM,res}/\Delta x^3$, where $\rho_{\rm DM}$, and $\rho_{\rm b}$ are respectively the DM and baryon density (including stars plus gas plus SMBHs), and where $f_{\rm b/DM}$ is the universal baryon-to-DM mass ratio. The max level of refinement is also enforced up to 4 minimum cell size distance around all SMBHs. Tracer particles (Cadiou et al., 2019) are added in the refined region with a fixed mass of $m_{\rm t} = 2.0\times10^4\,{\rm M}_\odot$ ($N_{\rm tot} \approx 1.3\times10^8$ particles) and are detailed in more depth in the next section. The description of the tracer particle scheme is detailed in section 4.6. There is on average 0.55 tracer per star and 22 per initial gas resolution element. Cells of size 35 pc and density $20\,{\rm cm^{-3}}$ contain on average one tracer per cell.

4.2.3 Lagrangian tracers

The peculiar evolution of cold flows is usually captured by their maximum temperature, as the gas that compose them never heated up above a given threshold (see section 4.2.6), which effectively selects the gas that crossed the virial radius without shocking. While AMR codes are particularly good at capturing shocks and trigger super-Lagrangian refinement in regions of interest, they fall

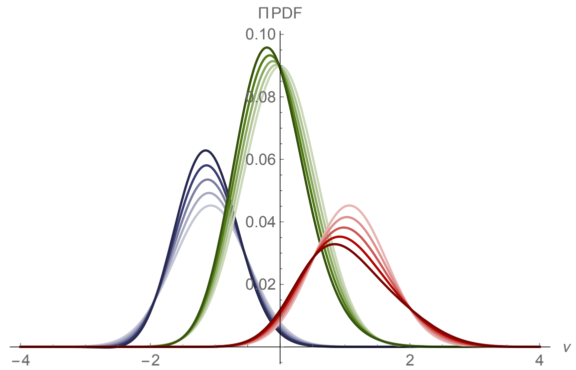

Figure 3.7: Predicted cosmic evolution of the product of extrema counts as a proxy for the event counts ($\mathcal{W}$ in blue, $\mathcal{F}$ in green and $\mathcal{P}$ in red) for the variances $\sigma = 0, 0.04, 0.08, 0.12, 0.16$ and an underlying scale invariant power spectra of index $n = -1$. The $\mathcal{F}$ counts have been rescaled by a constant $205/332$ factor to better match the actual counts. The predicted trend with σ are in qualitative agreement with the measured counts presented in figure 3.16.

given by the argument of the expectation in equation (3.6) multiplied by requirement on the sign of the two non-zero eigenvalues. For instance

$$\mathrm{cond}_{\mathcal{P}}(\boldsymbol{x}) = |J|\delta_{\rm D}^{(3)}(x_i)\delta_{\rm D}(D) \times \vartheta_{\rm H}(-\mathrm{tr}(x_{ik}))\vartheta_{\rm H}\left(\mathrm{tr}^2(x_{ik}) - \mathrm{tr}(x_{il}x_{lk})\right),$$

where the two Heaviside conditions ensure that the trace is negative and the minor positive so that the two eigenvalues are negative. From the joint two-point count of critical events, we can define the relative clustering of critical events of kind i, j smoothed at scales (R_x, R_y) and located at positions $(\boldsymbol{r}_x, \boldsymbol{r}_y)$, $\xi_{ij}(\boldsymbol{s})$ as

$$1 + \xi_{ij}(\mathbf{s}) = \frac{\langle \mathrm{cond}_i(\boldsymbol{x}) \times \mathrm{cond}_j(\boldsymbol{y})\rangle}{\langle \mathrm{cond}_i(\boldsymbol{x})\rangle\langle \mathrm{cond}_j(\boldsymbol{x})\rangle}\,, \tag{3.29}$$

with

$$\mathbf{s} \equiv \sqrt{2}\left(\frac{\boldsymbol{r}_x - \boldsymbol{r}_y}{\sqrt{R_x^2 + R_y^2}}\right), \tag{3.30}$$

the event separation between $\boldsymbol{x}(\mathbf{0})$ and $\boldsymbol{y}(\boldsymbol{s})$. Evaluating the expectation in equation (3.29) requires full knowledge of the joint statistics of the field $P(x, x_i, x_{ij}, x_{ijk}, y, y_i, y_{ij}, y_{ijk})$ (involving 40 variables, see section 3.A.2).

We rely on Monte-Carlo methods in MATHEMATICA in order to evaluate numerically equation (3.29). Namely, we draw random numbers from the conditional probability that $\boldsymbol{x}$ and $\boldsymbol{y}$ satisfy the joint PDF, subject to the condition that $x_k = 0$, $y_k = 0$, $x = \nu_1$ and $y = \nu_2$. For each draw $(\boldsymbol{x}^{(k)}, \boldsymbol{y}^{(k)})$ depending on the type of critical event hence the sign of $\mathrm{tr}(x_{ij})$ and $\mathrm{tr}^2(x_{ik}) - \mathrm{tr}(x_{ik}x_{kj})$ we drop or keep the sample; if it is kept, we evaluate $|J(\boldsymbol{x})|\delta_{\rm D}^{(\epsilon)}(D(\boldsymbol{x}))\,|J(\mathbf{y})|\delta_{\rm D}^{(\epsilon)}(D(\boldsymbol{y}))$ where $\delta_{\rm D}^{(\epsilon)}$ is a normalized gaussian of width ϵ, which in the limit of $\epsilon \to 0$ would correspond to a

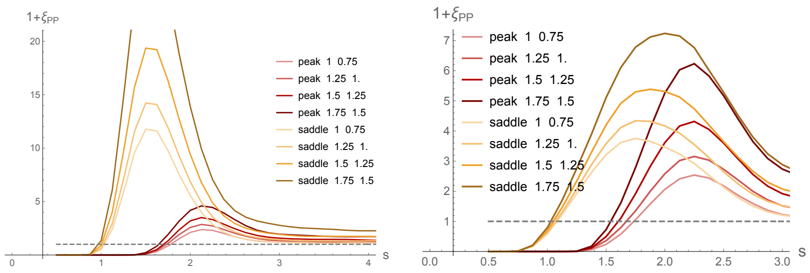

(a) 3D **(b)** 2D

Figure 3.8: (a): The auto-correlation of peak merger $\xi_{\mathcal{PP}}$ (in shades of red, as labelled in terms of the height of the two critical points) and the cross correlation of peak and filament merger $\xi_{\mathcal{PF}}$ (in shades of yellow, as labelled) as a function of separation s. As expected, the saddle mergers are clustered closer to the higher peak compared to the peak mergers. (b): The two-point correlation of events in 2D fields with scale invariant power spectra of index $n_{\rm s} = -1$

Dirac function imposing here that the two determinants are zero. Eventually

$$\langle \mathrm{cond}_i(\mathbf{x})\mathrm{cond}_j(\mathbf{y})\rangle \approx \frac{P_m(x=\nu_1, y=\nu_2, x_l=y_l=0)}{N} \sum_{k\in\mathcal{S}_{ij}} \left|J(\mathbf{x}^{(k)})\right| \delta_{\rm D}^{(\epsilon)}\left(D(\mathbf{x}^{(k)})\right) \left|J(\mathbf{y}^{(k)})\right| \delta_{\rm D}^{(\epsilon)}\left(D(\mathbf{y}^{(k)})\right),$$

where N is the total number of draws, P_m the marginal probability for the field values and its gradients, and $\mathcal{S}_{ij}$ is the subset of the indices of draws satisfying the constraints i, j on the Hessians. The same procedure can be applied to evaluate the denominator. Equation (3.29) then yields an estimation of $\xi_{ij}(s, \nu_1, \nu_2)$. This algorithm is embarrassingly parallel.

This is illustrated in figure 3.8a which shows the auto-correlation of peak merger $\xi_{\mathcal{PP}}$ on the one hand, and the cross correlation of peak and filament merger $\xi_{\mathcal{PF}}$ on the other at fixed merger height, as labelled. Here we used $\epsilon = 0.1$. Note that because equation (3.29) is a ratio, the prefactors in the counts involving scale all cancel out.

3.5.2 Correlation of peak merger along filament

Let us briefly present the two-point statistics of high density peak mergers while assuming for simplicity that the mergers occur along the same (straight) filament (discussed in section 3.4.2), as it is instructive and simpler. In this approximation we can resort to one dimensional statistics. In the high density limit, we may drop the Heaviside constraint on the sign of the eigenvalues since it anticorrelates with the height of the peak. Then the (1D) correlation function of peak mergers, $1 + \xi_{\nu_1\nu_2}(s)$ of height ν_1 and ν_2 becomes

$$\frac{\langle \delta_{\rm D}(x-\nu_1)\, x_{111}^2 \delta_{\rm D}(x_1)\, \delta_{\rm D}(x_{11})\;\; \delta_{\rm D}(y-\nu_2)\, y_{111}^2 \delta_{\rm D}(y_1)\, \delta_{\rm D}(y_{11})\rangle}{\langle \delta_{\rm D}(x-\nu_1)\, x_{111}^2 \delta_{\rm D}(x_1)\, \delta_{\rm D}(x_{11})\rangle \langle \delta_{\rm D}(y-\nu_2)\, y_{111}^2 \delta_{\rm D}(y_1)\, \delta_{\rm D}(y_{11})\rangle}$$

4.2 Methods

4.2.1 Equations

In this section, I detail the equations used throughout the remaining of the paper. I first derive the equation driving the evolution of the specific angular momentum (sAM) of the gas,

$$\boldsymbol{l} = \boldsymbol{r} \times \boldsymbol{v}. \tag{4.1}$$

To do so, let us start from Euler's equation and the mass conservation equation

$$\frac{\partial \rho}{\partial t} + \boldsymbol{\nabla}\cdot(\rho\boldsymbol{v}) = 0, \tag{4.2}$$

$$\frac{\partial \boldsymbol{v}}{\partial t} + (\boldsymbol{v}\cdot\boldsymbol{\nabla})\boldsymbol{v} = -\frac{\boldsymbol{\nabla}P}{\rho} - \boldsymbol{\nabla}\phi. \tag{4.3}$$

Taking the derivative of equation (4.1) w.r.t. time, one gets that

$$\frac{\mathrm{d}\boldsymbol{l}}{\mathrm{d}t} = \boldsymbol{r} \times \left(\frac{\partial \boldsymbol{v}}{\partial t} + (\boldsymbol{v}\cdot\boldsymbol{\nabla})\boldsymbol{v}\right) + \left(\frac{\partial \boldsymbol{r}}{\partial t} + (\boldsymbol{v}\cdot\boldsymbol{\nabla})\boldsymbol{r}\right) \times \boldsymbol{v}. \tag{4.4}$$

After trivial algebra, the rightmost part of the right hand side vanishes. The Lagrangian time derivative of the sAM then reads

$$\frac{\mathrm{d}\boldsymbol{l}}{\mathrm{d}t} = \boldsymbol{\tau}_P + \boldsymbol{\tau}_\phi, \tag{4.5}$$

where $\boldsymbol{\tau}_P \equiv -\boldsymbol{r} \times \boldsymbol{\nabla}P/\rho$, $\boldsymbol{\tau}_\phi = -\boldsymbol{r} \times \boldsymbol{\nabla}\phi$ are the specific pressure and gravitational torques. Here P and ρ are the pressure and density of the gas and ϕ is the gravitational potential. The Lagrangian rate of change describes the evolution of the sAM in the frame comoving with the gas. The potential is defined using Poisson equation

$$\nabla^2\phi = 4\pi G\rho_{\rm tot}, \tag{4.6}$$

where $\rho_{\rm tot}$ is the total matter density (DM, stars, gas and SMBHs). Using the linearity of equation (4.6), the total potential can be written as the sum of the potential due to each component $\phi = \phi_{\rm DM} + \phi_\star + \phi_{\rm gas}$[1]. One can similarly decompose the gravitational torques into three different components $\boldsymbol{\tau}_\phi = \boldsymbol{\tau}_{\phi,\rm DM} + \boldsymbol{\tau}_{\phi,\star} + \boldsymbol{\tau}_{\phi,\rm gas}$.

4.2.2 Numerical simulation

I have run a suite of three $50\,\mathrm{cMpc/h}$-wide cosmological simulations, hereafter named S1, S2, S3. The three simulations contain 6 halos with $M \gtrapprox 5 \times 10^{11}\,\mathrm{M}_\odot$, hereafter named A, B, C, D, E and F. Their properties are presented in Table 4.1. The size of the zoomed Lagrangian volume in the initial conditions is chosen to encapsulate twice the virial radius of the halo at $z = 2$. The simulation are started with a coarse grid of 128^3 (level 7) and several nested grids with increasing levels of refinement up to level 11. The adopted cosmology has a total matter density of $\Omega_m = 0.3089$, a dark energy density of $\Omega_\Lambda = 0.6911$, a baryonic mass density of $\Omega_{\rm b} = 0.0486$, a Hubble constant of $H_0 = 67.74\,\mathrm{km\,s^{-1}\,Mpc^{-1}}$, a variance at $8\,\mathrm{Mpc}$ $\sigma_8 = 0.8159$, and a non-linear power spectrum index of $n_s = 0.9667$, compatible with a Planck 2015 cosmology (Planck Collaboration, 2015).

The simulations include a metal-dependant tabulated gas-cooling function following Sutherland and Dopita, 1993 allowing gas to cool down to $T \sim 10^4\,\mathrm{K}$ via Bremsstrahlung radiation (effective until $T \sim 10^6\,\mathrm{K}$), via collisional and ionisation excitation followed by recombination (dominant for $10^4\,\mathrm{K} \leq T \leq 10^6\,\mathrm{K}$) and via Compton cooling. The metallicity of the gas in

[1] Here I neglect the contribution from SMBHs as it is negligible on galactic scales.

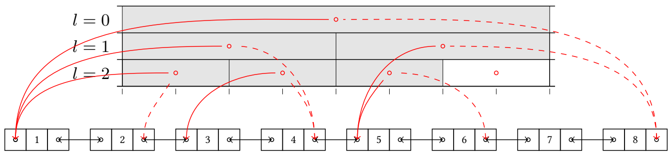

(a) Fully-linked state.

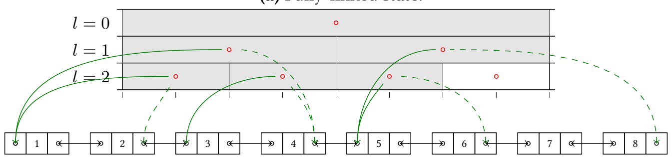

(b) Deposing particles to level 1.

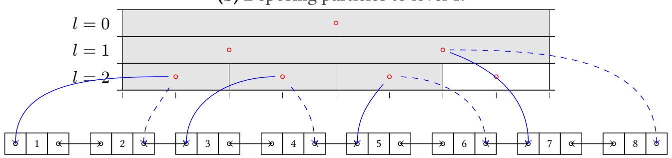

(c) Deposing particles to level 2.

Figure 4.1: Scheme of the linked list holding the particles and the AMR tree, refined octs are shown in grey. At the beginning of a step, each oct at all level has a pointer to the first (solid colored arrows) and last particle (dashed colored arrows) they contain (a). Starting from coarse levels down to finer levels, the code detaches particles from the coarse octs and attaches them to the corresponding child oct (b). If no child oct is found, the particles that are left are kept at the previous level, as is the case for the rightmost oct at level 1 (c). **[♡ Move me somewhere... or not?]**

where the expectation is over the Gaussian PDF whose covariance for the field $(x, x_1, x_{11}, x_{111}, y, y_1, y_{11}, y_{111})$ obeys

$$\begin{pmatrix} 1 & 0 & -\gamma & 0 & \gamma_{00} & \gamma_{01} & \gamma_{02} & \gamma_{03} \\ 0 & 1 & 0 & -\tilde{\gamma} & \gamma_{01} & \gamma_{11} & \gamma_{12} & \gamma_{13} \\ -\gamma & 0 & 1 & 0 & \gamma_{02} & \gamma_{12} & \gamma_{22} & \gamma_{23} \\ 0 & -\tilde{\gamma} & 0 & 1 & \gamma_{03} & \gamma_{13} & \gamma_{23} & \gamma_{33} \\ \gamma_{00} & \gamma_{01} & \gamma_{02} & \gamma_{03} & 1 & 0 & -\gamma & 0 \\ \gamma_{01} & \gamma_{11} & \gamma_{12} & \gamma_{13} & 0 & 1 & 0 & -\tilde{\gamma} \\ \gamma_{02} & \gamma_{12} & \gamma_{22} & \gamma_{23} & -\gamma & 0 & 1 & 0 \\ \gamma_{03} & \gamma_{13} & \gamma_{23} & \gamma_{33} & 0 & -\tilde{\gamma} & 0 & 1 \end{pmatrix}, \tag{3.31}$$

where for instance $\gamma_{02}(s) = \langle x(0) y_{22}(s) \rangle$. The dominant contribution in the large threshold $\nu_1, \nu_2 \gg 1$, large separation $s \gg 1$ regime reads

$$\Delta\xi^{0}_{\nu_1\nu_2}(s) = \frac{\nu_1\nu_2\left(\gamma_{00}(s) + \gamma\left(2\gamma_{02}(s) + \gamma\gamma_{22}(s)\right)\right)}{(1-\gamma^2)^2}, \tag{3.32}$$

which as expected scales like the underlying correlation, $\gamma_{00}(s)$, boosted by the bias factor $\nu_1\nu_2$ (Kaiser, 1984). In that limit, the sub-dominant correction to the correlation function involving the third derivative of the field reads

$$\Delta\xi^{1}_{\nu_1\nu_2}(s) = \frac{2\left(\tilde{\gamma}^2\gamma_{11}(s) + 2\tilde{\gamma}\gamma_{13}(s) + \gamma_{33}(s)\right)^2}{(1-\tilde{\gamma}^2)^2}, \tag{3.33}$$

where $\tilde{\gamma}$-weighted linear combination of the autocorrelation of $\nabla\Delta\delta$ and the cross correlation of $\nabla\Delta\delta$ and $\nabla\delta$ appear, evaluated at events separated by s. The assumption of successive mergings of peaks occurring along a straight filament is of course very idealised, and prevents us from considering cross correlations between peak mergers and e.g. filament mergers.

3.5.3 Conditional merger rates in vicinity of larger tides

In the context of galaxy formation, it is of interest to quantify conditional merger rates computed subject to tides imposed by the large scale structure to explain geographically the origin of assembly bias. To do so we must compute the conditional event counts, subject to a given large scale critical point at some distance $\boldsymbol{s}$ from the running point $\boldsymbol{x}$. The critical point can be e.g. a peak of a given geometry and height, if one is concerned with the impact of clusters on mergers trees of dark halos in their vicinity (Hahn et al., 2009; Ramakrishnan et al., 2019), or it could be a saddle point, as a proxy for a larger scale filament, when studying how halos growth stalls in such vicinity (Borzyszkowski et al., 2017; Musso et al., 2018). In turn this involves the joint expectation

$$\langle \mathrm{cond}_j(\boldsymbol{x})\, \delta_{\mathrm{D}}(y_i) |\det y_{ij}| \rangle\,. \tag{3.34}$$

Evaluating equation (3.34) requires full knowledge of the joint statistics of the field at $\boldsymbol{x}(\boldsymbol{0})$ and $\boldsymbol{y}(\boldsymbol{s})$, $\mathcal{P}(x, x_i, x_{ij}, x_{ijk}, y, y_i, y_{ij})$ (involving 30 variables). The correlations of the PDF involves the covariance of the field and its derivatives computed at two smoothing scales, R and R_c corresponding to the proxy for the timeline of the halos on the one hand and the large scale structure on the other hand. We can then marginalise over all variables, subject to e.g. imposing the height, ν_c and shape, μ_i^c of the large scale critical mode:

$$\langle \mathrm{cond}(\boldsymbol{x})\delta_{\mathrm{D}}(y_i)|\det y_{ij}|\delta_{\mathrm{D}}(x-\nu)\delta_{\mathrm{D}}(y-\nu_c)\vartheta_{\mathrm{H}}(-\lambda_i)\,\delta_{\mathrm{D}}(\mu_i-\mu_i^c)\rangle$$

where λ_i are the eigenvalues of x_{ij} and μ_i are the eigenvalues of y_{ij}. The conditions imposed by the mergers and the properties of the peaks and large scale environment reduces the number of integrals from 30 to 21. Section 3.C.3 describes how to sample conditional event counts using constrained realisation of Gaussian random fields.

For the sake of simplicity, let us illustrate here the conditional merger rates in 2D. Let us impose given large scale saddle with curvature $1/2, -1/3$ and look a the excess probability of having a a merger of type j at some distance r and orientation θ w.r.t. to the frame set by the saddle. **[♠ CP will do plot and conclude.]**

3.6 Measurements for Gaussian random fields

Let us validate the theory while counting critical events within realisations of Gaussian random fields. We then bin them to estimate their one and two point statistics.

3.6.1 Method

For each power-law power spectrum with spectral index $n_\mathrm{s} = -2, -1.5, -1, -0.5$, we have generated 200 gaussian random fields. We have also generated 200 gaussian random fields with a ΛCDM power spectrum using `mpgrafic` (Prunet et al., 2008) in a Planck Collaboration, 2018 cosmology generated using the Eisenstein and Hu, 1999 fitting formula. Each realisation will henceforth be called a "cube". Each cube has a size of 256^3 pixels and a physical extent of $100\,\mathrm{Mpc}/h$.[3] We have smoothed each cube using a Gaussian filter with scale ranging from $1\,\mathrm{Mpc}/h$ to $20\,\mathrm{Mpc}/h$ (2.56 px to 51.2 px). The smoothing operation were operated in Fourier space, assuming periodic boundary conditions. At each scale, we have detected all critical points (minima, saddle points and extrema) using the method detailed in section 3.C.1. We have then detected the critical events using the method detailed in section 3.C.2.

Additionally we have generated 200 2048^2 cubes with a power-law power spectrum with spectral index $n_\mathrm{s} = -1$ and a physical box size of $1\,000\,\mathrm{Mpc}/h$ which we smoothed with a Gaussian filter with scale ranging from $1\,\mathrm{Mpc}/h$ to $20\,\mathrm{Mpc}/h$.

3.6.2 Critical events counts

In this section we present the number density of critical event measured in cubes with a power-law power spectrum and compare the theoretical predictions of section 3.4.3 to measurements in cubes.

We first measured the ratio of the number of critical events of different kind. We found $r_{\mathcal{F}/\mathcal{P}} = r_{\mathcal{F}/\mathcal{W}} \approx 2.1$, regardless of the smoothing scale or the underlying power spectrum. This excess of about 2% in the ratio originates to an over-detection of saddle point with respect to local extrema. Theory predicts this ratio to be $N_\mathrm{saddle}/N_\mathrm{peak} \approx 3.055$ in 3D (see e.g. Codis et al., 2018, equation 2) while the measured value is 3.1. In the following of the chapter, we have corrected the excess number density of $\mathcal{F}, \mathcal{W}$ critical events.

Let us now proceed to the number count at fixed density. Figure 3.9 shows the PDF of the critical events as a function of their height for different power-law spectra ($n_\mathrm{s} = -2, -1.5, -1, -0.5$, ΛCDM). The critical events have been selected at scale $2.35\,\mathrm{Mpc}/h \leq R \leq 3.01\,\mathrm{Mpc}/h$ ($6.0\,\mathrm{px} \leq R \leq 7.7\,\mathrm{px}$). The lower boundary ensures that the critical points are well separated[4]. The upper boundary is fixed so that the smoothed cubes have consistent effective spectral parameters $\gamma_\mathrm{eff}(R)$ and $\tilde{\gamma}_\mathrm{eff}(R)$. Indeed the cubes have scale-dependant spectral parameters induced by the finiteness of the box and the discreteness of the grid (see e.g. Gay, 2011, figure 5.1). Errorbars

[3] The box size is only relevant in the ΛCDM case, as the power-law cases are scale invariant.

[4] Critical points are typically separated by $R_* \gtrsim 0.6R$ (for $n_\mathrm{s} < 0$), so $R = 6\,\mathrm{px}$ gives a typical separation of 3.6 px between critical points, which is larger than the number of points used to infer the curvature.

before it reaches the disk. The details of where this AM will end up are key to understand the AM distribution in galaxies, but also to understand to what extent their spin is aligned with the cosmic web. If the dominant forces acting on the AM are pressure forces, resulting from internal processes (SN winds, AGN feedback bubles), then the spin of the galaxy would likely be a result of chaotic internal processes and would lose its connection to the cosmic web. Similarly, if the AM is lost into thermal energy (which is then radiated away) in shocks, the galactic spin would be a weak function of the large-scale AM induced by the cosmic web. On the contrary, if the dominant forces are gravitational forces, then the spin-down of the cold gas is likely to drive a spin-up of either the disk or the dark matter halo, which themselves are the result of their past AM accretion history. In this last scenario, the details of which part(s) of the halo or the disk interact exchange AM with the infalling material would constrain models aimed to understand the evolution of the spin of galaxies.

Historically, the study of cold accretion has been particularly challenging in numerical simulations. Early simulations using SPH methods largely over-estimated the fraction of gas accreted cold (see e.g. Nelson et al., 2013, for a discussion on this particular issue) as a result of the difficulty to capture shock using SPH. AMR simulations do not suffer from this caveat (Ocvirk et al., 2008), yet they fail at providing the Lagrangian history of the gas — in particular its past temperature — which is required to detect the cold-accreted gas. In order to circumvent this limitation, most simulations relied on velocity-advected tracer particles (Dubois et al., 2013; Tillson et al., 2015). However, this approach yields a very biased tracer distribution that fails at reproducing correctly the spatial distribution of gas in filaments: most tracer particles end up in convergent regions (center of galaxies, center of filaments) while divergent regions are under-sampled. In order to reproduce more accurately the gas distribution, Genel et al., 2013 suggested to rely on a Monte-Carlo approach where tracer particle follow mass fluxes instead of being advected. Using this approach, Cadiou et al., 2019 showed that tracer particles are able to faithfully reproduce the gas distribution while providing the Lagrangian history of the gas, and in particular its past temperature and position.

In this chapter, I detail the results obtained from cosmological simulations of group progenitors as $z > 2$. I provide a detailed study of the evolution of the AM of the cold and hot gas. In particular, this chapter aims at answering the question of which forces are responsible for the spin-down and realignment of the AM of the gas accreted in the two modes of accretion (hot and cold). Section 4.2 presents the numerical setup and tools I used. In particular, I developed new numerical methods tailored to the problem of cosmic accretion: I developed a new tracer particle scheme for the AMR code Ramses. I also implemented new methods to extract the gravitational potential of the gas, stars and dark matter respectively as well as a new post-processing tool to compute pressure gradients. Section 4.3 presents a detailed study of the AM evolution of the cold and hot gas. It details the evolution of the magnitude and orientation of the AM and the different forces and torques at play in the different regions of the halos. Section 4.4, I discuss the results and their implication on the distribution of AM in the galaxy and the inner halo. Finally, section 4.5 wraps things up and concludes.

[♡ move this] In most AMR codes, the collisionless fluids (stars, DM, black holes) are represented as particles that live on the AMR grid. In Ramses, particles are stored in a doubly-linked-list ; this structure has the advantage to enable insertions and deletions in time $\mathcal{O}(1)$, at the cost of requiring $\mathcal{O}(N)$ of memory, where N is the number of particles. Each oct has also a pointer to the head and the tail of the linked particle list, as illustrated on figure 4.1.

initial tiny density fluctuations ot the primordial density field and under the effect of gravitational forces, matter departs underdense region to flow through cosmic sheets into filamentary structures. Dark matter then flows from these filaments towards high-density peaks that will later become halos. In the process, matter acquires properties in their journey through voids, sheets and filaments of the cosmic web which in turn affect the assembly of dark matter halos, as shown in chapter 3. Baryons follow the same initial fate as DM and flow from underdense regions to sheets. Yet, as they flow in sheets, pressure forces prevents them from shell-crossing so that they lose their normal velocity component. Following potential wells created by dark matter, baryons then flow towards filamentary structures where they lose a second component of their velocity and reach a dense-enough state to efficiently cool radiatively.

At first order, galaxies formation is affected by the mass of their dark matter host and the local environment, as encoded by the local density on sub-Mpc scales, as it is assumed that baryons have the same past accretion history as dark matter. These models have proven successful at explaining a number of observed trends, in particular against isotropic statistics, in the so-called halo model, yet they fail at explaining some effects such as spin alignments (Chisari et al., 2017; Codis et al., 2015b; Dubois et al., 2014), colour segregation (Kraljic et al., 2018; Kraljic et al., 2019; Laigle et al., 2018) or star formation rates (Kraljic et al., 2019; Malavasi et al., 2017). Indeed, galaxies form by converting their gas into stars and by successive mergers, which are in turn affected by the tides and large-scale modulations of the density field induced by the cosmic web. The detailed history of how the gas was acquired and how much angular momentum (AM) it brought, as well as the origin of the mergers should in principle impact the formation of the galaxy. Since the physical processes involved in dark matter halos formation differ from the baryonic processes at the core of galaxy formation, one can expect that the cosmic web will have a different impact, if any, on the formation of galaxies and may explain the disparity of their properties in similar-looking dark matter halos.

In particular, at fixed halo mass and local density, properties of galaxies such as their colour or the kinematic structure varies with their location in the cosmic web. One key process in the differential evolution of galaxies is gas accretion. Indeed, at large redshifts it has been suggested that the accretion of gas is dominated by flows of cold gas funnelled from the large scales to galactic scales (Birnboim and Dekel, 2003; Dekel and Birnboim, 2006). This mode of accretion has then be confirmed in numerical simulations using different methods (Nelson et al., 2013; Ocvirk et al., 2008) as the source of a significant fraction of the baryonic mass but also AM (Kimm et al., 2011; Tillson et al., 2015) and it has been proposed that these flows may feed supermassive black holes (Dubois et al., 2012), which in turn affect the inflow rates (Dubois et al., 2013; van de Voort et al., 2011a; van de Voort et al., 2011b). Using an extension of Tidal Torque Theory (TTT) (Peebles, 1969; Schaefer, 2009), Codis et al., 2015b showed that anisotropic environments, such as large-scale filamentary structures, biases the AM distribution to align it with the cosmic web. This gas will then fall in galaxies *via* cold flows, feeding disks with angular-momentum rich gas that is itself aligned with the tides of the cosmic web.

Recent works have shown that the flows are subject to a variety of processes: they may fragment (Cornuault et al., 2018) or be disrupted by hydrodynamical instabilities (Mandelker et al., 2016; Mandelker et al., 2018) but they are also sensible to feedback events (Dubois et al., 2013). In this context, Danovich et al., 2015 showed that in numerical simulations, cold flows are nevertheless able to feed galaxies with angular-momentum rich material. In this study, it was advanced that the AM acquired outside the halo is transported down to the inner halo; the gas then settles in a ring surrounding the disk, where gravitational torques spin the gas down to the mean spin of the baryons. Another study, albeit at larger redshifts, found that the dominant force was pressure (Prieto et al., 2017). Since their is not much freedom on the final AM of the galaxies, as constrained by their radius, the excess AM brought by cold flows has to be redistributed somehow

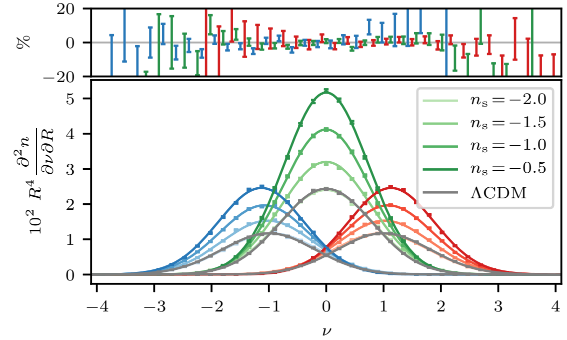

Figure 3.9: PDF of the critical events as a function of height in a scale invariant GRF as labelled. The left bundle corresponds to void mergers, the middle bundle to filaments mergers and the right bundle to peak mergers. The plain curve corresponds to the theory while the error bars correspond to the error on the mean extracted from 160 simulations. The grey lines are the results obtained for a ΛCDM power spectrum initially smoothed over a scale of $2.5\,\mathrm{Mpc}/h$. The top panel shows the residuals for $n_s = -2$. The detection algorithm is still accurate in 3D.

have been estimated using a bootstrap method ran on 400 subsamples each made of 50 randomly chosen cubes. Solid lines show the result of a fit of the theoretical formula to the cube data with free parameters $\hat{\gamma}, \hat{\tilde{\gamma}}$.

The effective spectral index $\hat{n}_s$ is fixed using $\gamma = \sqrt{(n_s+3)/(n_s+5)}$. We find values of γ and $\tilde{\gamma}$ consistent with the effective values measured directly in the cubes using equation (2.92). For example with $n_s = -2$ we measure in the cubes $\gamma_{\mathrm{eff}} = 0.62 \pm 0.02, \tilde{\gamma}_{\mathrm{eff}} = 0.72 \pm 0.01$ ($n_{s,\mathrm{eff}} = -1.75 \pm 0.13$) using equation (2.92). The mean values have been estimated with a sample of 100 cubes and the errors are the standard deviations of the sample. The fitting procedure on the PDF of the critical events yields $\hat{\gamma} = 0.621 \pm 0.002, \hat{\tilde{\gamma}} = 0.737 \pm 0.004$ ($\hat{n}_s = -1.74 \pm 0.02$). The relative difference between theory and measurements, presented on the upper panel of figure 3.9, show no systematic deviation of the measurements and is within a few percents in the region where most of the events are.

In order to further test the theoretical prediction, we have proceeded to the same analysis in the 2D case. The results are presented on figure 3.10 and show that the agreement between theory and measurements is of the order of the percent. Once again, no systematic deviation of the measurements is noted. The results in 2 and 3D confirm the analytical formula derived in section 3.4.3 and illustrate the accuracy of the detection algorithm presented in section 3.C. Interestingly, since the algorithm has been designed to make no assumption on the number of dimensions, it is expected to work as well in d dimensions.

3.6.3 Two point statistics

Let us now estimate the two-point statistics of critical events. Let us write formally A and B any two subsets of critical events. Their correlation function can be numerically estimated using

$$\xi_{AB}(s) = \frac{\langle AB \rangle}{f\sqrt{\langle AR_A \rangle \langle BR_B \rangle}}, \tag{3.35}$$

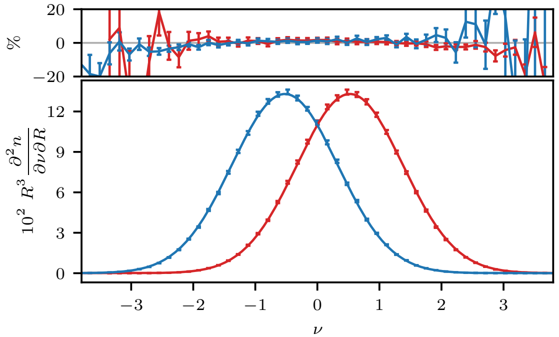

Figure 3.10: PDF of the critical events as a function of height in a scale invariant GRF in 2D with spectral index $n_s = -1$. The left curve corresponds to filament mergers and the right curve to peak mergers. The plain curve correspond to the theory while the error bars correspond to the error on the mean extracted from 200 simulations. The top panel shows the residuals. The agreement between the analytic prediction and the measurements reflects the accuracy of the algorithm presented in section 3.C in identifying critical events.

where R_A and R_B are uniformly distributed random points with $1/f$ times the number of points as A and B respectively. We have additionally checked that common estimators, such as the Landy-Szalay estimator yield similar results. This is further discussed in section 3.D, which shows that both estimators yield similar results at scales of interest to our analysis ($s = r/R \gtrsim 1$). For each cube in the simulation, we select all critical events in a thick slice of smoothing scales ($\Delta R/R = 0.3$). We then select two subsamples, the first is selected at an overdensity $\nu = 1$ with kind j and the second at $\nu = 0.7$ with kind k ($j, k \in \{\mathcal{P}, \mathcal{F}, \mathcal{W}\}$). The correlation functions are then given by the number of pairs at distance $s = r/R$ in all cubes using equation (3.35). The pair counting was done using a dual-tree algorithm, as described in Moore et al., 2001[5].

Figure 3.11 shows the measured correlation functions in 2D for a power law power spectrum with spectral index $n_s = -1$ (top panel) and in 3D with a ΛCDM power spectrum smoothed at scales between 1 and $20\,\mathrm{Mpc}/h$ (bottom panel). In both cases the $\mathcal{PF}$ correlation function (peak merger to filament merger correlation) peaks at $r \approx 1.5R$ while the $\mathcal{PP}$ correlation function (peak merger autocorrelation) peaks at $r \approx 2.5R$. This indicates that each halo merger is more likely to be followed by a filament merger compared to another halo merger. Interestingly, peak mergers are also more likely to be followed by void mergers. Indeed, a halo merger induces a topological defect, as it leads to a resulting over-connected halo. The defect is quickly corrected by a filament merger, decreasing the local connectivity of the halo back towards the cosmic average. Doing so another topological defect appears as a void becomes under-connected as one of its walls disappeared. This last defect is then corrected by a last void merger that makes the under-connected void disappear. On average, critical events appear so that the global ratio of peak-to-filament, filament-to-walls and wall-to-void stays constant as smoothing increases, so that the global connectivity is preserved. The link between critical events and global connectivity of the cosmic web is further discussed in section 3.7.2.

[5] See the scipy doc for more information.

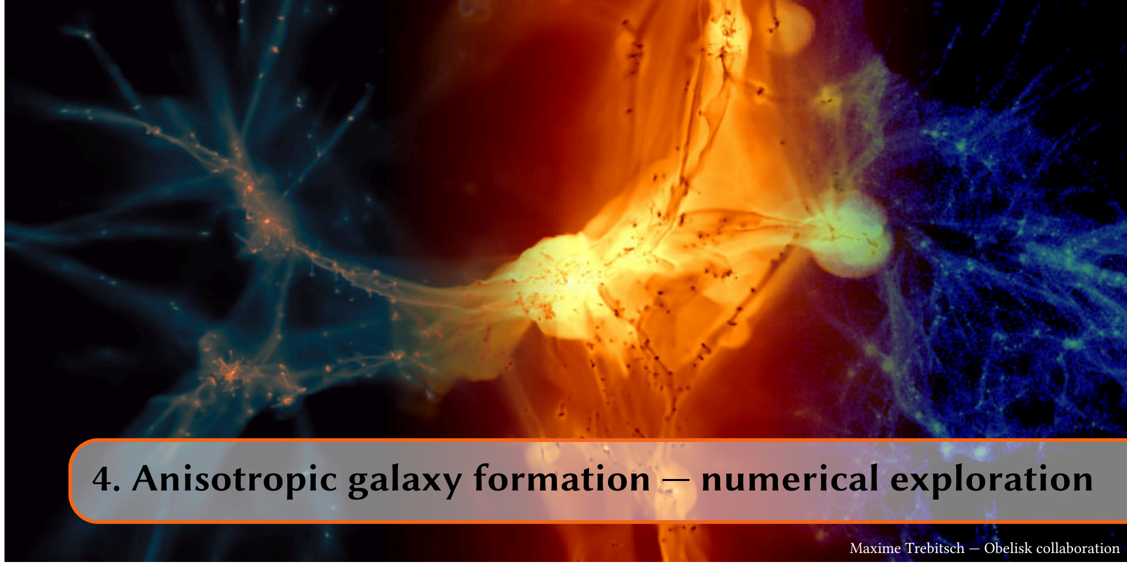

4. Anisotropic galaxy formation — numerical exploration

Maxime Trebitsch — Obelisk collaboration

Outline

4.1 Introduction

One of the success of the ΛCDM model is its ability to reproduce the large-scale structure of the Universe observed in galaxy distribution (e.g. Springel et al., 2006). These structure form out the

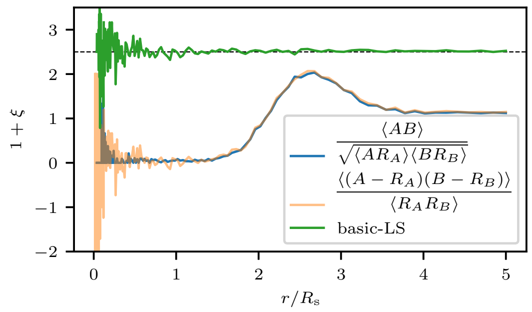

Figure 3.23: $\mathcal{PP}$ correlation function in the 2D case using the estimator of equation (3.35) (blue line) vs the Landy-Szalay estimator (light orange line). The difference (green line) has been shifted by 2.5 for visualisation purposes. The LS estimator yields a correlation function that is more noisy at small separations.

function. Let us restrict to two estimators, the first one being

$$\xi_{AB} = \frac{\langle AB \rangle}{f\sqrt{\langle AR_A \rangle \langle BR_B \rangle}}, \tag{3.85}$$

where A, B is the two catalogs we are cross correlating and R_A, R_B are random samples with $1/f$ times more data than A, B respectively. We compare this estimator to the popular Landy-Szalay (LS) estimator (Landy and Szalay, 1993; Szapudi and Szalay, 1999)

$$\xi_{AB,\text{LS}} = \frac{\langle (A - R_A/f)(B - R_B/f) \rangle}{\langle R_A R_B \rangle / f^2}. \tag{3.86}$$

The results are shown on figure 3.23. At large scales, both estimators converge to the expected value of one. However at small scales, the LS estimator is more noisy. This is due to **[♡ Simon, an idea?]**. Following a pragmatic approach we have used throughout all our analysis the estimator of equation (3.35).

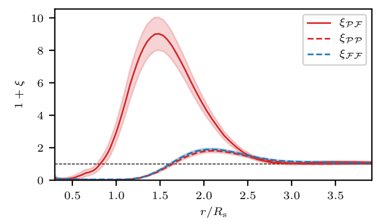

(a) 2D

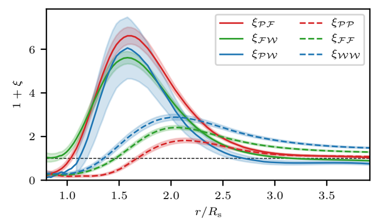

(b) 3D

Figure 3.11: (a): Correlation functions between critical events $\mathcal{P}, \mathcal{F}$ in 2D at fixed smoothing scale. (b): Correlation functions between critical events $\mathcal{P}, \mathcal{F}, \mathcal{W}$ in 3D at fixed smoothing scale. Pairs of critical events have been selected at $\nu = 0.7$ and $\nu = 1.0$. The correlation function of halo-merger with filament-merger, $\xi_{\mathcal{PF}}$, peaks at $r \sim 1.5R$ while the halo-merger autocorrelation functions $\xi_{\mathcal{FF}}$ peaks at $r \sim 2R$. This shows that halo-mergers are more likely to be followed by filament-mergers. The data have been filtered using a Savgol filter. Errorbars have been estimated assuming a Poisson noise on the sample.

3.7 Applications and discussion

The scope of application of the present formalism is obviously very wide. Rather than attempting to cover it all, only a few examples will be presented, while a more thorough investigation is left for future work.

In a cosmic framework, section 3.7.1 will first translate the one point statistics presented in the previous section into merger rates as a function of mass and redshift. Section 3.7.2 explains how mergers of filaments need to match that of peaks in order to preserve the connectivity of peaks. Section 3.7.3 explains how conditional merger counts in the vicinity of a filament explains how the environment drives assembly bias. Section 3.7.4 show how the critical events can be used to compress the initial cosmological condition into a very finite set of points as a mean to predict the properties of galaxies emerging from these conditions using machine learning tools. Section 3.7.5 illustrates how the wall merger rates yield constraint on modified gravity or primordial non gaussianities. Finally, applications to other fields of research in cosmology (intensity maps, weak lensing, void statistics) and beyond are discussed in section 3.7.6.

3.7.1 Merger rates in M, z space

The skeleton tree formalism over which the present work is built present some resemblance to Extended Press Schechter theory (EPS) and excursion set theories, but with noticeable differences. Let us highlight the advantages and limitations of the present formalism. In its original form, excursion set theory Bond et al., 1991 assumes that the steps involved in averaging over larger and larger scales are fully uncorrelated, hence ignores the correlation of the field on various scales.

It is straightforward to change variable from R to M ($= \alpha\frac{4}{3}\pi\bar{\rho}R^3$) and from ν to z using the spherical collapse condition with a Gaussian filter (equations 3.1 and 3.2), so that for condition c

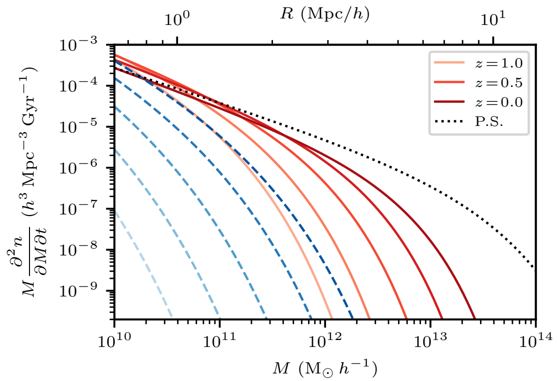

Figure 3.12: PDF of the halo merger rate (solid red lines) and the wall merger rate (dashed blue lines) as a function of redshift of formation, see the text for details. For small masses the merger rate follows the Press-Schechter (Press and Schechter, 1974) halo mass function (up to an **[♡ arbitrary]** renormalisation, black dotted line), while at larger masses the halo merger rate decays significantly faster. As expected, the transition mass increases with time. The same evolution is found for void mergers.

(peak, saddle, void) we have[6]

$$\left.\frac{\partial^2 n}{\partial \log M \partial z}\right|_c = \left.\frac{\partial^2 n}{\partial R \partial \nu}\right|_c \frac{\partial R}{\partial \log M}\frac{\partial \nu}{\partial z}$$

$$= -\left.\frac{\partial^2 n}{\partial R \partial \nu}\right|_c \frac{\delta_c}{3D(z)^2}\frac{\mathrm{d}D}{\mathrm{d}z}\alpha\left(\frac{3M}{4\pi\bar{\rho}}\right)^{1/3}, \tag{3.36}$$

where $\alpha \approx 2.1$ and $\bar{\rho} \approx 2.8 \times 10^{11}\, h^2 \mathrm{M}_\odot/\mathrm{Mpc}^3\, \Omega_\mathrm{M}$ (see e.g. Musso et al., 2018, Table A1).

From equations (3.13) and (3.36), we are in a position to count how many (peak, filament, void) mergers occur early or late in the accretion history of a certain mass or within some mass range, via straightforward integration. This also allows us to quantify the rate of small mergers within some time sequence.

For instance, equation (3.36) yields the number of expected mergers involving satellite of mass M at redshift z if a type of merger condition is imposed. Note that for collapsing filaments and walls the δ_c threshold should be different (Pogosyan et al., 1998).

Figure 3.12 shows the merger rate of peaks and voids as a function of the mass of non linearity. The cosmology-dependant terms of equation (3.36) have been computed using the code Colossus (Diemer, 2018) in a Planck cosmology. In order to evaluate the number density of critical events, we have assumed a scale-dependant equivalent power-law power spectrum[7]. At small masses, the peak merger rate behaves like a Press-Schechter function (up to a renormalisation) while at large masses, the decay is faster than Press-Schechter, see section 3.7.1.1 for details. **[♡ need checking] [♡ the rare event limit does not seem to fit in the picture? Mistake there?]** **[♠ discussion: distinguish minor major merger ratios]**

[6] Note that $\mathrm{d}D/\mathrm{d}z = -Df/(1+z)$ with $f \equiv \mathrm{d}\log D/\mathrm{d}\log a \sim \Omega_\mathrm{m}^{0.6}$.

[7] At each scale, the equivalent power-law power spectrum is given by the formula $n_{\mathrm{s,eq}} = -3 - 2\,\mathrm{d}\log\sigma/\mathrm{d}\log R$.

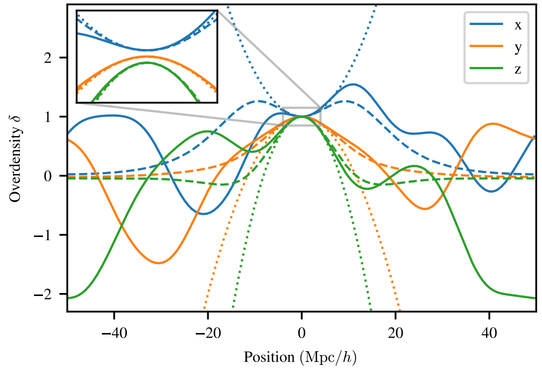

Figure 3.22: Density profile of a random field constrainted to a density $\delta = 1$, null gradient and a hessian with eigenvalues $\sigma_2/2, -\sigma/2, -\sigma$ in directions x, y, z at the centre of the box, assuming periodic boundary conditions. The expectation of the field is shown in dashed lines and the value of the field in one realisation is shown in solid lines. Dotted lines show the second order Taylor series of the field around the constrained point. The inset shows a zoom on the constrained zone. For the sake of clarity, each curve have been shifted by 0.02. At small distances from the constrain, the field resembles its mean and its Taylor expansion.

procedure may leave some heads unpaired (e.g. critical points at the largest smoothing scale do not merge but have no successor). In practice the unpaired heads typically account for less than a percent (0.5 % for $\Delta R = \alpha R \Delta \log R$ with $\alpha = 2$) of the total number of heads.

An alternative to the present algorithm could involve modifying Disperse to only retain points of lowest persistence.

3.C.3 Generation algorithm

We have used ConstrField coupled with MPgrafic from Prunet et al., 2008 to generate constrained realisations of a Gaussian random field. We generate an unsmoothed Gaussian random field, constrained to have a filament-type saddle point of height $\delta = 1$ ($\nu = 1.17$) at smoothing scale $R = 5\,\mathrm{Mpc}/h$. The eigenvalues of the Hessian are constrained to be $\{\lambda_1, \lambda_2, \lambda_3\} = \sigma_2\{-1/2, -1/2, -1\}$ with eigenvectors $\{\hat{x}, \hat{y}, \hat{z}\}$. Figure 3.22 shows the mean density profiles as well as one realisation. As expected, the density is locally entirely set by the constrain and have a parabola-like shape. At larger scales, the field decouples from the constrains resulting in large fluctuations around the mean value.

3.D Comparison of two-point correlation function estimators

In the field of cosmology, some efforts (see Kerscher et al., 2000, and references therein) have been dedicated to build unbiased estimators of the two point correlations. Indeed, such estimator are impacted by the size of the sample as well as finite volume effects if the catalog does not cover the entire sky. Because of periodic boundaries, we do not have problem with the size of the box. Let us take a pragmatic approach in order to pick a suitable estimator of the two-point correlation

8: **if** $c \notin P'_k$ **then**
9: $P'_k \leftarrow P'_k + \{p, c\}$ ▷ Found new progenitor
10: **end if**
11: **end for**
12: $P_k \leftarrow P'_k$
13: **for** c **in** $C_{R,k}$ **do** ▷ Loop over crit. points
14: **if** $c \notin P'_k$ **then** ▷ Keep only unpaired ones…
15: $H_k \leftarrow H_k + \{c\}$ ▷ …and add them to heads
16: $P_k \leftarrow P_k + \{c\}$
17: **end if**
18: **end for**
19: $R \leftarrow R(1 - \Delta \log R)$
20: **end while**
21: **return** H_k ▷ Heads are points with no successors at larger R
22: **end procedure**

Here, $\mathrm{SortedPairs}(X, Y, R_{\max})$ returns (x, y, d), where x, y are points in X, Y and $d \leq R_{\max}$ is their relative distance (in $(\boldsymbol{r}, R)$ space). The tuples are sorted by increasing distance. This can be efficently implemented using a KD-tree with periodic boundary conditions. BuildHeads builds all heads by using a watershed approach. Starting from the largest smoothing scales, it finds and discards all critical events that are progenitors of a head at any larger scale. The remaining points have no successor (they are the progenitor of nothing) and are hence heads.

Once the heads have been computed, the second step of the algorithm pairs them (line 9)

1: **procedure** FindHeadPairs($H_1, \ldots, H_d, R, \Delta R$) ▷ Find pairs of heads (crit. events)
2: $H_{R,k} \leftarrow \{c \in H_k \mid R \leq c.R < R + \Delta R\}$ ▷ Keep heads at scale R
3: $P \leftarrow \{\}$ ▷ Head pair list
4: **for** k **in** $1, \ldots, d-1$ **do**
5: $P \leftarrow P+$SortedPairs($H_{R,k}, H_{R,k+1}, R$)
6: $P \leftarrow P+$SortedPairs($H_{R,k+1}, H_{R,k}, R$)
7: **end for**
8: $P \leftarrow$ SortByDistance(P)
9: $P' \leftarrow \{\}$ ▷ Pairs with no double counts
10: **for** c_1, c_2, d **in** P **do**
11: **if** $c_1 \notin P'$ **and** $c_2 \notin P'$ **then**
12: $P' \leftarrow P' + \{c_1, c_2\}$
13: **end if**
14: **end for**
15: $E \leftarrow \{\}$ ▷ Critical events
16: **for** c_1, c_2 **in** P' **do**
17: $E \leftarrow E+$ CritEventData(c_1, c_2)
18: **end for**
19: **return** E
20: **end procedure**

Lines 5-6 ensure that the detection method is invariant by permutation of $k \leftarrow d - k + 1$. $\mathrm{CritEventData}(c_1, c_2)$ computes the properties (position, kind, gradient, …) of the critical events given two critical points. FindHeadPairs works as follow. It first finds all pairs of heads separated by less than a smoothing scale. It then loops over all pairs (sorted by increasing distance) and greedily consumes heads. Each head can only be paired once, to its closest not-yet-paired head of either the previous or next kind. This prevents for example F critical points points from being paired to a P and a W critical point, which would result in a double count. Note that this

3.7.1.1 Rare event limit

For the large ν limit, equation (3.36) yields

$$\frac{\partial^2 n}{\partial \log M \partial z}\Big|_c \propto \nu^4 M^{1/3} \exp\left(-\frac{\nu^2}{2(1-\frac{5}{9}\gamma^2)}\right), \tag{3.37}$$

so that the merger rate scales like $M^{(2n_s+4)/3}$, with an exponential cut off in $M^{(n_s+3)/3}$ given that $\nu^2 \propto \sigma_0^{-2} \propto R^{n_s+3} \propto M^{(n_s+3)/3}$. Note that the cutoff is $1/(1-\frac{5}{9}\gamma^2)$ faster than for the Press Schechter mass function. [♡ check]

The rate of void disappearance, equation (3.36)

3.7.2 Consistency with cosmic connectivity evolution

The properties of the initial random field was shown by Codis et al., 2018 to control to a large extent the connectivity of dark halos, as defined by the number of connected filaments (locally and globally) at a given cosmic time. The upshot of this work is that the packing of peaks (imposed by their exclusion zone) and saddles implies that 3-4 filaments typically dominate locally. Interestingly, the rate of filament disappearing must match the peak merger rate, in order to preserve this number. Beyond numerology, this rate is important because filaments later feed coherently dark halos, hence their lifespan matters in the subtle balance between environmentally driven disruption versus building up through filamentary cold gas inflow.

In practice, one should distinguish the local and global connectivity (see Codis et al., 2018, for more details). Unfortunately, the link between global connectivity and merger rates that was discussed in the present work does not translate straightforwardly to the local connectivity. Our qualitative understanding of the critical structure of Gaussian random fields remains in close relation to packaging: each vicinity of a critical event or point must by continuity occupy a certain volume of space, as set by its eigenvalues, which puts constrains on the position of other points in the vicinity. The idea is that e.g. before connecting a given peak to a peak of a different height, the field must first go through a local minima along the ridge, which distance is set by the 'width' of that peak. For events, the process of smoothing the field will impact both the local curvature but also the curvature of these other points. Hence it is expected that smoothing jointly disconnects neighbouring peaks as mergers occur: the ridges are smoothed out because technically their saddle points vanish.

We can quantify this process via the two point functions of these events. From the auto- and cross-correlations presented in section 3.5, we can define the ratio of the separation at the peak of these two correlations ($s_{ij} = \mathrm{argmax}_s \xi_{ij}(s)$) as a measure of the relative 'proximity' of the two events. Since this ratio $s_{\mathcal{PF}}/s_{\mathcal{PP}} \approx 3/4$ is smaller than one, it means the rate at which filaments disappear matches the merger rate, so that the typical number of filament per halo remains constant through cosmic time. Figure 3.13 presents a cartoon illustrating how smoothing induces a local $\mathcal{PFFP}$ sequence of mergers in 2D, which preserves the connectivity of peaks, and is consistent with the relative rates of events. Figure 3.14 (left panel) illustrates an analogous consistent $\mathcal{PF}^4\mathcal{P}$ sequence in 3D. The right panel shows how the local connectivity of 3 can also be preserved, as the weaker filaments typically lie off the plane.

Finally, the clustering of filament disappearance impacts the connectivity of peaks as they merge as discussed in the next section, (see figure 3.15, bottom right panel). This is a direct consequence of the clustering of events of the various types.

3.7.3 Assembly bias in the frame of filaments

Let us now make use of the merger statistics to study the impact of the large scale structures on assembly bias, following section 3.5.3. Previous works have highlighted the modulation

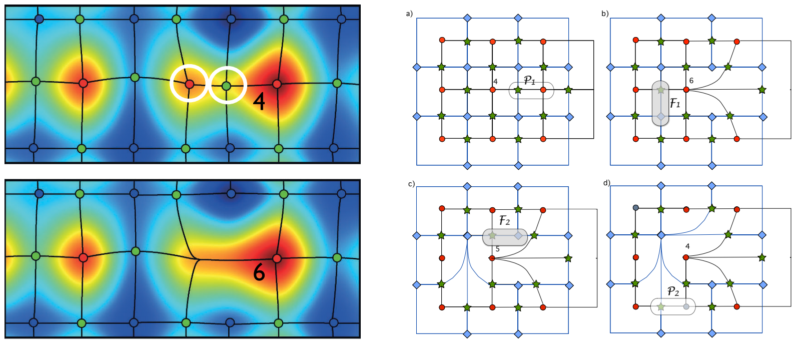

Figure 3.13: *Left*: Snapshots of the density field at two smoothing scales (colour coded from blue, low density to red high density). The black line represents density ridges/trough connecting the red peaks, and the blue voids via the green saddle points. As the two low persistence pair of peaks (in white) merge the connectivity increases from 4 to 6 (as labeled). The fate of this connectivity now depends on the nature and location of the next merger events inspired from Sousbie et al., 2011a. *Right*: As labelled from a) to d) an abstraction of the merger sequence of a 2D 'cosmic crystal' impacting the connectivity of the central peak. Ridges are shown in black while troughs are shown in dark blue. The red circles represent the peaks, the green stars the saddles and the blue diamonds the voids. A $\mathcal{P}_1$ merger (highlighted in light gray) rises the mean connectivity of the central peak from 4 to 6, but the next two $\mathcal{F}_{1,2}$ mergers (highlighted in darker gray) lower it back to 4. The next $\mathcal{P}_2$ merger (panel d) will reduce the void's connectivity. A more realistic representation of this process is also visible on figure 3.4.

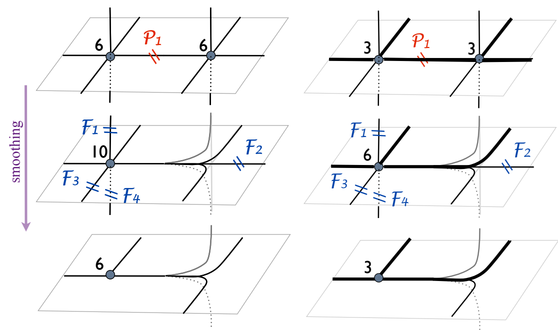

Figure 3.14: Following the cartoon shown in figure 3.13, the left panel shows a smoothing sequence (from top to bottom) which would preserve the connectivity of a 3D peak. It requires that each $\mathcal{P}$ merger should be followed by four $\mathcal{F}$ mergers in the vicinity. The right panel highlights how the multiplicity is preserved if one starts with 3 dominant co-planar filaments.

where $\boldsymbol{\Delta x} = \boldsymbol{x} - \boldsymbol{x}_\mathrm{c}$. The algorithm works as follow:

1. Solve equation (3.84) for each cell on the grid. We then get a set of points $(\boldsymbol{x}_\mathrm{c}^i, \boldsymbol{x}^i)$, where the former is the cell centre and the latter the closest critical point.
2. Remove all critical points found at $|\boldsymbol{x}_\mathrm{c}^i, \boldsymbol{x}^i|_\infty \geq \Delta x$, where Δx is the grid spacing.
3. For all critical point, compute the value of the hessian by interpolating linearly from the $2N$ (4 in 2D, 6 in 3D) neighbouring cells.
4. Compute the eigenvalues of the hessians and the type of the critical point (maximum, saddle point(s) or minimum).
5. Merge all critical points of the same kind closer than Δx. To do this, we first build a KD-Tree of the critical points and find all the pairs located at a distance $d_{ij} = |\boldsymbol{x}^i - \boldsymbol{x}^j|_\infty \leq \Delta x$. For each pair, we keep only the point that is the closest to its associated cell.

3.C.2 Critical events detection

The algorithm is based on the idea that each critical event has two predecessors at the previous smaller smoothing scale (two critical points). Conversely, each critical point has either a critical point successor of the *same kind* at the next (larger) smoothing scale or a critical event. Therefore, a way to detect critical events is to find critical points that do not have a successor. These points will be referred to as "heads" as they are the tip of a continuous line of critical points in the smoothing scale direction. Critical events are then found between pairs of heads of kind k and $k+1$ (e.g. a peak and a filament).

Following this idea, the algorithm can be decomposed in two steps: compute the heads of each kind, than find pairs of heads to detect critical events. In the following of the section, let us call R_0 (resp. R_1) the smallest (resp. largest) scale at which the field is smoothed. Let $C_{R,k} = \{\boldsymbol{r}_i, R\}_{i=1,\dots,N}$ be the set of the N critical points of kind k at scale R. The whole detection algorithm reads

1: **procedure** FindCritEvents($C_{R,k}, \alpha$)
2: $E \leftarrow \{\}$ ▷ All critical events
3: **for** k **in** $1, \dots, d$ **do** ▷ Find heads of critical points
4: $H_k \leftarrow$ BuildHeads($k, \Delta \log R$)
5: **end for**
6: $R \leftarrow R_0$
7: **while** $R \leq R_1$ **do** ▷ Find pairs of heads (crit. events)
8: $\Delta R \leftarrow R \times \Delta \log R$ ▷
9: $E \leftarrow E+$FindHeadPairs($H_1, \dots, H_d, R, \alpha\Delta R$)
10: $R \leftarrow R + \Delta R$
11: **end while**
12: **return** E
13: **end procedure**

The parameter α controls how far heads can be in in the smoothing scale direction, in units of $\log R$. A value of 1 looks for pairs of heads at the same scale, a value of 2 looks for pairs of heads at a scales $R, R+\Delta R$.

The first step (line 4) of the algorithm builds the set of heads H_k. It works as follow

1: **procedure** BuildHeads($k, \Delta \log R$) ▷ Build heads of kind k
2: $H_k \leftarrow C_{R_1,k}$ ▷ Initialize heads
3: $P_k \leftarrow H_k$ ▷ Initialize progenitors
4: $R \leftarrow R_1$
5: **while** $R \geq R_0$ **do**
6: $P'_k \leftarrow \{\}$ ▷ Initialize new progenitors at R
7: **for** p, c, d **in** SortedPairs($P_k, C_{R,k}, R$) **do**

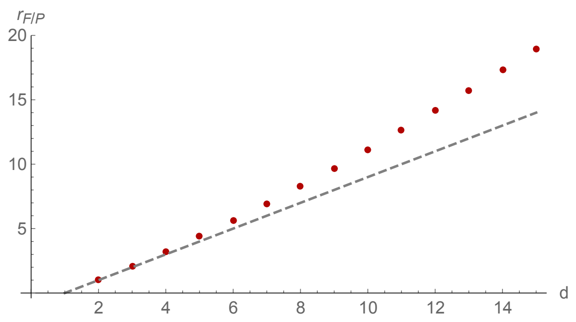

Figure 3.21: The ratio of peak to filament merger as a function of d. For reference, the first diagonal is shown as a dashed gray line as well. The ratio is approximately fitted as $d-1+((2d-4)/7)^{7/4}/2$ and shown as red dots. The dashed line is the identity.

one can easily derive

$$\frac{\partial N_i}{\partial R} = -N_i \times d \frac{R}{R_\star^2} \frac{1-\tilde{\gamma}^2}{\tilde{\gamma}^2} \tag{3.79}$$

which in d=3 for peaks reads ()

$$-\frac{\partial N_0}{\partial R} = 3N_0 \frac{R}{R_\star^2} \frac{1-\tilde{\gamma}^2}{\tilde{\gamma}^2} \tag{3.80}$$

$$= \frac{3R}{R_\star^3 \tilde{R}^2}(1-\tilde{\gamma}^2)\frac{29\sqrt{15}-18\sqrt{10}}{1800\pi^2} \tag{3.81}$$

which happens to be equal to the differential number counts of 3D critical events (equation (3.13)) but only if $C_{\rm odd}$ is computed with the approximation in equation (3.12) that boils down to (using equation (3.66))

$$C_{\rm odd} \approx \frac{3(1-\tilde{\gamma}^2)}{d(d+2)}\left(\frac{d}{2\pi}\right)^{d/2} \tag{3.82}$$

and if we drop (??) the volume factor $\mathcal{V}_2 = 2\pi^2$. The same result is found in 2D ans is still to be understood...

3.C Algorithms

The source code of the implementation can be found online. It is based on `Python` and the `Scipy` stack (Jones et al., 2001).

3.C.1 Critical points detection

This section presents the algorithm used to find the extrema in a N dimensional field. Let F, F_i and F_{ij} be a field evaluated on a grid, its derivative and its hessian. For any point $\boldsymbol{x}$ on the grid, we have the following relation

$$F_j(\boldsymbol{x}) = F_j(\boldsymbol{x}_{\rm c}) + (x_i - x_{{\rm c},i})F_{ij}(\boldsymbol{x}) + \mathcal{O}(\Delta x_i^2). \tag{3.83}$$

Critical points are found where $F_j' = 0$ by solving the linear system of equation

$$\Delta x_i F_{ij} = -F_j, \tag{3.84}$$

effect induced by large-scale filamentary structure on the assembly of dark matter halos and their galaxies therein. Indeed it is expected on theoretical ground that the typical accretion rate increases when going from filament centre towards nodes (Musso et al., 2018). Looking at galactic properties instead, Kraljic et al., 2019 showed that the galactic ratio of velocity-to-velocity-dispersion (v/σ) is also modulated as a function of the distance and orientation to the nearest filamentary structure. Using the framework developed in this work, we generate a suite of Gaussian random fields constrained to the presence of a proto-filament at its centre, the exact generation procedure being described in section 3.C.3. The proto-filament is defined at a scale $R = 5\,{\rm Mpc}/h$, is oriented along the z axis and lays in a wall in the yz plane. Using the set of constrained cubes, we compute the excess density of each kind of critical event with respect to the cosmic mean, at fixed smoothing scale (hence at fixed object mass) $2.5 \leq R \leq 5\,{\rm Mpc}/h$. The results are shown on figure 3.15. Let us first restrict ourselves to the halo merger rate (top left panel of figure 3.15). Going from the voids to the wall, from the wall to the filament and from the filament to the nearest node, the halo merger rate increases and the maximum halo merger rate is found at the location where a node is expected ($z \sim \pm 10\,{\rm Mpc}/h$). At larger scales, the field becomes unconstrained so that the merger rate falls back to its cosmic mean. We reproduce here from first principle the results of Borzyszkowski et al., 2017, showing that halos close to the filament centre are stalled: they do not undergo many merger nor do they accrete much as the local tidal fields channels all the matter towards the two surrounding nodes, bypassing the centre of the filament. Quantitatively, halos forming at the centre of the filament are found to have a halo merger rate close to the cosmic average, while those close to the nodes are expected to have 40% more mergers. Conversely, halos forming in a void next to a filamentary structure are expected to have a merger rate -20% smaller than the cosmic mean.

Let us now add to the emerging picture the filament coalescence rate. Filament merger rates act locally to decrease the connectivity of halos, as each filament merger will disconnect one filament from two halos. The top right panel of figure 3.15 shows that the merger rate is maximal along the wall and minimal along the filament. Going off the plane of the wall (x direction), the filament merger rate simply decreases towards the cosmic mean. Interestingly the filament merger rate is mininal in the nodes (-13%) and maximal in the wall ($+10\%$). As a consequence, halos forming close to a node have a larger halo merger rate but a smaller filament merger rate. This in turn will have an impact on the assembly of dark matter halos and their galaxies therein. In the wall where the filament merger rate is the highest, we expect filaments to merge faster than halos, resulting in halos with fewer connected filaments. This can be interpreted using the results of section 3.4.4. Indeed in a cosmic wall, the geometry is locally 2D so that the theoretically expected connectivity becomes 4 instead of 6.

The bottom left panel of figure 3.15 shows that the wall merger rate is decreased in walls and even more strongly in filaments. The minimum wall merger rate is found at the location of the node with a rate -40% smaller than the cosmic mean. Conversely, the wall merger rate is enhanced in the two voids surrounding the wall with a rate 20% above the cosmic mean.

The evolution of the connectivity with cosmic environnement is resumed by the bottom right panel of figure 3.15, which shows the ratio of halo mergers ($\mathcal{P}$ critical events) to filament mergers ($\mathcal{F}$ critical events), for which the cosmic mean is 2.055 (see equation (3.16)). Small values of $r_{\mathcal{F}/\mathcal{P}}$ indicate that halo merge faster than their surrounding filaments, so that the connectivity increases as halos grow. On the contrary, large values of $r_{\mathcal{F}/\mathcal{P}}$ indicate that filaments merge faster than halos, so that the connectivity decreases as halos grow. The bottom right panel of figure 3.15 shows that in nodes, the ratio drops to about $r_{\mathcal{F}/\mathcal{P}} \approx 1.1$. On the contrary halos forming in voids are expected to have a ratio of about 2.4. We therefore predict that, at fixed final mass, halos forming next to a node will grow an increasing number of connected filaments[8]. The expected

[8]Conversely Codis et al., 2015a found that when averaged over all large scale structures, connectivity increases

physical outcome of this process is that the streams feeding a galaxy growing next to a node will become more and more isotropic with increasing connectivity. Assuming that an isotropic acquisition of matter leads to a smaller amount of angular momentum being transferred down to the disk, we argue that this effect prevents the formation of gaseous disks in the vicinity of nodes. Conversely, we predict that halos growing in the neighbouring voids see their filaments destroyed faster than they merge, so that the halo is likely to grow with steadier flows coming from a few filaments (see also Codis et al., 2015a; Laigle et al., 2015, section 6.2.1, and 5 resp. for similar conclusions reached via the kinematic structure of large scale flows in filaments).

3.7.4 Modified gravity or primordial non-gaussianities

Voids are very interesting laboratory both for galaxy evolution and cosmology. They represent primitive environments for galaxies, where density is low and matter flow is still relatively curl-free. Void galaxies are therefore interesting probes for galaxy formation (e.g. Lindner et al., 1996). Voids are also a tool of choice to probe the cosmology or to test theory of modified gravity (e.g. Cai et al., 2015; Gay et al., 2012; Lavaux and Wandelt, 2012) as a mean to constrain the equation of state of dark energy. In particular, these authors have used the cosmic evolution of the size and the number of voids as constrains on $D(z)$. In the present formalism void disappear as a function of cosmic time via mergers of walls, hence the one point statistics of wall merger could be used as a cosmic probe.

Let us briefly quantify the effect first on simulations, and then compare to the proxy of Section 3.4.5 relying on known perturbative results. Figure 3.16 presents the redshift evolution of critical counts measured in 45 realisations of ΛCDM simulations in boxes of 500 Mpc$/h$ involving 256^3 particles evolved using Gadget (Springel et al., 2001) sampled on a 256^3 grid smoothed with a Gaussian filter over 6 Mpc$/h$. The algorithm described in section 3.C is used to identify and match the critical points.

At high redshift, the Gaussian prediction is recovered. At lower redshift, the $\mathcal{P}$ and $\mathcal{F}$ counts shift towards lower contrast, but resp. decrease and increase in amplitude, while the $\mathcal{W}$ counts increase in amplitude. Since the first halo to merge are due to high σ peaks, it is expected that the low-z PDFs are biased towards low densities. Similarly, the mean density of filamentary structure decreases with increasing time, as the less dense filaments take more time to gravitationally form, so that the PDFs of the filament mergers shifts to smaller densities at low z. The evolution of void structures with cosmological time is somehow the opposite as the one for peaks: early forming voids are the most underdense while late-time voids form out of less underdense regions. At fixed resolution, this results in a shift of the typical density of voids towards higher densities. Indeed, in the limit of infinite time, it is expected that the only voids found at a given size stem from $\nu = 0$, as any void with $\nu < 0$ will have had time to collapse earlier.

Finally, the qualitative similarity with the cosmic evolution of the measured event counts and the prediction shown in figure 3.7 is striking, strongly suggesting that indeed, the set of critical events in the initial condition do capture the upcoming cosmic evolution of the field.

From equation (3.27) the cosmic evolution of the rate of void of volume $\mathcal{V}$ merging during time interval δz can be expanded to first order in σ via equation (3.36) as

$$\frac{\partial^2 n}{\partial \log\mathcal{V}\partial z} = \frac{\partial^2 n}{\partial \log\mathcal{V}\partial z}\Big|_{\rm G} + \sigma(z)\frac{\partial^2 n}{\partial \log\mathcal{V}\partial z}\Big|_{\rm NG}, \tag{3.38}$$

where the first term reflects cosmic evolution of the rate of void disappearance presented in section 3.7.1, while the second term is obtained by substituting $\partial^2 n/\partial R\partial\nu\big|_{\rm G}$ by $\partial^2 n/\partial R\partial\nu\big|_{\rm NG}$ into equation (3.36). As discussed in section 3.4.5, the scaling of these non-Gaussian corrections yield

with mass.

Using equation (3.74) and equation (3.79) gives us a simple relation between the number density of critical points and the number density of critical events

$$N_i = \frac{1}{d\times \mathrm{d}\log R_*/\mathrm{d}R}\begin{cases}\mathcal{N}_0 & \text{if } i=0,\\ (\mathcal{N}_{i-1}+\mathcal{N}_i) & \text{if } 0<i<d-1,\\ \mathcal{N}_{d-1} & \text{if } i=d-1.\end{cases}$$

For Gaussian random fields, we also have the property that $N_i = N_{d-i-1}$ and $\mathcal{N}_i = \mathcal{N}_{d-i-2}$. This provides us with simple way to compute the ratio of critical events as a function of the ratio of the critical points. For any d, the ratio of filament to peak is connected to the ratio of $\mathcal{F}$ to $\mathcal{P}$ critical events

$$\frac{N_1}{N_0} = \frac{\mathcal{N}_0+\mathcal{N}_1}{\mathcal{N}_0} = 1+\frac{\mathcal{N}_1}{\mathcal{N}_0} = 1 + r_{\mathcal{F}/\mathcal{P}}. \tag{3.76}$$

As an example, let use derive the ratio of other critical points in dimensions up to 6D. For $d=4$,

$$\frac{N_1}{N_0} = \frac{N_2}{N_3} = 1 + r_{\mathcal{F}/\mathcal{P}} \approx 4.17,$$
$$\frac{N_2}{N_1} = \frac{\mathcal{N}_1+\mathcal{N}_2}{\mathcal{N}_0+\mathcal{N}_1} = \frac{\mathcal{N}_0+\mathcal{N}_1}{\mathcal{N}_0+\mathcal{N}_1} = 1.$$

For $d=5$,

$$\frac{N_1}{N_0} = \frac{N_3}{N_4} = 1 + r_{\mathcal{F}/\mathcal{P}} \approx 5.36,$$
$$\frac{N_2}{N_1} = \frac{N_2}{N_3} = \frac{\mathcal{N}_1+\mathcal{N}_2}{\mathcal{N}_0+\mathcal{N}_1} = \frac{r_{\mathcal{F}/\mathcal{P}} + r_{\mathcal{W}_1/\mathcal{P}}}{1+r_{\mathcal{F}/\mathcal{P}}} \approx 2.07.$$

For $d=6$,

$$\frac{N_1}{N_0} = \frac{N_4}{N_5} = 1 + r_{\mathcal{F}/\mathcal{P}} \approx 6.67,$$
$$\frac{N_2}{N_1} = \frac{N_3}{N_4} = \frac{\mathcal{N}_1+\mathcal{N}_2}{\mathcal{N}_0+\mathcal{N}_1} = \frac{r_{\mathcal{F}/\mathcal{P}} + r_{\mathcal{W}_1/\mathcal{P}}}{1+r_{\mathcal{F}/\mathcal{P}}} \approx 2.64,$$
$$\frac{N_3}{N_2} = 1.$$

[♠ it would be useful to give $N_0(d)$ here?] Given that Codis et al., 2018 provides an asymptotic limit for the connectivity, we can re-express it in terms of the ratio of critical events as

$$\frac{N_1}{N_0} = \frac{N_{d-2}}{N_{d-1}} = 1 + r_{\mathcal{F}/\mathcal{P}} = d + \frac{1}{2}\left((2d-4)/7\right)^{7/4}, \tag{3.77}$$

which in the large d limit, asymptotes to

$$r_{\mathcal{F}/\mathcal{P}} \overset{d\to\infty}{\sim} \frac{1}{2}\left(\frac{2}{7}\right)^{7/4} d^{7/4} \approx \frac{1}{17} d^{7/4}. \tag{3.78}$$

3.B.7 testing the link between critical pts and events counts

[♡ puzzling result → TO BE UNDERSTOOD]

From equation (3.79) and because for a Gaussian filter, we have

$$\frac{\mathrm{d}\sigma_i^2}{\mathrm{d}R^2} = -\sigma_{i+1}^2,$$

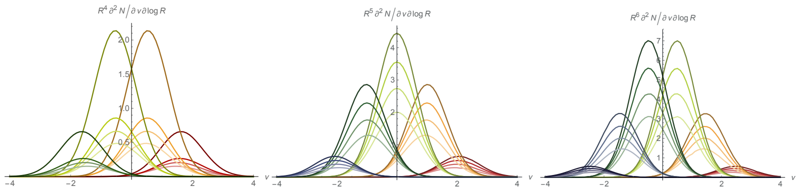

Figure 3.20: The PDF of critical events of the various types $(\mathcal{P}, \mathcal{F}, \mathcal{W}_1, \mathcal{W}_2)$ in 4D (*top*), in 5D (*middle*) and 6D (*bottom*) for $n_s = -2, -3/2, -1, -1/2$ from light to dark.

Finally, the d dimensional ratio of critical event of type j and k is simply given by

$$r_{j/k} = \left\langle \delta_{\rm D}(\lambda_j) \Big|\prod_{i\neq j} \vartheta_{\rm H}(\lambda_i-\lambda_j)\,\lambda_i\Big| \right\rangle \Big/ \left\langle \delta_{\rm D}(\lambda_k) \Big|\prod_{i\neq k} \vartheta_{\rm H}(\lambda_i-\lambda_k)\,\lambda_i\Big| \right\rangle$$

where the PDF to evaluate this expectation is given by equation (3.73). Note that these counts correspond to the area below each curve shown in figure 3.20. In 3D, we recover the ratio presented in the main text. In 4D the ratio is analytic and reads $2(57+25\pi-50\cot^{-1}(3))/(75\pi-2(57+50\cot^{-1}(2))) \approx$ 3.17 More generally,

$$\begin{aligned}
d=2:&\quad r_{\mathcal{F}/\mathcal{W}} = 1\,,\\
d=3:&\quad r_{\mathcal{F}/\mathcal{P}} = 2.06\,,\\
d=4:&\quad r_{\mathcal{F}/\mathcal{P}} = 3.17\,,\quad r_{\mathcal{W}/\mathcal{P}} = 3.17\,,\\
d=5:&\quad r_{\mathcal{F}/\mathcal{P}} = 4.36\,,\quad r_{\mathcal{W}_1/\mathcal{P}} = 6.72\,,\quad r_{\mathcal{W}_2/\mathcal{P}} = 4.36\,,\\
d=6:&\quad r_{\mathcal{F}/\mathcal{P}} = 5.67\,,\quad r_{\mathcal{W}_1/\mathcal{P}} = 11.97\,,\quad r_{\mathcal{W}_2/\mathcal{P}} = 11.97.
\end{aligned}$$

and $r_{\mathcal{W}_3/\mathcal{P}} = 5.67$. Note that these ratios are pure numbers and do not depend on the detailed shape of the underlying powerspectrum.

3.B.6 Self-consistency links with critical points counts

These results can be used to derive the connectivity as defined in Codis et al., 2018. Indeed, let us formally write N_i the number density of critical point of kind i in d dimensions and $\mathcal{N}_i$ the number density of critical event of kind $i - i + 1$. The evolution of N_i is given by

$$\frac{\partial N_i}{\partial R} = -\begin{cases} \mathcal{N}_0 & \text{if } i = 0,\\ (\mathcal{N}_{i-1} + \mathcal{N}_i) & \text{if } 0 < i < d-1,\\ \mathcal{N}_{d-1} & \text{if } i = d-1.\end{cases} \tag{3.74}$$

For Gaussian random fields, the number density of critical point can be formally written as

$$N_i = \frac{1}{R_*^d}\underbrace{\left\langle \Big|\prod_j \lambda_j\Big| \right\rangle \left\langle \delta_{\rm D}^{(3)}(x_i) \right\rangle}_{C_i},$$

where the PDF to evaluate the left part of the r.h.s. is given by equation (3.73). Here C_i is a number common to all power spectra. The derivative of N_i with respect to the smoothing scale is then

$$\frac{\partial N_i}{\partial R} = -N_i \times d\frac{{\rm d}\log R_*}{{\rm d}R}. \tag{3.75}$$

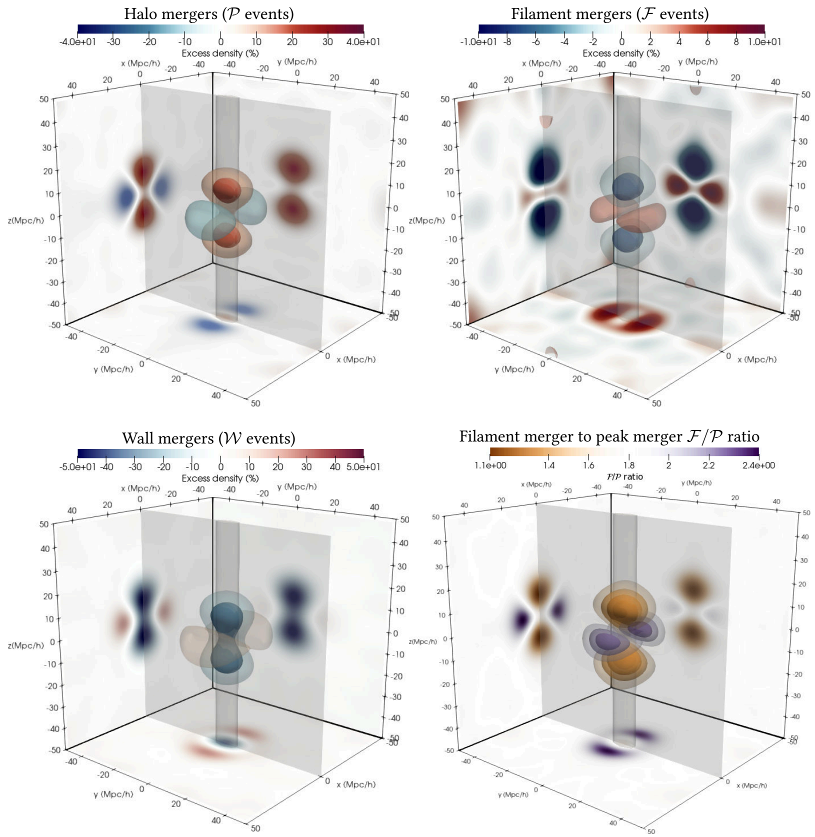

Figure 3.15: From left to right and top to bottom, peak-merger, filament-merger and wall-merger excess density around a large-scale proto-filament, illustrated by the vertical cylinder (z direction) and the wall in which it resides, illustrated by the grey plane (yz plane). The bottom right panel shows the local ratio of filament to peak mergers $r_{\mathcal{F}/\mathcal{P}}$. Each side of the cube shows a slice through the centre, shifted to the side of the plot for visualisation purposes. Red regions have an excess of critical events while blue regions have a deficit of critical events with respect to cosmic average. Interactive versions of these plots can be found online for the halo mergers, filament mergers, wall mergers and filament to peak merger ratio. Going from voids to wall, from wall to filament and from filament to the nearest node (along the z axis), the halo merger rate increases and the filament merger rate decreases. Halos in the filament are therefore stalled: they merge less than those in the nodes. At the same time, the filament merger rate decreases when going from the filament towards the node so that the mean connectivity, given by the ratio of halo merger to filament merger, is expected to increase.

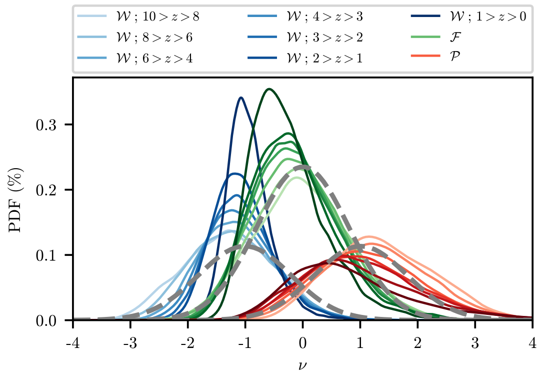

Figure 3.16: Critical events number count as a function of the rarity in dark-matter only simulations in different redshift bins as mentioned in the legend, with the same colours as figure 3.9. The curves have been normalised so that in each redshift bin, the integral of the three curves $(\mathcal{W}, \mathcal{P}, \mathcal{F})$ equals one. At high redshift, the merger rates resembles the Gaussian prediction (thick dashed gray lines, with an arbitrary normalisation). The skewness of the distributions increases with decreasing redshift as the field departs from gaussianity.

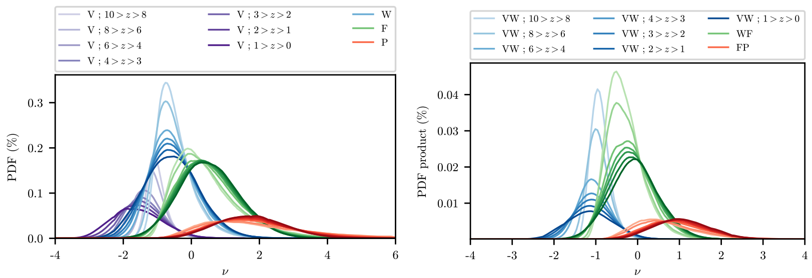

(a) Critical event PDF **(b)** Critical *point* PDf product

Figure 3.17: (a): Critical points number count as a function of the rarity in dark-matter only simulations in different redshift bins as mentioned in the legend. The curves have been normalised so that in each redshift bin, the integral of the four curves equals one. The purple bundle corresponds to voids, the blue one to walls, the green one to filaments and the red one to peaks. (b): Product of the PDFs. At large redshifts, the curves resemble the prediction of figure 3.7.

3.B.4 Critical event number counts in ND

It now follows that the critical event number counts of type j at height ν in dimension d read:

$$\frac{\partial^2 n_j^d}{\partial R\,\partial\nu} = \frac{R\,\mathcal{V}_d\,C_{d,\mathrm{odd}}}{\tilde{R}^2\,R_*^d}\left\langle \delta_{\mathrm{D}}(\lambda_j)\left|\prod_{i\neq j\leq d}\vartheta_{\mathrm{H}}(\lambda_i-\lambda_j)\,\lambda_i\right|\right\rangle, \tag{3.69}$$

where this expectation is computed using the conditional expectations presented in the previous section. Equation (3.69) is a function of ν because of the correlation between ν and $\sum_i \lambda_i$ seen in equation (3.59). Recalling the formal analogy with the flux of critical lines per unit hyper surface, [♠ check?]

$$\frac{\partial^2 n_{\mathcal{P}}^d}{\partial R\,\partial\nu} \overset{\gamma\nu\to\infty}{\sim} \frac{R}{\tilde{R}^2\,R_*^d}\frac{\mathcal{V}_d\,C_{d,\mathrm{odd}}}{\sqrt{2\pi}}\exp\left[-\frac{1}{2}\nu^2\right]\left(\frac{\nu}{R_0}\right)^{d-1},$$

in the large d large ν limit (Pogosyan et al., 2009). The contribution from the odd part of the distribution function, $C_{d,\mathrm{odd}}$ obeys

$$C_{d,\mathrm{odd}} = \left\langle\left|\sum_i x_{jii}\right||x_{jjj}|\delta_{\mathrm{D}}^{(d)}(x_i)\right\rangle, \tag{3.70}$$

where the expectation in equation (3.70) should be computed with the odd derivative PDF given in section 3.B.3. After a bit of algebra,

$$\begin{aligned} C_{d,\mathrm{odd}} = &\left(\frac{d}{2\pi}\right)^{\frac{d}{2}}\frac{2\sqrt{6}}{\pi}\sqrt{\frac{(d-1)\,(1-\tilde{\gamma}^2)}{d^2(d+2)^2(d+4)}}+\\ &\left(\frac{d}{2\pi}\right)^{\frac{d}{2}}\frac{6\,(1-\tilde{\gamma}^2)}{\pi d(d+2)}\tan^{-1}\left(\sqrt{\frac{3}{2}}\frac{\sqrt{d+4}\sqrt{1-\tilde{\gamma}^2}}{\sqrt{d-1}}\right) \end{aligned} \tag{3.71}$$

Finally, the volume $\mathcal{V}_d$ of the hyper-wedge corresponding to the marginalisation over the orientation of the Hessian obeys

$$\begin{aligned} \mathcal{V}_d &= \frac{1}{2^{d-1}d!}\iint d\mathrm{SO}(d) = \frac{1}{2^{d-1}d!}\prod_{i=1}^{n-1}\mathrm{Vol}(S^i),\\ &= \frac{1}{2^{d-1}d!}\prod_{i=1}^{n-1}\frac{2\pi^{(i+1)/2}}{\Gamma((i+1)/2)}, \end{aligned} \tag{3.72}$$

where $\mathrm{Vol}(S^i)$ denotes the i-dimensional volume (i.e. surface area) of the unit i-sphere in $\mathbb{R}^{i+1}$, the factor $d!$ comes from not sorting the eigenvalues and the factor 2^{d-1} from not imposing their sign. It follows that $\mathcal{V}_2 = \pi/2$, $\mathcal{V}_3 = \pi^2/3$, $\mathcal{V}_4 = \pi^4/12$, $\mathcal{V}_5 = \pi^6/45$ and $\mathcal{V}_6 = \pi^9/540$. The PDFs of critical events in 4D, 5D and 6D are shown in figure 3.20. Note that the intermediate signature events dominate in number over the extreme ones, in accordance with the relative number of critical points.

3.B.5 Ratios of critical events

From equation (3.59), the integration over ν yields the marginal probability of $\{\lambda_i\}$:

$$\mathcal{V}_d\prod_{i\leq d}d\lambda_i\prod_{i<j}(\lambda_j-\lambda_i)\exp\left(-\frac{1}{2}\mathcal{Q}_d(\{\lambda_i\})-\frac{1}{2}\left(\sum_i\lambda_i\right)^2\right). \tag{3.73}$$

In equation (3.58) $\mathcal{V}_d$ arises from the integration over the angles and is given by equation (3.72) below.

3.B.3 Joint PDF of the first and third derivatives

Here, we will look into the pdf of the first and third derivatives in d dimensions in order to compute the odd derivative term $C_{\rm odd}$ that enters critical event number counts in d dimensions.

First, let us note that the first derivatives are Gaussian distributed with individual variance $\langle x_i^2 \rangle = 1/d$ so that the probability for all first derivatives to be zero is **[♠ notation a homogeneiser]**

$$P(\nabla = 0) = \left(\frac{d}{2\pi}\right)^{d/2} . \tag{3.61}$$

Now let us study the statistics of the third derivatives. By symmetry, one can note that

$$\left\langle \left(\sum_i x_{1ii}\right)^2 \right\rangle = \frac{1}{d}, \tag{3.62}$$

because the third derivatives are rescaled by σ_3, and

$$\langle x_{1jj}^2 \rangle = \langle x_{111} x_{1jj} \rangle = \frac{1}{5} \langle x_{111}^2 \rangle = 3 \langle x_{1jj} x_{1kk} \rangle \quad \forall j \neq k \neq 1.$$

Therefore,

$$\frac{1}{d} = \langle x_{111}^2 \rangle + (d-1) \langle x_{1jj}^2 \rangle + 2(d-1) \langle x_{111} x_{1jj} \rangle + (d-1)(d-2) \langle x_{1kk} x_{1jj} \rangle \quad \forall j \neq k \neq 1$$

implies that $\langle x_{iii}^2 \rangle = 15/d(d+2)(d+4)$ and the full covariance matrix of the third derivatives is therefore now known. However, we are interested in statistics subject to a zero gradient constraint, in particular the three quantities of interest are (fixing d as the degenerate direction and assuming an implicit summation on the i indices)

$$\langle x_{ddd}^2 | x_d = 0 \rangle = \langle x_{ddd}^2 \rangle - \frac{\langle x_{dii} x_d \rangle^2}{\langle x_d^2 \rangle}, \tag{3.63}$$

$$\left\langle (x_{dii})^2 | x_d = 0 \right\rangle = \left\langle (x_{dii})^2 \right\rangle - \frac{\langle x_{ddd} x_d \rangle^2}{\langle x_d^2 \rangle}, \tag{3.64}$$

$$\langle x_{dii} x_{ddd} | x_d = 0 \rangle = \langle x_{dii} x_{ddd} \rangle - \frac{\langle x_d x_{ddd} \rangle \langle x_d x_{dii} \rangle}{\langle x_d^2 \rangle}, \tag{3.65}$$

which can easily be computed thanks to the additional relation $\langle x_{11}^2 \rangle = 3/d(d+2)$,

$$\langle x_{ddd}^2 | x_d = 0 \rangle = \frac{3}{d(d+2)} \left[\frac{5}{d+4} - \frac{3\tilde{\gamma}^2}{d+2} \right], \tag{3.66}$$

$$\left\langle (x_{dii})^2 | x_d = 0 \right\rangle = \frac{1-\tilde{\gamma}^2}{d}, \tag{3.67}$$

$$\langle x_{dii} x_{ddd} | x_d = 0 \rangle = \frac{3}{d(d+2)} (1 - \tilde{\gamma}^2). \tag{3.68}$$

joint estimates for the cumulants (Codis et al., 2013), hence a measure of $f_{\rm NL}$ or a parametrisation of modified gravity.

3.7.5 Critical events as input to Machine learning

There is a long tradition of relying on merger trees of dark halos extracted from simulations as a mean to tag the halos with physical properties (see, e.g. Benson, 2010, and reference therein). One of the long term main motivation for the present work is to extend this strategy to the other two merger trees, (filaments and walls), and to rely on modern segmentation techniques to identify which combination of events are most likely to lead to galaxies of a certain type to be produced in cosmological simulations. This strategy is likely to be efficient and rewarding, as the set of critical events is a very strong compression of the set of initial conditions, and because once the segmentation has been done, the subset of events which are in the past lightcone of a galaxy with a given tag have physical meaning. For instance, recent disconnect of filaments are likely to impact gas infall hence star formation and disc reformation. The set of critical events represents a useful effective topological compression of the initial conditions which will impact the upcoming 'dressed' mergers (i.e. the cosmic evolution of peaks *and* their filaments and walls). Note that the exact relative configuration of critical events in the smoothing-position space may be of relevance, and is not fully captured by the sole knowledge of the one and two point statistics. In order to asses this, we can rely on machine learning techniques.

3.7.5.1 Predicting v/σ from past lightcone of Horizon-AGN

Let us illustrate this strategy on the catalogue of synthetic galaxies from the cosmological simulation Horizon-AGN, for which we have classified them based on their morphology via a continuous kinematic proxy, v/σ. This ratio is computed from the 3D velocity distribution of stellar particles of each galaxy. In the frame of the angular momentum of that galaxy, the velocity is decomposed into cylindrical components v_r, v_θ, v_z, and the rotational velocity of a galaxy v is defined as the mean of v_θ of individual stars. The average velocity dispersion of the galaxy $\sigma^2 = (\sigma_r^2 + \sigma_\theta^2 + \sigma_z^2)/3$ is computed using the velocity dispersion of each velocity component σ_r, σ_θ and σ_z. This ratio allows us to separate rotation-dominated ($v/\sigma \gg 1$) from dispersion-dominated ($v/\sigma \ll 1$) galaxies. For each central galaxy identified in the simulation, we identify the Lagrangian counter part of all dark matter particles within its host halo. This defines a connexe gravitational patch within which we can identify all critical events. Hence, the simulation provides us with a set of relations for k patches and three types of critical events $j \in [\mathcal{P}, \mathcal{F}, \mathcal{W}]$

$$\left(\{\Delta \boldsymbol{r}_{j,i}, R_{j,i}, \nu_{j,i}\}_{i \leq n_{j,k}}\right)_{j \in [\mathcal{P},\mathcal{F},\mathcal{W}]} \to v/\sigma_k \,, \tag{3.39}$$

where $\Delta \boldsymbol{r}_{j,i}$ is the relative position *within the patch* of the critical event i of type j measured w.r.t. the centre of mass of the patch, $\nu_{j,i}$ is its contrast, and $R_{j,i}$ the corresponding scale, while v/σ_k is the ratio of the patch k. Let us call $\mathcal{E}_k$ the l.h.s. of this relation. Standard machine learning tools (nearest neighbourg, gradient boosted trees, decision tree, etc), allows us to build a predictor, $P_r(\mathcal{E})$ from a subset of $(\mathcal{E}_k \to v/\sigma_k)_{k \leq K_{\rm train}}$. From this training, we can do one of two things: i) use it as a black box to associate v/σ_k to other patches for which we computed their set of events, $\mathcal{E}_k$; ii) identify which features in this event set is responsible for the corresponding value of v/σ. The former would be of interest e.g. in the context of covariance estimates for weak lensing surveys, as it would allow us to generate a low cost synthetic galaxy catalogues which include morphology as a tag. The latter could be implemented over sets of simulations which implement different feedback recipees as a mean of disentangling the relative impact of environment and sub grid physics.

3.7.5.2 The impact of extended critical sets

Let us first illustrate the former on synthetic galaxies from Horizon-AGN. While it is beyond the scope of this work to explore fully the latter, let us provide numerical evidence why the extra knowledge of critical event of type $\mathcal{F}$ and $\mathcal{W}$ are of interest to increase the accuracy of the estimation. **??** shows the relationship between the predicted and the measured v/σ_k^j for the validation set when the full set $\{\mathcal{E}_k^j\}_{j\in[\mathcal{P},\mathcal{F},\mathcal{W}]}$ is used (top left panel) or only subsets $\{\mathcal{E}_k^{\mathcal{P}}\}$, $\{\mathcal{E}_k^{\mathcal{F}}\}$, and $\{\mathcal{E}_k^{\mathcal{W}}\}$ are used (from left to right and top to bottom).

3.7.5.3 Early versus late critical events

We can also test to what extent the more recent events are more relevant to present morphology by restricting our training to subsets of events skewed towards the larger scales. In order to do this we introduce a threshold $R_{\rm min}$ and define new sets of events as

$$\{\mathcal{E}^j_{k,R_{\rm min}}\} = \left(\{\Delta \mathbf{r}_{j,i}, R_{j,i}, \nu_{j,i}\}_{i\leq n_{j,k}}\right)_{R_{j,i}\leq R_{\rm min}}\,, \tag{3.40}$$

where the set is now subject to some chosen upper-bound $R_{\rm min}$ on the allowed $R_{j,i}$. **??** shows the evolution of the quality of the fit as a function of $R_{\rm min}$.

3.7.5.4 Configuration versus distances or size

Finally, let us consider the importance of the relative distance $|\boldsymbol{r}_{j,i}-\boldsymbol{r}_{j',i'}|$ versus configuration $|\hat{\boldsymbol{r}}_{j,i}\cdot\hat{\boldsymbol{r}}_{j',i'}|$ of events. **??** (left panel) shows the quality of the fit when using only the relativeangles, or only the (position) relative distances between events. **??** (left panel) shows the quality of the fit when restricting ourselves to events higher than a given threshold.

Beyond the scope of this work, when co-analysing the evolution of galactic properties with critical point mergers, one could relate the various (filament, wall) mergers to special events in terms of change in connectivity and feedback (e.g. quenching of AGN activity by filament disconnect). It could also be interesting to see if spin flip correlates with filaments or wall vanishing. The twin simulation, Horizon-noAGN could be analysed jointly to study its specific impact.

3.7.6 Discussion

[♠ discuss other works and link with excursion set theory]

Intensity mapping (Madau et al., 1997) also provides a test bench for applying the present formalism to sequences of 2D maps as a function of redshift. Existing (e.g. Chime, Shaw et al., 2014) or upcoming surveys e.g. SKA, Camera et al., 2015 will indeed provide both extrema and merger counts extracted from sets of maps at various redshifts. The cosmology dependence of extrema counts is through $(R_\star,\gamma)$ and the relevant cumulants, whereas the cosmology dependence of event counts also involve $(\tilde{R},\tilde{\gamma})$ and higher order cumulants at fixed level of non gaussianity (e.g. involving 3rd order derivative of the field to first order as discussed in section 3.4.5). Hence studying both counts as a function of redshift will prove complementary.

It is of interest to follow the position of all critical points (not just the maxima) explicitly as a function of true cosmic time in galaxy catalogue extracted from hydrodynamical simulations, so as to assess i) the impact of biasing involved in selecting specific tracers and ii) how non-linear clustering impacts the statistics. This is done illustratively using 330 snapshots of galaxies extracted from Horizon-AGN (shown on figure 3.1 at redshift zero with its set of walls and filaments), for which the critical points are derived using DisPerSE with a persistence threshold of $\sigma/100$. The algorithm described in section 3.C is used to match merging critical points as a function of redshift. The set of events are then binned as a function of log density for 4 redshift bins and shown on figure 3.18. Gravitational clustering has skewed the PDFs, but most dramatically galaxies poorly trace under dense regions, hence the number of wall mergers plummeted.

The cross-correlations associated to SZ, CIB and the convergence maps of weak lensing map from the CMB measured by Planck and SPT provide other opportunities for implementing event

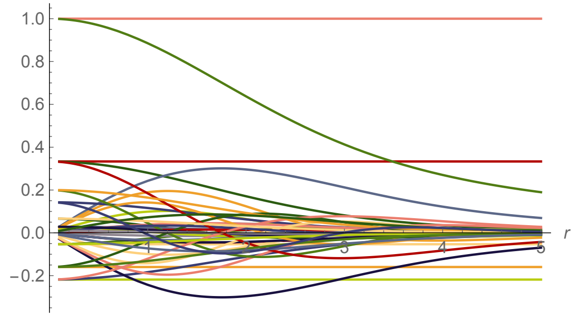

Figure 3.19: The correlation functions entering equation (3.55) for a scale invariant powerspectrum of index $n_s=-3/2$.

3.B Critical events in ND

For the sake of completeness and possible interest in other fields of research, let us present the one point statistics of critical events in arbitrary dimension d.

3.B.1 Spectral parameters

In this section we provide definitions for the spectral parameters of a d dimensional Gaussian random fields. Let us first define the variance of the i-th derivative of the field

$$\sigma_i(R) = \frac{1}{2\pi^2}\int {\rm d}k\, k^2 P(k) k^{2i} W^2(kR), \tag{3.56}$$

where $P(k)$ is the power spectrum and $W(kR)=\exp\big(-(kR)^2/2\big)$. The characteristic scales R_0, R_* and $\tilde{R}$ are defined by equation (2.90) and the spectral parameters γ and $\tilde{\gamma}$ are defined by equation (2.91). In d dimension for a power-law power spectrum with index n, we have

$$\frac{R_0^2}{R^2}=\frac{2}{n+d},\quad \frac{R_*^2}{R^2}=\frac{2}{n+d+2},\quad \frac{\tilde{R}^2}{R^2}=\frac{2}{n+d+4},$$
$$\gamma^2=\frac{n+d}{n+d+2},\quad \tilde{\gamma}^2=\frac{n+d+2}{n+d+4}. \tag{3.57}$$

3.B.2 Joint PDF of the field and its second derivatives

[♡ understand or remove] From Pogosyan et al., 2009 the probability of measuring the set of d eigenvalues of the d dimensional Hessian $\{\lambda_i\}$ and density ν obeys

$$\mathcal{V}_d \prod_{i\leq d} d\lambda_i \prod_{i<j}(\lambda_j-\lambda_i)\exp\left(-\frac{1}{2}Q_\gamma(\nu,\{\lambda_i\})\right)\,, \tag{3.58}$$

where Q_γ is a quadratic form in λ_i and ν given by

$$Q_\gamma(\nu,\{\lambda_i\}) = \nu^2 + \frac{\left(\sum_i\lambda_i+\gamma\nu\right)^2}{(1-\gamma^2)} + \mathcal{Q}_d(\{\lambda_i\})\,, \tag{3.59}$$

with

$$\mathcal{Q}_d(\{\lambda_i\}) = (d+2)\left[\frac{1}{2}(d-1)\sum_i\lambda_i^2 - \sum_{i\neq j}\lambda_i\lambda_j\right]. \tag{3.60}$$

with an implicit summation over repeated indices and symmetrization between parenthesised indices (for instance: $t_{aa(j}\delta_{kl)} = [t_{aaj}\delta_{kl}+t_{aak}\delta_{lj}+t_{aal}\delta_{jk}]/3$ and so on). Equation (3.44) depends only on a single correlation parameter: γ. A similar procedure can be performed for the joint probability of the first and third derivatives of the fields, $P_1(x_i, x_{ijk})$ by defining the following nine parameters (see also Hanami, 2001)

$$u_i \equiv \nabla_i u, \quad v_i \equiv \frac{1}{2}\epsilon^{ijk}\nabla_i\left(\nabla_j\nabla_j - \nabla_k\nabla_k\right)x\,, \text{ with } j<k\,,$$
$$w_i \equiv \sqrt{\frac{5}{12}}\nabla_i\left(\nabla_i\nabla_i - \frac{3}{5}\Delta\right)x\,, \tag{3.48}$$

and replacing the variables $(x_{i11}, x_{i22}, x_{i33})$ with (u_i, v_i, w_j). In that case, the only cross-correlations in the vector $(x_1, x_2, x_3, u_1, v_1, w_1, u_2, v_2, w_2, u_3, v_3, w_3, x_{123})$ which do not vanish are between the same components of the gradient and the gradient of the Laplacian of the field:

$$\langle x_i u_i\rangle \quad = \quad \tilde\gamma/3, \quad i = 1,2,3, \tag{3.49}$$

where $\tilde\gamma$ was defined in equation (2.91). This allows us to write:

$$P_1(x_i, x_{ijk}) = \frac{105^{7/2}3^3 \exp\left(-\frac{1}{2}\left(Q_1+Q_3\right)\right)}{(2\pi)^{13/2}(1-\tilde\gamma^2)^{3/2}}\,, \tag{3.50}$$

with the quadratic forms:

$$Q_1 = 3\sum_i\left(\frac{(u_i-\tilde\gamma x_i)^2}{(1-\tilde\gamma^2)} + x_i^2\right), \tag{3.51}$$
$$Q_3 = 105\left(x_{123}^2 + \sum_{i=1}^{3}(v_i^2+w_i^2)\right),$$
$$= \frac{35}{2}\,\overline{x}_{ijk}\overline{x}_{ijk}\,. \tag{3.52}$$

3.A.2 Two point PDFs

Calling $\mathbf{x} = (x, x_i, x_{ij}, x_{ijk})$ and $\mathbf{y} = (y, y_i, y_{ij}, y_{ijk})$, the Joint PDF reads

$$\mathcal{P}_2(\mathbf{x},\mathbf{y}) = \frac{\exp\left[-\frac{1}{2}\begin{pmatrix}\mathbf{x}\\ \mathbf{y}\end{pmatrix}^{\mathrm{T}}\cdot\mathbf{C}^{-1}\cdot\begin{pmatrix}\mathbf{x}\\ \mathbf{y}\end{pmatrix}\right]}{\det|\mathbf{C}|^{1/2}\,(2\pi)^{15}}\,, \tag{3.53}$$

where $\mathbf{C}$ is the covariance matrix which depends on the separation vectors only because of homogeneity

$$\mathbf{C} = \begin{pmatrix}\mathbf{C_{xx}} & \mathbf{C_{xy}}\\ \mathbf{C_{xy}^{\mathrm{T}}} & \mathbf{C_{yy}}\end{pmatrix}. \tag{3.54}$$

Note that $\mathbf{x}^{\mathrm{T}}\cdot\mathbf{C}_{\mathbf{x}}^{-1}\cdot\mathbf{x}$ is given by $Q_0(x)+Q_2(x)+Q_1(x)+Q_3(x)$, where the Q_i are given by equations (3.44) and (3.52). The cross terms will involve correlations of all components of $\mathbf{x}$ and $\mathbf{y}$

$$\mathbf{C_{xy}} = \langle\mathbf{x}\cdot\mathbf{y}^{\mathrm{T}}\rangle\,. \tag{3.55}$$

The correlation length of the various components of $\mathbf{C_{xy}}$ differ, as higher derivatives decorrelate faster, see figure 3.19. Note that the separations are measured in units of R, whereas the Q_i are independent of R.

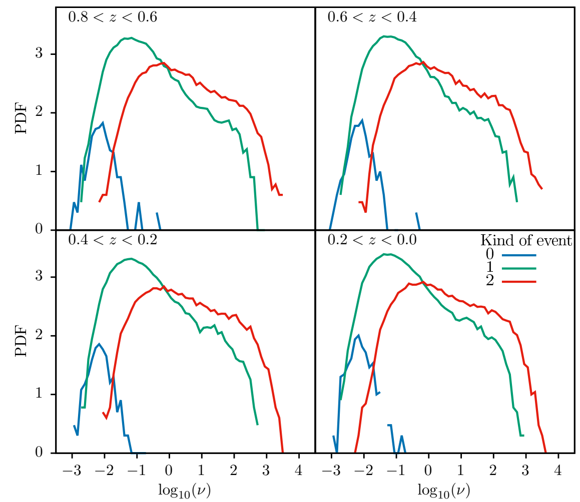

Figure 3.18: PDF of the critical events extracted from the galaxy catalogue of Horizon-AGN as a function of the log galaxy density for a range of cosmic time as labelled. When compared to figure 3.16, the PDFs of the are strongly biased, with much fewer walls hence wall mergers detected. From Nicolas Cornuault, private communications.

counts in 2D as a function of smoothing. Beyond the restricted knowledge of critical points, one could also follow critical lines, surfaces and volumes as a function of cosmic time, hence defining event surfaces, volumes and 4-volume in space time. Conversely, in the context of understanding the impact of black holes on galaxy formation, past AGN activity may be imposed by requiring that one had a set of high density contrast event at very early time.

3.7.6.1 Applications beyond cosmology

The present analysis was mostly restricted to (quasi) Gaussian random fields, because of their relevance in cosmology and also because in this context the theory can be developed in some details (as Gaussian process define a Morse function on a scale-by-scale basis). But the concept of bifurcation of critical points in a one parameter set of random field extends beyond Gaussianity. Any system involving random field controlled by one parameter could in principle be investigated with this framework in order to identify bifurcation/merger of ridges (though the specific role played by Gaussian smoothing would clearly generally not hold). For instance, critical events in dust maps (such as Collaboration, 2018; Meisner and Finkbeiner, 2014) could be used as an alternative statistics to quantify the properties of the underlying turbulence, a process which is known to display self similarities.

A wild range of important physical processes occur when rare events collide, hence boosting probabilities and passing thresholds, which in the context of this work corresponds mergers of rare peaks (e.g. analysing dust map emission or disintegration events in Fermi maps). In this context, the process of interest is the appearance of pairs of critical points as one 'unsmooths' the field: this will corresponds to the generation of pairs of critical points. Following the results of section 3.B.4 formalism could be extended to situations where the field whose evolution is investigated corresponds to probability distributions living in higher dimensions (or on more complex manifolds).

3.7.6.2 Streaming decompression algorithm

In the context of streaming of hierarchical images the set of critical events within a 2D image characterises its multi-scale topology. It would therefore be of interest to send beforehand a description of this set as a mean of prioritising which sub region of the image needs to be streamed first because the topology of its excursion (i.e. the local parsimonious representation of the image as iso-contours) has changed. This would allow the received image to acquire its most important higher resolution features first.

3.8 Conclusion

As a proxy for cosmic evolution, we computed the rate of merging critical points as a function of smoothing scale from the initial cosmic landscape to forecast special events driving the assembly of dark halos and possibly galaxies. We considered all sets of critical points coalescence, including wall-saddle to filament-saddle and wall-saddle to minima, as they impact the topology of galactic infall, such as filament disconnection or void disappearance.

- We studied critical events of all types, their clustering properties, and presented analytical formulae for the one-point statistics of these events in fields of dimensions up to 6.
- We provided covariant formulation of the skeleton tree formalism which allowed us to also compute the two-point statistics for critical events.
- We showed how critical events can be used as tags for machine learning and quantified the effectiveness of such sets or predicting galactic morphology.
- We extended to higher dimensions the count statistics and found asymptotic expression for event counts.
- We related the event count to extrema counts and found consistency relations for the global counts. This yields an analytical prediction of connectivity of peak in four dimension: $\kappa_4 = 200\pi/(75\pi - 114 - 100\cot^{-1}(2)) \approx 8.35$.
- We showed that the correlation of critical events is qualitatively consistent the preservation of the connectivity of dark halos, and that merger rates measured in the frame of cosmic saddles are consistent with assembly bias being driven by the environment.
- Gravitational clustering introduces non Gaussianities which decreases the relative total number of peak mergers. This trend is captured by the Edgeworth expansion of the critical event statistics.
- We discussed briefly other applications in parameter estimation for cosmology, astrophysics and other fields of research.

We have only touched on practical applications for the forecasting of special events in a multi-scale landscape. It should prove to be a fruitful field of research in astronomy and beyond for the next decade.

3.A Joint PDFs

Let us present here the PDF of the field and its (up to 3rd) derivative which will allow us to compute the expectations involved in the main text.

3.A.1 One point PDFs

Since the odd and even variables of Gaussian random fields do not correlate, let us write the joint PDF as $P_{\rm G} = P_0(x, x_{kl})P_1(x_i, x_{ijk})$. The expression for $P_0(x, x_{kl})$ for the Gaussian field was first given by Bardeen et al., 1986. Introducing the variables

$$u \equiv -\Delta x = -(x_{11} + x_{22} + x_{33})\,, \tag{3.41}$$

$$w \equiv \frac{1}{2}(x_{11} - x_{33})\,, \tag{3.42}$$

$$v \equiv \frac{1}{2}(2x_{22} - x_{11} - x_{33})\,, \tag{3.43}$$

in place of diagonal elements of the Hessian (x_{11}, x_{22}, x_{33}) one finds that $u, v, w, x_{12}, x_{13}, x_{23}$ are uncorrelated. Importantly, the field, x is only correlated with u and

$$\langle xu\rangle = \gamma, \quad \langle xv\rangle = 0, \quad \langle xw\rangle = 0, \quad \langle xx_{kl}\rangle = 0,\ k \neq l,$$

where γ is the same quantity as in equation (2.91). The full expression of $P_0(x, x_{kl})$ is then

$$P_0(x, x_{kl}) = \frac{5^{1/2}15^2}{(2\pi)^{7/2}(1-\gamma^2)^{1/2}} \exp\left(-\frac{1}{2}\left[Q_0 + Q_2\right]\right)\,,$$

with the quadratic forms Q_0 and Q_2 given by

$$Q_0 = x^2 + \frac{(u-\gamma x)^2}{(1-\gamma^2)} \tag{3.44}$$

$$Q_2 = 5v^2 + 15(w^2 + x_{12}^2 + x_{13}^2 + x_{23}^2) = \frac{15}{2}\,\overline{x}_{ab}\overline{x}_{ab}\,, \tag{3.45}$$

where the last identity is demonstrated in Pogosyan et al., 2009 and involves the detraced tensors:

$$\bar{t}_{ij} = t_{ij} - \frac{1}{3}t_{aa}\delta_{ij}\,, \tag{3.46}$$

$$\bar{t}_{ijk} = t_{ijk} - \frac{3}{5}\,t_{aa(j}\delta_{kl)}\,, \tag{3.47}$$